

TECHNISCHE UNIVERSITÄT MÜNCHEN

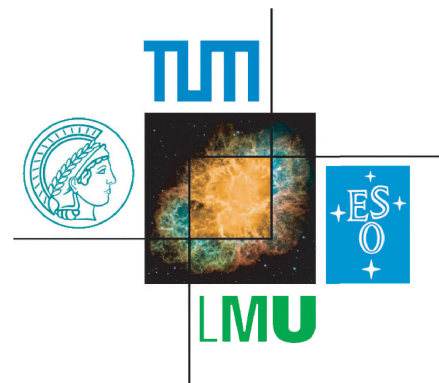
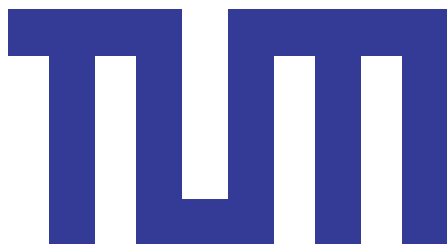
Physik-Department E12 - Dense and strange hadronic matter

Strange baryonic resonances below the  $\bar{K}N$  threshold

-

Results from  $p + p$  reactions at the HADES  
experiment

Johannes Stephan Siebenson





# TECHNISCHE UNIVERSITÄT MÜNCHEN

Physik-Department E12 - Dense and strange hadronic matter

## Strange baryonic resonances below the $\bar{K}N$ threshold

-

## Results from $p + p$ reactions at the HADES experiment

Johannes Stephan Siebenson

Vollständiger Abdruck der von der Fakultät für Physik der Technischen Universität München zur Erlangung des akademischen Grades eines

Doktors der Naturwissenschaften (Dr. rer. nat.)

genehmigten Dissertation.

Vorsitzender: Univ.-Prof. Dr. Norbert Kaiser

Prüfer der Dissertation: 1. Univ.-Prof. Dr. Laura Fabbietti

2. Univ.-Prof. Dr. Stefan Schönert

Die Dissertation wurde am 28.02.2013 bei der Technischen Universität München eingereicht und durch die Fakultät für Physik am 18.04.2013 angenommen.



## Zusammenfassung

Die Eigenschaften von Kaonen ( $K$ ) und Anti-Kaonen ( $\bar{K}$ ) in Kernmaterie wurden in den vergangenen Jahren vielfach untersucht, da sie von großer Bedeutung für das Verständnis der nuklearen Zustandsgleichung sind. Im Allgemeinen wird erwartet, dass Anti-Kaonen im Kernmedium einem attraktiven Potential ausgesetzt sind und ihre effektive Masse als Funktion der Dichte abnimmt. Dies könnte zur Folge haben, dass bei hohen Kerndichten Kaon-Kondensate auftreten, was wiederum enormen Einfluss auf die Kompressibilität von Neutronensternen haben könnte. Die Produktion von Kaonen in Schwerionenkollisionen unterhalb der Schwellenenergie wurde von der KaoS und der FOPI Kollaboration an der Gesellschaft für Schwerionenforschung (GSI) untersucht. Dabei wurden Hinweise auf eine abnehmenden Anti-Kaon Masse in Kernmaterie entdeckt. Allerdings erweist sich die Interpretation der Daten als sehr kompliziert. Ein Grund dafür ist, dass die In-Medium-Eigenschaften der Anti-Kaonen stark durch ihre Kopplung an Hyperon-Resonanzen beeinflusst werden. Von großer Bedeutung sind dabei die s-Wellen Resonanz  $\Lambda(1405)$  und die p-Wellen Resonanz  $\Sigma(1385)$ , welche beide unterhalb der  $\bar{K}N$  Schwelle liegen. Da es sich bei dem  $\Lambda(1405)$  um ein molekülähnliches Teilchen, bestehend aus einem quasi-gebundenen  $\bar{K}N$  Zustand und einer  $\pi\Sigma$  Resonanz, handelt, ist dessen Spektralfunktion besonders eng mit der  $\bar{K} - N$  Wechselwirkung bei niedrigen Energien verknüpft. Um die Eigenschaften von Anti-Kaonen in Kernmaterie vorhersagen und die experimentellen Daten richtig interpretieren zu können, müssen daher zunächst die Vakuumeigenschaften der Hyperon-Resonanzen  $\Lambda(1405)$  und  $\Sigma(1385)$  genau verstanden sein.

Aus diesem Grund untersucht die vorliegende Arbeit die Produktion von  $\Sigma(1385)^+$  und  $\Lambda(1405)$  in Proton-Proton Reaktionen bei 3.5 GeV kinetischer Energie. Die analysierten Daten stammen von dem HADES Experiment an der GSI und wurden im Jahre 2007 aufgenommen. Da es zurzeit keine vergleichbaren Messungen in diesem Energiebereich und diesem Stoßsystem gibt, können die präsentierten Ergebnisse neue Einblicke in die Vakuumeigenschaften und Produktionsmechanismen von  $\Lambda(1405)$  und  $\Sigma(1385)$  verschaffen.

Im ersten Teil der Arbeit wird die Rekonstruktion des  $\Sigma(1385)^+$  in der Reaktion  $p + p \rightarrow \Sigma(1385)^+ + n + K^+$  diskutiert. Um das physikalisch interessante Signal extrahieren zu können, musste zunächst der durch Fehlidentifizierung von Teilchen verursachten Untergrund verstanden und modelliert werden. Dazu wurde eine spezielle Sideband Methode verwendet. Des Weiteren wurde ein Simulationsmodell entwickelt, das die experimentellen Daten in allen Observablen beschreiben kann. Dieses Modell wurde anschließend verwendet, um die Daten auf Akzeptanz und Effizienz zu korrigieren. Mit Hilfe dieser Methoden konnten schließlich die Breit-Wigner Masse und Breite der  $\Sigma(1385)^+$  Resonanz zu  $m_0 = 1383.2 \pm 0.8_{-1.5}^{+0.1}$  MeV/c<sup>2</sup> und  $\Gamma_0 = 40.2 \pm 2.1_{-2.8}^{+1.2}$  MeV/c<sup>2</sup> extrahiert werden. Der totale Wirkungsquerschnitt für die obige Reaktion wurde zu  $\sigma = 22.42 \pm 0.99 \pm 1.57_{-2.23}^{+3.04}$   $\mu\text{b}$  bestimmt. Zusätzlich wurden differentielle Wirkungsquerschnitte für die Winkelverteilungen in den Center-of-mass-, Gottfried-Jackson- und Helizitäts-Bezugssystemen untersucht. Die beobachteten Winkelverteilungen deuten darauf hin, dass das  $\Sigma(1385)^+$  bevorzugt in peripheren Reaktionen durch den Austausch von leichten Mesonen, wie Pionen oder Kaonen, produziert wird. Außerdem zeigen die Verteilungen im Helizitäts-Bezugssystem Hinweise darauf, dass das  $\Sigma(1385)^+$  teilweise aus dem Zerfall einer schweren  $\Delta$  Resonanz stammt ( $p + p \rightarrow \Delta^{++} + n \rightarrow (\Sigma(1385)^+ + K^+) + n$ ).

Da die präsentierten Daten vollständig korrigiert wurden, sind sie optimal geeignet, um mit zukünftigen Theorierechnungen verglichen zu werden. Das ermöglicht, einen genauen Einblick in die verschiedenen Produktionsmechanismen dieses Teilchens zu bekommen. Des Weiteren können die Daten dazu verwendet werden, durch eine genauere Behandlung der  $\Sigma(1385)$  Reso-

nanz, Transportmodelle weiter auszubauen. Das wird ein entscheidender Schritt sein, um die in Schwerionenkollisionen beobachteten Kaon- und Anti-Kaon-Verteilungen richtig zu interpretieren.

Der zweite Teil der Arbeit bezieht sich auf die Reaktion  $p + p \rightarrow \Lambda(1405) + p + K^+$ , wobei das  $\Lambda(1405)$  in den  $\Sigma^\pm \pi^\mp$  Zerfallskanälen rekonstruiert wurde. Die Analyse dieses Prozesses basierte auf einigen Methoden, die schon für die Rekonstruktion des  $\Sigma(1385)^+$  entwickelt wurden. Differenzielle Verteilungen wurden mit Hilfe eines Simulationsmodells beschrieben, das zusätzliche Reaktionen, wie zum Beispiel  $p + p \rightarrow \Sigma(1385)^0 + p + K^+$ ,  $p + p \rightarrow \Lambda(1520) + p + K^+$  und  $p + p \rightarrow \Sigma^- + \Delta^{++}(1232) + K^+$ , beinhaltet. Aus den korrigierten Daten konnten dann Wirkungsquerschnitte für all diese Reaktionen bestimmt werden. Diese sind wiederum wichtige Eingangsparameter für Transportmodelle. Ein interessantes Ergebnis dieser Arbeit ist die Beobachtung, dass das  $\Lambda(1405)$  eine Verschiebung zu einer kleineren Masse als seiner nominellen Masse aufweist. Dies ist überraschend, da die meisten gemessenen Spektralverteilungen des  $\Lambda(1405)$  Massen um oder über  $1405 \text{ MeV}/c^2$  ergeben. Um diese Massenverschiebung zu verstehen, wurden mehrere Interpretationsmöglichkeiten untersucht. Diese basieren zum einen auf neuen theoretischen Rechnungen. Zum anderen wurde ein eigenes Modell entwickelt, das die Massenverschiebung auf Interferenzen zwischen dem  $\Lambda(1405)$  Signal und dem nicht-resonanten Untergrund zurück führen kann. Die präsentierten Spektralverteilungen des  $\Lambda(1405)$  können außerdem mit weiteren, zukünftigen Theorierechnungen verglichen werden, was hoffentlich zu einem verbesserten Verständnis der Anti-Kaon - Nukleon Wechselwirkung bei kleinen Energie beiträgt.

Im letzten Teil der Arbeit werden Tests zum Auflösungsvermögen und zur Strahlungshärte von  $n^+p$  Siliziumdetektoren vorgestellt. Diese Detektoren bilden das Herzstück des Pion Trackers CERBEROS, welcher für eine zukünftige Pionen-Strahlzeit am HADES Experiment verwendet werden soll. Pion-induzierte Reaktionen vervollständigen das HADES Programm, das bis dato nur auf Schwerionenkollisionen und Proton-induzierte Reaktionen konzentriert war. In dieser kommenden Pion-Strahlzeit sind weitere Untersuchungen der  $\Lambda(1405)$  und  $\Sigma(1385)$  Resonanz geplant. Zusätzlich sollen die Eigenschaften von Kaonen und Anti-Kaonen in kalter Kernmaterie untersucht werden. Zusammen mit den hier erzielten Ergebnissen aus  $p + p$  Reaktionen kann HADES damit einen wichtigen Beitrag zu dem vorgestellten Forschungsgebiet liefern.

## Abstract

The properties of kaons ( $K$ ) and anti-kaons ( $\bar{K}$ ) in nuclear matter have been investigated extensively in the last years because they are of great importance for the understanding of the nuclear equation of state. In general, it is expected that anti-kaons experience an attractive potential in the nuclear medium so that their effective mass decreases as a function of density. This could lead to the formation of kaon condensates at high densities, which, on the other hand, would have crucial impact on the compressibility of neutron stars.

The sub-threshold production of kaons in heavy ion collision was studied by the KaoS and FOPI collaboration at the Gesellschaft für Schwerionenforschung (GSI). In these studies hints for a dropping anti-kaon mass in nuclear matter were found. However, it turns out that the interpretation of the data is very complicated. One reason for this is that the in-medium properties of anti-kaons are strongly influenced by their coupling to hyperon resonances. Especially important are the s-wave resonance  $\Lambda(1405)$  and the p-wave resonance  $\Sigma(1385)$ , both located below the  $\bar{K}N$  threshold. As the  $\Lambda(1405)$  is considered as a molecular like particle, consisting of a  $\bar{K}N$  quasi-bound state and a  $\pi\Sigma$  resonance, its spectral shape is intimately linked to the low energy  $\bar{K} - N$  interaction. Therefore, in order to make reliable predictions on the in-medium properties of anti-kaons and to interpret the experimental data correctly, it is crucial that the vacuum properties of the hyperon resonances are well understood.

Following this line of reasoning, the present work investigates the production of  $\Sigma(1385)^+$  and  $\Lambda(1405)$  in proton-proton reactions at 3.5 GeV kinetic energy. The analyzed data stem from the HADES experiment at GSI and were recorded in the year 2007. Since there are currently no comparable measurements available in the studied energy range and collision system, the presented results can provide new insight into the vacuum properties and production mechanisms of  $\Lambda(1405)$  and  $\Sigma(1385)$ .

In the first part of this thesis, the reconstruction of the  $\Sigma(1385)^+$  in the reaction  $p + p \rightarrow \Sigma(1385)^+ + n + K^+$  is described. In order to extract the physically relevant signal, it was necessary to understand and model the background due to particle misidentification. For this purpose, a dedicated sideband method was used. Furthermore, a simulation model was developed, which is able to describe the experimental data in all observables. This model was then used to apply acceptance and efficiency corrections to the data. With help of this method the Breit-Wigner mass and width of the  $\Sigma(1385)^+$  resonance could be extracted to  $m_0 = 1383.2 \pm 0.8_{-1.5}^{+0.1}$  MeV/ $c^2$  and  $\Gamma_0 = 40.2 \pm 2.1_{-2.8}^{+1.2}$  MeV/ $c^2$ . The total cross section of the reaction from above was determined to  $\sigma = 22.42 \pm 0.99 \pm 1.57_{-2.23}^{+3.04}$   $\mu b$ . Additionally, the differential cross sections for the angular distributions in the center-of-mass-, Gottfried-Jackson- and helicity-reference frames are presented. The observed angular distributions indicate that the  $\Sigma(1385)^+$  is preferably produced in peripheral reactions via the exchange of light mesons, like pions or kaons. Moreover, the distributions in the helicity-reference frame show clear indications that the  $\Sigma(1385)^+$  partially stems from the decay of a heavy  $\Delta$  resonance ( $p + p \rightarrow \Delta^{++} + n \rightarrow (\Sigma(1385)^+ + K^+) + n$ ).

As the presented data are fully corrected, they are perfectly suited to be compared to future theory models. This will allow to get insight into the different production mechanisms of the particle. The data can also be used to extend present transport models by a more precise treatment of the  $\Sigma(1385)$  resonance. This will be an important step towards a reliable interpretation of the kaon and anti-kaon distributions measured in heavy ion collisions.

The second part of the thesis is devoted to the reaction  $p + p \rightarrow \Lambda(1405) + p + K^+$ , where the  $\Lambda(1405)$  was reconstructed in the  $\Sigma^\pm \pi^\mp$  decay channels. The analysis of this process was based

on several methods which have already been developed for the reconstruction of the  $\Sigma(1385)^+$ . Differential distributions were again described with help of a simulation model, which accounts for additional reactions like, for example,  $p + p \rightarrow \Sigma(1385)^0 + p + K^+$ ,  $p + p \rightarrow \Lambda(1520) + p + K^+$  and  $p + p \rightarrow \Sigma^- + \Delta^{++}(1232) + K^+$ . The corrected data were then used to extract cross sections for all those reactions. These are important input parameters for transport models. An interesting result of this work is that the  $\Lambda(1405)$  shows a shift to masses below its nominal mass. This is surprising, as most of the measured spectral shapes of the  $\Lambda(1405)$  provide masses around or above  $1405 \text{ MeV}/c^2$ . In order to understand this mass shift, several possible interpretations were investigated. These interpretations are, one the one side, based on new theoretical calculations. On the other side, an own model was developed, which can trace back the observed mass shift to interferences between the  $\Lambda(1405)$  signal and the non-resonant background. Furthermore, the presented spectral shapes of the  $\Lambda(1405)$  can be compared to additional, upcoming theoretical approaches, which will hopefully contribute to an improved understanding of the low energy anti-kaon - nucleon dynamics.

In the last part of the thesis, tests of the resolution and radiation hardness of  $n^+p$  silicon detectors are presented. These detectors will be the core of the pion tracker CERBEROS, which will be used for an upcoming pion beam time at the HADES experiment. Pion-induced reactions will complement the HADES program, which till now was focused on heavy ion collisions and proton-induced reactions. In this future pion beam time, further investigations of the  $\Lambda(1405)$  and  $\Sigma(1385)$  resonances are planned. Additionally, the properties of kaons and anti-kaons in cold nuclear matter will be studied. Together with the obtained results on  $p + p$  reactions, HADES will provide an important contribution to the presented research topic.

# Contents

<b>1</b>	<b>Introduction</b>	<b>1</b>
1.1	Strong interaction and the QCD phase diagram . . . . .	1
1.2	Chiral symmetry and the origin of hadron masses . . . . .	3
1.3	In-medium properties of kaons . . . . .	5
1.4	$\bar{K}N$ dynamics and the $\Lambda(1405)$ hyperon . . . . .	8
1.5	Kaonic nuclear clusters . . . . .	15
1.6	Motivation and aims of this work . . . . .	16
<b>2</b>	<b>The HADES experiment</b>	<b>19</b>
2.1	Detector system . . . . .	20
2.1.1	The target . . . . .	20
2.1.2	The RICH detector . . . . .	21
2.1.3	The magnet . . . . .	21
2.1.4	The MDC chambers . . . . .	21
2.1.5	The META system . . . . .	22
2.1.6	The Forward Wall . . . . .	23
2.1.7	Trigger decision and data acquisition . . . . .	23
2.1.8	The $p + p$ experiment at 3.5 GeV . . . . .	24
2.2	Particle identification . . . . .	24
2.2.1	Identification via energy loss . . . . .	25
2.2.2	Time-of-flight reconstruction . . . . .	26
2.2.3	Invariant and missing mass technique . . . . .	27
2.3	Simulations . . . . .	27
2.3.1	Simulation tools . . . . .	28
2.3.2	Acceptance and efficiency corrections . . . . .	28
<b>3</b>	<b>Measurement of the <math>\Sigma(1385)^+</math> resonance in proton-proton interactions</b>	<b>33</b>
3.1	$\Sigma(1385)^+$ production in proton-proton reactions - General considerations . . . . .	34
3.1.1	$\Sigma(1385)^+$ production and decay . . . . .	34
3.1.2	Production mechanisms and reference frames . . . . .	35
3.1.2.1	The One-Boson-Exchange model . . . . .	35
3.1.2.2	CMS angle . . . . .	38
3.1.2.3	Gottfried-Jackson angle . . . . .	39
3.1.2.4	Helicity angle . . . . .	40
3.1.2.5	$\Sigma(1385)^+$ decay distribution . . . . .	41
3.2	Analysis procedure . . . . .	44
3.2.1	Data selection . . . . .	44
3.2.1.1	Particle identification . . . . .	44
3.2.1.2	$\Lambda(1116)$ and neutron reconstruction . . . . .	46
3.2.2	Background description and signal extraction . . . . .	49

3.3	Angular distributions, simulation model and efficiency corrections . . . . .	54
3.3.1	$\Sigma(1385)^+$ angular distribution in the CMS . . . . .	54
3.3.2	Neutron angular distribution in the CMS . . . . .	56
3.3.3	Helicity angle in the $n - K^+$ reference frame . . . . .	58
3.3.4	Development and tuning of the simulation model . . . . .	61
3.4	Results and discussion . . . . .	64
3.4.1	$\Sigma(1385)^+$ line shape and properties . . . . .	64
3.4.2	Angular distributions and production cross section . . . . .	66
3.4.3	Decay angular distribution of the $\Sigma(1385)^+$ . . . . .	69
3.4.4	Summary . . . . .	70
<b>4</b>	<b>Search for the <math>\Lambda(1405)</math> hyperon in proton-proton reactions</b>	<b>73</b>
4.1	General analysis procedure . . . . .	73
4.1.1	Data selection . . . . .	75
4.1.2	Extraction of the $\Sigma$ hyperons . . . . .	78
4.1.3	$\Lambda(1405)$ spectra . . . . .	79
4.2	Evaluation of the simulation model . . . . .	82
4.2.1	The contribution of $\Delta(1232)$ and $K^{*0}(892)$ . . . . .	82
4.2.2	Angular distributions in the CMS . . . . .	84
4.2.3	CMS angles, G-J angles and helicity angles . . . . .	86
4.3	Results and discussion . . . . .	90
4.3.1	Corrected mass spectra . . . . .	90
4.3.2	Cross sections . . . . .	92
4.3.3	Interpretation . . . . .	96
4.3.3.1	$\Lambda(1405)$ or $\Sigma(1385)^0$ ? . . . . .	96
4.3.3.2	Comparison to other experiments . . . . .	97
4.3.3.3	Interpretation in the phenomenological approach . . . . .	101
4.3.3.4	What about interference effects? . . . . .	103
4.3.3.5	Summary . . . . .	108
<b>5</b>	<b>The HADES pion tracker</b>	<b>111</b>
5.1	Pion beam physics and the pion tracker CERBEROS . . . . .	111
5.1.1	Physics motivation . . . . .	111
5.1.2	The pion tracker project . . . . .	113
5.2	Resolution and efficiency of the silicon detectors . . . . .	115
5.2.1	Signal to noise ratio . . . . .	116
5.2.2	Detector efficiency . . . . .	118
5.3	Radiation hardness . . . . .	119
5.3.1	The NIEL hypothesis . . . . .	120
5.3.2	Leakage current measurement at MLL . . . . .	121
<b>6</b>	<b>Summary and Outlook</b>	<b>127</b>
<b>A</b>	<b>Appendix to the <math>\Sigma(1385)^+</math> analysis</b>	<b>131</b>
A.1	Origin of the background . . . . .	131
A.2	Sideband method . . . . .	133
A.3	Different Breit-Wigner parameterizations . . . . .	137
A.4	Acceptance and efficiency corrections . . . . .	139

---

A.5	Test of the simulation model . . . . .	144
<b>B</b>	<b>Appendix to the <math>\Lambda(1405)</math> analysis</b>	<b>149</b>
B.1	Extraction of the differential cross section for $\cos(\theta_{CMS}^{A*})$ . . . . .	149
B.2	Further tests of possible contributing reactions . . . . .	154
B.3	Additional angular distributions . . . . .	155
B.4	Parameterization of $C_{eff}(m)$ and $T_{\Sigma\pi}$ . . . . .	160
<b>C</b>	<b>Appendix to the pion tracker tests</b>	<b>163</b>
C.1	Signal-noise separation of the remaining silicon detectors . . . . .	163
C.2	Determination of $\beta$ . . . . .	164
	<b>Bibliography</b>	<b>167</b>
	<b>Danksagung</b>	<b>179</b>



# 1 Introduction

## 1.1 Strong interaction and the QCD phase diagram

The theoretical framework of Quantum Chromo Dynamics (QCD) describes the strong interaction between quarks and gluons, the fundamental constituents of atomic nuclei. The name “chromo” has its origin in the definition of a color charge, which is carried by the quarks and the gluons and which is used to define a local symmetry. In fact, QCD is a non-abelian  $SU(3)$  gauge theory, in which the gauge bosons, namely the gluons, carry color charge as well. This leads to interesting phenomena like gluon-gluon coupling, color confinement and asymptotic freedom.

Color confinement is an effect which appears at low energies or equivalently at large distances. In this regime, the interaction strength between quarks and gluons gets such large that quarks and gluons can never be observed as isolated or free particles. Instead, hadronization sets in, where several quarks accumulate to colorless objects, the so-called hadrons. Two types of hadrons have yet been confirmed experimentally. Mesons are hadrons which consist of a quark - anti-quark pair. These are unstable particles, which decay after a certain time (e.g.  $\pi^- \rightarrow \mu^- + \bar{\nu}_\mu$ ). The second hadron type are the baryons, which consist of three constituent quarks. Baryons are in general unstable, too. Only the lightest baryons, the proton and approximately the neutron, are stable.

From the theoretical point of view it is difficult to describe the hadronic phase of matter since the strong coupling constant  $\alpha_S$  is large in this energy regime and the QCD Lagrangian can thus not be treated perturbatively. Therefore, new methods have been developed like effective field theories (e.g.  $\chi$ PT) with hadrons being the relevant degrees of freedom instead of quarks. With the improvement of the computational power also lattice QCD becomes more and more important and successful in the description of the confined phase of nuclear matter [Gup97].

A second characteristic phenomenon of QCD is called asymptotic freedom. It tells us that the strong force becomes weak at small distances or equivalently at large energy or momentum transfer reactions. Associated with this is a decreasing coupling constant  $\alpha_S$ , which allows theory to apply perturbative methods in order to make quantitative predictions on those processes. In fact, the asymptotically free behavior of QCD and the energy dependence of  $\alpha_S$  was confirmed experimentally by measurements of multi jet production in high energy  $e^+ - e^-$  annihilation experiments [Bet07]. Asymptotic freedom further implies that at very high temperatures or densities a transition from the confined hadron phase to a deconfined plasma of freely moving quarks and gluons appears. In this so-called Quark-Gluon-Plasma (QGP), hadrons do not exist anymore and quarks and gluons become the relevant degrees of freedom.

These complex, energy dependent structures of strongly interacting matter are summarized in the QCD phase diagram of Figure 1.1. The properties of nuclear matter in the different phases are subject to the nuclear equation of state (EoS), which interrelates macroscopic state variables like temperature  $T$ , density  $\rho$ , pressure  $P$  etc. The determination of the nuclear EoS is one of the major goals of modern nuclear physics as it allows to predict and to understand the properties of

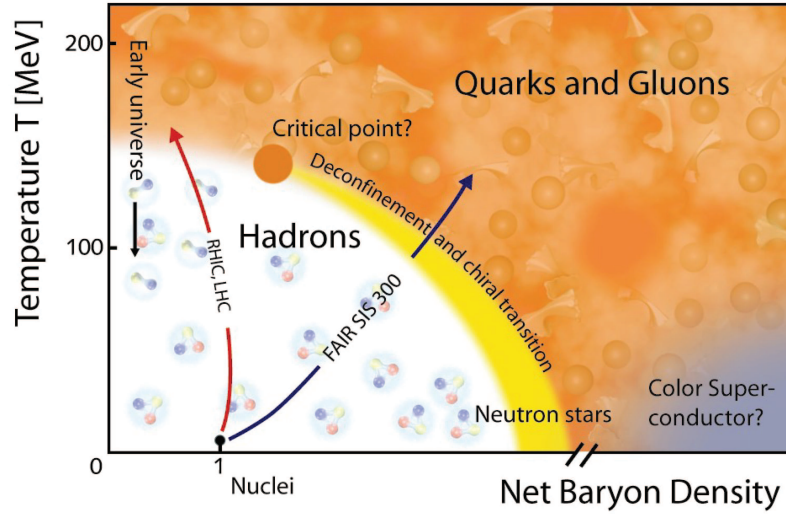


**Figure 1.1:** QCD phase diagram from [Lor08]. The QGP is separated from the hadronic phase by a phase transition of first order. At lower densities a second order phase transition is reached at the critical point. At even lower densities a smooth cross-over replaces the sharp phase transition. At high baryon densities experimentally unexplored phases like a color superconductor are expected to appear.

the universe at extreme conditions, like they appear in supernovae explosions or in the interior of neutron stars. To explore the phase diagram and the EoS is, however, a challenge to physical research and requires the simultaneous understanding of macroscopic and microscopic observables. For this purpose, information from nuclear physics (e.g. properties of the giant monopole resonance), from heavy ion experiments (flow data, particle yields etc.) but also latest findings from astronomy (e.g. neutron star mass measurements) must be combined to a common picture [Dan01].

The phase diagram of Figure 1.1 shows that at low temperatures and low baryo-chemical potentials  $\mu_B$  (low baryon densities  $\rho_B$ ) strongly interacting matter is characterized by the existence of hadrons (hadron gas). With increasing temperature a smooth cross-over to the Quark-Gluon-Plasma (QGP) is expected at  $T_c \approx 170$  MeV. This prediction was already confirmed by lattice QCD calculations [Dan01, FH11]. In fact, it is assumed that the early universe has experienced such a cross-over from the QGP to the hadronic phase at  $\mu_B \approx 0$ . Present high energy heavy ion experiments at LHC and RHIC probe the low density range of the phase diagram and aim to characterize the properties of the QGP (see e.g. [JM12, d'E09, A<sup>+</sup>05a, Esk95]).

For increasing baryon densities, the phase transition happens at lower and lower temperatures. Accompanied with the change from the confined to the deconfined phase is a restoration of the spontaneously broken chiral symmetry (see section 1.2). The exploration of the hadronic phase at moderate densities of 1-3 times normal nuclear density ( $\rho_0 = 0.16 \text{ fm}^{-3}$ ) and temperatures of 80-100 MeV is possible with heavy ion experiments like HADES, FOPI or KaoS, which operate at SIS18 energies of several GeV kinetic energy per nucleon.

The KaoS collaboration, for example, has measured  $K^+$  yields in sub-threshold heavy-ion reactions ( $C + C$  and  $Au + Au$  at 0.8-1.5 GeV per nucleon). Via comparison of their data to transport model predictions, they could conclude that the EoS of isospin symmetric nuclear matter (approximately equal number of protons and neutrons) is rather soft in the tested density region [STC<sup>+</sup>12]. Indeed, kaons ( $K^+$  and  $K^0$ ) are an important probe for testing the nuclear

EoS. In sub-threshold heavy ion collisions, kaons are produced in the early high density phase of the fireball evolution. Their long mean free path allows them to carry the information on their production process out of the collision zone directly to the detectors of the experiment. As the probability of sub-threshold kaon production rises with increasing density, the measured kaon yield is sensitive to the reached degree of compression during the collision.

Another important topic in this research field are the in-medium properties of hadrons. It is expected that hadrons are substantially influenced by the hot and dense nuclear environment in which they are produced. This can result in modified in-medium masses, induced by attractive or repulsive interaction with the surrounding nucleons. Of special interest in this context is the influence of chiral symmetry. In fact, the HADES experiment was designed to find experimental evidence for the onset of chiral symmetry restoration in heavy ion collisions. For this purpose, the electromagnetic decay of mesons like  $\rho$  and  $\omega$  into di-electrons is measured and possible in-medium modifications of those mesons are investigated.

But HADES possesses also excellent capabilities for the identification of particles with strangeness content like, for example, kaons ( $K$ ), anti-kaons ( $\bar{K}$ ),  $\Lambda$ s etc. Indeed, anti-kaons and  $\Lambda$ s are expected to have considerably lower masses when they are embedded into a nuclear medium. As a consequence, the production threshold of these particles is reduced so that the appearance of  $\Lambda$ s and  $\bar{K}$ s might be energetically favorable at high baryon densities. This effect would substantially soften the EoS and was thus assumed to have large impact on the maximum mass of neutron stars [SB08, WCSB12, RBW05]. The recent measurement of a two solar mass neutron star (PSR J1614-2230) [DPR<sup>+</sup>10] can, however, only be explained with a rather stiff EoS, which disfavors the predicted appearance of anti-kaons or  $\Lambda$ s. Also with respect to the measured soft EoS in heavy ion collisions (see discussion above), it is difficult to understand such a high mass neutron star [STC<sup>+</sup>12]. This discrepancy indicates, on the one side, the importance of the symmetry energy, which characterizes the influence of isospin asymmetry on the nuclear EoS. On the other side, it becomes clear that the exploration of the phase diagram and the determination of the nuclear EoS requires a detailed understanding on how the hadron properties are influenced by the nuclear medium.

The present work is related to the study of anti-kaons. As will be shown later, the strong coupling of anti-kaons to hyperon resonances substantially influences their in-medium properties. Of special interest is here the coupling to two hyperons, located below the  $\bar{K}N$  threshold, namely the  $\Lambda(1405)$  and the  $\Sigma(1385)$ . The vacuum properties of the  $\Lambda(1405)$  and the  $\Sigma(1385)$  are investigated in this work.

Before the characteristics of anti-kaons are discussed in more detail, one needs to understand why modification of hadrons are expected at all in the nuclear medium. For this purpose, one has to have a closer look at the origin of the hadron masses itself.

## 1.2 Chiral symmetry and the origin of hadron masses

The origin of the particle masses is a fundamental question in modern physics. With the development of the Higgs mechanism, the finite masses of the gauge bosons  $W^+$ ,  $W^-$  and  $Z^0$ , as well as the masses of the elementary fermions (like quarks) can be understood [Daw94]. The Higgs mechanism alone, however, can still not explain the observed large hadron masses. In fact, the nucleon has a mass of  $m_N \approx 940 \text{ MeV}/c^2$ , while its constituents, the up and the down quarks, have only very small masses of  $m_{u,d} = 5 - 10 \text{ MeV}/c^2$ . The question which arises is therefore: How is it possible that the hadrons which are composed out of the three lightest quarks are

relatively heavy, while the quarks themselves are almost massless (this is at least true for up and down quarks)? The answer to this question is that the hadron masses are generated dynamically by the spontaneous breakdown of chiral symmetry in the physical vacuum.

The QCD Lagrangian is characterized by a number of symmetries. Exactly fulfilled are the local  $SU(3)_{color}$  symmetry and a global  $U(1)$  symmetry, which is responsible for baryon number conservation [RW00]. In the limit of vanishing masses for the three lightest quarks, a global vector and axial-vector symmetry in the  $SU(3)_{flavor}$  space is present as well. These two symmetries can be translated into a  $SU(3)_L \times SU(3)_R$  symmetry, which preserves the handedness (chirality) of left- and right-handed hadrons in strong interaction processes. This is the origin of the name chiral symmetry (chiral is the Greek word for “hand”). By taking into account that the quark masses are finite, chiral symmetry is explicitly broken. Nevertheless, some experimental results, for example on the weak pion decay, suggest that chiral symmetry is still a good symmetry [Koc95].

However, there arises a peculiarity when studying the mass spectrum of mesons. Chiral symmetry implies that hadrons can be connected to each other via chiral transformations, which are isospin and parity transformations [Web11]. Those hadrons must therefore be degenerated, which means that they must have the same mass. When studying the measured meson mass spectrum of Figure 1.2, it becomes clear that isospin symmetry is obviously fulfilled (see e.g.  $\pi^+$ ,  $\pi^-$  and  $\pi^0$  degeneration). On the other hand, the isospin multiplets with different parity are not degenerated at all (see also [S<sup>+</sup>05]). For example, the chiral partner of the  $\rho$  meson, the  $a_1$  meson, is almost two times heavier. This observation seems to contradict a preserved chiral symmetry.

The solution of this issue is that chiral symmetry is spontaneously broken. In analogy to a ferromagnetic system, the spontaneous symmetry breakdown preserves the symmetries of the underlying Lagrangian, but breaks the symmetry of the ground state. As a result, the chiral partners with opposite parity can indeed have different masses, even though the QCD Lagrangian itself is (almost) invariant under chiral symmetry operations. The order parameter quantifying the spontaneous chiral symmetry breaking is the expectation value of the quark condensate  $\langle q\bar{q} \rangle$ . It is non-zero in the physical vacuum. This quark condensate can be understood as a superfluid

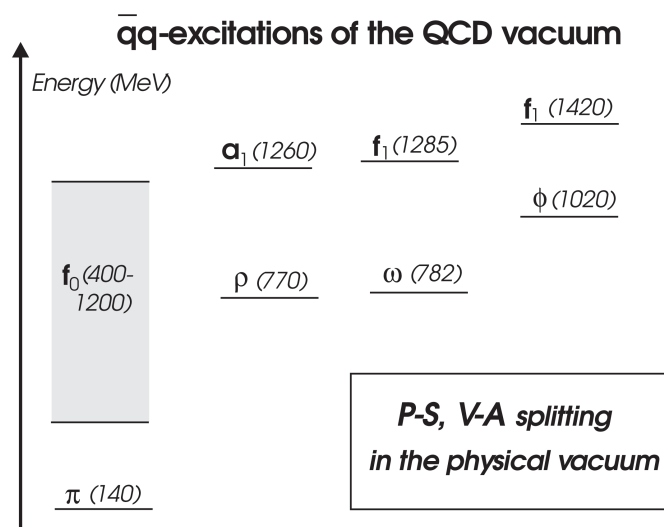


**Figure 1.2:** Experimentally observed mass spectrum of low mass mesons, taken from [RW00].

phase of quark - anti-quark pairs, occupying the physical vacuum [PS95, Ple12]. In this model hadrons are treated as excitations of the chiral condensate.

With the spontaneous breakdown of chiral symmetry eight (almost) massless Goldstone bosons (pions, kaons and the  $\eta$  meson) appear. The fact that the Goldstone bosons are not exactly massless is attributed to the explicit breaking of chiral symmetry by the finite bare quark masses. The pion mass ( $m_\pi \approx 140 \text{ MeV}/c^2$ ) is given by the Gell-Mann-Oakes-Renner relation [Koc95]:

$$m_\pi^2 f_\pi^2 = -\frac{m_u + m_d}{2} \langle 0 | u\bar{u} + d\bar{d} | 0 \rangle \quad (1.1)$$

where  $f_\pi$  is the pion decay constant. The pion mass  $m_\pi$  is indeed determined by the bare quark masses  $m_u$  and  $m_d$ , but also by the spontaneous chiral symmetry breaking and the associated quark condensate expectation value in the vacuum  $\langle 0 | u\bar{u} + d\bar{d} | 0 \rangle$ .

In a similar way the nucleon mass is generated by the effect of chiral symmetry breaking. The linear  $\sigma$ -model in [Koc95] gives the following expression for  $M_N$ :

$$\begin{aligned} M_N &= g_\pi v_0 + \Sigma_{\pi N} \\ \text{with } \Sigma_{\pi N} &= \frac{m_u + m_d}{2} \langle N | u\bar{u} + d\bar{d} | N \rangle \end{aligned} \quad (1.2)$$

The contribution from spontaneous chiral symmetry breaking is determined by the term  $g_\pi v_0$ , whereas the contribution from the explicit symmetry breaking is parameterized in the pion-nucleon sigma-term ( $\Sigma_{\pi N}$ ).

Going from the physical vacuum to finite densities and temperatures, chiral symmetry is expected to be (partially) restored and, as a consequence, the expectation value of the quark condensate  $\langle q\bar{q} \rangle$  should reduce or even vanish. With the considerations from above it is therefore expected that the mass spectrum of hadrons changes significantly when the particles are embedded in a nuclear environment [BR91, Ple12]. This, on the other hand, offers an indirect possibility to explore chiral symmetry restoration. Indeed, the HADES experiment is searching for in-medium mass modifications of vector mesons (e.g.  $\rho$  and  $\omega$ ), produced in heavy ion collisions and decaying into  $e^+e^-$  pairs [A<sup>+</sup>11, A<sup>+</sup>12c]. However, as pointed out in [BLR<sup>+</sup>98], even if such modifications are found, they cannot be easily related to a (partial) restoration of chiral symmetry. In fact, also the coupling of those mesons to nucleon excitations has a considerable impact on their in-medium properties.

For the following thesis the behavior of the strange Goldstone bosons, namely the kaons, is of special interest. Their in-medium properties shall therefore be discussed in more detail in the next part. In this context also the importance of the coupling to strange baryonic resonances like  $\Lambda(1405)$  and  $\Sigma(1385)$  shall be emphasized.

### 1.3 In-medium properties of kaons

Kaons are the lightest mesons with strangeness content. Even though they are considered to be Goldstone bosons, the explicit chiral symmetry breaking via the bare strange quark mass of  $95 \text{ MeV}/c^2$  [B<sup>+</sup>12] results in an observed kaon mass of  $\approx 500 \text{ MeV}/c^2$ . In the vacuum kaons ( $K^+$  and  $K^0$ ) with strangeness  $S = -1$  and anti-kaons ( $K^-$  and  $\bar{K}^0$ ) with strangeness  $S = 1$  are degenerated. This changes in the nuclear medium. In a simple ansatz the interaction between

kaons and nucleons can be handled within chiral perturbation theory ( $\chi$ PT) [RBW05], where at lowest order two s-wave interaction terms contribute. The scalar term is attractive and equal for kaons and anti-kaons. This term is attributed to the breaking of chiral symmetry. The second s-wave term results from vector interactions, called Weinberg-Tomozawa term. It is repulsive for kaons and attractive for anti-kaons [RBW05, HOL<sup>+</sup>12, Fuc06]. In [LSW94] the density dependent kaon mass shift was derived to (see [HOL<sup>+</sup>12]):

$$\Delta m_K^2(\rho) = -\frac{\Sigma_{KN}}{f_K^2} \rho_S - \frac{\Delta f_K^2 m_K^2}{f_K^2} \pm \frac{m_k (\rho_u - \rho_s)}{4f_K^2} + O(m_{u,s}^0) \quad (1.3)$$

From this result, the in-medium mass of kaons is expected to slightly rise with increasing baryon density, whereas the anti-kaon mass should decrease, as it is illustrated in Figure 1.3. The predicted behavior has a major impact on the nuclear EoS at higher densities and with this also on the possible properties of neutron stars. Already Kaplan and Nelson [KN86, NK87] predicted that anti-kaons may condense at densities around  $3\rho_0$ . In neutron star matter, where such densities can easily be reached, neutrons, protons and electrons are in beta equilibrium via processes like  $n \rightarrow p + e^- + \bar{\nu}_e$  and  $p + e^- \rightarrow n + \nu_e$  [RBW05]. As these particles are fermions, they induce a Fermi pressure, which counteracts the gravitational compression. If, however, the anti-kaon mass drops below the chemical potential of electrons ( $\mu_e$ ), processes like  $e^- \rightarrow K^- + \nu_e$  and  $n \rightarrow p + K^-$  become possible. These processes reduce the number of electrons and neutrons and thus reduce the Fermi pressure. On the other hand, kaons are bosons, which can condensate at  $p = 0$ , and they do therefore not induce any additional pressure. Hence, the appearance of kaon condensation softens the EoS substantially. The resulting low incompressibility of the nuclear matter constrains the maximum mass of neutron stars. The reason is that at high masses gravitation is strong enough to shrink the neutron star below its Schwarzschild radius; it transforms into a black hole. In fact, the measurement of a two solar mass neutron star (PSR J1614-2230) [DPR<sup>+</sup>10] excludes most of the theoretical models assuming a very soft EoS induced by kaon condensation.

These considerations illustrate why the determination of the in-medium kaon properties has attracted so much attention in the last decades.

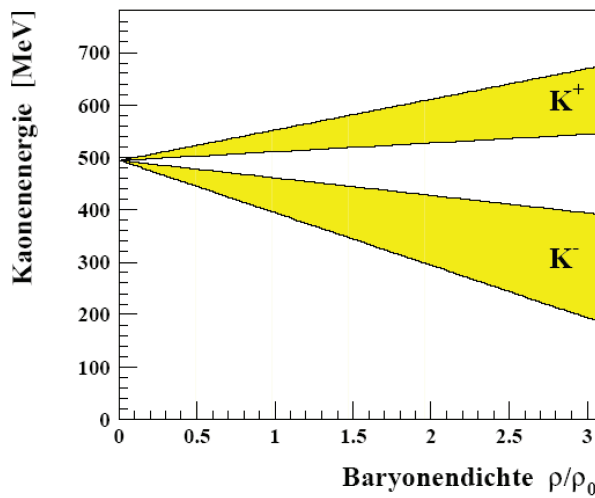
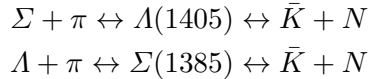


**Figure 1.3:**  $K^+$  and  $K^-$  energy (mass) as a function of baryon density [Stu01]. The yellow bands indicate predictions from several theoretical models.

The situation is already quite clear for kaons. It has been confirmed experimentally that kaons feel a repulsive mean field potential of 20-40 MeV at normal nuclear density [B<sup>+</sup>97, A<sup>+</sup>10], which is in agreement with the predictions from equation (1.3).

For anti-kaons, however, the situation is less satisfying. Indeed, indications for an attractive potential or equivalently a dropping  $K^-$  mass have been found by several experiments. For instance, the measurement of the energy shift in kaonic atoms is sensitive to the anti-kaon properties at nuclear matter densities between 0 and  $\rho_0$ . The obtained experimental results suggest that already at these low densities an attractive interaction between the  $\bar{K}$  and the nucleus is present [FGB94].

Moreover, the FOPI and the KaoS collaboration have analyzed yields and flow patterns of  $K^+$  and  $K^-$  produced in heavy ion collisions and in  $p+A$  reactions [Her96, L<sup>+</sup>99, S<sup>+</sup>06]. By comparison to transport models, they find agreement with the assumption of a repulsive potential for kaons. For anti-kaons, no consistent description is obtained, but some observables indeed point towards an attractive potential. The observation of an enhanced  $K^-/K^+$  ratio in A+A collisions compared to N+N collisions, for example, can be interpreted as an indication that the  $K^-$  mass drops in the medium and thus makes anti-kaon production energetically more easy. The interpretation of those data is, however, complicated. On the one side, the authors of [A<sup>+</sup>09b] have shown that feed-down effects from  $\phi$  meson decay ( $\phi \rightarrow K^+ + K^-$ ) play an important role for the observed  $K^-$  spectra. On the other side, it was emphasized in [RBW05, Lut04, Fuc06] that several inelastic strangeness exchange channels are open, which allow to produce anti-kaons in heavy ion experiments from secondary collisions of hyperons and pions  $Y + \pi \leftrightarrow \bar{K} + N$ . As strangeness exchange is the main source for anti-kaon production in sub-threshold reactions, a detailed understanding of these processes is required in order to interpret the observed  $K^-$  spectra correctly. Especially the strong coupling to the s-wave resonance  $\Lambda(1405)$  and to the p-wave resonance  $\Sigma(1385)$ , both located close below the  $\bar{K}N$  threshold, is important in this context since a dropping anti-kaon mass in the medium could allow for processes like:



A self-consistent many body evaluation of the  $Y + \pi$  in-medium cross section is presented in [Lut04], where the authors find that  $\bar{K}$  production via the  $\Sigma(1385)$  resonance can indeed significantly increase the observed anti-kaon yield. Consequently, they claim that transport model simulations need to incorporate the  $\Sigma(1385)$  production processes. Only in this way they can be used to interpret the observed  $K^-$  spectra. Therefore, it is important to measure the  $\Sigma(1385)$  at SIS energies (see [Lut04]).

On the other hand, it has turned out that the simple  $\chi$ PT ansatz from above is not sufficient to describe the properties of anti-kaons in the nuclear environment (see also discussion in section 1.4). The reason is again the strong coupling of anti-kaons to the strange resonances  $\Lambda(1405)$  and  $\Sigma(1385)$ . Particularly the  $\Lambda(1405)$  turns out to be crucial in this context. Self-consistent coupled channel calculations have been performed to determine the in-medium propagator of the  $\bar{K}$  [RBW05, Lut04, HOL<sup>+</sup>12, RO00]. A typical example of the resulting anti-kaon spectral function is shown in Figure 1.4. The distribution is given for different medium densities and different  $\bar{K}$  momenta ( $q = 0$  GeV/c and  $q = 0.5$  GeV/c). At momentum  $q = 0$  GeV/c, where the spectral function can be correlated to the  $\bar{K}$  mass, the distribution is very broad so that the in-medium  $\bar{K}$  cannot even be considered as a quasi-particle anymore. With increasing densities the spectral function gets more and more weight at lower energies, which is in agreement with the dropping mass scenario of Figure 1.3. An interesting effect is visible at low densities, where

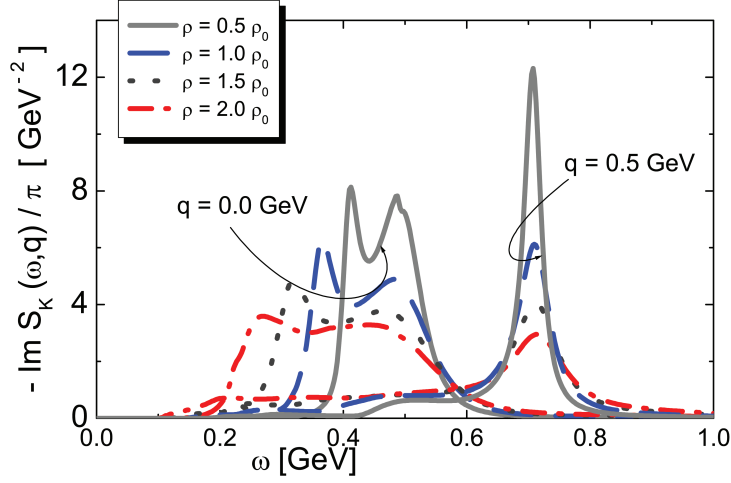


**Figure 1.4:** Anti-kaon spectral function obtained from a self-consistent coupled channel calculation [Lut04]. The function is evaluated at several different nuclear densities and at two different kaon momenta.

a two peak structure is observed. The appearance of such a structure can be understood in a crude picture, proposed in [RBW05]. Here the upper peak is correlated to the dressed  $\bar{K}$  meson, propagating through the nuclear medium. The lower peak can be seen as a second  $\bar{K}$  state, where the strong coupling to strange resonances transforms the anti-kaon to a  $\Lambda(1405)$  - nucleon-hole state. At higher densities the  $\Lambda(1405)$  melts and the two peaks merge into one. For increasing momenta, the anti-kaon partially regains its quasi-particle character, but still shows a very broad low energy tail.

With these considerations it becomes clear that the anti-kaon spectral function in the nuclear medium develops a very complex structure, which cannot be derived from pure  $\chi$ PT. One reason for these structures is the strong coupling to hyperons like  $\Lambda(1405)$ . In [Lut04, HJ12] it was explicitly pointed out that the quantitative determination of the anti-kaon spectral function in the nuclear environment is difficult and needs a good understanding of the anti-kaon - nucleon dynamics in free space. Therefore, it is important to measure the properties of  $\Lambda(1405)$ .

The nature of the  $\Lambda(1405)$  and its important role for the low energy  $\bar{K}N$  dynamics will be discussed in detail in the next section.

## 1.4 $\bar{K}N$ dynamics and the $\Lambda(1405)$ hyperon

The interaction between mesons and baryons in the low energy regime is usually approached within chiral perturbation theory ( $\chi$ PT) [BNW05, HJ12]. This ansatz works well for pion-nucleon and kaon-nucleon interactions, but it fails to describe the  $\bar{K}N$  dynamics. Indeed,  $\chi$ PT predicts an attractive s-wave interaction between anti-kaons and nucleons in the isospin  $I = 0$  configuration and, thus, an attractive potential in the nuclear medium (see Figure 1.3). However, the analysis of  $K^-p$  scattering data [Mar81] came to the result that the  $K^-p$  scattering length  $a^{(0)}$  is negative, which points to a repulsive force between the  $K^-$  and the proton at threshold. This discrepancy to the prediction of  $\chi$ PT is explained with the appearance of the  $\Lambda(1405)$  hyperon. In fact, the interaction between the  $\bar{K}$  and the nucleon is assumed to be sufficient strong to form a quasi-bound state just below the  $\bar{K}N$  threshold (1433 MeV), which is identified with the s-wave  $\Lambda(1405)$

resonance of isospin  $I = 0$ . The appearance of such a state results in a repulsive contribution to the scattering amplitude at threshold [RBW05]. Thus, the existence of the  $\Lambda(1405)$  is crucial for the interpretation of the  $\bar{K} - N$  dynamics.

Today, the Particle Data Group (PDG) [B<sup>+</sup>12] lists the  $\Lambda(1405)$  as a four star resonance with the quantum numbers  $I(J^P) = 0\left(\frac{1}{2}^-\right)$ . Its nominal mass and width are 1405.1 MeV/ $c^2$  and 50 MeV/ $c^2$ , respectively. It decays exclusively via the strong interaction into  $\Sigma^0 + \pi^0$ ,  $\Sigma^+ + \pi^-$  or  $\Sigma^- + \pi^+$ , each channel having a branching ratio of 33.3%. The decay into  $K^- + p$  is not possible because the resonance is located below the  $\bar{K}N$  threshold. Concerning the internal structure of  $\Lambda(1405)$ , the considerations from above suggest that this resonance cannot be treated as a standard 3-quark baryon, but it appears to be a molecular like state, composed (partially) of a  $\bar{K}$  and a nucleon. Indeed, the properties of  $\Lambda(1405)$  are difficult to be interpreted within the quark model. For instance, its nominal mass is about 100 MeV/ $c^2$  smaller than the one of its spin-orbit partner, the  $\Lambda(1520)$  ( $I(J^P) = 0\left(\frac{3}{2}^-\right)$ ). This is different to the non-strange sector, where the  $L = 1$  spin-orbit partners, the  $N(1535)$  and the  $N(1520)$ , are almost degenerated [HJ12]. Another point is the observed line shape, which appears to be different from a usual Breit-Wigner type structure. This anomaly is attributed to the vicinity of the  $\bar{K}N$  threshold.

The theoretical discovery of the  $\Lambda(1405)$  goes back to the year 1959, when Dalitz and Tuan predicted this resonance from the analysis of the measured  $\bar{K}N$  scattering data [DT59, DT60]. Two years later, first experimental evidence for the  $\Lambda(1405)$  was reported by the ALSTON 61B experiment, where the reaction  $K^- p \rightarrow \Sigma \pi \pi \pi$  was investigated and where the  $\Lambda(1405)$  appeared as a resonance structure in the invariant mass spectrum of  $\pi$  and  $\Sigma$  [A<sup>+</sup>61]. In the following years further evidence for this particle was found in  $K^- + p$  and  $\pi^- + p$  reactions [Hem85, TEFK73]. Since the interpretation of those  $\Lambda(1405)$  data within a perturbative theory is not possible, new methods had to be developed. Nowadays, non-perturbative coupled-channel techniques based on the chiral unitary approach are used to handle this issue. In this ansatz, where hadrons are used as the effective degrees of freedom, the  $\Lambda(1405)$  is generated dynamically from the interaction of mesons and baryons. In fact, the  $\Lambda(1405)$  turns out to be an interference of a quasi-bound  $\bar{K}N$  state and a  $\pi\Sigma$  resonance. To understand the dynamical generation of the  $\Lambda(1405)$ , the basic idea behind the coupled-channel approach shall be presented at this point.

The low energy s-wave interaction between the octet of pseudoscalar mesons and the octet of  $J^P = \frac{1}{2}^+$  baryons with total strangeness  $S = -1$  is described within a Lippman-Schwinger equation of the form [HW08, JOO<sup>+</sup>03]:

$$T_{ij}(\sqrt{s}) = V_{ij}(\sqrt{s}) + V_{il}(\sqrt{s})G_l(\sqrt{s})T_{lj}(\sqrt{s}) \quad (1.4)$$

where  $T_{ij}(\sqrt{s})$  is the energy dependent scattering matrix element, representing the scattering amplitude from channel  $i$  into channel  $j$ . The channels  $i$  and  $j$  stand for a certain meson-baryon pair. With Fermi's Golden Rule the differential cross section can be determined from the scattering matrix ( $\left(\frac{d\sigma}{d\Omega}\right)_{ij} \propto |T_{ij}|^2$ ).  $V_{ij}$  is the interaction kernel given, for example, by the leading order Weinberg-Tomozawa term;  $G_l$  is the meson-baryon loop integral, associated with the propagator of the intermediate meson ( $m_l$ ) and baryon ( $M_l$ ):

$$G_l(\sqrt{s}) = i \int \frac{d^4q}{2\pi^4} \frac{2M_l}{[(P-q)^2 - M_l^2 + i\varepsilon] (q^2 - m_l^2 + i\varepsilon)} \quad (1.5)$$

A schematic picture of the recursive equation (1.4) is given in Figure 1.5.

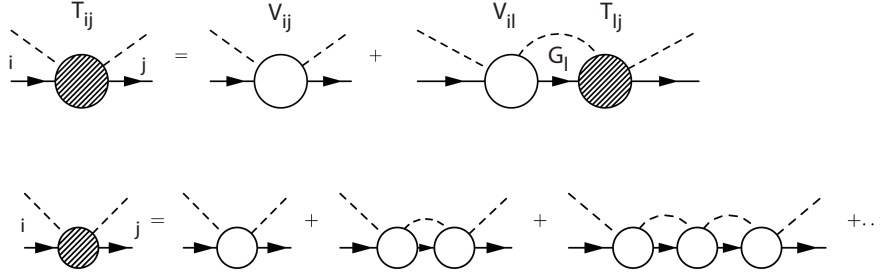


**Figure 1.5:** Illustration of the Lippmann-Schwinger equation (1.4) (upper picture) and the expansion of the Lippmann-Schwinger equation to an infinite sum (lower picture) [HJ12].

In order to calculate the scattering process from channel  $i$  into channel  $j$ , an infinite sum has to be evaluated, where all possible intermediate channels  $l$  can appear. The scattering process is therefore determined by the coupling of different channels.

If only the isospin  $I = 0$  case is considered, the possible contributing channels are:  $\bar{K}N$ ,  $\Sigma\pi$ ,  $\eta\Lambda$  and  $K\Xi$ . However, it turns out that the coupling between the  $\bar{K}N$  and  $\Sigma\pi$  channels is especially strong [HW08], which allows to treat  $T_{ij}$  as an effective  $2 \times 2$  matrix. By solving the Lippmann-Schwinger equation, the obtained scattering matrix  $T_{ij}$  develops two poles in the complex energy plane below the  $\bar{K}N$  threshold (see Figure 1.6) [JOO<sup>+</sup>03, ORB02, HNJH03, BNW05, BMN06, HW08, J<sup>+</sup>10, HJ12]. The first pole, located at  $\approx 1420$  MeV/ $c^2$ , is mainly identified with a quasi-bound  $\bar{K}N$  state, resulting from the strong attraction in this channel. The  $\bar{K} - N$  binding energy can be extracted from this result to 12 MeV. The small imaginary part of the pole ( $Im(z = \sqrt{s})$ ) is correlated to a small decay width  $\Gamma$ . In contrast to this, the second pole is located at lower energies ( $\approx 1390$  MeV/ $c^2$ ), far in the imaginary part of the complex energy plane. This pole is associated with a broad  $\pi\Sigma$  resonance, which couples strongly to the  $\pi\Sigma$  channel.

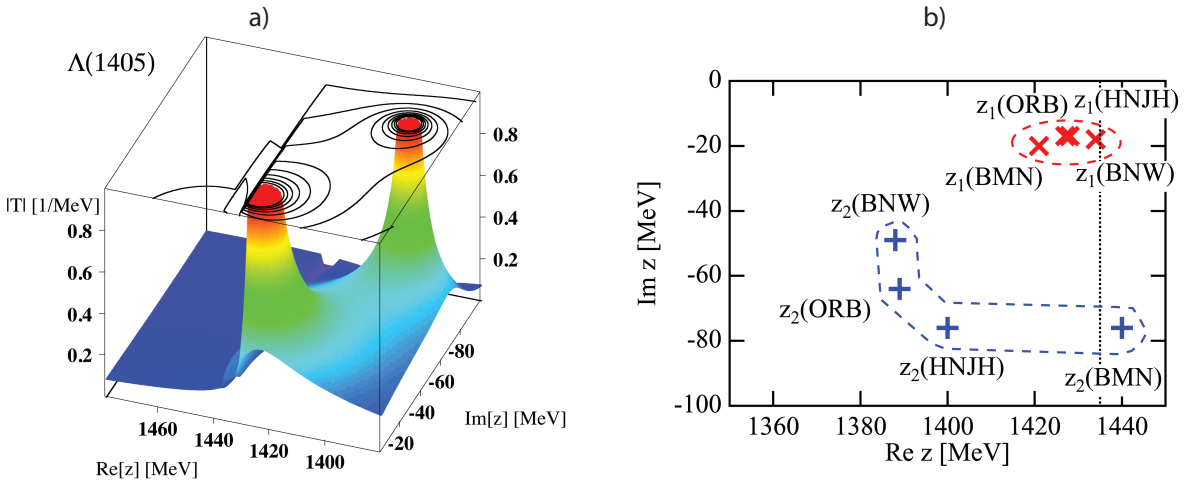


**Figure 1.6:** Double pole structure of  $\Lambda(1405)$ . Panel a) shows a 3-dimensional representation of the scattering matrix  $|T|$  in the complex energy plane ( $Re(z), Im(z)$ ) [HJ12]. Panel b) from [HW08] is a 2-dimensional projection with predictions from different theoretical approaches. The red crosses indicate the position of the first pole, coupling mainly to  $\bar{K}N$ . The blue crosses are the predictions for the  $\pi\Sigma$  pole.

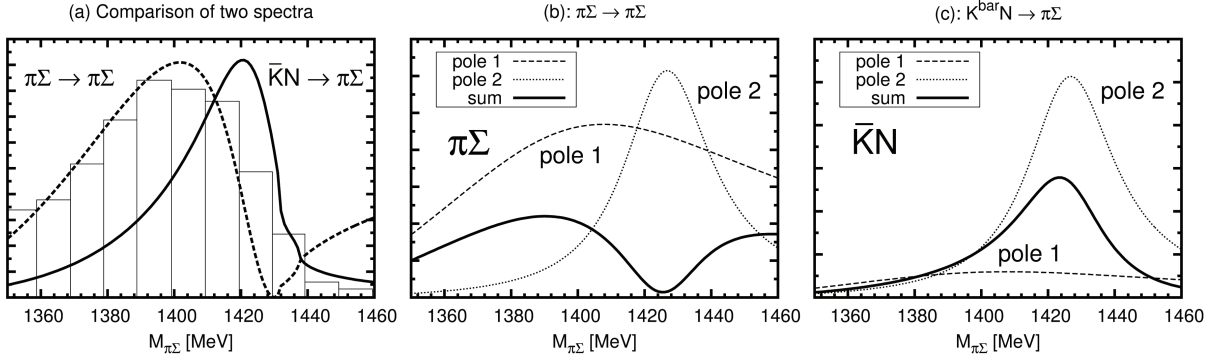


**Figure 1.7:**  $\pi\Sigma$  invariant mass spectra with  $I = 0$  in arbitrary units, taken from [HJ12, J<sup>+</sup>10, JOO<sup>+</sup>03]. Panel a): chiral unitary model calculation of the  $\pi\Sigma$  invariant mass spectra for  $\bar{K}N \rightarrow \pi\Sigma$  (solid line) and  $\pi\Sigma \rightarrow \pi\Sigma$  (dashed line) scattering. The histogram denotes an experimental invariant mass spectrum of the  $\Sigma^+\pi^-$  decay channel of [Hem85]. Panel b) and c) show model calculations of the  $\pi\Sigma$  spectra from the interference of two Breit-Wigner terms. The dashed (dotted) line denotes the spectrum of the first pole (second pole), while the solid line shows the spectrum calculated by the coherent sum of both poles.

The  $\Lambda(1405)$  line shape, observed in the  $\pi\Sigma$  invariant mass distribution, is indeed nothing else than a convolution of these two poles. In this sense the  $\Lambda(1405)$  is a dynamically generated resonance of a quasi-bound  $\bar{K}N$  state and a  $\pi\Sigma$  resonance. Furthermore, since this particle results from the  $\bar{K}N$ - $\pi\Sigma$  channel coupling, its properties are strongly correlated with the  $\bar{K}N$  interaction at low energies.

Exactly this channel coupling leads to an interesting effect: the observed line shape and mass peak of the  $\Lambda(1405)$  depends on the experiment itself (see Figure 1.7). In fact, depending on the scattering entrance channel, different weights can be given to the different poles. In case of  $K^-p$  scattering below threshold, which can for example be realized by off-shell kaons or nucleons, the  $T_{K^-p \rightarrow \pi\Sigma}$  matrix element of equation (1.4) is excited and, as a consequence, dominant weight is given to the first pole. The  $\Lambda(1405)$  mass peak therefore appears around  $1420 \text{ MeV}/c^2$  (see solid line in panel a) and c)). On the other hand, if  $\pi\Sigma$  scattering is realized, the  $T_{\pi\Sigma \rightarrow \pi\Sigma}$  element is excited and large weight is given to the second pole. The  $\Lambda(1405)$  then shows its maximum around  $1405 \text{ MeV}/c^2$  (see dashed line in panel a) and solid line in panel b)).

The predicted entrance channel dependence of the  $\Lambda(1405)$  line shape has been confirmed experimentally. Figure 1.8 compares  $\pi\Sigma$  invariant mass spectra obtained in  $\pi^- + p$  reactions (blue dashed histogram) [TEFK73] and in  $K^- + p$  reactions (solid red histogram) [P<sup>+</sup>04]. As the first reaction is assumed to proceed strongly via the  $\pi\Sigma$  entrance channel [HHO<sup>+</sup>03], the excitation of  $T_{\pi\Sigma \rightarrow \pi\Sigma}$  is large and the obtained spectrum peaks at a low mass of  $\approx 1395 \text{ MeV}/c^2$ . Compared to this, the authors of [MOR05] have shown that the  $K^- + p$  reaction couples strongly to the  $T_{K^-p \rightarrow \pi\Sigma}$  element, resulting in a narrow resonance structure at  $\approx 1420 \text{ MeV}/c^2$ . The theoretical predictions based on these assumptions are shown as vertical dashed lines in Figure 1.8. They are in good agreement with the experimental findings. In [MOR05] these results are interpreted as an evidence for the two pole structure of the  $\Lambda(1405)$ .

Although all these considerations suggest that the  $\bar{K}N$  dynamics and the associated nature of the  $\Lambda(1405)$  are well under control, a detailed understanding is still missing. This becomes evident in Figure 1.9, showing measured  $\Lambda(1405)$  signals in  $\Sigma\pi$  invariant mass spectra in comparison with different theoretical approaches. While the agreement with the data is good for all predictions, the

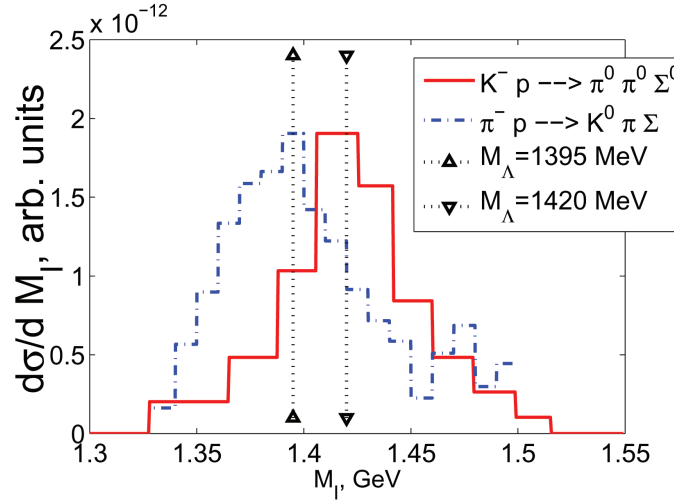


**Figure 1.8:**  $\pi\Sigma$  invariant mass spectra from [TEFK73] and [P<sup>+</sup>04] compared to calculations (vertical dashed lines). The difference in the two line shapes is taken as a proof for the two pole structure of the  $\Lambda(1405)$ . The figure is taken from [MOR05].

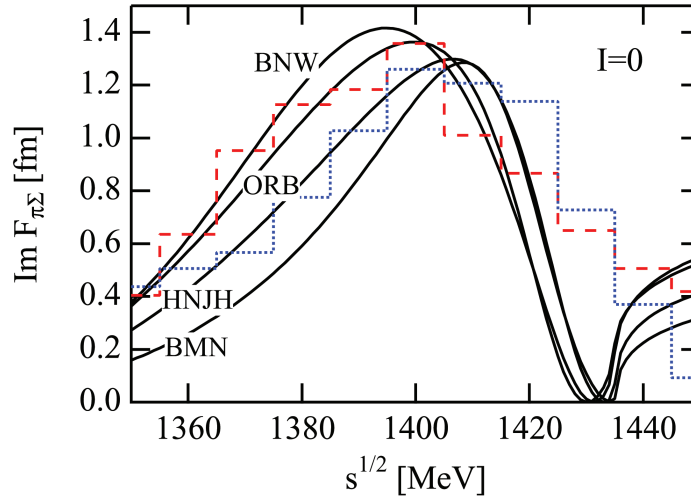


**Figure 1.9:** Comparison of the imaginary part of the  $\pi\Sigma \rightarrow \pi\Sigma$  scattering amplitude from different theoretical approaches (see [HW08]) with experimental data. The red dashed histogram represents data from [TEFK73] in the  $\Sigma^+\pi^-$  decay channel. The blue dotted histogram is a sum of the  $\Sigma^-\pi^+$  and  $\Sigma^+\pi^-$  invariant mass from [Hem85].

different theory models differ quite a lot from each other. These discrepancies are associated with the uncertainties in the position of the second pole  $z_2$  (see Figure 1.6) and are a consequence of the lack of experimental data. In fact, the coupled channel approach works with free parameters, the so-called subtraction constants [HW08]. These constants have to be fixed by fitting the theory model to existing experimental results. In general, one distinguishes between three subclasses of data, which all set important constraints for the model:

- **Above the  $\bar{K}N$  threshold** elastic  $K^-p \rightarrow K^-p$  and inelastic  $K^-p \rightarrow \Sigma\pi$  scattering data constrain the scattering matrix  $T_{ij}$  (see e.g. [IHW11]). The available experimental results are, however, limited in statistic.
- **At the  $\bar{K}N$  threshold** the  $K^-p$  scattering length gets accessible by precision measurements of the energy shift in kaonic hydrogen. In these experiments the electron of hydrogen is replaced by a  $K^-$ . Since the  $K^-$  and the proton wave functions have a certain overlap, they feel already the strong force. This shifts and broadens the energy levels compared to the electro-magnetic expectation values. By measuring the K-series X-rays of kaonic hydrogen, the shift  $\Delta E$  and the width  $\Gamma$  of the 1s state can be reconstructed. With help of the Deser-Trueman formula [DGBT54, BNW05] these observables can be related to the scattering length  $a_{K^-p}$ :

$$\Delta E - \frac{i}{2}\Gamma = \alpha^3 \mu_c a_{K^-p} \quad (1.6)$$

where  $\alpha$  is the fine-structure constant and  $\mu_c$  is the reduced mass of the  $K^-p$  system. Recently, new high precision data on kaonic hydrogen have been published by the SIDDHARTA collaboration [B<sup>+</sup>11]. As these data fix the  $K^-p$  scattering amplitude exactly at threshold, they give important constraints for any extrapolation of the  $\bar{K}N$  dynamics below or above threshold.

- **Below the  $\bar{K}N$  threshold** the kaon-nucleon scattering amplitude can only be constrained indirectly by measuring the  $\pi\Sigma$  mass spectra, where the  $\Lambda(1405)$  resonance appears. As pointed out in [HW08], the quality of existing data on this observable is rather limited, which is the main reason for the uncertainties between the different theory models.

Therefore, new experimental effort has been started aiming to remeasure the  $\Lambda(1405)$  and to improve the situation in this way. In the sector of  $\gamma$ -induced reactions the CLAS collaboration has recently taken high statistic data sets of  $\gamma+p \rightarrow \Lambda(1405)+K^+$  reactions at different incident  $\gamma$  energies [MS10]. The reconstruction of the  $\Lambda(1405)$  has been achieved for all three decay channels. First results on the corresponding  $\pi\Sigma$  invariant mass distributions are shown in Figure 1.10 a). As expected, the spectral shape of the  $\Lambda(1405)$  is clearly different from a usual Breit-Wigner type curve. Furthermore, the observed mass of  $\approx 1420$  MeV/ $c^2$  indicates that the first pole of the  $\Lambda(1405)$  might play a dominant role in the production mechanism. On the other hand, the comparison between the three line shapes reveals striking differences in the spectral shapes. These differences are attributed to isospin interference effects in the  $\Sigma\pi$  invariant mass distributions [NOTR99]. In fact, the  $\Sigma\pi$  states can be decomposed into different isospin components:

$$|\Sigma^-\pi^+\rangle = -\frac{1}{\sqrt{6}}|2,0\rangle - \frac{1}{\sqrt{2}}|1,0\rangle - \frac{1}{\sqrt{3}}|0,0\rangle \quad (1.7)$$

$$|\Sigma^+\pi^-\rangle = -\frac{1}{\sqrt{6}}|2,0\rangle + \frac{1}{\sqrt{2}}|1,0\rangle - \frac{1}{\sqrt{3}}|0,0\rangle \quad (1.8)$$

$$|\Sigma^0\pi^0\rangle = -\sqrt{\frac{2}{3}}|2,0\rangle - \frac{1}{\sqrt{3}}|0,0\rangle \quad (1.9)$$

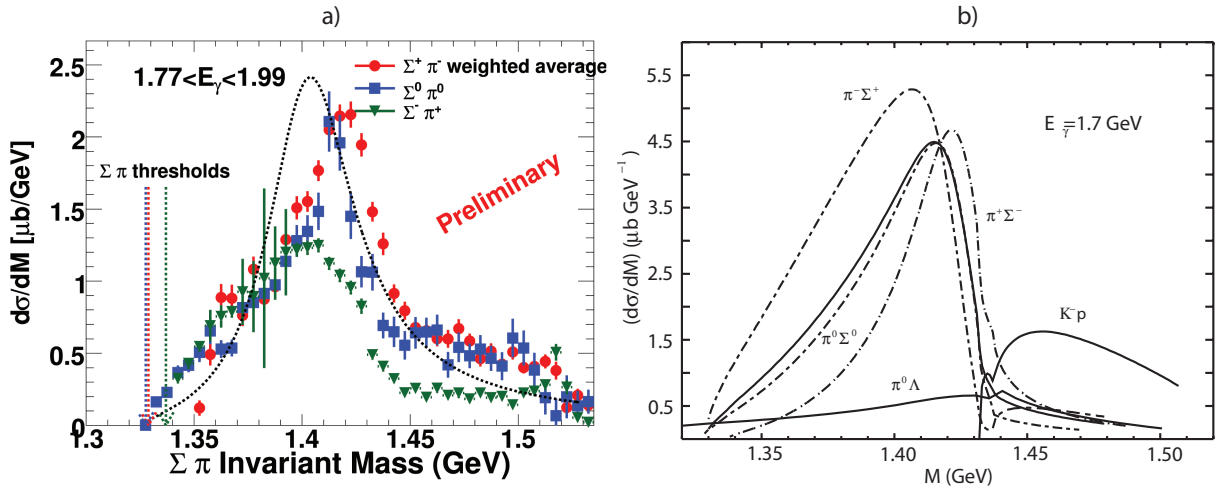


**Figure 1.10:** Panel a): Invariant mass distributions in the three  $\Sigma\pi$  channels measured by the CLAS collaboration [MS10]. Panel b): Theoretical prediction of the  $\Lambda(1405)$  spectral shape in  $\gamma$ -induced reactions [NOTR99]. The dashed lines show the expected distributions in the three  $(\Sigma\pi)^0$  final states. The solid line is a superposition of these three spectra scaled by a factor of  $1/3$ .

The finally observed invariant mass spectrum must therefore be seen as a coherent sum of different isospin contributions.

Whereas the  $I = 2$  contribution is expected to be negligible [NOTR99], the interference between  $I = 0$  and  $I = 1$  can be significant. Since the  $\Lambda(1405)$  is an  $I = 0$  particle, the invariant mass distributions in the charged  $\Sigma^+\pi^-$  and  $\Sigma^-\pi^+$  channels do not show the pure  $\Lambda(1405)$  signal, but a certain contamination by  $I = 1$  states must be considered. On the other hand, the “golden”  $\Sigma^0\pi^0$  decay channel can be considered as a pure  $I = 0$  state so that the  $\Sigma^0\pi^0$  invariant mass distribution indeed reveals the pure structure of the  $\Lambda(1405)$ . Contributions from other particles like  $\Sigma(1385)^0$  can be excluded in this case. The theoretical prediction on the  $\Lambda(1405)$  shape for  $\gamma$ -induced reactions at the same photon energy is shown in Figure 1.10 b). The calculated  $\Sigma^0\pi^0$  signal peaks at around  $1415 \text{ MeV}/c^2$ . The positive and negative signs of the interference terms shifts the  $\Sigma^+\pi^-$  spectrum to lower masses and the  $\Sigma^-\pi^+$  spectrum to higher masses, respectively. By summing up these two distributions, the interference terms cancel out and only the incoherent sum of  $I = 0$  and  $I = 1$  remains (solid line). Comparing the shapes in the experimental data with the theoretical predictions, not much similarities can be found. Especially the relative location of the  $\Sigma^-\pi^+$  and  $\Sigma^+\pi^-$  distribution is interchanged. This discrepancy is at the moment under investigation [M<sup>+</sup>13].

In order to really improve the understanding of the  $\Lambda(1405)$  resonance, it is not enough to have good statistics only for  $\gamma$ -induced reactions. In fact, the entrance channel dependence of the observed  $\Lambda(1405)$  spectral shape requires that also other reactions, like  $\pi^- + p$ ,  $K^- + p$  or  $p + p$ , are systematically investigated. Furthermore, careful theoretical studies for each of these reactions have to be performed as well [HHO<sup>+</sup>03].

The importance of the entrance channel dependence is further discussed in chapter 4 when the results of this work are compared to other measurements.

## 1.5 Kaonic nuclear clusters

Starting from 2002 a completely new interest in the  $\Lambda(1405)$  resonance and the associated  $\bar{K}N$  dynamics was expressed thanks to the prediction of deeply bound nuclear clusters. Indeed, the strong attraction in the  $I = 0$  state might be sufficient to form cluster objects of two or more nucleons bound together by anti-kaons. The simplest representation of a kaonic nuclear cluster is the  $ppK^-$  state, predicted in [AY02]. A schematic picture of the  $ppK^-$  is given in Figure 1.11, where the  $K^-$  acts like a glue between the two protons. The initially assumed binding energy of this state was considerably strong ( $B_{ppK^-} \approx 48$  MeV,  $\Gamma_{ppK^-} \approx 61$  MeV). It was furthermore concluded that this strong binding allows to overcompensate the stiff nuclear incompressibility so that kaonic clusters become very dense objects [AYOW10]. In this sense the possible existence of  $ppK^-$  has crucial impact on the nuclear EoS. However, the predictions made in these early works are criticized in [HW08] as they are deduced from a purely phenomenological approach, normally referred as AY-ansatz. In this ansatz the  $\Lambda(1405)$  is interpreted as an almost pure  $K^-p$  bound state with a negligible contribution of the  $\pi\Sigma$  state. Therefore, the nominal  $\Lambda(1405)$  mass of  $1405$  MeV/ $c^2$  is associated with a binding energy of  $27$  MeV between the anti-kaon and the proton. This is in contradiction to the much smaller binding energy of  $12$  MeV obtained in the coupled channel approach, constrained by chiral  $SU(3)$  (called chiral ansatz). Indeed, the question if the  $\Lambda(1405)$  is of single pole nature (AY-ansatz) or of double pole nature (chiral ansatz) is still a controversially discussed topic.

Coming back to kaonic clusters, realistic coupled channel Fadeev calculations are, for example, performed in [IS07]. Also here a  $ppK^-$  quasi-bound state with a binding energy of  $\approx 80$  MeV and a relatively large width of  $\approx 75$  MeV is found. In [HW08] it is, however, pointed out that all investigations concerning kaonic clusters are limited in their predictive power as the relevant energy range is far below the  $\bar{K}N$  threshold. Again, the only accessible observable below this threshold is the  $\Lambda(1405)$ . Its detailed understanding is therefore a necessary precondition for any serious statement about the possible existence or non-existence of deeply bound kaonic clusters. Besides these theoretical works, also first experimental hints for the  $ppK^-$  were reported. The FINUDA collaboration has measured  $K^-$  absorption on the nuclei. By studying the invariant mass distribution of  $\Lambda$  and proton, which is assumed to be the dominant decay channel of  $ppK^-$ , they find a resonance structure at  $2250$ - $2230$  MeV/ $c^2$  [A<sup>+</sup>05b] (see Figure 1.12, a)). The interpretation of this structure as a  $ppK^-$  bound state with a binding energy of  $115$  MeV and a width of  $67$  MeV is discussed controversially as this structure may also result from  $\Lambda$ -proton final state interactions [OT06].

Recently, the authors of [Y<sup>+</sup>10] reported on an indication of  $ppK^-$  formed in proton-proton re-

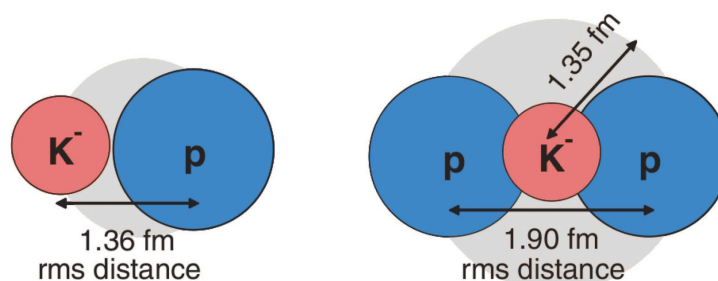


**Figure 1.11:** Structure and dimension of the  $\Lambda(1405)$  (left) and of the  $ppK^-$  state (right), predicted in [AY02].

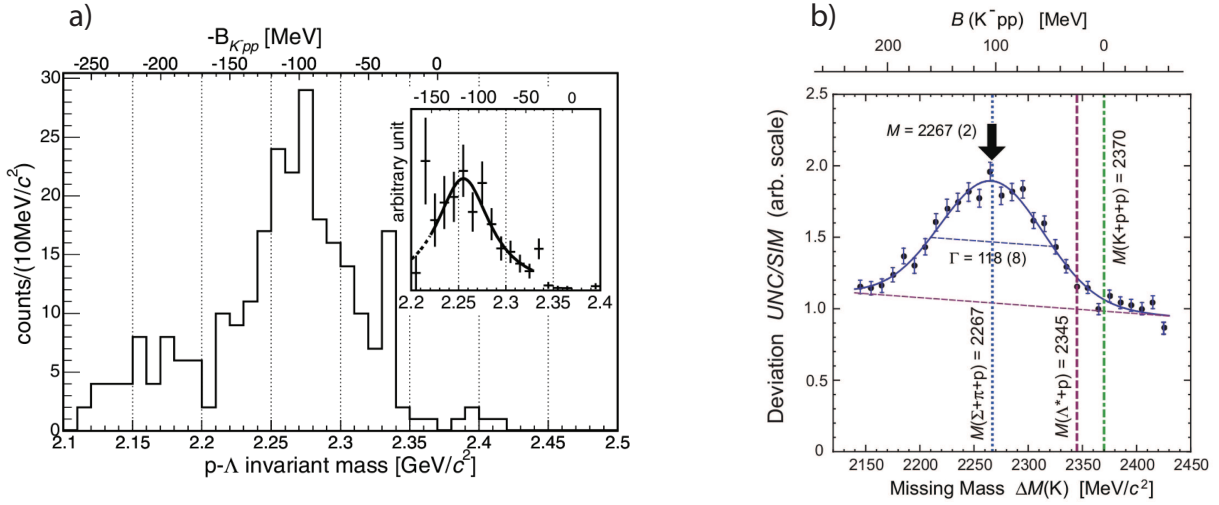


**Figure 1.12:** Experimental results on the search for  $ppK^-$ . Panel a) shows the  $\Lambda p$  invariant mass spectrum measured in  $K^-$  absorption experiments [A<sup>+</sup>05b]. Panel b) shows the  $\Lambda p$  deviation spectrum, which has been obtained from the analysis of proton-proton reactions at the DISTO experiment [Y<sup>+</sup>10].

actions ( $p + p \rightarrow ppK^- + K^+$ ). Dividing the experimental  $\Lambda p$  invariant mass spectrum by the spectrum obtained from phase space simulations of the reaction  $p + p \rightarrow p + K^+ + \Lambda$ , a clear enhancement is observed at 2270 MeV/ $c^2$ , associated with a binding energy of around 100 MeV (see Figure 1.12, b)). But also here the interpretation is difficult as the opening of the  $\Sigma\pi N$  channel at these energies might result in a cusp effect, leading to a similar distribution. The hunt for the  $ppK^-$  is continued by the HADES and the FOPI collaboration, both analyzing  $p+p$  reactions [Epp12a, Mün10]. The results will shed new light on the interesting topic of kaonic nuclear clusters.

## 1.6 Motivation and aims of this work

The present work is organized as follows:

After a short introduction into the HADES experiment, chapter 3 and 4 discuss the analysis of the reactions:

$$p + p \rightarrow \Sigma(1385)^+ + n + K^+ \quad (1.10)$$

$$p + p \rightarrow \Lambda(1405) + p + K^+ \quad (1.11)$$

The used  $p + p$  data set was measured by the HADES collaboration at a beam kinetic energy of 3.5 GeV in the year 2007. Both particles, the  $\Lambda(1405)$  and the  $\Sigma(1385)$ , are located directly below the  $\bar{K}N$  threshold ( $\approx 1433$  MeV). Their properties might thus have an important influence on the in-medium dynamics of anti-kaons.

In contrast to  $\Lambda(1405)$ , the  $\Sigma(1385)^+$  is not an exotic, molecular like state, but it is well known as a usual 3-quark baryon. The Particle Data Group (PDG) [B<sup>+</sup>12] lists this particle as a four star resonance with quantum numbers  $I(J^P) = 1\left(\frac{3}{2}^+\right)$ , pole mass  $m_0 = 1382.8 \pm 0.35$  MeV/ $c^2$  and width  $\Gamma_0 = 36 \pm 0.7$  MeV/ $c^2$ . Moreover, the  $\Sigma(1385)$  is considered to be the first excited

state of the  $\Sigma$  hyperon, similar to the  $\Delta(1232)$  being the first excitation of the nucleon.

The properties of the  $\Sigma(1385)$  become less clear when it is embedded in the nuclear medium. In particular its influence on anti-kaons is far from being understood at the moment (see [LKM08]). The vicinity of the  $\Sigma(1385)$  resonance below the  $\bar{K}N$  threshold might, for example, substantially increase the anti-kaon production via strangeness exchange reactions in heavy ion collisions. Therefore, in order to interpret the  $K^-$  distributions measured in these reactions, it is crucial to incorporate the  $\Sigma(1385)$  dynamics into transport models [Lut04]. This, however, should be based on a precise understanding of the vacuum properties of the  $\Sigma(1385)$ . Constraints on the line shape, the production cross sections or angular distributions are thereby provided by measurements of elementary reactions. In this sector most of the present knowledge about the  $\Sigma(1385)^+$  was obtained in  $\gamma + p$  and  $K^- + p$  reactions (see [K<sup>+</sup>11, Bau84]);  $p + p$  reactions, on the other hand, are rather unexplored with only one measurement at an incident proton momentum of 6 GeV/c [C<sup>+</sup>68b]. This work shall improve the situation by providing first precise data on  $\Sigma(1385)^+$  production in the SIS18 energy range.

One aim of the analysis in chapter 3 is to extract the spectral shape of the  $\Sigma(1385)^+$  as well as its Breit-Wigner mass and width. The determination of these quantities is important in the context of possible in-medium modifications of the  $\Sigma(1385)$ . Indeed, this resonance, if produced in a nuclear environment, is expected to show a substantial attractive mass shift of around 60 MeV/c<sup>2</sup>, accompanied by an increase of the decay width [LK02]. The upcoming HADES results on  $\Sigma(1385)$  production in  $Ar + KCl$  and  $p + Nb$  reactions in comparison with this work might therefore help to reveal the real in-medium properties of the  $\Sigma(1385)$ .

A second aim of the analysis is to study the  $\Sigma(1385)^+$  production process and to determine total and differential cross sections for several observables. Of particular importance in this context are the CMS-, Gottfried-Jackson- and helicity-angle distributions, as they reflect the production dynamics in the reaction (1.10). By providing fully acceptance and efficiency corrected data, the distributions in these observables can be compared to upcoming theory models like One-Boson-Exchange models, and can thus yield important information about the production mechanism of the  $\Sigma(1385)^+$ . In this way the different contributing meson exchange processes as well as the involved partial waves can be disentangled. This will also help to constrain the  $\Sigma(1385)$  dynamics in transport models.

With the successful reconstruction of the  $\Sigma(1385)^+$ , it is proved that the developed analysis methods are well suited for the study of hyperon production in proton-proton reactions so that the investigation of the  $\Lambda(1405)$  resonance can be started.

The motivation for measuring the  $\Lambda(1405)$  has been extensively discussed in the preceding sections. Its unique role in the low energy  $\bar{K}N$  dynamics makes  $\Lambda(1405)$  the “holy grail” of anti-kaon physics. Only with a detailed understanding of this resonance, issues like kaonic clusters and possible in-medium kaon condensation can be seriously faced. At present, precise data in  $\gamma$ -induced reactions are going to shed new light on the nature of the  $\Lambda(1405)$ . However, the double pole character of this resonance manifests itself in varying properties which depend on the entrance channel. Therefore, the innermost structure of the  $\Lambda(1405)$  can only be accessed if it is measured in different initial reactions. In the sector of proton-proton reactions not much is known about this particle, especially as only one measurement exists [Z<sup>+</sup>08], which itself is hampered by statistics. This work aims to improve the situation by delivering first data on the  $\Lambda(1405)$  produced in  $p + p$  reactions and decaying into the  $\Sigma^+\pi^-$  and  $\Sigma^-\pi^+$  channel.

Chapter 4 describes the challenging reconstruction of the  $\Lambda(1405)$  line shape. The observed spectrum will hopefully help to clarify the controversial discussion about the positions and the relative contributions of the two poles. Together with the new results on the  $K^-p$  scattering

length [B<sup>+</sup>11], these data can substantially contribute to a better understanding of the low energy  $\bar{K}N$  dynamics.

It has to be stressed out at this point that  $p + p$  reactions suffer from the fact that they are not well explored by theory. The production of the  $\Lambda(1405)$  and the  $\Sigma(1385)$  is always a three particle production process (see reactions (1.10) and (1.11)). The large number of degrees of freedom in those processes requires that theory models consider several contributing exchange diagrams. Furthermore, as two baryons appear in the final state, final state interactions may play a major role and have to be incorporated in any realistic approach. Because of these difficulties, not much theory groups have yet started to calculate hyperon production in  $p + p$  reactions. The present work will hopefully trigger new theoretical effort in this sector.

In chapter 5 the CERBEROS pion tracker system is introduced. Indeed, the HADES collaboration plans to complement their ongoing studies on heavy ion reactions and proton-induced reactions by measuring also  $\pi^-$ -induced reactions. As it will be discussed, those reactions can give additional insight into the in-medium kaon dynamics. Furthermore, it is also planned to re-measure the properties of  $\Lambda(1405)$  and  $\Sigma(1385)$  in  $\pi^- + p$  reactions. As pion beams are secondary beams, it is necessary to develop a special pion tracking detector which, in case of HADES, will be based on  $n^+p$  silicon strip detectors. This thesis presents first tests on the resolution, efficiency and radiation hardness of these detectors. The tests are necessary in order to proof that the proposed detectors are precise enough to resolve pion signals and that they are stable enough to survive a high intensity beam period.

## 2 The HADES experiment

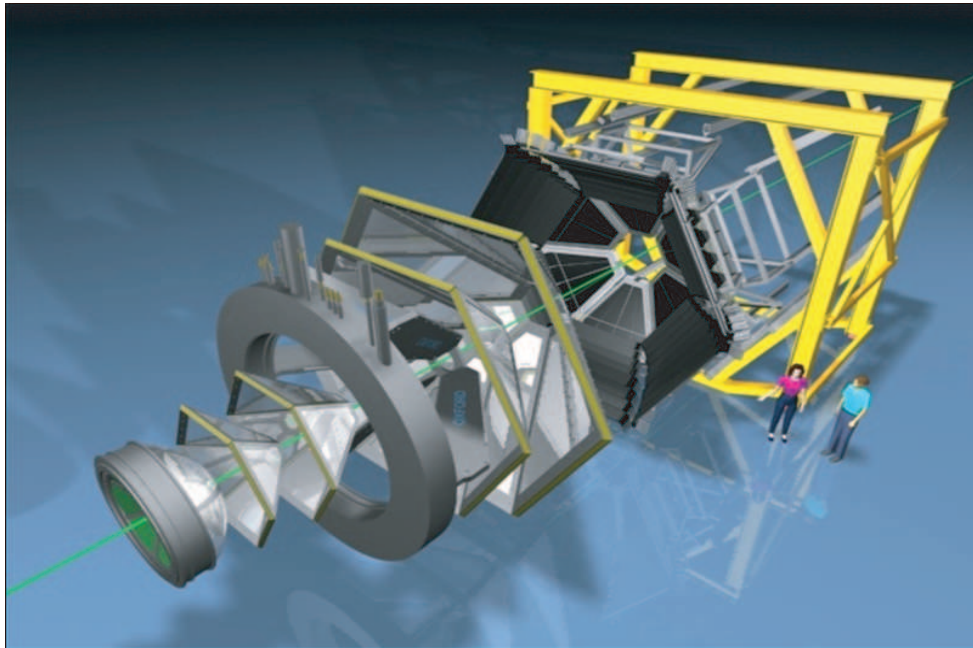


**Figure 2.1:** HADES detector system in an expanded view. The green line indicates the beam, coming from the lower left corner.

The **H**igh **A**cceptance **D**i-**E**lectron **S**pectrometer (HADES) is operating at the SIS18 accelerator (SchwerIonen Synchrotron) at the GSI Helmholtzzentrum für Schwerionenforschung in Darmstadt, Germany. HADES is a fixed target experiment with its focus on the measurement of heavy ion reactions at incoming beam kinetic energies of 1-2 GeV per nucleon (A GeV). The detector system was designed to measure possible in-medium modifications of the light vector mesons  $\rho$ ,  $\omega$  and  $\phi$  via their rare leptonic decay into  $e^+e^-$  pairs [LKW92, SS94]. These modifications can yield information on the quark-gluon condensate and the associated (partial) restoration of chiral symmetry at densities of 1-3 times normal nuclear density and at temperatures between 80-100 MeV. Vector mesons are especially interesting as their lifetimes are comparable to the duration of the compression phase of the heavy ion reaction, and they therefore mostly decay within the nuclear medium. On the other hand, the lepton pairs from the decay do not interact strongly with the surrounding medium and, hence, carry the undistorted information on the in-medium properties of their mother particle.

Recently, it has been shown that the detector system is not only suited for the reconstruction of lepton pairs, but it shows also very good performance on the identification of hadrons. This opened the door to the interesting research topic of strangeness physics [A<sup>+</sup>09b, A<sup>+</sup>09a, Sch08]. The following sections introduce the HADES detector setup, the different methods for particle identification and the used simulation tools.

## 2.1 Detector system

The HADES detector system consists of six identical sectors, arranged around the beam axis (see Figure 2.1). It has almost full azimuthal coverage combined with a polar angle acceptance for single particle tracks, ranging from  $15^\circ$  to  $85^\circ$ . In that way the setup is optimized for the detection of di-leptons produced in the SIS18 energy range. Figure 2.2 is a cut-through plot showing two opposite HADES sectors in the vertical plane. The blue, green and red lines are possible particle tracks in the detector.

In the following part the different detector components are presented. A very detailed description of the HADES experiment can be found in [A<sup>+</sup>09c].

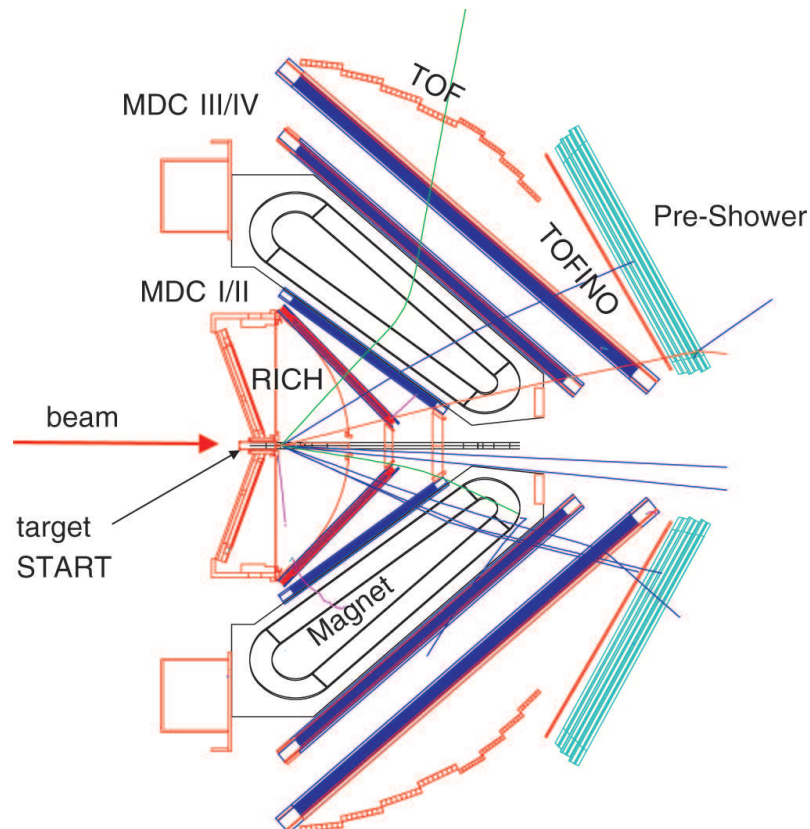


**Figure 2.2:** Side view of the HADES detector system, showing two opposite sectors. All detector components but the Forward Wall are included in the picture. The colored, curved lines indicate possible particle tracks.

### 2.1.1 The target

The reaction target is located in the center of the field-free space in front of the superconducting magnet coils. Here the beam particles collide with the nuclei of the target and new particles are produced. For the investigation of heavy ion collisions or  $\pi + A$  and  $p + A$  reactions, a segmented solid state target is used. Elementary reactions (like  $p + p$  or  $d + p$ ) are studied with liquid hydrogen targets [Web11].

### 2.1.2 The RICH detector

The produced particles eventually pass the RICH detector, which encloses the target and covers the full HADES acceptance. RICH is a hadron blind Ring-Imaging Cherenkov detector, designed to detect single photons. The radiator volume is filled with  $C_4F_{10}$  having a characteristic Lorentz factor for Cherenkov radiation of  $\gamma_{thr} = 18$ . Since only electrons and positrons can reach this value in the SIS18 energy range, the detector is blind for muons and hadrons. The  $e^+$  or  $e^-$  induced Cherenkov photons are reflected from an aluminum coated carbon mirror, pass a  $CaF_2$  window and enter the  $CH_4$  filled photon detector volume, where they hit  $CsI$  photo cathodes. The knocked out photo electrons are detected by six Multi-Wire Proportional Chambers (MWPC), equipped with individual pad readout. The RICH geometry is chosen in a way that the Cherenkov rings, which are seen by the pads, have always the same diameter. This simplifies the online ring search, needed for the LVL2 trigger condition (see below). By matching the detected ring position with a reconstructed particle track, electron and positron candidates are identified.

In this work the information from the RICH detector was not used because only hadron signals were analyzed.

### 2.1.3 The magnet

A charged particle traversing a magnetic field is bended according to the Lorentz force. The measurement of the bending radius determines directly the momentum of the particle. This principle is also exploited in the HADES experiment.

A superconducting ironless electromagnet, consisting of six coils, is implemented between the MDC planes II and III. The coils are placed symmetrically around the beam axis in between two MDC sectors. They can be operated with a maximum current of 3464 A and induce an asymmetric toroidal magnetic field in the full azimuthal region. The design of the magnet foresees relatively low field intensities in the different detector systems (e.g.  $B \approx 0.08$  T in MDC I). A large field is only obtained in between the two MDC layers II and III with  $B_{max} = 3.6$  T within the coil boxes and  $B_{max} = 0.9$  T in the center of a sector, located in the middle of two coils.

### 2.1.4 The MDC chambers

For the reconstruction of the particle tracks, HADES is equipped with four planes of Multi-Wire-Drift Chambers (MDC I-IV). Each plane consists of six identical trapezoidal chambers, symmetrically placed around the beam axis. The chambers themselves are composed out of about 1200 tungsten wires, arranged in six different wire planes. They are continuously flushed with a Helium based counting gas (He:isobutan = 60:40). A charged particle, traversing the MDC chamber, ionizes the gas along its trajectory. The produced electrons drift in the electric field of the wires, are multiplied by avalanche effects and finally reach the wires, where they induce an electronic signal. By arranging the six wire layers in different stereo angles, the wire signals can be combined to clusters so that a position resolution of  $\sigma_x \approx 140 \mu\text{m}$  is achieved. In that way the penetration point of the particle can be determined with high precision. The MDC layers I and II are almost in a field-free region so that both hit points can be extrapolated to a straight track, which points to the event vertex. This is an important feature for the primary vertex reconstruction.

For the determination of the particle track, the hit positions in MDC I and II are combined to an

inner track segment and the information from MDC III and IV are combined to an outer track segment. These two segments are deflected to each other due to the magnetic field in between MDC II and III. The Runge-Kutta algorithm takes the segments and eventually the hit positions in the META detectors (see below) as start parameters and solves the equation of motion in a numeric way, considering the precisely determined magnetic field map. The obtained particle track points from the target to the META detectors and comprises the knowledge on the particle momentum and the traversed path length. In this way a momentum resolution of  $\frac{\Delta p}{p} = 1 - 4\%$  is achieved.

Besides the hit position, the MDC chambers provide information on the energy loss  $\Delta E$  of the particle, ionizing the counting gas. The TDC readout chips of the MDCs deliver the Time over Threshold (ToT) of the signal. This is the time range within which the electronic signal of the electron avalanche is above an adjusted threshold. Therefore, the ToT is directly related to the energy loss  $dE/dx$ . This feature is exploited for the hadron identification, as it will be discussed later.

### 2.1.5 The META system

The Multiplicity Electron Trigger Array (META) is used for time-of-flight measurements and the determination of the particle multiplicity. It consists of three independent detector subsystems:

- The **TOF** detector is an arrangement of 64 plastic scintillators per sector. It covers the polar angle range from  $\theta = 44^\circ$  to  $\theta = 88^\circ$  (see Figure 2.2). A charged particle hitting a scintillator module induces photon emission. These photons are detected by Photo-Multiplier-Tubes (PMTs), which measure the arrival time as well as the signal height. From these information the particle time-of-flight and energy loss can be deduced. The double sided readout of the TOF scintillators results in an intrinsic time resolution of  $\sigma_t = 150$  ps.
- Also the **TOFino** detector consists of plastic scintillators, covering the angle range from  $\theta = 15^\circ$  to  $\theta = 45^\circ$ . It has a low granularity of only eight paddles per sector, which increases the double hit probability. As the scintillators are read out only on one side, the intrinsic time resolution is rather poor ( $\sigma_t \approx 400$  ps).
- The **PreSHOWER** detector is an electromagnetic shower detector, located directly behind TOFino. Charged particles produce an electromagnetic shower in the  $Pb$  converter planes and the embedded Multi-Wire chambers collect the shower signals. Since the signals induced by hadrons and leptons are different for  $p > 400$  MeV/c, this detector supplements the  $e^+$  and  $e^-$  identification power of RICH.

The PreSHOWER is additionally characterized by a high granularity, which is optimized to push the double hit probability in central  $Au + Au$  collisions below 5%. In this way also the poor position resolution of TOFino is compensated.

Starting from 2009, the HADES detector has been exposed to a major upgrade. Besides the installation of new electronic readout systems, the TOFino detector was replaced by Resistive Plate Chambers (RPCs), which deliver a much better time resolution of around 100 ps combined with a very high granularity [AP<sup>+</sup>04, G<sup>+</sup>07]. This step was necessary in order to facilitate measurements of heavy ion collisions like  $Au + Au$ . Indeed, this experiment has been performed in 2012.

The measurement of the arrival time in the META detectors is supplemented by the determination of a reaction time with help of a start detector. Usually, polycrystalline diamond detectors are

positioned in front of the target and deliver a time signal as soon as they are traversed by a beam particle. These detectors are characterized by large radiation hardness (up to  $10^9$  ions/s) and a very good time resolution ( $\sigma_t = 30$  ps). The combination of the start time and the hit time in the META detectors allows to determine the time-of-flight of the corresponding particle. This information is an important ingredient for the particle identification, as will be discussed later.

### 2.1.6 The Forward Wall

The HADES detector was initially designed with a polar acceptance from  $\theta = 15^\circ$  to  $\theta = 85^\circ$ . In order to measure  $d + p$  reactions, it is, however, necessary to detect the spectator protons, which predominantly fly into the forward region [L<sup>+</sup>09]. For this reason a Forward Wall (FW) scintillator hodoscope was installed 7 m downstream the target, covering the polar angles from  $0.33^\circ$  to  $7.17^\circ$  at full azimuthal acceptance. The segmentation of the FW into 300 scintillating cells allows for a measurement of the particle hit position, but also the time-of-flight ( $\sigma_t = 700$  ps) and the energy loss can be reconstructed. However, as the forward region is not covered by the MDC detectors, no momentum can be assigned to the particles hitting the FW.

The FW was first tested during the  $p + p$  run at 3.5 GeV, and, despite the missing momentum information, it turned out to be helpful in the data analysis of this beam time [A<sup>+</sup>12b]. For the recently recorded  $Au + Au$  data, the FW is of special interest, as it allows to reconstruct the reaction event plane and, thus, to study flow patterns. In the presented work the FW information is, however, not used.

### 2.1.7 Trigger decision and data acquisition

Reactions between incoming beam particles and the target nucleons create new particles, which may fly through the detector systems, where they leave characteristic signals. These signals are read out by the HADES DAQ system and can serve as an input to the Central Trigger System (CTS) which subsequently transmits a trigger signal. The trigger decision is in general a two step process:

- **LVL1 trigger:** Detector signals can either be induced by particle hits or by random noise. The second case can be suppressed by requiring that two or more detectors deliver a signal at the same time. The LVL1 trigger condition is based on this principle. The hit multiplicity in the META detectors corresponds to the hit multiplicity of charged particles. Only if this multiplicity exceeds an adjustable minimum value, the event is further processed. In this way also the centrality of the reaction can be selected.
- **LVL2 trigger:** This trigger is supposed to enhance events with  $e^+$  and  $e^-$  tracks. Online Image Processing Units (IPUs) search for electron candidates in the data of the different detector systems and eventually send a single LVL2 trigger decision.

After a positive trigger decision has been transmitted, the EventBuilders (EB) combine the electronic information from all subsystems to a common event structure, which is saved to disc. In order to not bias the analysis concentrating only on hadrons, a downscaled number of pure LVL1 events is stored as well.

### 2.1.8 The $p + p$ experiment at 3.5 GeV

In this thesis  $p + p$  data at an incident kinetic beam energy of 3.5 GeV were analyzed. This value translates into a center-of-mass (CM) energy of  $\sqrt{s} = 3.176$  GeV. The data were taken in April 2007, so the detector was still equipped with the TOFinio detector. The used liquid hydrogen target had a diameter of 25 mm and a length of 50 mm. It was cooled down to 20 K at atmospheric pressure, resulting in an interaction probability of 0.7%. During the three weeks beam time, a total amount of  $1.2 \cdot 10^9$  LVL1 events was stored. The LVL1 trigger decision was set to a META hit multiplicity of three (M3). Due to the LVL1 downscaling, only every third pure LVL1 event was saved to disc.

Since the energy deposition of protons in diamond detectors is too low to estimate the reaction time, no start detector was available during this beam time. This is a clear disadvantage as the time-of-flight measurement is important for the particle identification. The start time of the event could, however, be reconstructed in the data analysis.

## 2.2 Particle identification

The HADES tracking system uses the raw detector signals to reconstruct particle tracks. The obtained information are saved in so-called DST files, which are the basic data format for any HADES analysis. DSTs are arranged in a tree structure, where each physical event is characterized by the reconstructed tracks in this event. The particle tracks carry the information on the particle momentum  $\vec{p}$ , the arrival time in the META detectors  $t_{META}$ , the track length from the primary vertex to the META detector  $l_{META}$ , the energy loss in the different detector systems  $dE/dx$  and so on. The DST tree structure is illustrated in Figure 2.3. At this stage of the analysis the track has not yet a particle ID, meaning that it is unknown if the track is referring to a proton, a pion, etc. To determine the ID, several observables can be used. In case of di-lepton analysis the information, provided by the RICH detector, are essential. In this work, however, only hadrons are of interest. Their identification can in general be done in two independent ways.

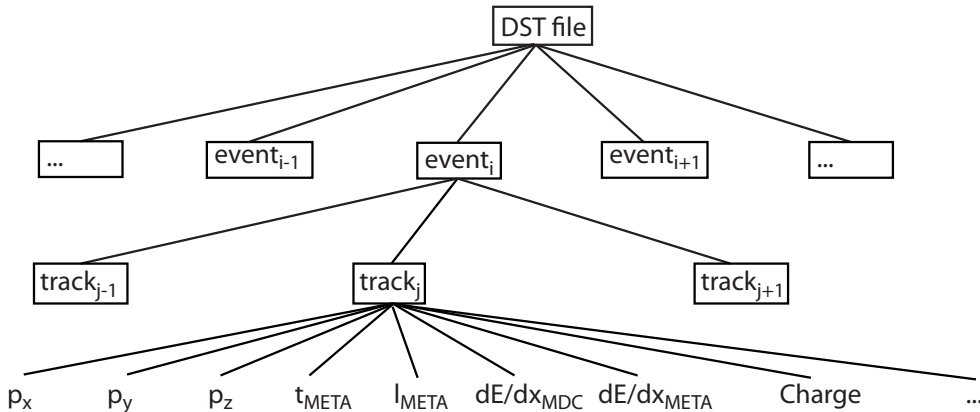


**Figure 2.3:** Tree structure of DST files.

### 2.2.1 Identification via energy loss

A charged particle traversing a medium ionizes the atoms in this medium by transferring part of its kinetic energy to the shell electrons. The associated energy loss per covered distance  $\Delta x$  is expressed in the well known Bethe-Bloch formula [Bet30]:

$$-\left\langle \frac{dE}{dx} \right\rangle = 4\pi N_A r_e^2 m_e c^2 z^2 \frac{Z}{A} \frac{1}{\beta^2} \left[ \frac{1}{2} \ln \left( \frac{2m_e c^2 \beta^2 \gamma^2 T_{max}}{I^2} \right) - \beta^2 - \frac{\delta}{2} \right] \quad (2.1)$$

with:

$z$  : charge of the incident particle

$Z, A$  : atomic and mass number of the traversed medium

$m_e$  : mass of the electron

$r_e$  : Bohr electron radius

$N_A$  : Avogadro number

$I$  : mean excitation potential of the material

$\delta$  : density correction

The maximal transferred kinetic energy  $T_{max}$  is limited to:

$$T_{max} = \frac{2m_e c^2 \beta^2 \gamma^2}{1 + 2\gamma m_e/M + (m_e/M)^2} \quad (2.2)$$

with:

$M$  : mass of the incident particle

The formula (2.1) can be applied if the particle mass is large compared to the electron mass. The energy loss  $dE/dx$  then just depends on the velocity  $\beta$  and the charge  $z \cdot e$  of the particle. On the other hand, the velocity can be expressed by the momentum and the particle mass:

$$p = c\beta\gamma m \quad (2.3)$$

Thus, the energy loss as a function of momentum should be different for different particle species (different particle masses). As both, the energy loss  $dE/dx$  and the momentum  $p$ , are provided by the track candidates in the DST files, this method can be used for the particle identification. The energy loss in the MDC chambers vs. the momentum times charge for all tracks is shown in Figure 2.4. Signals due to protons and pions are visible as accumulations around the theoretical Bethe-Bloch curves (black lines). While the proton and  $\pi^+$  signals are clearly separable at low momenta, their distributions start to overlap for momenta larger than 1000 MeV/c. In case of the  $K^+$  and the  $K^-$  mesons no signals are visible. The reason for that is two folded. On the one hand, kaon production at these energies is suppressed by a factor of around 100 compared to the production of non-strange hadrons. On the other hand, the  $dE/dx$  resolution in the MDC chambers is low, so that the signals from all particle species partially overlap. Therefore, the expected small signal of kaons is totally covered by the ones of the pions and protons. The  $dE/dx$  vs. momentum distribution in the TOF and TOFinio detectors show a similar behavior without clear indications of kaons (see e.g. Figure 3.7).

The particle identification is done with graphical cuts around the theoretical Bethe-Bloch curves. If a particle track lies within such a cut, it is identified to be of that special particle species. The

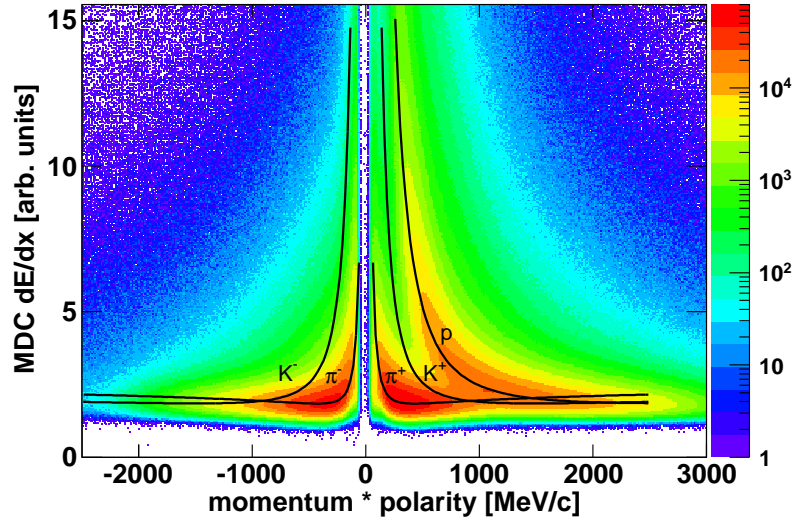


**Figure 2.4:**  $dE/dx$  vs. track momentum times charge for the MDC detector system. The black lines indicate the theoretical Bethe-Bloch curves of protons, pions and kaons. The particle identification is done by using graphical cuts on these distributions.

track is then tagged with the additional information on the particle mass, which is characteristic for each species, and with this information the 4-vector of the track can be calculated.

It has to be emphasized that this identification method is not unambiguous. In fact, it might happen that, for example, a proton track falls within the pion graphical cut and is therefore tagged as a pion. This phenomenon is called misidentification. It plays an important role, especially for the identification of kaons. Indeed, kaons are also identified with help of graphical  $dE/dx$  cuts, even though their signals are not visible in Figure 2.4. The so obtained kaons are in most of the cases misidentified pions and protons; they are therefore called kaon *candidates*. Examples for the different graphical cuts are given in chapter 3.

### 2.2.2 Time-of-flight reconstruction

The knowledge of the time-of-flight ( $tof$ ) of the particle offers a second, independent particle identification method. By taking the traveled path length  $l_{META}$  from the event vertex to the hit in the META detectors, the velocity of the particle can be calculated ( $v = \beta \cdot c = l_{META}/tof$ ). Taking the additional information of the track momentum  $p$ , the mass  $m$  of the reconstructed particle gets accessible:

$$p = mc \frac{\beta}{\sqrt{1 - \beta^2}} \quad (2.4)$$

As the rest mass is a characteristic quantity for each particle species, this method can be used for the particle identification. Unfortunately, the HADES setup was not equipped with a start detector during the  $p+p$  experiment so that no common start time information  $t_{Start}$  is available. This, however, is necessary in order to determine the time-of-flight ( $tof = t_{META} - t_{Start}$ ). To overcome this problem, a time-of-flight reconstruction algorithm has been developed. This algorithm works on an event-hypothesis basis, where in each event pions and protons are identified

with help of graphical  $dE/dx$  cuts. The velocity of these particles is then determined from formula (2.4) and a common start time of the reaction is calculated. Details on this procedure can be found in [Siel0a].

It will be shown in the next chapter that this method of particle identification is important to increase the purity of the kaon candidates.

### 2.2.3 Invariant and missing mass technique

Till now, only direct identification methods, where the particles leave characteristic signals in the HADES detectors, were considered. There are, however, two additional procedures, which are particularly relevant for short-living or neutral particles.

A particle with a short lifetime might decay before it has the chance to interact with any detector. Those particles can still be reconstructed via their decay products. If all the  $n$  decay particles are measured by the detector setup, the sum of their 4-momenta  $(E_i, \vec{p}_i)$  determines the 4-momentum of the mother track  $(E, \vec{p})$ , and this in turn allows to calculate the mass of the mother particle:

$$m_{inv} = \frac{1}{c^2} \sqrt{E^2 - (\vec{p})^2 c^2} = \frac{1}{c^2} \sqrt{\left(\sum_{i=1}^n E_i\right)^2 - \left(\sum_{i=1}^n \vec{p}_i\right)^2 c^2} \quad (2.5)$$

This procedure is, for example, applied for the measurement of  $\Lambda$  hyperons decaying into a proton and a pion. The invariant mass distribution of  $M(p, \pi^-)$  would show a characteristic  $\Lambda$  peak at around 1115 MeV/ $c^2$ .

The second method is the so-called missing mass technique. It is applicable only in elementary reactions, where all particles but one are reconstructed. Exploiting energy and momentum conservation, the 4-momentum of the missing particle can be determined from all other particles so that the missing particle mass can be calculated:

$$\begin{aligned} m_{miss} &= \frac{1}{c^2} \sqrt{E^2 - (\vec{p})^2 c^2} = \\ &= \frac{1}{c^2} \sqrt{\left(E_b + E_t - \sum_{i=1}^n E_i\right)^2 - \left(\vec{p}_b + \vec{p}_t - \sum_{i=1}^n \vec{p}_i\right)^2 c^2} \end{aligned} \quad (2.6)$$

where  $(E_b, \vec{p}_b)$  and  $(E_t, \vec{p}_t)$  are the 4-momenta of the beam and the target particle, respectively. The missing mass technique is especially interesting for reactions with one neutral particle in the final state. As neutral particles cannot be detected directly by HADES, this method is the only possibility to reconstruct such particles.

The following chapters contain several examples, where these two methods are further illustrated.

## 2.3 Simulations

Simulations are an important tool to interpret physical data. They allow to compare different assumptions about the underlying production mechanisms to experimentally observed distributions. In that way a qualitative and quantitative picture about the contributing reactions can be obtained.

On the other hand, simulations are needed to understand the detector response to incoming signals. With this knowledge the experimental data can be corrected for the effects of the limited detector efficiency and acceptance.

### 2.3.1 Simulation tools

Event generators simulate the production of particles based on physical assumptions. The obtained particle tracks are propagated through the detector volume, where the response of the detector systems is imitated. The HADES simulation framework is based on a three step process.

#### **PLUTO**

PLUTO is a Monte Carlo based event generator, developed for the HADES experiment [F<sup>+</sup>07, F<sup>+</sup>10]. It allows to imitate thermal particle production in nucleus-nucleus collisions, but can also serve as a generator for elementary reactions like  $p+p$ . For the present work only the second case is of interest. Different reactions like, for example,  $p+p \rightarrow \Sigma(1385)^+ + n + K^+$  can be simulated independently from each other. The so obtained data set is an incoherent sum of all simulated reactions. For the event generation, PLUTO uses adjustable input parameters like cross sections, decay branching ratios, spectral functions of resonances and angular distributions. The particle production is then calculated according to the available phase space volume. As PLUTO has no information about the surrounding detector volume, the particles are simulated with straight 3-vectors in the position space.

#### **HGeant**

The particle track information, delivered by PLUTO, is used as an input for the simulation software HGeant [HAD08], which is based on the Fortran package Geant [CER95]. In this step the interaction of the particles with the detector materials is simulated. This includes also scattering processes, secondary collisions, energy loss and track curvature in the magnetic field. To guarantee realistic simulations, the detailed geometry of HADES was implemented in this software tool.

#### **SimDST**

In a last step the answer of the detectors to the particle hits is transformed into a realistic signal. In this digitization procedure, electronic signals are created, where noise, inefficiencies and finite resolution effects are incorporated. The simulated detector response is processed in exactly the same way as it is done for the real data. The particle tracks are, for example, reconstructed from the hit points in the MDCs by applying the Runge-Kutta algorithm and the obtained information about particle momentum, energy loss etc. are stored. In this sense the SimDST files correspond to the DST files, produced for the real data.

Starting from this level, the simulations can be analyzed in the same way as the experimental data.

### 2.3.2 Acceptance and efficiency corrections

The experimental distributions reconstructed in this work are always folded with inefficiencies of the HADES detector system. The acceptance and efficiency correction procedure is supposed to compensate for these effects so that the undistorted physical information can be extracted from the data.



was simulated by assuming isotropic production of all particles in the CMS so that the distribution  $Sim_{org}(\cos(\theta_{K^+}))$  is flat (see solid blue histogram in Figure 2.5). When processing these simulations through all the simulation and analysis steps, the distribution for  $\cos(\theta_{K^+})$  can again be reconstructed. This new distribution is called  $Sim_{final}(\cos(\theta_{K^+}))$  and is shown as the solid red histogram in Figure 2.5. It looks completely different and is drastically reduced compared to the originally simulated distribution  $Sim_{org}(\cos(\theta_{K^+}))$ . Especially the isotropic (flat) behavior is not visible anymore. This is a consequence of the different inefficiencies, discussed before. The missing entries for  $\cos(\theta_{K^+}) > 0.7$  can, for example, be attributed to the acceptance hole in the forward direction.

Dividing the reconstructed distribution by the initially simulated distribution, a one dimensional efficiency matrix  $M_{eff}(\cos(\theta_{K^+}))$  is obtained. If real data are analyzed, an experimental distribution for  $\cos(\theta_{K^+})$  can be reconstructed ( $Exp(\cos(\theta_{K^+}))$ ) as well. This distribution can be multiplied with the inverse of the efficiency matrix (black histogram in Figure 2.5) and in this way a corrected experimental distribution  $Exp_{corr}(\cos(\theta_{K^+}))$  is obtained:

$$Exp_{corr}(\cos(\theta_{K^+})) = M_{eff}^{-1}(\cos(\theta_{K^+})) \cdot Exp(\cos(\theta_{K^+})) \quad (2.9)$$

$$\text{with } M_{eff}(\cos(\theta_{K^+})) = \frac{Sim_{final}(\cos(\theta_{K^+}))}{Sim_{org}(\cos(\theta_{K^+}))} \quad (2.10)$$

The distribution  $Exp_{corr}(\cos(\theta_{K^+}))$  is now compensated for the different inefficiency effects, and it should therefore reveal the real angular distribution of the  $K^+$  in the CMS.

However, things are not that easy, and it is important to understand that the values of the efficiency matrix are not unambiguous. The reason is that only a one dimensional observable has been considered. In fact, the efficiency matrix  $M_{eff}(\cos(\theta_{K^+}))$  can be expressed as follows:

$$M_{eff}(\cos(\theta_{K^+})) = \frac{\int d^3\vec{p}_p d^3\vec{p}_{\pi^+} d^3\vec{p}_{\pi^-} p_{K^+}^2 dp_{K^+} d\varphi_{K^+} P_{total} \cdot F_{Sim}}{\int d^3\vec{p}_p d^3\vec{p}_{\pi^+} d^3\vec{p}_{\pi^-} p_{K^+}^2 dp_{K^+} d\varphi_{K^+} F_{Sim}} \quad (2.11)$$

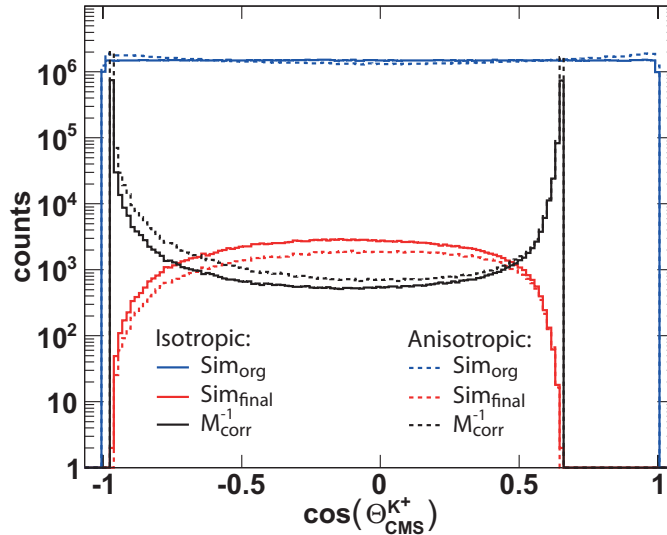


**Figure 2.5:** Illustration of efficiency corrections for the observable  $\cos(\theta_{K^+})$ . The solid histograms show the obtained distributions for isotropic production of the particles. The dashed histograms result from a simulation model with anisotropic production of the particles in the CMS.

$F_{Sim} = F_{Sim}(\vec{p}_p, \vec{p}_{K^+}, \vec{p}_{\pi^+}, \vec{p}_{\pi^-})$  is the simulated distribution of reaction (2.7) and it depends on the momenta of all final state particles. The one dimensional efficiency matrix is now obtained by integrating over an 11-dimensional phase space volume. This is problematic since the result of that integration depends on the used simulation model  $F_{Sim}$  itself. Indeed, if one uses a different simulation model, where the particles are not produced isotropically in the CMS system, but where they follow a certain angular distribution, the matrix  $M_{eff}$  is changed (see dashed histograms in Figure 2.5). Obviously, the corrected experimental distribution  $Exp_{corr}(\cos(\theta_{K^+}))$  is different if one corrects with the one or the other simulation model.

Therefore, before correcting the experimental data, it is necessary to first find an appropriate simulation model  $F_{Sim}$ . This model needs to describe the uncorrected experimental data in all phase space regions. Only in this way it is guaranteed that the kinematics in the real data are correctly imitated so that the integration procedure in equation (2.11) delivers the correct one dimensional efficiency matrices. Also for the correction of the  $\Sigma(1385)^+$  and  $\Lambda(1405)$  signals, proper simulation models had to be found. The way how this was done is explained in the following chapters.



### 3 Measurement of the $\Sigma(1385)^+$ resonance in proton-proton interactions

The following chapter describes the exclusive reconstruction of the reaction  $p + p \rightarrow \Sigma(1385)^+ + n + K^+$ . The presented analysis allowed to precisely determine the spectral shape of the  $\Sigma(1385)^+$  and to extract its production cross section. In order to get insight into the production mechanisms of the reaction, several angular distributions in the CMS-, Gottfried-Jackson- and helicity-frames were investigated. Strong evidence was found that the  $\Sigma(1385)^+$  resonance is produced in peripheral collisions via the exchange of light mesons, like pions or kaons. Furthermore, the helicity angle distributions show indications that the  $\Sigma(1385)^+$  partially stems from the decay of a heavy  $\Delta^{++}$  resonance with a mass of around 2035 MeV/ $c^2$  and a width of around 250 MeV/ $c^2$ . The results of this work can give major constraints and input parameters for an improved incorporation of the  $\Sigma(1385)$  dynamics into transport models, which are used to simulate heavy ion collisions. Especially the contributions of intermediate resonances like  $\Delta^{++}$  to the formation of final state resonances are often unknown. This knowledge is, however, crucial for a precise modeling of particle production in those transport codes.

Moreover, the investigation of the  $\Sigma(1385)^+$  resonance is also relevant for the  $\Lambda(1405)$  analysis of chapter 4. As the  $\Sigma(1385)$  and the  $\Lambda(1405)$  are close in mass and have similar decay channels (see chapter 4), the study and understanding of these two resonances is correlated. In fact, several methods developed for the reconstruction of the  $\Sigma(1385)^+$  will also find their application in the analysis of the  $\Lambda(1405)$  resonance.

The following chapter is divided into four parts:

The first section discusses general aspects of hyperon production in proton-proton reactions. For that purpose, the One-Boson-Exchange (OBE) model is introduced and discussed. Furthermore, the CMS-, Gottfried-Jackson- and helicity-reference frames are presented and the sensitivity of the associated angular distributions to the production mechanism is depicted.

The second section describes the technical part of the analysis. The cuts applied for the event selection are discussed first. After that the determination and treatment of the non-physical background due to particle misidentification is presented in detail. With help of simulations the pure  $\Sigma(1385)^+$  signal can finally be extracted within the HADES acceptance.

In the third section of the chapter a simulation model is developed, which reproduces the kinematics in the experimental data consistently and thus allows to correct the data for the effects induced by the limited HADES efficiency and acceptance. Within this context several observables, especially different angular distributions, are investigated and interpreted. The development of the model requires the use of simulations with anisotropic  $\Sigma(1385)^+$  production and the inclusion of an intermediate  $\Delta^{++}$  resonance.

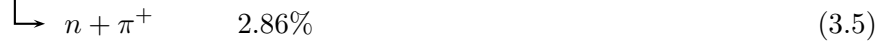
Finally, the total and differential production cross sections of the reaction  $p + p \rightarrow \Sigma(1385)^+ + n + K^+$  could be extracted. A discussion of the obtained results, which have been published in [A<sup>+</sup>12a], concludes the chapter.

### 3.1 $\Sigma(1385)^+$ production in proton-proton reactions - General considerations

#### 3.1.1 $\Sigma(1385)^+$ production and decay

In the following part the production of  $\Sigma(1385)^+$  in proton-proton interactions at 3.5 GeV kinetic beam energy is investigated. Strangeness and baryon number conservation requires that the  $\Sigma(1385)^+$  hyperon is produced together with another baryon and a kaon. Hence, one of the energetically cheapest possibilities is to produce it via reaction (3.1), where also a neutron and a  $K^+$  appear in the final state. The  $\Sigma(1385)^+$  resonance itself decays strongly into three different states, which always consist of a hyperon and a meson. It depends on the detector system and the applied analysis method which of these decay channels can be investigated.

Generally, the purest analysis in terms of background contributions is the exclusive analysis. It requires that all particles in the final state are reconstructed and identified. In chapter 2 it has been mentioned that HADES is only suited for charged particle identification. For this reason, channels with maximum one neutral particle in the final state are candidates for an exclusive analysis. The single neutral particle can then still be reconstructed via the missing mass technique (see section 2.2.3). Therefore, the only possible channel for such an analysis is channel (3.2), which has also the largest branching ratio of 56.33%. The fact that the four final state particles ( $p, K^+, \pi^+, \pi^-, n$ ) are different, excludes already combinatorial background in the analysis. Concerning statistics and purity, this channel is thus the most promising one, and it was therefore chosen for the reconstruction of the  $\Sigma(1385)^+$ .



For completeness it must be mentioned that the associated production of the  $\Sigma(1385)^+$  together with a proton and a  $K^0$  is expected to have a large production cross section as well. However, the  $K^0$  decays in 35% of all cases via a  $K_S^0$  into a  $\pi^+$  and a  $\pi^-$  so that the final state contains two  $\pi^-$  and two protons. The exclusive analysis would therefore have to deal with a certain contribution of combinatorial background. Furthermore, instead of four, this channel can have six charged

particles in the final state. If all these particles shall be reconstructed, the acceptance is reduced significantly.

### 3.1.2 Production mechanisms and reference frames

Before details about the analysis procedure of channel (3.2) are discussed, it is important to get a general understanding on how particle production happens in proton-proton reactions. Later on, the reaction  $p+p \rightarrow \Sigma(1385)^+ + n + K^+$  will be investigated in several angular distributions. This allows to develop a simulation model that reproduces the kinematics in the experimental data. In fact, the different angular distributions are sensitive to the characteristics of the reaction process. Therefore, the meaning of these distributions shall be discussed in the following section.

#### 3.1.2.1 The One-Boson-Exchange model

The reaction studied in this work produces a  $\Sigma(1385)^+$ , a neutron and a  $K^+$  from the initial collision of two protons (see reaction (3.1)). The fact that the  $\Sigma(1385)^+$  is not a stable particle, but further decays into a  $\Lambda$  and a  $\pi^+$ , is neglected in the first place. In this way a pure three particle production process is assumed.

Similar reactions, but with the production of ground state hyperons (for example  $p+p \rightarrow \Lambda + p + K^+$  or  $p+p \rightarrow \Sigma^+ + n + K^+$ ), have been investigated extensively in the last years [BCN66, C<sup>+</sup>68b, AB<sup>+</sup>10]. In these experiments it was found that the nucleon and the hyperon are not produced isotropically but that they show strong angular distributions. As an example, Figure 3.1 presents results for the reaction  $p+p \rightarrow \Lambda + p + K^+$ , measured at a beam momentum of 6.6 GeV/c [FS67].

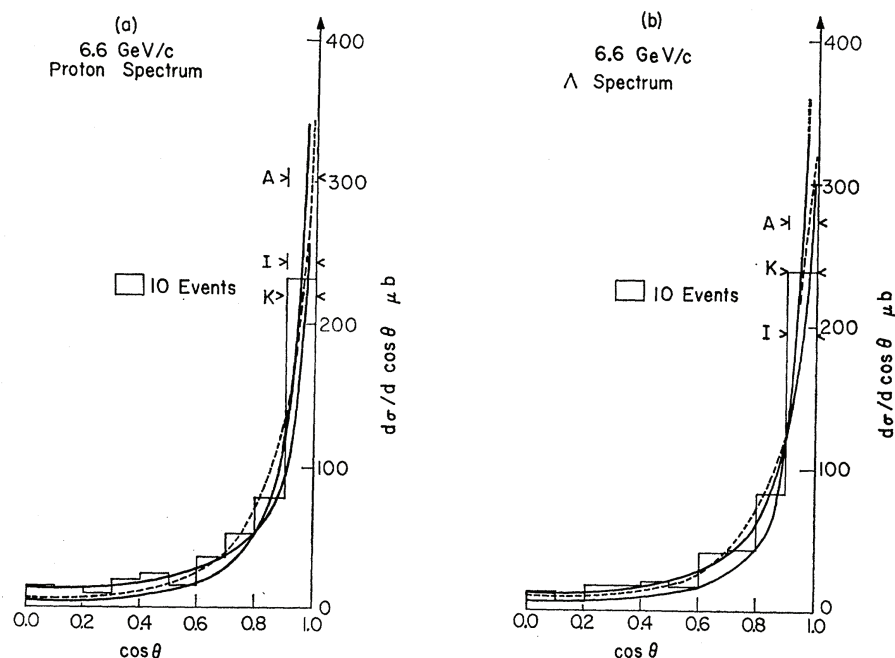


**Figure 3.1:** Center-of-mass system (CMS): Absolute value of the cosine of the proton (a) and of the  $\Lambda$  (b) angle to the incoming proton direction, measured at 6.6 GeV/c beam momentum [FS67]. Solid and dashed lines indicate different predictions of OBE models.

The two figures show the absolute values of the cosine of the proton angle (panel (a)) and of the  $\Lambda$  angle (panel (b)) to the initial proton direction. These angles are calculated in the proton-proton center-of-mass system (CMS). The observed angular distributions are both peaking at  $|\cos(\theta) = 1|$ , which suggests that the particles are preferably emitted along the direction of the incoming protons.

An explanation for this phenomenon can be given by the One-Boson-Exchange (OBE) model. In this model it is assumed that the initial protons exchange a (virtual) strange or non-strange boson. The interaction between the boson and the protons results in the production of the final state particles. Some possible diagrams, representing the so-called t-channel exchange, are illustrated in Figure 3.2 [FS67]. Here  $Y$  stands for hyperons (e.g.  $\Lambda$ ,  $\Sigma^+$  etc.),  $N$  stands for the ground state nucleons ( $p$  and  $n$ ), and  $N^*$  stands for every kind of nucleon resonances, might it be an isospin  $\frac{1}{2}$   $N^*$  state or an isospin  $\frac{3}{2}$   $\Delta$  state. For the sake of simplicity the exchange of a non-strange meson is from now on just referred to pion exchange; strange meson exchange is abbreviated as kaon exchange.

The properties of the exchange diagrams and of the observed angular distributions are largely determined by the exchange meson itself. The exchange of a heavy meson leads to very central  $p+p$  collisions, where the nucleon and the hyperon are produced rather isotropically in the CMS. Light meson exchange, on the other hand, is correlated with very peripheral  $p+p$  collisions. In this case the exchange boson transfers mostly small 4-momentum so that the particles are preferably emitted in the direction of the initial protons. This explains the anisotropic angular distributions for hyperons and nucleons observed by several experiments (see e.g. [C<sup>+</sup>68b, BCN66, FS67]).

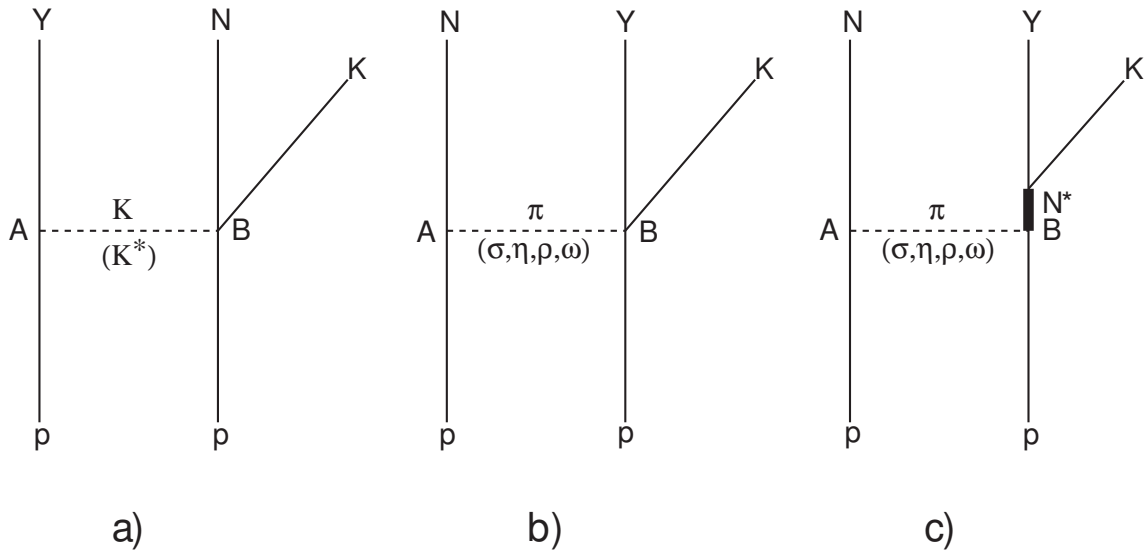


**Figure 3.2:** Different graphs representing t-channel strange meson exchange (a) or non-strange meson exchange (b, c). In panel c) an intermediate nucleon resonance is produced, which decays into a hyperon and a kaon. The two vertices, appearing in all graphs, are labeled with A and B.

The OBE model describes the boson exchange process with help of the Chew-Low formula [C<sup>+</sup>68b]:

$$\frac{d^3\sigma}{d(M^2) d(\Delta^2) d\Omega} \propto \frac{\Delta^2 + (m_p - m')^2}{(\Delta^2 + \mu^2)^2} k M \frac{d\sigma(M)}{d\Omega} \quad (3.8)$$

$$\text{with } k = \frac{1}{M} \left[ \frac{1}{4} M^4 - \frac{1}{2} M^2 (m_p^2 + \mu^2) + \frac{1}{4} (m_p^2 - \mu^2)^2 \right]^{\frac{1}{2}}$$

where the different parameters have the following meaning:

- $\Delta^2$  is the squared 4-momentum of the exchange meson, which is transferred to the produced baryon of mass  $m'$  at the vertex A of Figure 3.2.
- $\mu$  and  $m_p$  are the masses of the exchange meson and the proton, respectively.
- $M$  is the invariant mass of the two final state particles emerging from vertex B (e.g.  $\Lambda$  and  $K^+$  in case of pion exchange).
- $\frac{d\sigma(M)}{d\Omega}$  is the differential two particle production cross section at vertex B. For example for the reaction  $\pi^0 + p \rightarrow \Lambda + K^+$  in case of pion exchange.
- $k$  is a kinematic factor, which can be identified with the momentum of the exchange meson (e.g.  $\pi^0$ ) in the center-of-mass system of the two produced particles at vertex B (e.g.  $\Lambda$  and  $K^+$ ).

With this parameterization one is able to reproduce the forward peaking of the experimental data in Figure 3.1 rather well (see solid and dashed lines). This can be easily understood by considering the denominator in equation (3.8). It contains the term  $(\Delta^2 + \mu^2)^2$ , which prefers low momentum transfer  $\Delta^2$ , correlated with a small deflection of the outgoing particles to the incoming particles. Furthermore, the appearance of the squared meson mass ( $\mu^2$ ) in the denominator takes into account that the anisotropy effect is largest for light mesons. Indeed, the model would give a more isotropic distribution of the produced particles in the CMS if, for example,  $\rho$  meson exchange instead of pion exchange is considered [HKAY12]. Information on the exchange meson are thus accessible by studying angular distributions in the CMS.

A further important point of the presented model is the term  $\frac{d\sigma(M)}{d\Omega}$  in equation (3.8). It accounts for the differential cross section of the  $2 \rightarrow 2$  reaction at vertex B in Figure 3.2. This differential cross section might be characterized by certain angular distributions or the production of intermediate  $N^*$  resonances. Hence, this quantity influences the production dynamics and with this also the angular distributions. However,  $\frac{d\sigma(M)}{d\Omega}$  is usually an unknown function, which can be accessed by studying the so-called Gottfried-Jackson and helicity angles.

With help of the OBE model one gets an idea on how particle production happens in proton-proton reactions and which quantities are of importance in this context. The experimental data presented in this work are perfectly suited for the development of theoretical models based on the OBE approach. As fully corrected CMS, Gottfried-Jackson and helicity angular distributions are presented, access to all important observables is provided. The meaning and the interpretation of these distributions are discussed in the following parts. For this purpose, it is again useful to consider the graphs in Figure 3.2 and to take the OBE model as a working hypothesis.

### 3.1.2.2 CMS angle

The center-of-mass system (CMS) is the Lorentzian frame, where the beam and target proton ( $p_b$  and  $p_t$ ) have identical momenta in opposite directions. Hence, the total momentum in this frame is 0 (see Figure 3.3).

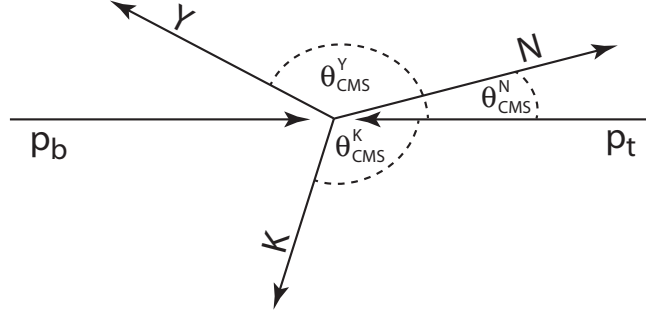


**Figure 3.3:** Three particle production in the CMS frame.

The production angle  $\cos(\theta_{CMS}^i)$  of the particles  $Y$ ,  $N$  and  $K$  is especially interesting in connection with the OBE model. As pointed out before, the angular distributions of the three final state particles are often anisotropic in this reference frame (see results in Figure 3.1). As the proton-proton system is a symmetric system, also the angular distributions must be symmetric with respect to  $\cos(\theta_{CMS}^i) = 0$ .

The OBE model suggest that the production anisotropy is influenced by the exchange meson itself. As an example, the case of pure kaon exchange (see Figure 3.2, panel a)) is considered. Due to the low momentum transfer at vertex A, the hyperon  $Y$  is preferably emitted under a low deflection angle and the resulting angular distribution in  $\cos(\theta_{CMS}^Y)$  is anisotropic. Because of momentum conservation, the summed 3-momentum of the nucleon and the kaon, which are produced at vertex B, has to compensate the 3-momentum of the hyperon ( $\vec{p}_N + \vec{p}_K = -\vec{p}_Y$ ). Therefore, the angular distributions of  $N$  and  $K$  must be anisotropic as well. Since momentum conservation can be realized by different values of  $\vec{p}_N$  and  $\vec{p}_K$ , the expected anisotropies for the nucleon and the kaon are less pronounced than the one of the hyperon. Thus, kaon exchange could lead to the strongest production anisotropy in the CMS for the hyperon.

At this point one has to take into account that also the differential cross section  $\frac{d\sigma(M)}{d\Omega}$  (see equation (3.8)) of  $N$  and  $K$  at vertex B can be anisotropic. This obviously influences the distributions of  $\cos(\theta_{CMS}^N)$  and  $\cos(\theta_{CMS}^K)$ . In general, this effect additionally increases the anisotropy of the nucleon and the kaon in the CMS [FS67]. On the other hand, the properties of  $\frac{d\sigma(M)}{d\Omega}$  have absolutely no influence on the angular distribution of the hyperon.

One can thus conclude: In case of kaon exchange, the hyperon is the leading particle, which is only influenced by the kinematics at vertex A. Its angular distribution in the CMS is expected to be anisotropic. The angular distributions of the nucleon and the kaon reflect the hyperon kinematics so that their angular distributions are anisotropic as well. However, their distributions are additionally influenced by the properties of  $\frac{d\sigma(M)}{d\Omega}$  at vertex B.

In case of pion exchange (see Figure 3.2 b) and c)), the roles of the hyperon and the nucleon are exchanged. Now the nucleon is the leading particle, which should show the strongest anisotropy. The hyperon and the kaon distributions are kinematical reflections, additionally influenced by the production process ( $\frac{d\sigma(M)}{d\Omega}$ ) at vertex B.

Furthermore, it was shown that the mass of the exchange boson determines the strength of the anisotropy. Light meson exchange results in very anisotropic distributions, whereas the exchange of heavy mesons can be identified if the CMS distributions are more isotropic.

In summary, the angular distributions in the CMS are sensitive to the characteristics of the exchange meson. However, the interpretation of these distributions is still difficult, as they are in general correlated with the differential cross section  $\frac{d\sigma(M)}{d\Omega}$  at the vertex B. This quantity gets accessible in the Gottfried-Jackson angle.

### 3.1.2.3 Gottfried-Jackson angle

The Gottfried-Jackson (G-J) frame is the rest frame of two out of the three produced particles. The kinematics of all initial and final state particles in case of the  $K$ - $N$  ( $K$ - $Y$ ) rest frame is illustrated in Figure 3.4.

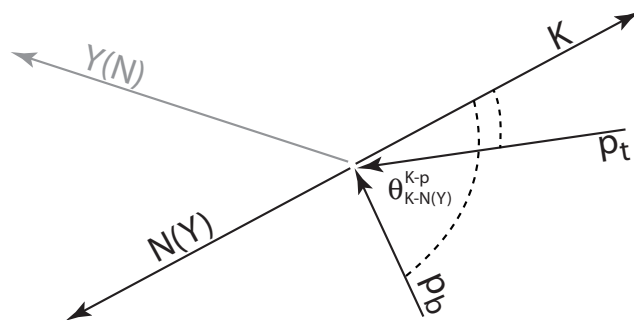


**Figure 3.4:** Gottfried-Jackson frame and angles in case of kaon (pion) exchange. The angle of the produced kaon to the incoming proton is calculated for both, the beam type proton ( $p_b$ ) and the target type proton ( $p_t$ ).

In the G-J frame, the G-J angle is defined as the angle between one of the rest frame particles (e.g. the kaon) and the initial proton ( $\theta_{K-N(Y)}^{K-p}$ ). The superscript ( $K-p$ ) stands for the two particles, between which the angle is measured; the subscript ( $K-N(Y)$ ) indicates which rest frame is used. Completely equivalent to the angle between the kaon and the proton is the angle between the produced baryon and the proton ( $\theta_{K-N(Y)}^{N(Y)-p}$ ), as those two angles add up to  $180^\circ$ .

The motivation to study the G-J angles arises from the fact that in case of kaon (pion) exchange, the  $K$ - $N$  ( $K$ - $Y$ ) rest frame is equivalent to the rest frame of the exchanged meson and the proton, contributing to the vertex B of Figure 3.2 [AB<sup>+</sup>10]. In this way the initial  $2 \rightarrow 3$  reaction is reduced to a pure  $2 \rightarrow 2$  reaction of the form  $K(\pi) + p \rightarrow N(Y) + K$ . Hence, the kinematics at vertex A do not influence this observable; only the kinematics at vertex B play a role. The G-J frame can thus be used to determine the properties of  $\frac{d\sigma(M)}{d\Omega}$ . Every wave, contributing at vertex B, should reflect itself in the corresponding G-J angular distribution. This is also true if the particle production does not happen directly, but via an intermediate resonance (see Figure 3.2 c)). The internal angular momentum of the resonance is then reflected in this observable. It has to be noticed that the distributions in the G-J frames do not have to be symmetric at all. The reason is the asymmetric reaction system, where either a kaon or a pion collides with a proton. Another peculiarity arises from the fact that the two initial protons are indistinguishable. It is thus not known which of those protons contributes to the reaction at vertex B. For this reason, the angular distribution is calculated by using the angle to both protons (see Figure 3.4).

To illustrate the importance of the G-J frame, the example of *pure* pion exchange with pure s-wave scattering at vertex B is considered. Just due to the low momentum transfer with the pion, one expects a strong anisotropy of  $\cos(\theta_{CMS}^N)$ . The angular distribution  $\cos(\theta_{K-Y}^{K-p})$  in the G-J frame is completely independent from this. As s-wave scattering is assumed at vertex B, the distribution of  $\cos(\theta_{K-Y}^{K-p})$  must be flat. In this sense the transformation from the CMS to the G-J frame disentangles the kinematical effects of particle exchange from the influence of  $\frac{d\sigma(M)}{d\Omega}$  at vertex B. This, however, is only true if *pure* pion exchange is present. An additional contribution of kaon exchange changes the interpretation, as in this case the kaon and the hyperon do not emerge from the same vertex. As a result, the distribution  $\cos(\theta_{K-Y}^{K-p})$  is influenced by the kinematics at vertex A and vertex B.

Altogether, the G-J frame with its angular distribution  $\cos(\theta_{K-N(Y)}^{K-p})$  can give a unique access to  $\frac{d\sigma(M)}{d\Omega}$  at vertex B only if pure kaon (pion) exchange is present. As soon as also pion (kaon) exchange contributes, a kinematical correlation with the CMS distributions distorts this information. A concrete example can be found in section 3.4.

For completeness it has to be mentioned that there is also a third possible G-J frame, namely the rest frame of  $Y$  and  $N$ . The G-J angle in this frame is only meaningful in case of baryon exchange with the production of  $Y$  and  $N$  at vertex B. This case is not considered in the graphs of Figure 3.2. The corresponding angular distribution will be examined later on, as it also reflects the kinematics in the distributions  $\cos(\theta_{CMS}^N)$  and  $\cos(\theta_{CMS}^Y)$  (see section 3.4).

### 3.1.2.4 Helicity angle

The helicity angle is defined in the same rest frame as the G-J angle, but instead of calculating the angle of the kaon to the initial proton, the angle to the third produced particle is used (see Figure 3.5). In this sense the helicity angle interrelates only the kinematics of the three output

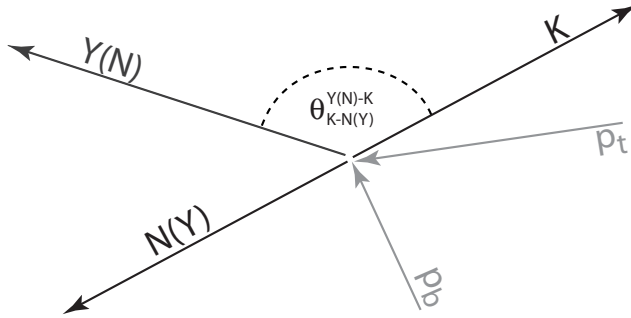


**Figure 3.5:** Helicity angle in the  $N(Y)$ - $K$  rest frame.

particles of the reaction; the initial protons are not considered. The helicity angle distribution is a special projection of the Dalitz plot, and is thus a proper observable to identify the kinematics behind the particle production. A uniformly populated Dalitz plot should result in isotropic helicity angle distributions; a physical or kinematical effect, distorting the Dalitz plot, will reflect itself in anisotropic helicity angle distributions [AB<sup>+</sup>10]. Therefore, the helicity angle is an ideal tool to study final state interaction but also to identify the possible contributions of intermediate resonances, decaying into two of the three final state particles. Indeed, the production of  $Y$

and  $K$  turned out to proceed partially via such an intermediate resonance (see e.g. [AB<sup>+</sup>10, C<sup>+</sup>68b]). As an example, one can assume pion exchange with the associated production of a nucleon resonance at vertex B. The angular distributions  $\cos(\theta_{K-N}^{Y-N})$  and  $\cos(\theta_{Y-N}^{Y-K})$  will show characteristic behaviors, which reflect the mass and width of the resonance. In contrast to this, the helicity angle distribution, calculated in the rest frame of the two decay particles ( $\cos(\theta_{Y-K}^{Y-N})$ ), is not influenced by the mass and width of the resonance. Only if the resonance carries angular momentum  $L > 0$  and only if it is polarized, this distribution will be different from isotropy [A<sup>+</sup>11]. However, as soon as more than one nucleon resonance contributes to the decay into  $Y$  and  $K$ , interference effects can influence the distribution  $\cos(\theta_{Y-K}^{Y-N})$  as well [AB<sup>+</sup>10].

In summary, the three particle production process has been discussed on the basis of altogether nine possible angular distributions; three CMS angles, three G-J angles and three helicity angles. As already mentioned, not all of these observables are kinematically independent from each other. In fact, the exit phase space of a  $2 \rightarrow 3$  reaction has nine dimensions. Energy and momentum conservation constrains this down to a five dimensional hypersurface. Including azimuthal symmetry around the beam axis, only four independent degrees of freedom remain.

### 3.1.2.5 $\Sigma(1385)^+$ decay distribution

Till now, the discussion was limited to a three particle production process. The subsequent decay of the  $\Sigma(1385)^+$  has been totally neglected. By discarding this assumption, another reference frame gets accessible, namely the G-J frame of the decay particles  $\Lambda$  and  $\pi^+$  (see Figure 3.6). This

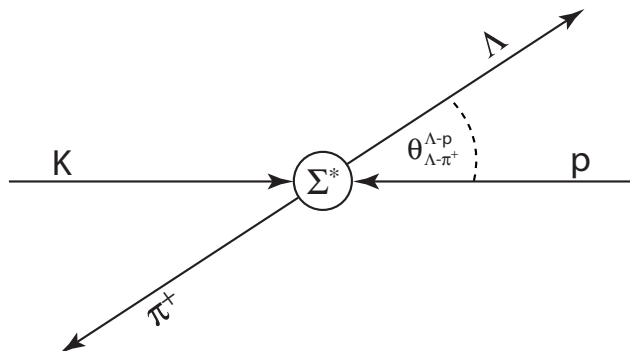


**Figure 3.6:** G-J frame for the decay products of the  $\Sigma(1385)^+$ . One incoming particle is assumed to be a kaon.

frame coincides with the rest frame of the  $\Sigma(1385)^+$  itself. In fact, the angular distributions in this reference frame can deliver further information about the exchange meson in the peripheral proton-proton collision.

For the sake of simplicity, it has been assumed that only the lightest mesons, namely pseudo scalar mesons like  $\pi$  and  $K$  with  $J^P = 0^-$  are exchanged. This assumption is now rejected and also vector mesons  $J^P = 1^-$  are considered to take part in the process. The distributions in the  $\Lambda-\pi^+$  reference frame are especially sensitive to the relative contribution of  $K$  and  $K^*$  exchange [W<sup>+</sup>11]. In order to understand the connection between the the decay distribution and the exchange meson, it is assumed that the  $\Sigma(1385)^+$  resonance is exclusively produced via kaon exchange. The  $\Lambda-\pi^+$  reference frame is then equivalent to the rest frame of the incoming kaon and the incoming proton (see Figure 3.6).

The angular distributions of the decay  $W(\theta, \varphi)$  are determined by the quantum numbers of the participating particles. In the helicity amplitudes framework,  $W(\theta, \varphi)$  can be expressed as follows [GJ64, Jac64]:

$$W(\theta, \varphi) \propto \sum_{\lambda_\alpha, \lambda_\beta, m, m'} |M(\lambda_\alpha, \lambda_\beta)|^2 e^{i(m-m')\varphi} d_{m, \lambda}^{s_d}(\theta) d_{m', \lambda}^{s_d}(\theta) \langle m | \rho_d | m' \rangle \quad (3.9)$$

where

- $\lambda_\alpha$  and  $\lambda_\beta$  are the possible helicities of the decay particles  $\alpha$  and  $\beta$ ;  $\lambda = \lambda_\alpha - \lambda_\beta$
- $M(\lambda_\alpha, \lambda_\beta)$  is a factor determining the sign of the summands (see [GJ64])
- $s_d$  is the spin of the intermediate resonance  $d$ , decaying into  $\alpha$  and  $\beta$
- $m$  and  $m'$  are the spin projections of  $s_d$
- $d(\theta)$  are special rotation matrices (see [GJ64])
- $\rho_d$  is the spin-density matrix of the state  $d$

The spin-density matrix  $\rho_d$  carries information about the production process of  $d$ . Considering explicitly the example of  $d$  being a  $J = \frac{3}{2}$  state, like  $\Sigma(1385)^+$ , the matrix looks like follows [GJ64]:

$$\rho_d = \begin{pmatrix} \rho_{3,3} & \rho_{3,1} & \rho_{3,-1} & i\rho_{3,-3} \\ \rho_{3,1}^* & \frac{1}{2} - \rho_{3,3} & i\rho_{1,-1} & \rho_{3,-1}^* \\ \rho_{3,-1}^* & -i\rho_{1,-1} & \frac{1}{2} - \rho_{3,3} & -\rho_{3,1}^* \\ -\rho_{3,-3} & \rho_{3,-1} & -\rho_{3,1} & \rho_{3,3} \end{pmatrix} \quad (3.10)$$

If  $d$  decays into a  $J_\alpha = \frac{1}{2}$  particle (like  $\Lambda$ ) and a  $J_\beta = 0$  particle (like  $\pi^+$ ), equation (3.9) can be written as:

$$\begin{aligned} W(\theta, \varphi) \propto & \rho_{3,3} \sin^2(\theta) + \left(\frac{1}{2} - \rho_{3,3}\right) \left(\frac{1}{3} + \cos^2(\theta)\right) - \\ & - \frac{2}{\sqrt{3}} \text{Re} \rho_{3,-1} \sin^2(\theta) \cos(2\varphi) - \frac{2}{\sqrt{3}} \text{Re} \rho_{3,1} \sin(2\theta) \cos(\varphi) \end{aligned} \quad (3.11)$$

The elements of the spin-density matrix thus get accessible by measuring the decay angular distributions. If only the variable  $\theta$  is investigated, the integration over  $\varphi$  simplifies the expression to:

$$W(\theta) \propto \rho_{3,3} \sin^2(\theta) + \left(\frac{1}{2} - \rho_{3,3}\right) \left(\frac{1}{3} + \cos^2(\theta)\right) \quad (3.12)$$

With this only the diagonal elements of  $\rho_d$  contribute to the final equation (3.12). These diagonal elements can be associated with the possible spin projections  $m$  of the resonance;  $\rho_{33}$  represents  $m = \pm\frac{3}{2}$ , and  $\frac{1}{2} - \rho_{3,3}$  represents  $m = \pm\frac{1}{2}$ .

Coming back to the example of pure kaon exchange, the colliding system can either consist of a pseudo-scalar kaon ( $J^P = 0^-$ ) and a proton ( $J^P = \frac{1}{2}^+$ ) or a vector kaon  $K^*$  ( $J^P = 1^-$ ) and a proton. In the first case only the  $m = \pm\frac{1}{2}$  states can be populated. The element  $\rho_{3,3}$  is thus 0 and the decay distribution follows a  $\frac{1}{3} + \cos^2(\theta)$  function. Compared to this, the exchange of  $K^*$  delivers an additional spin of 1 and by adding this to the spin  $\frac{1}{2}$  of the proton, also the

$m = \pm\frac{3}{2}$  states can be excited. A  $\sin^2(\theta)$  contribution in the decay angular distribution is a clear indication for such a process.

From this discussion one sees that by investigating the decay distribution of the  $\Sigma(1385)^+$ , one can get additional information on the exchanged mesons. However, it has to be pointed out that the considerations above were made under the assumption that only kaon exchange is present. In the case of proton-proton reactions this is certainly not the case, as also  $\pi$ ,  $\rho$ , etc. exchange can contribute. The interpretation of the decay distribution  $W(\theta)$  is thus more difficult and requires advanced theory models.

All the discussed angular distributions in the different reference frames will be investigated in the following sections. On the basis of these investigations an appropriate simulation model for the reaction  $p + p \rightarrow \Sigma(1385)^+ + n + K^+$  will be developed, which can be used for the acceptance and efficiency corrections.

## 3.2 Analysis procedure

This section discusses the different analysis steps, developed to extract the  $\Sigma(1385)^+$  signal in proton-proton reactions. The first part presents the general analysis procedure with the different data selection cuts. This part repeats some of the results, already presented in [Sie10a].

To obtain the pure  $\Sigma(1385)^+$  signal, it is also necessary to determine and to understand the contributing background sources. The second part of this section therefore describes the evaluation of the misidentification background. By the inclusion of simulations also the physical background sources can be controlled, and finally the pure  $\Sigma(1385)^+$  signal can be extracted.

### 3.2.1 Data selection

Considering channel (3.2), the general analysis procedure is the following:

1. Select events which contain the four charged particles  $p$ ,  $K^+$ ,  $\pi^+$  and  $\pi^-$ .
2. Reconstruct the intermediate  $\Lambda(1116)$  via its decay products ( $p$  and  $\pi^-$ ).
3. Extract the neutron signal with help of the missing mass technique.
4. Reconstruct the  $\Sigma(1385)^+$  from the invariant mass of the  $\Lambda$  and the  $\pi^+$ .

#### 3.2.1.1 Particle identification

The first step in the analysis was the selection of events with the proper particle candidates, namely a proton, a  $K^+$ , a  $\pi^+$  and a  $\pi^-$  candidate (see channel (3.2)). Therefore, events were selected with three positively and one negatively charged particles. In order to decide if the obtained events contain also the proper particle species, the energy loss method, presented in section 2.2.1, was applied. Figure 3.7 shows the energy loss  $dE/dx$  as a function of the reconstructed laboratory momentum for all particle tracks in all events of the measured  $p + p$  data. The picture is separated for the MDC system (panel a)) and the TOFinio system (panel b)). The theoretical Bethe-Bloch curves for pions, kaons and protons are indicated by the solid black lines [Sch08]. Pion and proton candidates were identified with help of the MDC  $dE/dx$  information. The corresponding graphical cuts are shown as the black dashed lines in Figure 3.7, panel a). Indeed, only the MDC information was used to select these two particle species. Kaon candidates were selected in a similar way. A positively charged particle was identified as a kaon candidate if it lies within the kaon MDC  $dE/dx$  cut (not shown in panel a)), and, in order to increase the purity, it must at the same time lie within the kaon TOFinio  $dE/dx$  cut (dashed line in panel b)). A  $dE/dx$  information is also available for the TOF detector system, but due to the kinematics of the proton-proton reaction system, only a negligible amount of kaons reaches such large polar angles.

Despite of the fact that no kaon signals are visible in the Figure 3.7 a) or b), the selection of kaon candidates via  $dE/dx$  cuts turned out to be essential for the kaon identification [A<sup>+</sup>09b, Sie10a]. Concerning the purity of the event selection, the clear pion and proton signals in Figure 3.7 a) allow to identify these two particle species rather unambiguously. This is not the case for the kaon candidates, where a huge contamination by misidentified pions and protons is expected. This hypothesis is supported by studying the  $K^+$  mass distribution in Figure 3.8. The mass of the  $K^+$  candidates was determined from the time-of-flight reconstruction method of section 2.2.2.

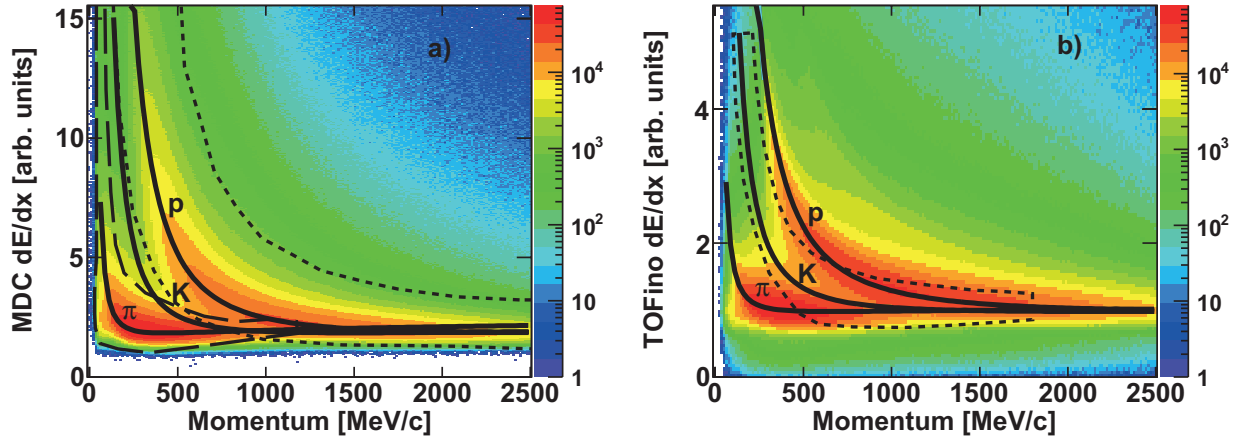


**Figure 3.7:**  $dE/dx$  vs. momentum for all detected particles in MDCs (panel a)) and TOFino (panel b)) [HAD09]. Modified Bethe-Bloch curves are indicated by the solid black lines. The dashed lines in a) show the MDC cuts for protons (short dashed) and pions (long dashed) and in (b) the TOFino cut for kaons.

The picture shows two peaks, one located around the nominal pion mass, the second one located around the nominal proton mass. In the vicinity of the nominal  $K^+$  mass no such structure is visible. This confirms the conclusion from Figure 3.7 that the contamination of the  $K^+$  candidates by misidentified pions and protons is orders of magnitude larger than the true kaon signal. Still, the kaon candidates must contain a certain amount of true kaons, but the very limited resolution of the time-of-flight reconstruction method does not yet allow to see them in Figure 3.8. Nevertheless, the mass information was used to further purify the kaon candidates. By selecting only events, where the mass of the  $K^+$  candidate lies within the range from 280  $\text{MeV}/c^2$  to 780  $\text{MeV}/c^2$  (gray shaded area in Figure 3.8), most of the misidentified pions and protons were removed, whereas the true kaons, even though not visible at this level, mostly survived this cut.

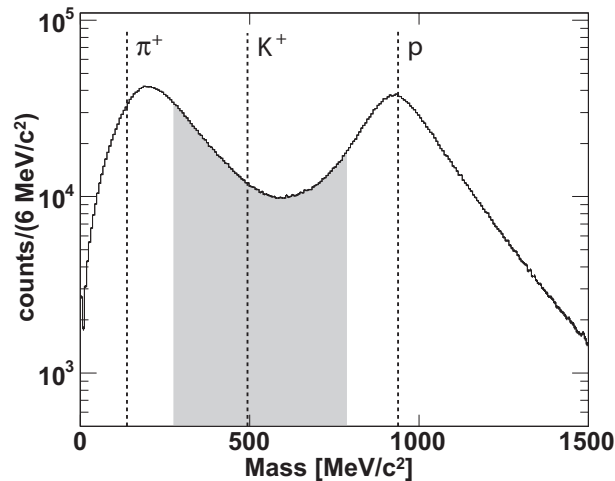


**Figure 3.8:** Reconstructed mass distribution of  $K^+$  candidates. Vertical lines indicate the nominal masses of  $\pi^+$ ,  $K^+$  and proton. The gray shaded area (280  $\text{MeV}/c^2$ –780  $\text{MeV}/c^2$ ) indicates the  $K^+$  mass cut.

### 3.2.1.2 $\Lambda(1116)$ and neutron reconstruction

The selection of the particle candidates, according to the final state of channel (3.2), was only the first step of the  $\Sigma(1385)^+$  analysis. Additionally, the intermediate and neutral particles, appearing in the reaction, have to be considered. The intermediate  $\Lambda$  hyperon could be reconstructed from its decay products, namely the proton and the  $\pi^-$ . The topology of the  $\Lambda$  decay (see Figure 3.9) was used to define further cuts for the event selection.

The  $\Lambda$  has a decay length  $c\tau = 7.89$  cm [B<sup>+</sup>12]. The proton, with its mass of around 938 MeV/ $c^2$ , is close to the  $\Lambda$  mass, whereas the  $\pi^-$  is much lighter. Considering momentum and energy conservation during the  $\Lambda$  decay, the proton should fly almost in the same direction as the  $\Lambda$ ; the pion can take a quite different direction. A possible track and decay topology of the  $\Lambda$  is illustrated in Figure 3.9.

The tracking procedure of HADES delivers, besides the track momentum, also the track position in the three dimensional position space. This information can be used to calculate vertices, intersection points etc. For the  $\Lambda$  reconstruction, the intersection point of the  $\pi^+$  and the  $K^+$  candidate of each event was defined as the primary vertex (red dot in Figure 3.9). The intersection point between the proton and the  $\pi^-$  was defined as the secondary vertex (blue dot). As only two tracks were used for the vertex reconstruction, the position resolution is limited to 0.5-1.0 cm [Sch09]. Furthermore, the minimum distance between the proton and the  $\pi^-$  ( $d_{p\pi^-}$ ) as well as the closest approach of the  $\pi^-$  and the proton to the primary vertex ( $d_{\pi^-}$  and  $d_p$ ) were calculated. If the proton and the  $\pi^-$  stem from the decay of a  $\Lambda$  hyperon, the average distance between the primary and the secondary vertex ( $d_\Lambda$ ) should be in the order of cm; the distance between the  $\pi^-$  and the proton track should be small. The argumentation about energy and momentum conservation from before also suggests that the  $\pi^-$  track has in general a larger distance to the primary vertex ( $d_{\pi^-}$ ) than the proton track ( $d_p$ ). With these considerations,  $\Lambda$  selection cuts were defined. The cuts, which turned out to be appropriate for the analysis, and which were applied to the data sample, are listed in Table 3.1.

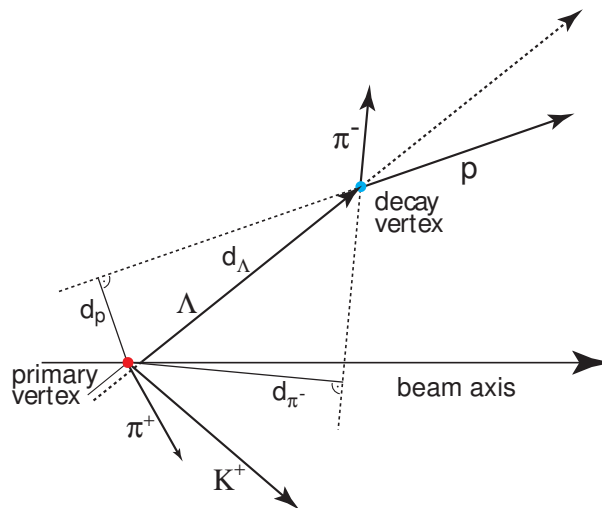


**Figure 3.9:** Topology of the  $\Lambda$  track and decay. Colored points indicate the primary and secondary vertices [Sch08].

<i>Cut on:</i>	<i>Values</i>
Distance of secondary vertex to primary vertex	$d_{\Lambda} > 15$ mm
Minimum distance between proton and $\pi^{-}$ track	$d_{p\pi^{-}} < 20$ mm
Distance of $\pi^{-}$ track to primary vertex	$d_{\pi^{-}} > d_p$

**Table 3.1:** Applied cuts on the  $\Lambda$  track topology.

With these additional requirements, the invariant mass  $M(p, \pi^{-})$  of the remaining events is plotted in Figure 3.10. A clear  $\Lambda$  signal on top of a large background is visible. The signal was fitted with a Gaussian function together with a Landau function and a polynomial (red line). In this way the  $\Lambda$ -peak position was extracted to  $1115.2$  MeV/ $c^2$ , close to its nominal value of  $1115.7$  MeV/ $c^2$  [B<sup>+</sup>12]. The width of  $2.5$  MeV/ $c^2$  is fully attributed to the finite momentum resolution of the HADES detector, as the  $\Lambda$  itself is a weakly decaying particle with almost vanishing decay width. Even after all the cuts applied so far, there is still a considerable background below the signal peak. The origin of this background is partially of non-physical nature, namely due to events, where particles have been misidentified. On the other hand, not every event with a proton, a  $\pi^{+}$ , a  $\pi^{-}$  and a  $K^{+}$  in the final state does necessarily have to have also a  $\Lambda$  as an intermediate state. In this case, the combination of the proton with the  $\pi^{-}$  results in a so-called physical background. The exact determination and understanding of the background below the  $\Lambda$  signal is, however, not of importance for this analysis.

By integrating the spectrum in Figure 3.10 within a  $2\sigma$  window around the extracted  $\Lambda$  mass (from  $1110$  MeV/ $c^2$  to  $1120$  MeV/ $c^2$ ), the signal to background ratio was determined to  $S/B = 0.28$ . A cut on the same mass range (vertical gray lines in Figure 3.10) was applied to enhance the fraction of events containing a  $\Lambda$  hyperon. Only these remaining events were further analyzed.

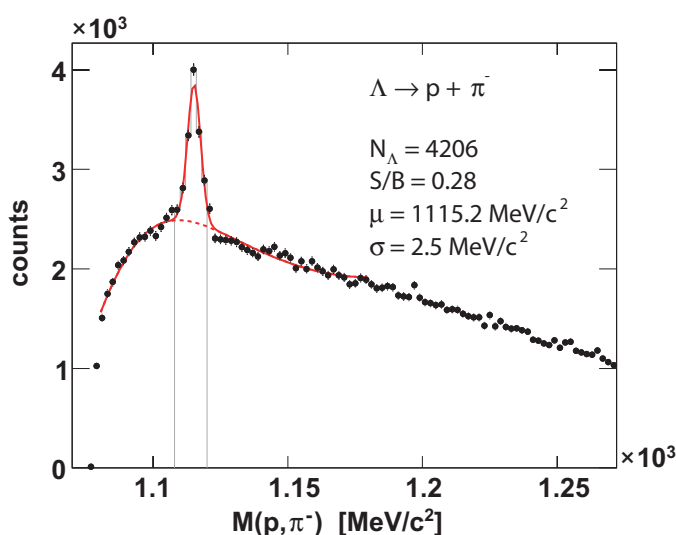


**Figure 3.10:** Invariant mass of proton and  $\pi^{-}$ . Red line indicates the fit of a Gaussian function (for the signal) together with a Landau function and a polynomial (for the background). Vertical gray lines indicate a  $2\sigma$  cut around the signal peak.

The next step was the selection of the neutron, appearing in channel (3.2). As already mentioned, the neutron cannot be detected directly, but, since it is the only neutral particle in the reaction, the missing mass method can be applied (see section 2.2.3). The missing mass to the four charged particles  $MM(p, K^+, \pi^+, \pi^-)$  is plotted in Figure 3.11. A clear neutron signal is visible on top of a background. The signal peak was fitted with a Gaussian function, giving a mean value of  $938.9 \text{ MeV}/c^2$  (nominal neutron mass is  $939.6 \text{ MeV}/c^2$  [B<sup>+</sup>12]) and a width of  $12.4 \text{ MeV}/c^2$ . Again the non-zero width is only attributed to the finite detector resolution. The origin and the description of the background in Figure 3.11 will be discussed in detail in the next section. For the extraction of the  $\Sigma(1385)^+$  signal, a  $5\sigma$  cut from  $877 \text{ MeV}/c^2$  to  $1000 \text{ MeV}/c^2$  (vertical dashed lines) was applied.

Finally, the 4-vector of the  $\Lambda$  candidate was calculated from the 4-vectors of the proton and the  $\pi^-$ . By combining this  $\Lambda$  track with the 4-vector of the  $\pi^+$ , the invariant mass of those two particles could be calculated for the so far selected event sample, and the result is plotted in Figure 3.12. The data show a resonance structure around  $1380 \text{ MeV}/c^2$ , which is associated with the  $\Sigma(1385)^+$  hyperon. Below the resonance, a flat background distribution is visible. The extraction of the pure  $\Sigma(1385)^+$  after evaluating the background will be presented in the next section.

At this point of the analysis, it is instructive to investigate again the mass distribution of all the remaining  $K^+$  candidates. Figure 3.13 shows this distribution after all the mentioned cuts have been applied ( $dE/dx$  cuts,  $\Lambda$ -Vertex cuts,  $\Lambda$  invariant mass cut, neutron missing mass cut) but without the cut on the kaon mass. Comparing this to Figure 3.8, the arise of the peak structure around  $500 \text{ MeV}/c^2$  proves that the data selection has mainly extracted true kaons out of the bunch of initial kaon candidates. However, the picture also suggests that there are still a lot of  $\pi^+$  and also some protons, misidentified as kaons. Even by applying the  $K^+$  mass cut (gray shaded area in Figure 3.13), their contribution cannot be rejected totally. This means that also in Figure 3.12 a certain misidentification background is expected below the  $\Sigma(1385)^+$  signal. Therefore, it is important to understand the origin of this misidentification background and to find a method how to handle it.

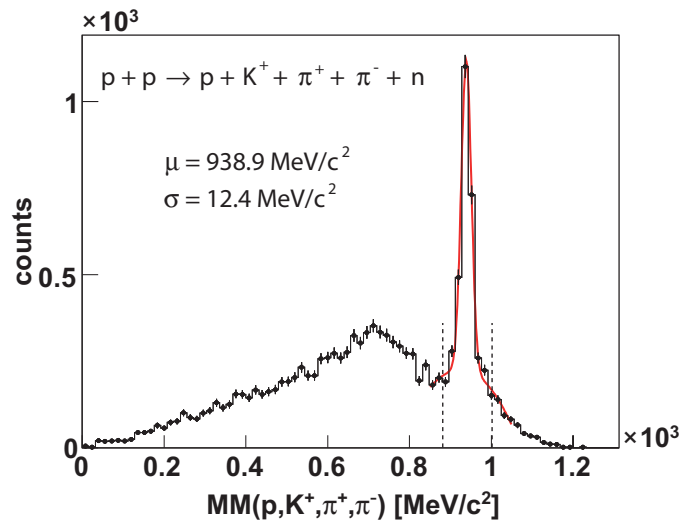


**Figure 3.11:** Missing mass to proton,  $K^+$ ,  $\pi^+$  and  $\pi^-$ . The neutron signal is fitted with a Gaussian function (red line). The vertical dashed lines indicate the  $5\sigma$  cut range.

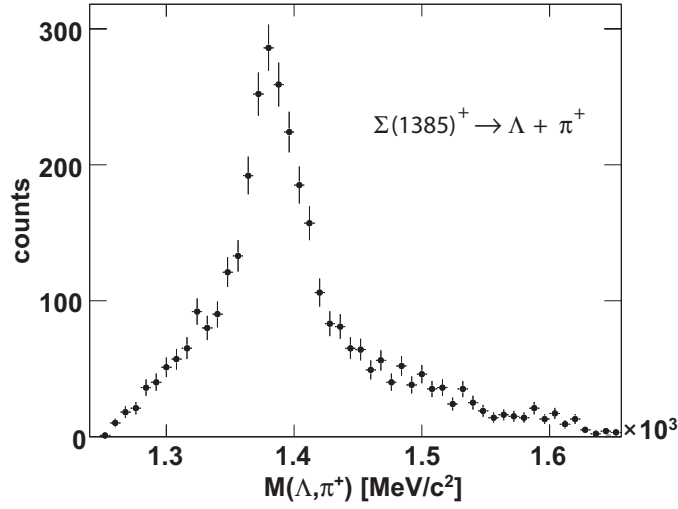


**Figure 3.12:** Invariant mass of the  $\Lambda$  hyperon and the  $\pi^+$  showing a  $\Sigma(1385)^+$  resonance.

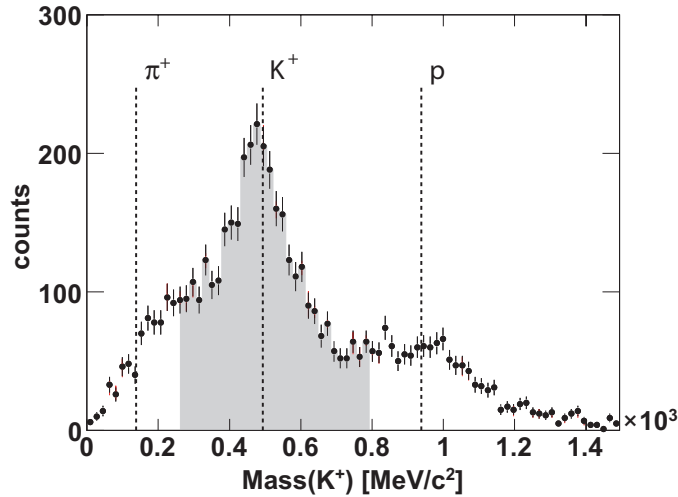


**Figure 3.13:** Mass distribution of all kaon candidates after applying  $dE/dx$  cuts,  $\Lambda$ -Vertex cuts, the  $\Lambda$  invariant mass cut and the neutron missing mass cut. The gray shaded area ( $280 \text{ MeV}/c^2 - 780 \text{ MeV}/c^2$ ) indicates the  $K^+$  mass cut.

### 3.2.2 Background description and signal extraction

For the evaluation of the different background sources, the spectrum in Figure 3.11 is considered first. It turned out that the broad structure left to the neutron peak can be completely attributed to misidentification events, where either a pion or a proton has been misidentified as a kaon. A detailed discussion about this can be found in appendix A.1. The description of the background was done with a sideband method, which uses experimental data to evaluate the contribution due to misidentified pions and protons. In appendix A.2 the functional principle of this sideband method is explained extensively. Here, only the result is presented in Figure 3.14. The red histogram shows the evaluated contribution by misidentified pions, whereas the blue histogram corresponds to misidentified protons. The sum of the pion and proton contribution (gray





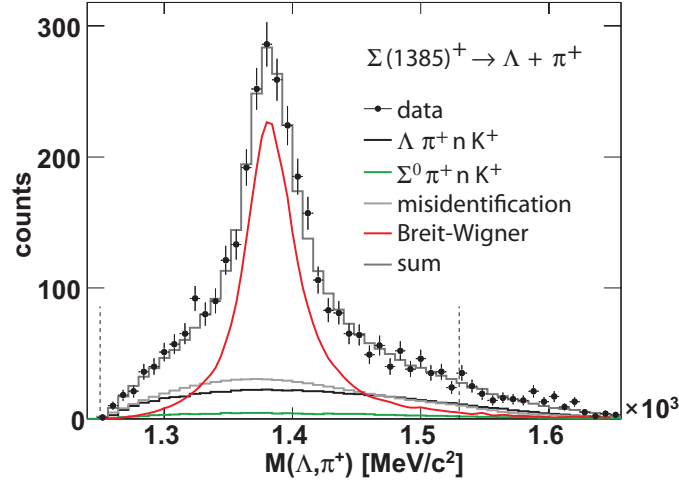


**Figure 3.15:** Invariant mass of  $\Lambda$  and  $\pi^+$ . The experimental data are described by a sum of different contributions from misidentification background, simulations and a relativistic Jackson p-wave Breit-Wigner fit (see equation (3.16)).

( $\Lambda$  and  $\pi^+$ ) in the  $\Sigma(1385)^+$  rest frame for a  $\Sigma(1385)^+$  mass of  $m$  and  $m_0$ , respectively.  $\Gamma_0$  corresponds to the nominal width of the  $\Sigma(1385)^+$  resonance, whereas  $\Gamma$  is the mass dependent width, which is determined by  $\Gamma_0$ ,  $q$ ,  $q_0$ ,  $m$ ,  $m_0$  and the Blatt-Weisskopf correction term  $F_1(q)$ .  $R=1/197.327 \text{ MeV}^{-1}$  is the centrifugal barrier parameter. With  $\hbar = c = 1$  all parameters are given in units of MeV. As the  $\Sigma(1385)^+$  is a p-wave resonance, the choice of a p-wave Breit-Wigner is natural. The Blatt-Weisskopf term [VHQ72] is needed to absorb possible divergences in the mass dependent width  $\Gamma$ .

It has to be noted that the experimental distribution in Figure 3.15 is partially influenced by the limited HADES acceptance and inefficiencies in the analysis procedure (see discussion in section 2.3.2). The reconstructed  $\Sigma(1385)^+$  resonance might therefore deviate from a perfect Breit-Wigner shape. To correct for these effects, the Breit-Wigner in equation (3.16) was folded with the mass dependent efficiency factor  $C_{Eff}(m)$ , which has been determined with simulations of channel (3.13) (for details about the correction procedure see, for example, appendix A.4). The function  $C_{Eff}(m)$  is shown in Figure 3.16. Besides this efficiency factor, also a phase space factor  $C_{PS}(m)$  was included. It accounts for the fact that the phase space, available in the three particle production of  $\Sigma(1385)^+$ ,  $K^+$  and neutron, is limited and decreases with increasing  $\Sigma(1385)^+$  mass. As the production cross section is connected to the available phase space via Fermi's Golden Rule, the limited phase space suppresses the population of large  $\Sigma(1385)^+$  masses. The factor  $C_{PS}(m)$  has been extracted from simulations as well. It is shown together with  $C_{Eff}(m)$  in Figure 3.16.

In order to quantify the different contributions in Figure 3.15, the experimental data were fitted with:

1. the fixed distribution of the misidentification background.
2. the contribution of the simulated channel (3.15), fixed in yield by the fit to the neutron spectrum in Figure 3.14.
3. the simulated distribution of channel (3.14), scaled by one fit parameter.

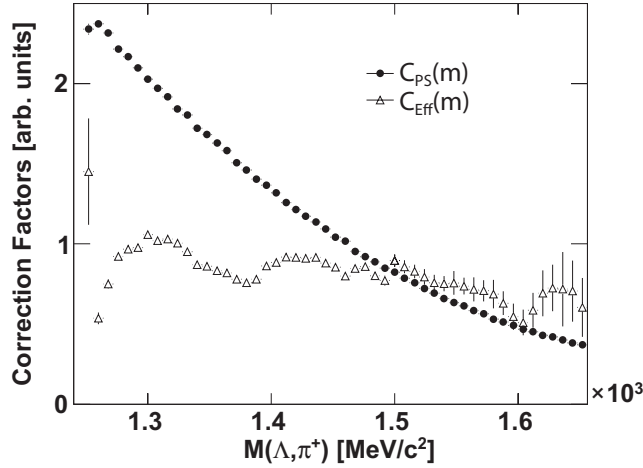


**Figure 3.16:** Breit-Wigner correction factors, accounting for the limited efficiency of the  $\Sigma(1385)^+$  reconstruction and the limited available production phase space. See text for details.

4. the  $\Sigma(1385)^+$  signal, expressed by equation (3.16), with three fit parameters ( $A$ ,  $m_0$ ,  $\Gamma_0$ ).

The fit with altogether four free parameters was performed within the vertical dashed lines in Figure 3.15, which considers that higher mass resonances like  $\Sigma(1560)^+$  [B<sup>+</sup>12] might give a small contribution to the experimental data. The result of the fitting procedure is shown in the gray histogram, giving an excellent description of the experimental data, which is expressed in a normalized  $\chi^2$  value of  $\chi^2/ndf \approx 1.0$ . The obtained pole mass of  $m_0 = 1383.2 \pm 0.8$  MeV/ $c^2$  (only statistical error) for the  $\Sigma(1385)^+$  is in good agreement with the value quoted in [B<sup>+</sup>12] ( $1382.8 \pm 0.35$  MeV/ $c^2$ ). The extracted width of  $\Gamma_0 = 40.2 \pm 2.1$  MeV/ $c^2$  is, however, about 4 MeV/ $c^2$  larger than the nominal value ( $36 \pm 0.7$  MeV/ $c^2$ ). This effect cannot be attributed to the limited resolution of HADES. By folding the Breit-Wigner formula in equation (3.16) with the term  $C_{Eff}(m)$ , the fit was not only corrected for the limited acceptance and efficiency of the analysis, but also for the broadening of the resonance due to the limited momentum resolution in the track reconstruction. On the other hand, the  $\Sigma(1385)^+$  width quoted in [B<sup>+</sup>12] is an average value of several measurements. In each of these measurements, the width has been extracted by a Breit-Wigner fit to the experimental data. The parameterizations of the Breit-Wigner functions were, however, different. In appendix A.3 it is investigated how different Breit-Wigner parameterizations influence the fit results for  $m_0$  and  $\Gamma_0$ . There it is also argued that formula (3.16) is the most reasonable choice for describing the  $\Sigma(1385)^+$  signal.

As the different contributions in Figure 3.15 have been quantified with help of the fitting procedure, the pure  $\Sigma(1385)^+$  signal could be extracted. For this purpose, the misidentification background as well as the simulated distributions of channel (3.14) and channel (3.15) were subtracted. The result is shown in Figure 3.17. The Breit-Wigner function (red line), obtained from the fit to Figure 3.15, gives a perfect description of the data points. By integrating the spectrum within a  $6\sigma$  interval ( $\sigma = \Gamma_0/2.35$ ), the total number of reconstructed  $\Sigma(1385)^+$  events is about 1700. This is sufficient to perform differential studies, where angular distributions can be investigated.

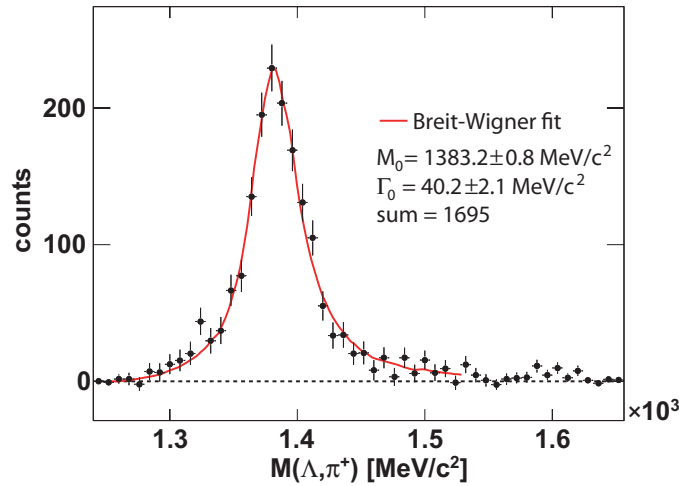


**Figure 3.17:** Invariant mass of  $\Lambda$  and  $\pi^+$  after background subtraction. The red line shows the Breit-Wigner fit function with the parametrization of equation (3.16).

### 3.3 Angular distributions, simulation model and efficiency corrections

So far, only data within the geometrical acceptance of the HADES experiment and within the efficiency of the event reconstruction have been considered. One major goal of the analysis is, however, to provide corrected experimental distributions, which later on can be compared directly to theoretical predictions. As it was shown in section 2.3.2, acceptance and efficiency correction are done with help of simulations. Therefore, it is crucial to find an appropriate simulation model for the reaction (3.13). The following section describes the strategy, used to extract such a model. For this purpose, different observables, especially angular distributions, were investigated. On the basis of these observables the experimental data were interpreted and a simulation model could be developed. This model was tuned until it described the experimental data consistently. In this way it is guaranteed that the kinematics and the phase space coverage of the data is reproduced so that the model could finally be used for the corrections.

#### 3.3.1 $\Sigma(1385)^+$ angular distribution in the CMS

As a starting point, the production angle of the  $\Sigma(1385)^+$  candidate in the CMS is considered. Figure 3.18 shows the distribution of  $\cos(\theta_{CMS}^{\Sigma^*})$ , where the 4-vector of  $\Sigma^*$  is calculated from the invariant vector of the  $\Lambda$  and the  $\pi^+$ . The shown data (black dots) are the same as illustrated in Figure 3.15, only the observable has been changed. Included in Figure 3.18 is the contribution by misidentification background (light gray histogram), where the shape and the yield was fixed by the sideband method. As experimental data were used to describe this contribution, the shape is expected to be correct. The black and the green histograms show the contributions by the simulated reactions (3.14) and (3.15). Their yields were fixed by the fitting procedure to the spectra in Figure 3.14 and 3.15. In the simulations of these two reactions all particles were produced isotropically. This assumption will turn out to be sufficient for a good description of the experimental data. The red histogram shows simulations of  $\Sigma(1385)^+$  production via reaction (3.13). As a first guess, also this reaction was simulated with all particles being produced

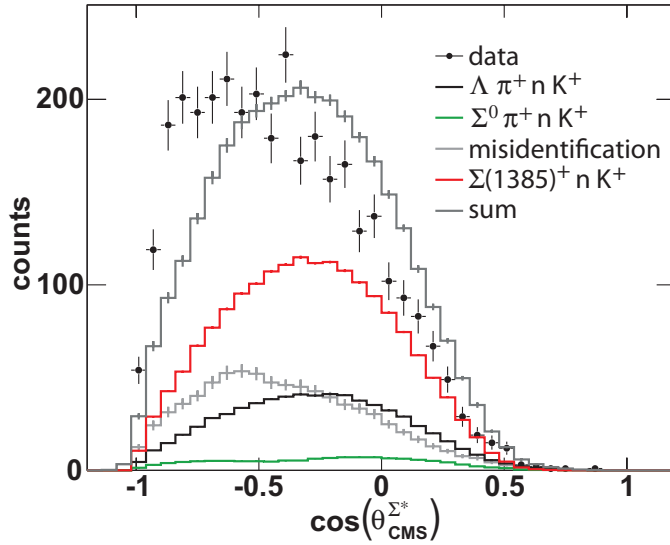


**Figure 3.18:** Angular distribution of the  $\Sigma(1385)^+$  candidate in the proton-proton center-of-mass system (CMS). The different channels are simulated with isotropic distributions (see text for details).

isotropically. The yield of this contribution was fixed by integral normalization. The sum of all contributions is given in the solid grey histogram.

By looking at Figure 3.18, one immediately notices that all the distributions are not symmetric with respect to  $\cos(\theta_{CMS}^{\Sigma^*})$ . This must be attributed to the limited HADES acceptance, which, in this case, covers mainly the backward region and highly suppresses the forward region.

Furthermore, one observes a clear difference between the experimental data and the simulations. The experimental data show a significantly stronger preference of the backward hemisphere ( $\cos(\theta_{CMS}^{\Sigma^*}) < 0$ ). This indicates that the  $\Sigma(1385)^+$  hyperon, produced via reaction (3.13), is not emitted isotropically in the CMS, but with a certain angular distribution.

To extract the correct angular distribution, the experimental data were subdivided into seven independent data samples, each covering a different region of  $\cos(\theta_{CMS}^{\Sigma^*})$ . The analysis procedure from above was applied to all subsamples, and the extracted pure  $\Sigma(1385)^+$  signal was corrected for acceptance and efficiency effects. In a first approach, the isotropic simulations of reaction (3.13) were used for these corrections. Details about the correction procedure and about the extraction of (differential) cross sections can be found in appendix A.4.

Figure 3.19 shows the finally obtained differential cross section of the reaction  $p+p \rightarrow \Sigma(1385)^+ + n + K^+$  as a function of  $\cos(\theta_{CMS}^{\Sigma^*})$ . The cross section value in each bin is normalized to the corresponding bin width. The included error bars are statistical only. The distribution indicates that the  $\Sigma(1385)^+$  production is indeed anisotropic with a strong preference in the forward and backward direction, that means along the initial proton directions. In this sense the distribution fulfills the expectations from the OBE model (compare to Figure 3.1).

It has to be noticed that, even though the forward angles are almost not covered, the distribution does not look completely symmetric. This is a clear indication that the isotropic simulation model is not sufficient for precise corrections so that a better model is needed.

In order to quantify the observed anisotropy, the data points in Figure 3.19 were fitted with Legendre polynomials up to fourth order (see red line). Since the distribution must be symmetric, only the even Legendre polynomials were used. The corresponding fitting function

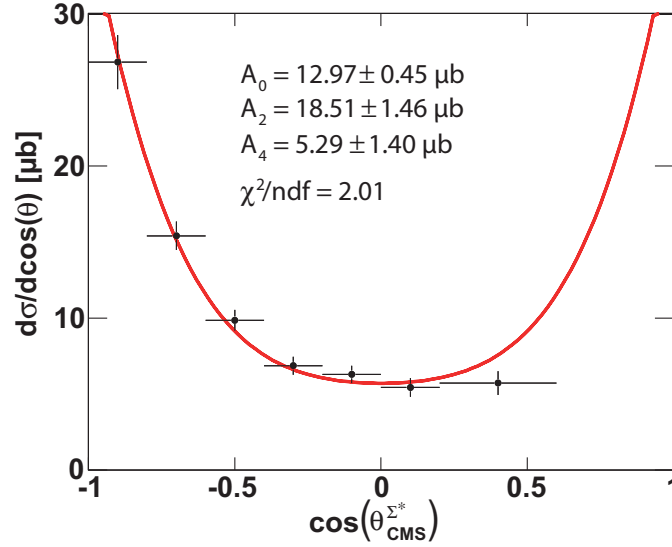


**Figure 3.19:** Differential cross section of the reaction (3.13) for the observable  $\cos(\theta_{CMS}^{\Sigma^*})$ . Data points are fitted with only even Legendre polynomials up to fourth order.

$F(x = \cos(\theta_{CMS}^{\Sigma^*}))$  reads as follows:

$$\begin{aligned}
 F(x) &= A_0 P_0 + A_2 P_2 + A_4 P_4 & (3.17) \\
 F(x) &= A_0 + A_2 \frac{1}{2} (3x^2 - 1) + A_4 \frac{1}{8} (35x^4 - 30x^2 + 3)
 \end{aligned}$$

$A_0$ ,  $A_2$  and  $A_4$  are free fit parameters, and their values are indicated in Figure 3.19 as well. Since the data points do not cover the full region from  $\cos(\theta_{CMS}^{\Sigma^*}) = -1$  to  $\cos(\theta_{CMS}^{\Sigma^*}) = 1$ , the total cross section is estimated by integrating the fit function. The integral of any sum of Legendre polynomials is:

$$\int_{-1}^1 \sum_i A_i P_i(x) dx = 2A_0 \quad (3.18)$$

In this way the total production cross section of reaction (3.13) is determined to  $\sigma = 2A_0 = 25.9 \pm 0.9 \mu b$ . However, as the wrong simulation model was used for the efficiency corrections, also this cross section value might be wrong. The correct cross section will be extracted later on, after tuning the simulations.

### 3.3.2 Neutron angular distribution in the CMS

Since the  $\Sigma(1385)^+$  hyperon shows such a strong production anisotropy, it is instructive to study also the kinematically strongly correlated angular distribution of the neutron in the CMS. The neutron 4-vector was calculated as the missing vector to the proton,  $K^+$ ,  $\pi^+$  and  $\pi^-$ . The distribution of  $\cos(\theta_{CMS}^n)$  is plotted in Figure 3.20. As in the case of Figure 3.18, the experimental data are compared to the sum of misidentification background and the isotropic simulations of the channels (3.13), (3.14) and (3.15). The HADES acceptance limits the neutron

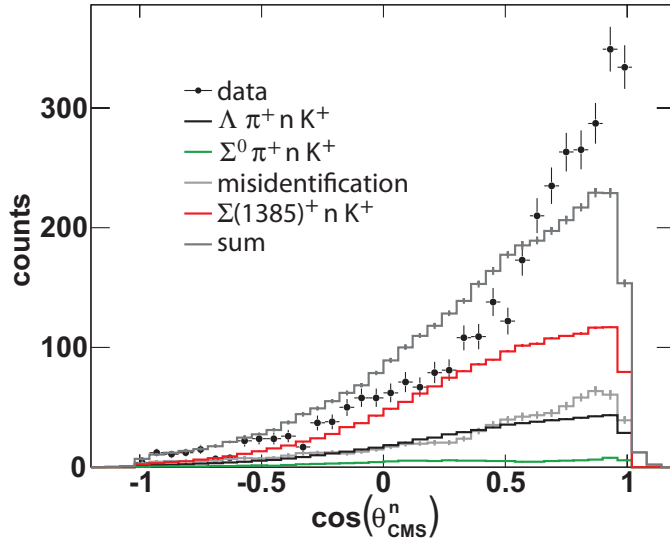


**Figure 3.20:** Angular distribution of the neutron candidate in the proton-proton center-of-mass system (CMS). The channels (3.13), (3.14) and (3.15) are simulated with isotropic particle production.

distribution to the forward hemisphere. Since the two observables  $\cos(\theta_{CMS}^{\Sigma^*})$  and  $\cos(\theta_{CMS}^n)$  are kinematically correlated, it is expected that the isotropic simulations of channel (3.13) are not able to reproduce the experimental data in Figure 3.20. Indeed, the experimental distribution shows a stronger peaking at forward angles. Due to kinematic reasons, the neutron has to be produced mainly back to back with the  $\Sigma(1385)^+$  in the CMS. Thus, the distribution in Figure 3.20 is fully consistent with the results in Figure 3.18.

The quantitative extraction of the production anisotropy was again done by subdividing the data into different areas of  $\cos(\theta_{CMS}^n)$ , and correcting each data sample individually, as it is presented in appendix A.4. The differential cross section as a function of  $\cos(\theta_{CMS}^n)$  is shown in Figure 3.21. Like the  $\Sigma(1385)^+$ , the neutron is preferably emitted into the forward and backward region along the direction of the incoming protons. The distribution itself is, however, not completely symmetric, which must again be attributed to the inadequate simulation model with purely isotropic distributions.

The data points in Figure 3.21 were also fitted with Legendre polynomials and the resulting fit parameters  $A_0$ ,  $A_2$  and  $A_4$  are indicated in the figure. It is interesting to see that, by integrating the fit function, the total production cross section of reaction (3.13) is determined to  $\sigma = 2A_0 = 17.7 \pm 0.6 \mu b$ , which deviates significantly from the value extracted from Figure 3.19. This is just another proof that the simple simulation model, used to correct the data, is not sufficient. A precise extraction of the differential and total cross section requires a more adequate model.

Furthermore, it is worth to notice that the anisotropy for the neutron angle distribution seems to be less prominent than the one of the  $\Sigma(1385)^+$  (compare to Figure 3.19). Based on the argumentation of section 3.1.2.2, this might be a first hint that kaon exchange dominates over pion exchange in this reaction.

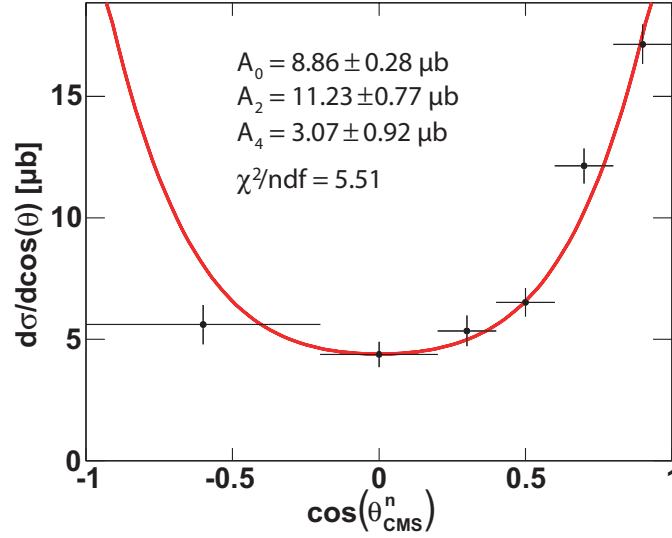


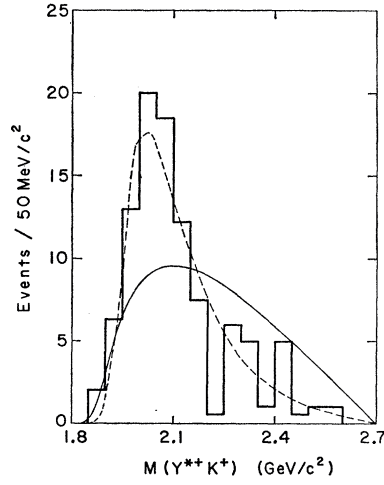
**Figure 3.21:** Differential cross section of the reaction (3.13) for the observable  $\cos(\theta_{CMS}^n)$ . Data points are fitted with only even Legendre polynomials.

### 3.3.3 Helicity angle in the $n - K^+$ reference frame

Till now, it was always assumed that the  $\Sigma(1385)^+$  hyperon is produced directly (non-resonant) via the reaction (3.13). Many experiments in the past have proved, however, that hyperon production processes to a large extent via intermediate resonances (see, for example, [AB<sup>+</sup>10, C<sup>+</sup>68b]). Even for the  $\Sigma(1385)^+$  the following process was found in proton-proton reactions:  
 $\Sigma(1385)^+$  **resonant:**

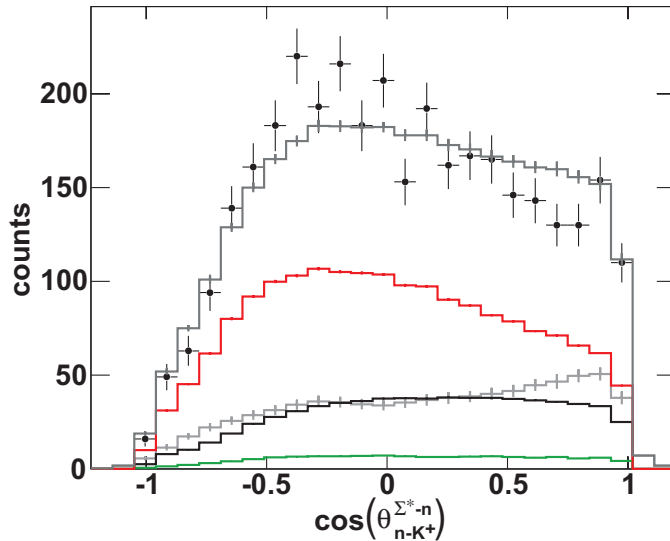


Figure 3.22 shows the invariant mass spectrum of  $\Sigma(1385)^+$  and  $K^+$ , extracted from proton-proton data at an incident proton momentum of 6 GeV/c [C<sup>+</sup>68a]. Here, only peripheral events with  $|\cos(\theta_{CMS}^n)| > 0.9$  have been selected. The spectrum shows a broad but clear peak structure around 2000 MeV/c<sup>2</sup>. The authors of [C<sup>+</sup>68a] claim that these data cannot be described by pure non-resonant  $\Sigma(1385)^+$  production (solid line) but an admixture of around 85% resonant production via an intermediate  $\Delta^{++}$  resonance with a Breit-Wigner mass of around 2035 MeV/c<sup>2</sup> is needed (dashed line). They associate this signal with the four star  $\Delta(1950)$  resonance, listed in [B<sup>+</sup>12].



**Figure 3.22:** Invariant mass distribution of  $\Sigma(1385)^+$  and  $K^+$  taken from [C<sup>+</sup>68a]. The dashed line shows a fit with 100% resonant  $\Sigma(1385)^+-K^+$  production. The solid line shows 100% non-resonant  $\Sigma(1385)^+-K^+$  production.

To test if the HADES data are consistent with the hypothesis of a  $\Delta$  resonance, the helicity angle distribution of  $\cos(\theta_{n-K^+}^{\Sigma^*-n})$  is analyzed in Figure 3.23. Indeed, according to the argumentation of section 3.1.2.4, this distribution must be influenced by the presence of a resonance decaying into  $\Sigma(1385)^+$  and  $K^+$ . The simulation models, used for the channels (3.14) and (3.15), were the same as before. For the contribution of the  $\Sigma(1385)^+$  hyperon, the non-resonant simulations of reaction (3.13) from above were used. To account for the anisotropy in the  $\Sigma(1385)^+$  production, these simulations were additionally folded (weighted) with the function  $F(\cos(\theta_{CMS}^{\Sigma^*}))$ , extracted by fitting the data in Figure 3.19. In fact, this folding has no direct influence on the



**Figure 3.23:** Helicity angle distribution in the neutron- $K^+$  reference frame. The data are shown inside the HADES acceptance. The color code for the different simulated channels is the same as in Figure 3.18 and 3.20.

distribution in  $\cos(\theta_{n-K^+}^{\Sigma^*-n})$ , as this observable is kinematically independent from the distribution in  $\cos(\theta_{CMS}^{\Sigma^*})$ . Only because the acceptance for isotropic and anisotropic production is different, the folding slightly influences the shape of the red histogram in Figure 3.23. The inclusion of the production anisotropy into the simulation model is thus necessary in order to allow a comparison to the experimental distribution. It is obvious that the experimental distribution in Figure 3.23 still differs from the simulated one. Such a difference is expected, if the corresponding Dalitz plot is not just populated uniformly, but if kinematical or physical effects distort the Dalitz plot.

In order to find out the origin of this deviation, the differential cross section for  $\cos(\theta_{n-K^+}^{\Sigma^*-n})$  is investigated in Figure 3.24, panel a). The acceptance corrections in this case were done with the weighted simulations of reaction (3.13). The obtained distribution (black data points) is not flat but shows a peak-like structure around  $\cos(\theta_{n-K^+}^{\Sigma^*-n}) = -0.3$ . This can be an evidence for the presence of an intermediate resonance in the production mechanism. To test this hypothesis, the experimental data are compared to non-resonant and resonant simulations. The simulations of the non-resonant  $\Sigma(1385)^+$  production, according to reaction (3.13), are completely isotropic in the helicity angle (red histogram in Figure 3.24, panel a)). This is true even though the simulations were weighted with the production anisotropy of the  $\Sigma(1385)^+$  in the CMS, proving that the two distributions are kinematical independent. As a comparison, the blue histogram shows simulations of the reaction (3.19). Here, the  $\Delta^{++}$  was simulated with a Breit-Wigner mass of 2035 MeV/c<sup>2</sup> and a width of 250 MeV/c<sup>2</sup>, taking the spectrum in Figure 3.22 as a reference. If the  $\Sigma(1385)^+$  and the  $K^+$  are indeed stemming from a resonance decay, the phase space that they can populate is reduced compared to the non-resonant case. As a consequence, characteristic peak structures appear in the helicity angle distribution, which reflect the mass and width of the resonance. In the presented case, the assumed  $\Delta^{++}$  mass and width create a broad peak around  $\cos(\theta_{n-K^+}^{\Sigma^*-n}) = -0.3$ . The experimental spectrum in Figure 3.23 can thus be taken as a hint that the reaction (3.19) contributes to the formation process of the final state  $\Sigma(1385)^+$ ,  $K^+$  and neutron.

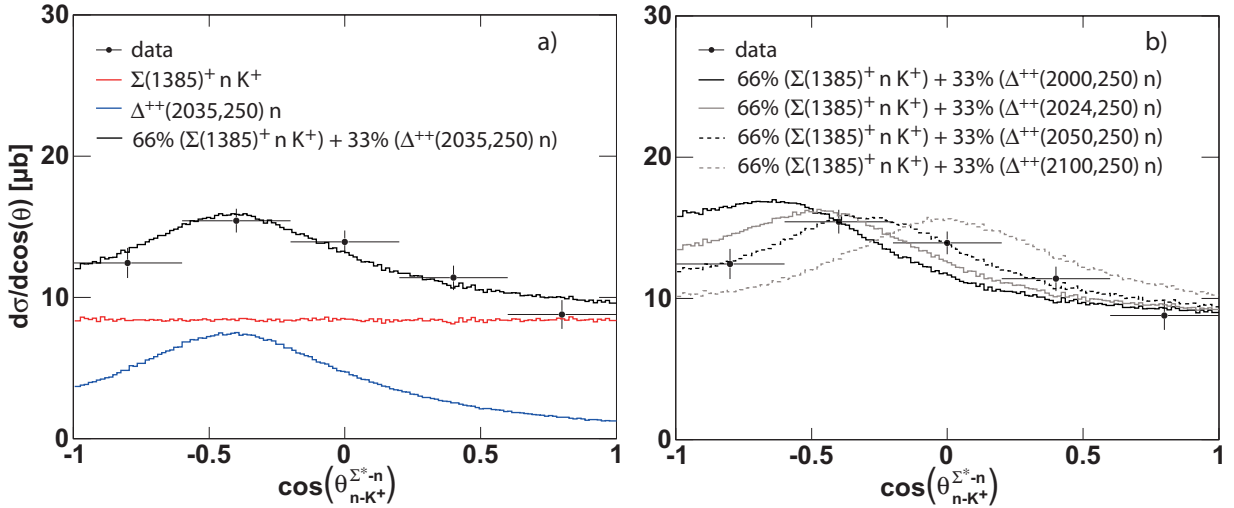


**Figure 3.24:** Helicity angle distribution. Panel a): Experimental data are compared to simulations of non-resonant  $\Sigma(1385)^+$  production and resonant  $\Sigma(1385)^+$  production via a  $\Delta^{++}(2035,250)$  decay. The  $\Delta^{++}$  is simulated with a Breit-Wigner mass of 2035 MeV/c<sup>2</sup> and width of 250 MeV/c<sup>2</sup>. Panel b): Same as a), but data are compared to simulations with different  $\Delta^{++}$  masses.

To extract the relative contributions of resonant (reaction (3.19)) and non-resonant (reaction (3.13)) production, the blue and the red histograms were fitted to the experimental data points. The result is the black histogram, composed of 33% resonant and 66% non-resonant  $\Sigma(1385)^+$  production. The agreement with the data is excellent.

In Figure 3.24, panel b), the sensitivity of the helicity angle distribution to the assumed  $\Delta^{++}$  mass is studied. For this purpose, the simulated Breit-Wigner mass has been shifted by -35, -10, +15 and +65 MeV/c<sup>2</sup> compared to the value of 2035 MeV/c<sup>2</sup>, used in panel a). The width has not been changed and the  $\Delta^{++}$  contribution was always assumed to be 33%. In this way the different histograms are obtained. They indicate that the helicity angle distribution is indeed sensitive to the properties of the  $\Delta^{++}$  resonance, as the peak position increases with increasing mass. By comparing the different simulation models to the experimental data, it becomes clear that the two extrem cases of a  $\Delta^{++}(2000,250)$  and a  $\Delta^{++}(2100,250)$  are not compatible with the experimental findings. However, the agreement between the data and the  $\Delta^{++}(2050,250)$  assumption is as good as the achieved agreement in panel a). A precise determination of the resonance shape and mass is thus not possible with these data.

### 3.3.4 Development and tuning of the simulation model

The study of angular distributions has delivered important insight into the production process of the  $\Sigma(1385)^+$ . On the one side, the anisotropy in the CMS angles supports the scenario of peripheral meson exchange. On the other side, the helicity angle distribution suggests that a considerable fraction, namely around 33%, of the  $\Sigma(1385)^+$  are produced via an intermediate  $\Delta^{++}$  resonance. These results were used to develop a simulation model, which allowed for final acceptance and efficiency corrections. For this purpose, two assumptions were made:

1. Following the fit results to Figure 3.24, panel a), it is assumed that 33% of the  $\Sigma(1385)^+$  stem from the decay of an intermediate  $\Delta^{++}(2035,250)$ . The exchange graphs in Figure 3.2 suggest that the reaction (3.19) can only be mediated via non-strange meson (pion) exchange with the production of the  $\Delta^{++}$  at vertex B and of the neutron at vertex A. In the CMS these two particles are then going back to back. The exchange process was imitated by performing isotropic simulations of the reaction (3.19), which were subsequently weighted with a function  $F(\cos(\theta_{CMS}^n))$ , extracted from the data. Furthermore, the  $\Delta^{++}$  was simulated to decay isotropically into  $\Sigma(1385)^+$  and  $K^+$ . Thus, the vertex B in Figure 3.2, panel c) has only an s-wave contribution, resulting in an isotropic G-J angle distribution in the corresponding  $\Sigma(1385)^+-K^+$  reference frame.
2. The remaining 66% of the  $\Sigma(1385)^+$  production is of non-resonant nature, which can either be mediated by non-strange (pion) or strange meson (kaon) exchange. In order to account for the strong production anisotropy of the  $\Sigma(1385)^+$ , observed in Figure 3.19, it was assumed that the non-resonant part is produced via kaon exchange. In section 3.1.2.2 it has been explained why kaon exchange usually results in a strong anisotropy for the produced hyperon. The kaon exchange process was imitated by folding the isotropic simulations of reaction (3.13) with a function  $F(\cos(\theta_{CMS}^{\Sigma^*}))$ , which had to be determined from the data as well. In this way the two particle production of the neutron and the  $K^+$  at vertex B (see Figure 3.2, panel a)) was simulated to be isotropic. Consequently the G-J angle distribution in the neutron- $K^+$  reference frame must be flat.

In summary, two independent contributions were simulated: resonant  $\Sigma(1385)^+$  production via pion exchange and non-resonant  $\Sigma(1385)^+$  via kaon exchange. Both simulations were added incoherently. Even though the obtained model is much simpler than a full OBE model (see e.g. equation (3.8)), it turned out to be completely sufficient to perform proper efficiency corrections. The anisotropy for the  $\Sigma(1385)^+$  and the neutron production was quantified by the folding functions  $F(\cos(\theta_{CMS}^{\Sigma^*}))$  and  $F(\cos(\theta_{CMS}^n))$ . They were extracted from the experimental data with help of an iterative procedure:

First, the non-resonant simulations of reaction (3.13) were weighted with the  $\Sigma(1385)^+$  anisotropy extracted in Figure 3.19, namely with:

$$F(x = \cos(\theta_{CMS}^{\Sigma^*})) = 12.97P_0(x) + 18.51P_2(x) + 5.29P_4(x) \quad (3.20)$$

At the same time, the simulations of reaction (3.19) were folded with the neutron anisotropy according to Figure 3.21:

$$F(x = \cos(\theta_{CMS}^n)) = 8.86P_0(x) + 11.23P_2(x) + 3.07P_4(x) \quad (3.21)$$

The sum of these folded simulations was used to correct the experimental data in the observables  $\cos(\theta_{CMS}^{\Sigma^*})$  and  $\cos(\theta_{CMS}^n)$ . The obtained differential cross sections were then used to find new folding functions. After that the procedure was repeated.

The way how the folding functions were extracted is exemplified in Figure 3.25, which shows already the final result after three steps of iterations. Panel a) shows the differential cross section in  $\cos(\theta_{CMS}^{\Sigma^*})$  and panel b) in  $\cos(\theta_{CMS}^n)$ . The experimental data (black dots) were fitted with Legendre polynomials (black lines). Additionally included in panel a) is the anisotropic distribution, obtained from the simulations of reaction (3.19) (blue histogram). By subtracting this resonant part of the simulations from the black Legendre function, a new function was obtained (red line), which could be attributed to the pure non-resonant part of the model. This function was at the same time the new weight function  $F(\cos(\theta_{CMS}^{\Sigma^*}))$  for the non-resonant

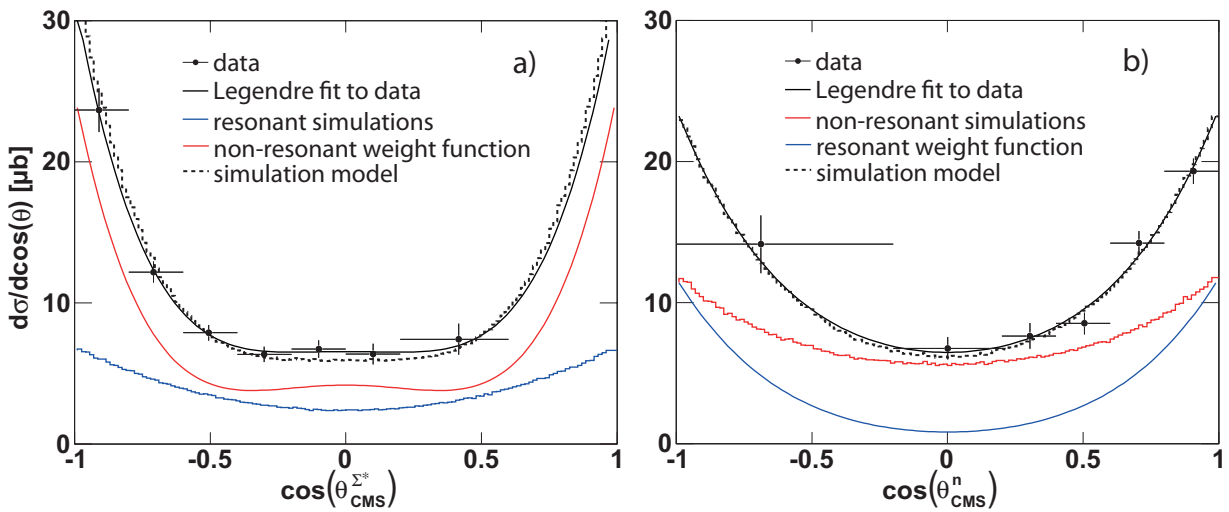


**Figure 3.25:** Differential cross section for  $\cos(\theta_{CMS}^{\Sigma^*})$  (a) and  $\cos(\theta_{CMS}^n)$  (b). The data were used to extract a simulation model (see text for details).

simulations of reaction (3.13).

In the same way the weight function  $F(\cos(\theta_{CMS}^n))$  for the resonant simulations of reaction (3.19) (blue line) was extracted from panel b). Therefore, the non-resonant simulations (red histogram) were subtracted from the Legendre fit. After three steps of iteration, good agreement between data and the simulation model, indicated in the black dashed histograms, was obtained. In this way the model was fixed and could then be tested on different observables.

For that purpose, all the angular distributions, mentioned before, are first studied within the HADES acceptance and efficiency in Figure 3.26, where the experimental data are compared to the developed simulation model. The first row shows the production angles of the  $\Sigma(1385)^+$ , the neutron and the  $K^+$  in the CMS. The second row shows the angles in the three possible G-J

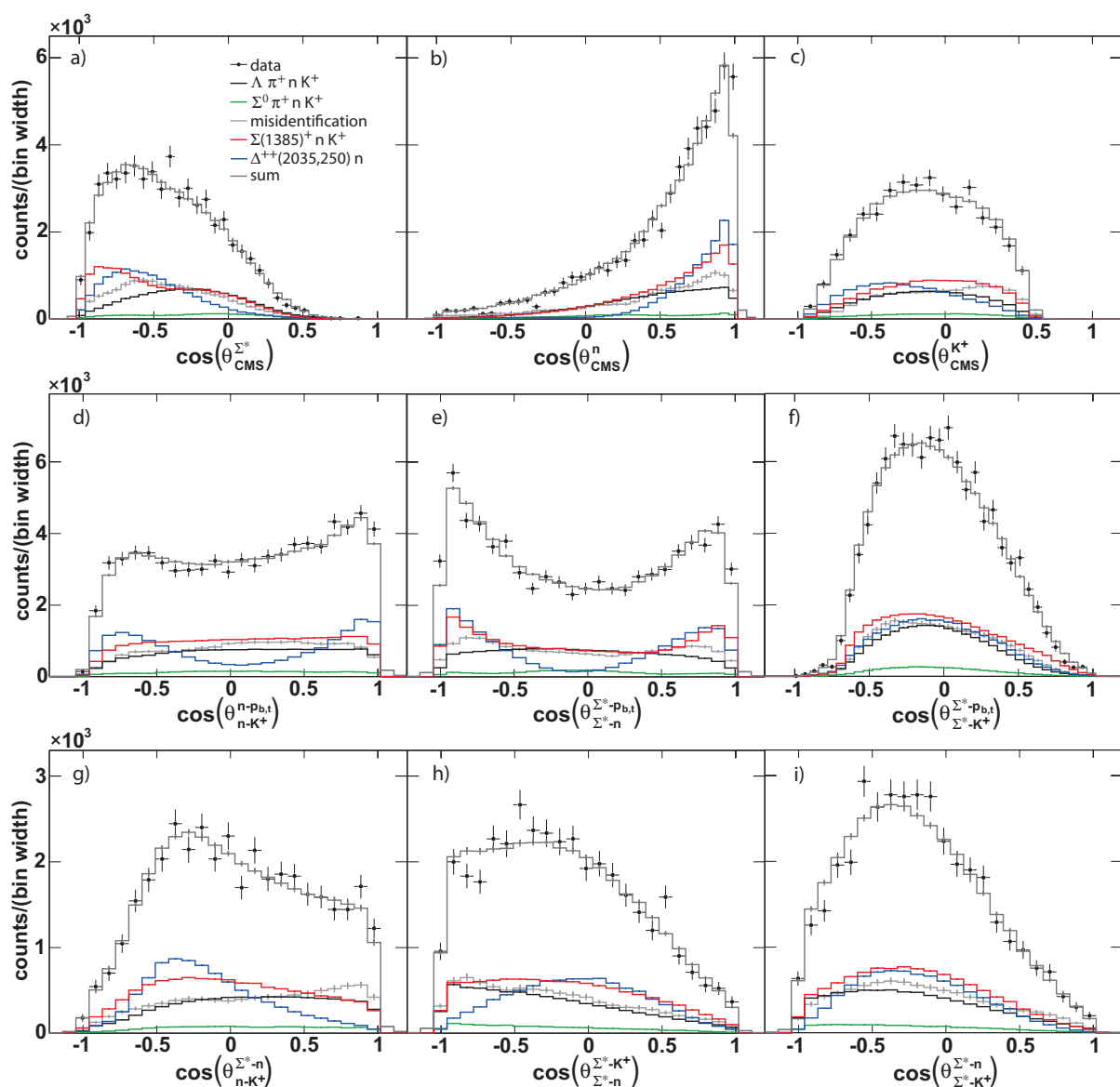


**Figure 3.26:** Angular distributions in experimental data and simulations. First row: production angles of the  $\Sigma(1385)^+$ , the neutron and the kaon in the CMS. Second row: distributions for the three G-J angles. Third row: distributions for the three helicity angles.

frames. Here, the label  $p_{b,t}$  stands for the beam and target type proton, to which the angles are measured. The last row compares the distributions for the three helicity angles. The contribution of non-resonant  $\Sigma(1385)^+$  production is shown in the red histograms. The simulations of  $\Delta^{++}$  production are indicated in the blue histograms.

In all nine pictures an excellent description of the experimental data is achieved. This is not surprising in case of panel a), b) and g) since the simulation model has been tuned exactly on these three observables. For the six remaining observables the situation is different. Here the model is delivering predictions, which match perfectly to the experimental data. This indicates already that the kinematics are rather under control in the assumed simulation model.

However, in order to further verify that the simulation model provides a satisfactory description of the experimental data, several other observables, like invariant mass spectra and opening angle distributions have been additionally investigated. A critical discussion of these studies can be found in appendix A.5. The achieved results give the final proof that the simulations appropriately describe the kinematics in the experimental data within the limited, but large HADES acceptance. The required preconditions are thus fulfilled, and the developed model could be used for the efficiency correction procedure (see discussion in section 2.3.2).

The corrected experimental distributions are presented and discussed in the next section.

## 3.4 Results and discussion

With the developed simulation model, the experimental data could finally be corrected for the effects of the finite acceptance and efficiency. The corrected distributions could then be normalized with help of proton-proton elastic data (see, for example, appendix A.4) so that (differential) cross sections were extracted.

### 3.4.1 $\Sigma(1385)^+$ line shape and properties

First, the invariant mass distribution  $M(\Lambda, \pi^+)$  of Figure 3.17 is considered. After correcting and normalizing these data, the resulting  $\Sigma(1385)^+$  spectral shape is shown in Figure 3.27. Also indicated in the picture is the result of a fit with the Breit-Wigner function (3.16). However, as the data are corrected, the factor  $C_{Eff}(M)$  was excluded from the fit. The obtained fit parameters for the  $\Sigma(1385)^+$  mass and width are identical with the ones obtained for the uncorrected data (see Figure 3.17), namely  $m_0 = 1383.2 \text{ MeV}/c^2$  and  $\Gamma_0 = 40.2 \text{ MeV}/c^2$ . This is expected because it does not matter if the Breit-Wigner fit function is folded with the acceptance and efficiency matrix  $C_{Eff}(M)$ , or if the data are corrected instead.

The gray shaded band indicates the systematic uncertainties on the extracted  $\Sigma(1385)^+$  signal. The source of systematic errors are the applied event selection cuts, which might act differently on experimental data and simulations. These uncertainties were estimated by varying the ranges of the cuts on the  $K^+$  mass (see Figure 3.8), on the invariant  $\Lambda$  signal (see Figure 3.10) and on the neutron signal (see Figure 3.14) by  $\pm 20\%$ . Additionally, the  $dE/dx$  cuts for the particle identification were narrowed and broadened (see Figure 3.7). In total, 29 different cut combinations were tested. For each cut combination, the data were treated in the same way as described before, including the determination of the misidentification background, the fitting of the different simulations and the final efficiency corrections. By overlaying the resulting  $\Sigma(1385)^+$  spectra to the original one, the maximum deviation in each bin was taken as the systematic error.

As the error band in Figure 3.27 is rather narrow, it can be concluded that the extracted  $\Sigma(1385)^+$

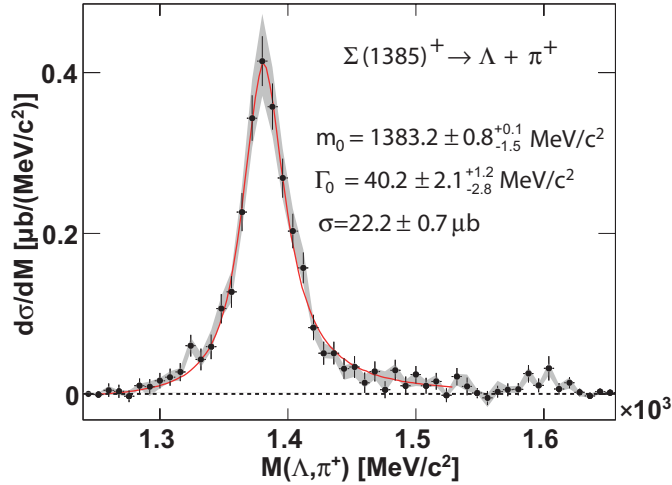


**Figure 3.27:** Corrected  $\Sigma(1385)^+$  line shape. The red line is a Breit-Wigner fit to the black data points. The gray band indicates the systematic error on the  $\Sigma(1385)^+$  shape (see text for details).

line shape is well under control.

The systematics on the  $\Sigma(1385)^+$  mass and width were obtained by fitting each of the 29 cut-variation spectra with the Breit-Wigner function and extracting individual values for  $m_0$  and  $\Gamma_0$ . The maximum deviation from the values quoted above were considered as the systematic errors. In this way the following values were obtained:

$$\begin{aligned} m_0 &= 1383.2 \pm 0.8^{+0.1}_{-1.5} \text{ MeV}/c^2 \\ \Gamma_0 &= 40.2 \pm 2.1^{+1.2}_{-2.8} \text{ MeV}/c^2 \end{aligned}$$

Combining both, the statistical and the systematic errors, the achieved results agree within the errors with the PDG values [B<sup>+</sup>12].

Last but not least, the production cross section could be extracted by integrating the spectrum in Figure 3.27. It is determined to  $\sigma = 22.2 \pm 0.7 \mu b$ . The systematic errors on the cross section are specified, when differential distributions are discussed.

At this point it has to be mentioned that the largest part of the present knowledge about the  $\Sigma(1385)^+$  hyperon has been gained from photon and kaon induced reactions [K<sup>+</sup>12a, Bau84, ABS81]. With the line shape shown in Figure 3.27, first precise data on this resonance in  $p + p$  collisions at SIS18 energies are presented. In contrast to the previous experiments, the background below the signal was not treated as a simple polynomial function, but an adequate model was developed, which describes the different background sources either with experimental data or with help of simulations. This model was tested systematically on different observables and allowed to accurately determine the background shape below the  $\Sigma(1385)^+$  signal. By including additionally the evaluation of the systematic errors, a precise spectral shape of the  $\Sigma(1385)^+$  resonance is obtained. The results on the extracted mass and width have been included in the particle summary table of the Particle Data Group (PDG) [B<sup>+</sup>12].

The presented work is also interesting in the context of  $\Sigma(1385)^+$  production in heavy ion collisions. As pointed out in the introduction, the  $\Sigma(1385)^+$  is expected to experience an attractive interaction in the nuclear medium, resulting in a mass shift of about 60 MeV and a broadening of about a factor of two already at normal nuclear density [LK02]. The extracted properties can thus serve as a bench mark for any interpretation of the  $\Sigma(1385)^+$  signal in heavy ion data.

### 3.4.2 Angular distributions and production cross section

As mentioned in the beginning of this chapter, angular distribution can give a unique insight into the underlying production processes of a particle reaction. Especially information about the exchange meson(s), the different contributing partial waves and possible intermediate resonances can be extracted from the CMS-, G-J- and helicity-angle distributions. Figure 3.28 shows the differential cross sections of the reaction  $p + p \rightarrow \Sigma(1385)^+ + n + K^+$  for the nine possible angles in three reference frames. The gray shaded boxes indicate the systematic errors, which were determined in the same way as discussed above. However, not all combinations of the different kaon mass cuts,  $\Lambda$  cuts and neutron cuts were used, but only the cases where the three cuts were

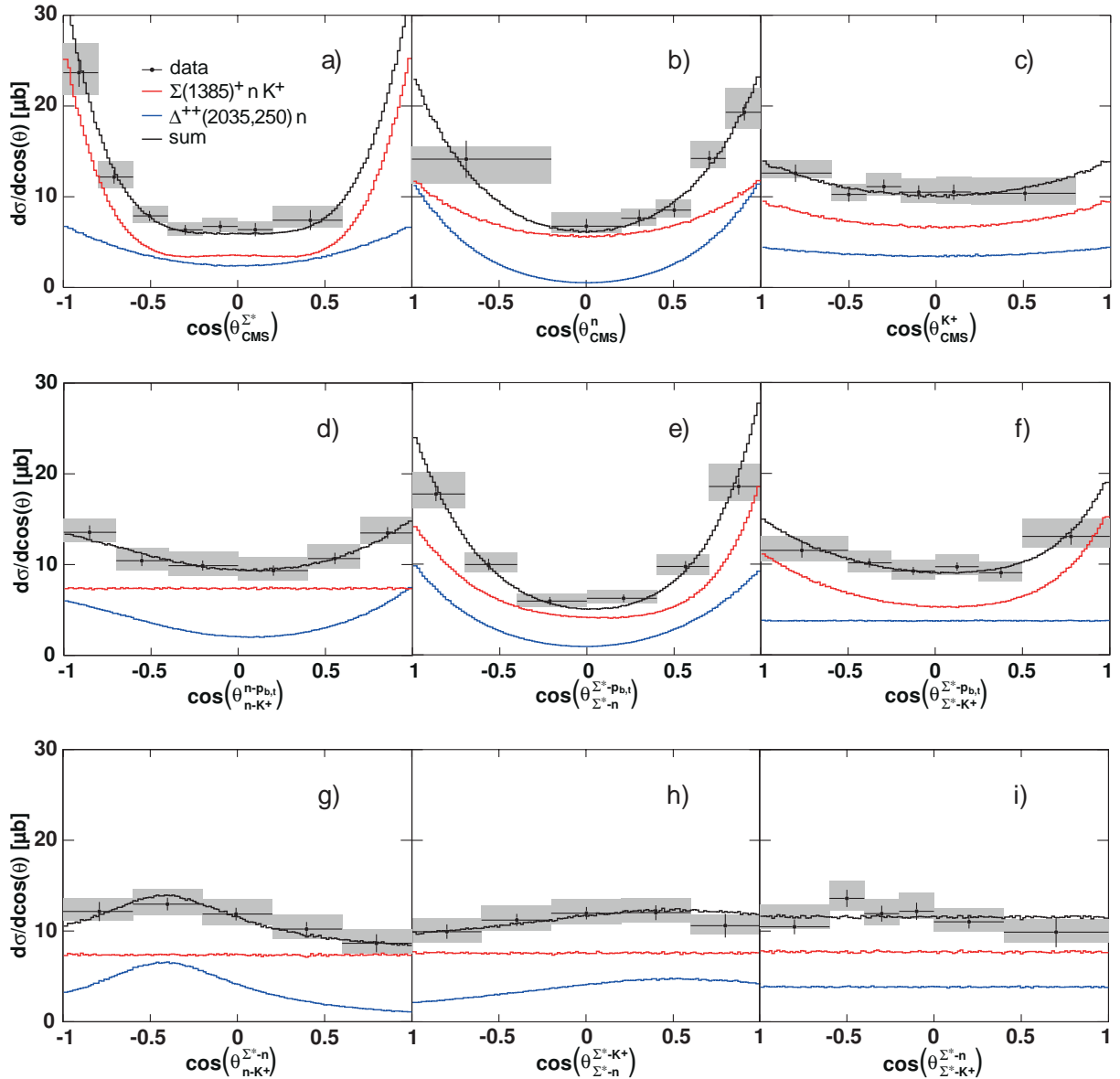


**Figure 3.28:** Differential cross sections in experimental data and simulations. First row: production angles of the  $\Sigma(1385)^+$ , the neutron and the  $K^+$  in the CMS. Second row: differential cross sections in the three G-J angles. Third row: differential cross sections in the three helicity angles.

opened by 20% and the case where the kaon mass cut was narrowed by 20%. Also the variation of the  $dE/dx$  cuts was included. This reduced number of systematic variations was necessary in order to keep enough events for the differential analysis. Compared to the experimental data are the simulations of non-resonant  $\Sigma(1385)^+$  production (red histograms) and resonant  $\Sigma(1385)^+$  production via an intermediate  $\Delta^{++}(2035,250)$  resonance (blue histograms). The incoherent sums of both contributions are shown in the black histograms. As in the case of the uncorrected distributions in Figure 3.26, the predictions of the simulation model are in perfect agreement with the experimental data.

The first row of Figure 3.28 shows the CMS angles. It is important to notice that the  $\Sigma(1385)^+$ , the neutron and the  $K^+$  angular distributions are now symmetric with respect to  $\cos(\theta_{CMS}) = 0$ . This indicates that the applied corrections are appropriate. Furthermore, the strong anisotropies in the  $\Sigma(1385)^+$  and in the neutron production angle support the hypothesis that the reactions are of peripheral nature. Due to the fact that the  $K^+$  is the lightest of the three particles and that it is always produced at vertex B (see Figure 3.2), the  $K^+$  angular distribution shows only a small anisotropy. Interesting is the observation that the  $\Sigma(1385)^+$  distribution is steeper than the one of the neutron. This could be an indication that strange meson exchange (e.g. kaon exchange) dominates the  $\Sigma(1385)^+$  production process (see discussion in section 3.1.2.2).

The second row of Figure 3.28 shows the G-J angles. They give access to the contributing partial waves at the vertex B of the exchange diagrams. This information is partially disturbed if both, strange and non-strange meson exchange, contribute (see discussion in section 3.1.2.3). To understand this statement, one has to have a closer look at panel d). For the simulations of non-resonant  $\Sigma(1385)^+$  production, strange meson exchange with an s-wave contribution at vertex B was assumed. In this case the neutron in the neutron- $K^+$  reference frame is produced isotropically; the distribution ( $\cos(\theta_{n-K^+}^{n-pbt})$ ) must therefore be flat (see red histogram). The experimental data are, however, not flat. In the simulations this effect is explained by the contribution of resonant  $\Sigma(1385)^+$  production through the  $\Delta^{++}$  resonance, which is mediated by non-strange meson (e.g. pion) exchange (blue histogram). Since the neutron is produced at vertex A in such a process, the distribution in  $\cos(\theta_{n-K^+}^{n-pbt})$  does not characterize vertex B, but is highly correlated with the neutron production angle in the CMS ( $\cos(\theta_{CMS}^n)$ ). Consequently,  $\cos(\theta_{n-K^+}^{n-pbt})$  is anisotropic. At the same time the distribution is asymmetric, which is typical for the G-J frames (see discussion in section 3.1.2.3).

The same argumentation holds for panel f), where the  $\Sigma(1385)^+-K^+$  G-J frame is studied. This frame characterizes vertex B in case of non-strange meson exchange, but not in case of strange meson exchange. Therefore, the non-resonant simulations are anisotropic (red histogram), and, since the  $\Delta^{++}$  was simulated to decay isotropically, the resonant simulations are flat (blue histogram). Also here, the simulations are in good agreement with the experimental data.

The G-J angle in the  $\Sigma(1385)^+$ -neutron reference frame (panel e)) reflects the CMS angular distributions of both, the  $\Sigma(1385)^+$  and the neutron. Consequently, the experimental distribution as well as the simulated distributions are rather anisotropic.

Altogether, the simple simulation model assumes that the differential cross section  $\frac{d\sigma(M)}{d\Omega}$  at vertex B is isotropic in the both cases of strange and non-strange meson exchange so that the observed anisotropies in the experimental data only reflect the CMS angular distributions.

The third row of Figure 3.28 shows the helicity angles. Panel g) has already been discussed. It shows a clear peak structure, which is well reproduced by assuming that 33% of the  $\Sigma(1385)^+$  stem from an intermediate  $\Delta^{++}$  resonance (blue histogram). The non-resonant simulations (red

histogram) are flat in this observable.

In panel h) a similar effect is visible. The presence of resonant simulations produces a small bump around  $\cos\left(\theta_{\Sigma^*-n}^{\Sigma^*-K^+}\right) = 0.5$ . In total, the deviation from an isotropic distribution is less evident compared to panel g), but still the experimental data seem to show this behavior as well. Finally, the helicity angle in the  $\Sigma(1385)^+-K^+$  frame is studied in panel i). The distribution is flat for both simulation models. Although the data are in fairly well agreement with the simulations, one can see a small anisotropy in the experimental distribution. The origin of that is unknown, but it might indicate that either interference effects between different production channels are present and (or) that the assumed  $\Delta^{++}(2035,250)$  is partially polarized (see discussion in section 3.1.2.4).

Summarizing all those results, the data seem to be in very good agreement with the following hypothesis, used for the simulation model:

- The reaction  $p+p \rightarrow \Sigma(1385)^+ + n + K^+$  processes via meson exchange with corresponding strong anisotropies of the angular distributions in the CMS.
- Around 33% of the  $\Sigma(1385)^+$  yield is produced via non-strange meson (e.g. pion) exchange followed by the production of an intermediate  $\Delta^{++}$  resonance with a mass of around 2035 MeV/ $c^2$  and a width of around 250 MeV/ $c^2$ ; the remaining 66% are attributed to strange meson (e.g. kaon) exchange with non-resonant  $\Sigma(1385)^+$  production (see also section 3.3.4).
- The production at vertex B is isotropic (s-wave like) in case of both exchange processes.

At this point it has to be stressed out that, even though the developed simulation model reproduces the experimental data very well, it must not be seen as an unique interpretation of the data. In fact, the developed model is much simpler than a full OBE approach. The meson exchange process, for example, was imitated by simply folding phase space simulations with angular distributions. Also the assumed properties of the  $\Delta^{++}$  resonance are only a rough estimation. It cannot even be proven unambiguously that a  $\Delta^{++}$  resonance contributes at all because also other effects can cause anisotropies in the helicity angles. It might also be the case that several  $\Delta^{++}$  resonances contribute and interfere. The used simulation model does not account for these effects.

On the other hand, the goal of the analysis was to find a model, which describes the kinematics in the experimental data correctly so that appropriate acceptance and efficiency corrections can be performed. This goal has certainly been reached. By applying those corrections, it was possible to deliver differential cross sections, which reflect the kinematics of the  $\Sigma(1385)^+$  production process. Therefore, these new HADES data are perfectly suited to be compared to any (more sophisticated) theoretical approach. In this way it will be possible to disentangle the contribution of  $\pi$ ,  $\rho$ ,  $K$ ,  $K^*$  etc. exchange and to determine the real contribution of possible  $\Delta^{++}$  resonances. The presented data have thus the potential to give a new insight into the  $\Sigma(1385)^+$  production mechanisms in  $p+p$  reactions at SIS18 energies. This will help to improve transport models, used to simulate heavy ion reactions. As pointed out in [Lut04], only if the dynamics of the  $\Sigma(1385)$  hyperon are incorporated accurately, the  $K^-$  yields measured in these reactions can be interpreted correctly, and can provide information about the  $K^-$  dynamics in the nuclear medium.

In this context an important quantity is the total production cross section of the reaction  $p+p \rightarrow \Sigma(1385)^+ + n + K^+$ . It can be extracted individually from each picture of Figure 3.28 by

integrating either the experimental data or the simulations. The obtained results scatter only within the statistical errors. The final value is taken as the mean value of all nine results:

$$\sigma = 22.42 \pm 0.99 \pm 1.57_{-2.23}^{+3.04} \mu b$$

The first error of the cross section is only statistical. The second error is an additionally included systematic error from the normalization to  $p + p$  elastic data [HAD11]. The asymmetric errors are the systematic errors of the analysis procedure.

The obtained cross section for the  $\Sigma(1385)^+$  can now be compared to the cross sections of the ground state hyperon  $\Sigma^+(1189)$ . Figure 3.29 shows measured cross sections of the reaction  $p + p \rightarrow \Sigma^+ + n + K^+$  and  $p + p \rightarrow \Sigma(1385)^+ + n + K^+$  as a function of the excess energy  $\varepsilon$ . The values for  $\Sigma^+$  production are a compilation of different experiments, extracted from [B<sup>+</sup>10, V<sup>+</sup>10, SHHM07, BFM<sup>+</sup>88]. The red and the blue star show the cross section for  $\Sigma(1385)^+$  production extracted in this work and in [K<sup>+</sup>70], respectively. The HADES data point is located at an excess energy of  $\varepsilon \approx 360$  MeV. Here, the cross section of the excited  $\Sigma$  is a factor two smaller than the one of the ground state  $\Sigma$ , but still the two values are compatible within the shown error bars. The weak energy dependence of the cross sections for excess energies above 200 MeV seems to be a common characteristic of both reactions. This analogy can be seen as consistency check for the obtained results.

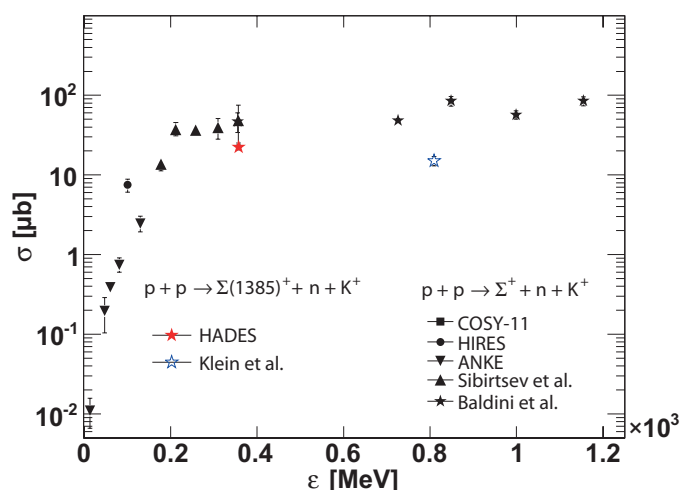


**Figure 3.29:** Cross section as a function of the excess energy for the reaction  $p + p \rightarrow \Sigma^+ + n + K^+$  and for  $p + p \rightarrow \Sigma(1385)^+ + n + K^+$ . See text for details.

### 3.4.3 Decay angular distribution of the $\Sigma(1385)^+$

Information about the exchange particle can also be extracted by studying the decay distribution of the  $\Sigma(1385)^+$  in the  $\Lambda-\pi^+$  reference frame (see discussion in section 3.1.2.5). Figure 3.30 shows the differential cross section as a function of  $\cos(\theta_{\Lambda-\pi^+}^{\Lambda-pbt})$ . The data follow a small but clear  $\cos^2(\theta)$  dependency, which might reveal the relative contribution of  $K$  and  $K^*$  exchange. Quantitative informations on this are obtained by fitting the data with the function (red line in

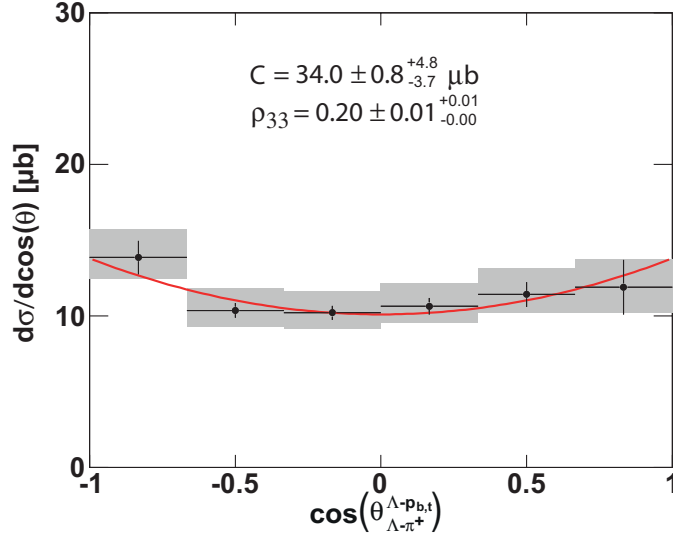


**Figure 3.30:** Differential cross section in the  $\Lambda\text{-}\pi^+$  G-J frame. Data are fitted with the function (3.22) (red line).

Figure 3.30):

$$\frac{d\sigma}{d\cos(\theta)} = C \left( \rho_{33} \sin^2(\theta) + \left( \frac{1}{2} - \rho_{33} \right) \left( \frac{1}{3} + \cos^2(\theta) \right) \right) \quad (3.22)$$

The obtained values for  $C$  and  $\rho_{33}$  are shown in the figure. The factor  $\rho_{33} \approx 0.2$  is close to what has been reported in [W<sup>+</sup>87] for the decay of the  $\Delta^{++}(1232)$  resonance in  $p + p \rightarrow \Delta^{++}(1232) + n$  reactions. The result indicates that the excitation of the  $m = \pm \frac{3}{2}$  states of the  $\Sigma(1385)^+$  is not 0. This would mean that  $K^*$  exchange is not negligible in the  $\Sigma(1385)^+$  formation process. These conclusions can, however, only be drawn if the  $\Sigma(1385)^+$  is exclusively produced via kaon exchange processes (see section 3.1.2.5). It is at the moment not clear to which extent this is fulfilled. Indeed, the data indicate that part of the  $\Sigma(1385)^+$  production happens via an intermediate  $\Delta^{++}$  resonance. Such a process requires the exchange of a non-strange meson, like a pion or a rho. The influence of non-strange meson exchange on the distribution in Figure 3.30 and the extraction of the real contributions of  $K^*$  and  $K$  exchange requires more sophisticated models.

### 3.4.4 Summary

The exclusive analysis of the reaction  $p + p \rightarrow \Sigma(1385)^+ + n + K^+$  at a beam kinetic energy of 3.5 GeV has been presented. The  $\Sigma(1385)^+$  was reconstructed in the  $\Lambda + \pi^+$  decay mode. In order to understand the non-physical background in the experimental spectra, a dedicated sideband method was used. Additional physical background sources, like the non-resonant production of  $\Lambda\text{-}\pi^+$  pairs, was simulated. In this way it was possible to extract the pure  $\Sigma(1385)^+$  signal. By fitting the signal with a p-wave Breit-Wigner function, the pole mass and the width of the resonance could be determined.

Furthermore, the dynamics of the reaction  $p + p \rightarrow \Sigma(1385)^+ + n + K^+$  were investigated. For this purpose, the angular distributions in the CMS-, G-J- and helicity-frames were studied. At the

---

same time, a simulation model was developed. This model was tuned iteratively until it was able to describe the experimental data consistently. Afterwards, these simulations could be used for acceptance and efficiency corrections. The corrected CMS distributions of the  $\Sigma(1385)^+$  and the neutron show strong anisotropies, which is the expected behavior if meson exchange dominates the particle production process. Also the distribution in helicity angle is clearly different from isotropy. The simulation model explains this effect by assuming that about 1/3 of the  $\Sigma(1385)^+$  yield stems from the decay of a heavy  $\Delta^{++}$  resonance.



## 4 Search for the $\Lambda(1405)$ hyperon in proton-proton reactions

In this chapter the reconstruction of the  $\Lambda(1405)$  hyperon from its decay into the charged  $\Sigma^\pm\pi^\mp$  states is presented. This decay has so far never been measured in proton-proton reactions. It will become clear that the description and the understanding of the experimental data is not possible if only  $\Lambda(1405)$  production is considered. In fact, a significant part of the obtained spectra must be attributed to other contributing reactions, like  $p + p \rightarrow \Sigma(1385)^0 + p + K^+$ ,  $p + p \rightarrow \Lambda(1520) + p + K^+$ ,  $p + p \rightarrow \Sigma^- + \Delta^{++}(1232) + K^+$  etc. By studying several observables and by carrying out simulations, the relative contributions of these reactions can be disentangled. Finally, a consistent description of the experimental data is obtained, from which the properties of the  $\Lambda(1405)$  can be extracted. An interesting and surprising result of this work is that the reconstructed  $\Lambda(1405)$  spectrum appears well below  $1400 \text{ MeV}/c^2$ .

The chapter is organized as follows:

The first section briefly discusses the technical part of the analysis. Here the data selection methods are described and the treatment of the misidentification background is presented. At the same time, full-scale simulations are carried out, which are used to get a first interpretation of the data.

Afterwards, in the second part of the chapter, the simulation model is improved and tuned until it consistently describes the experimental data. For this purpose, several observables are investigated, which allow to determine the relative contributions of all relevant strangeness channels. The obtained simulation model is then also used to apply acceptance and efficiency corrections. In the third part of the chapter, the final results, which have also been published in [A<sup>+</sup>13, A<sup>+</sup>12d], are presented. On the basis of the corrected experimental distributions, cross sections for all contributing reactions are determined. The extracted  $\Lambda(1405)$  spectral shape is then compared to the results of other experiments. Finally, first calculations, which were carried out to interpret the new data, are discussed. In this context, also the possible influence of interference effects, which might play an important role for the obtained spectral shape of  $\Lambda(1405)$ , is investigated.

### 4.1 General analysis procedure

The energetically cheapest way to produce  $\Lambda(1405)$  in  $p + p$  reactions is the reaction (4.1) with the associated production of a proton and a  $K^+$ . The  $\Lambda(1405)$  can be reconstructed in one of the three  $\Sigma\pi$  decay channels. Especially interesting in terms of purity is the exclusive analysis, with maximum one neutral particle in the final state. Such an analysis can be carried out for the channels (4.2)-(4.4). Most desirable, however, would be to study the “golden”  $\Sigma^0\pi^0$  decay via channel (4.5) (see also discussion in section 1.4). The reason is that this channel is not contaminated by isospin 1 states like  $\Sigma(1385)^0$ . Indeed,  $\Lambda(1405)$  and  $\Sigma(1385)^0$  are both broad resonances, which are very close in mass, so that their mass spectra completely overlap.

Furthermore, their production and decay schemes are quite similar, as can be seen by comparing the reactions (4.1) and (4.7).

$$p + p \xrightarrow{3.5\text{GeV}} \Lambda(1405) + K^+ + p \quad (4.1)$$

$$\begin{array}{l} \rightarrow \Sigma^- + \pi^+ \\ \quad \downarrow \\ \quad n + \pi^- \quad 33.33\% \end{array} \quad (4.2)$$

$$\begin{array}{l} \rightarrow \Sigma^+ + \pi^- \\ \quad \downarrow \\ \quad p + \pi^0 \quad 17.19\% \end{array} \quad (4.3)$$

$$\begin{array}{l} \quad \downarrow \\ \quad n + \pi^+ \quad 16.11\% \end{array} \quad (4.4)$$

$$\begin{array}{l} \rightarrow \Sigma^0 + \pi^0 \\ \quad \downarrow \\ \quad \Lambda + \gamma \end{array}$$

$$\begin{array}{l} \quad \downarrow \\ \quad p + \pi^- \quad 21.35\% \end{array} \quad (4.5)$$

$$\begin{array}{l} \quad \downarrow \\ \quad n + \pi^0 \quad 12.02\% \end{array} \quad (4.6)$$

$$p + p \xrightarrow{3.5\text{GeV}} \Sigma(1385)^0 + K^+ + p \quad (4.7)$$

$$\begin{array}{l} \rightarrow \Sigma^- + \pi^+ \\ \quad \downarrow \\ \quad n + \pi^- \quad 5.85\% \end{array} \quad (4.8)$$

$$\begin{array}{l} \rightarrow \Sigma^+ + \pi^- \\ \quad \downarrow \\ \quad p + \pi^0 \quad 3.02\% \end{array} \quad (4.9)$$

$$\begin{array}{l} \quad \downarrow \\ \quad n + \pi^+ \quad 2.83\% \end{array} \quad (4.10)$$

$$\begin{array}{l} \rightarrow \Lambda + \gamma \\ \quad \downarrow \\ \quad p + \pi^- \quad 0.83\% \end{array} \quad (4.11)$$

$$\begin{array}{l} \quad \downarrow \\ \quad n + \pi^0 \quad 0.47\% \end{array} \quad (4.12)$$

$$\begin{array}{l} \rightarrow \Lambda + \pi^0 \\ \quad \downarrow \\ \quad p + \pi^- \quad 55.59\% \end{array} \quad (4.13)$$

$$\begin{array}{l} \quad \downarrow \\ \quad n + \pi^0 \quad 31.15\% \end{array} \quad (4.14)$$

The only differences in the two reactions are the branching ratios and the structure in the neutral decay channels. As  $\Lambda(1405)$  is an isospin 0 resonance, it can decay into the pure isospin 0 state  $\Sigma^0\pi^0$ .  $\Sigma(1385)^0$ , on the other hand, is an isospin 1 resonance, which decays instead into  $\Lambda\pi^0$ . Hence, the two final states just differ by one  $\gamma$ . That difference allows already to separate the two resonances, and this is why the decay  $\Lambda(1405) \rightarrow \Sigma^0\pi^0$  is called “golden” channel. In [A<sup>+</sup>12b] the  $p + p$  data of HADES were analyzed exactly for these neutral channels. Unfortunately, the obtained statistic was not sufficient to extract a clear  $\Lambda(1405)$  signal in this analysis. The  $\Sigma(1385)^0$ , however, could be unambiguously separated and identified, which later on allowed to extract also a total production cross section for the reaction  $p + p \rightarrow \Sigma(1385)^0 + p + K^+$  of  $5.56 \pm 0.48_{-1.06}^{+1.94} \mu\text{b}$  [Epp12b].

This result opens the new possibility to investigate the  $\Lambda(1405)$  from its charged decay into

$\Sigma^\pm\pi^\mp$ . A separation from  $\Sigma(1385)^0$  is not possible as this resonance decays into  $\Sigma^\pm\pi^\mp$  as well. Nevertheless, as the total production cross section of  $\Sigma(1385)^0$  is known, also its contribution to the charged channel analysis is known. Furthermore, its branching ratio into these channels is about six times lower than for  $\Lambda(1405)$  so that the contamination by  $\Sigma(1385)^0$  is expected to be low.

On the basis of these considerations, the following part concentrates on the analysis of  $\Lambda(1405)$  in the decay channels (4.2) and (4.4), which both have the same final state configuration of  $p, K^+, \pi^+, \pi^-$  and  $n$ .

These are at the same time the particles which had also to be selected for the reconstruction of the  $\Sigma(1385)^+$ . Indeed, the analysis of  $\Sigma(1385)^+$  and  $\Lambda(1405)$  have similarities, and some of the methods, developed in the last chapter, will also find their application in this part.

### 4.1.1 Data selection

A first attempt for the analysis of  $\Lambda(1405)$  in the charged decay channels was already carried out in [Sie10a]. The event selection is discussed in this work, while hereafter the analysis procedure is briefly addressed.

The first analysis step was to select events with three positively and one negatively charged particles. The identification of proton, kaon and pion candidates was then done with  $dE/dx$  cuts (see e.g. Figure 3.7). In this way a data sample was obtained, which was again dominated by pions and protons misidentified as kaons. Therefore, in order to purify the kaon candidates, a kaon mass cut between 350 and 650  $\text{MeV}/c^2$  was applied (see e.g. Figure 3.8).

The obtained missing mass to proton,  $K^+$ ,  $\pi^+$  and  $\pi^-$  ( $\text{MM}(p, K^+, \pi^+, \pi^-)$ ) from the remaining events is presented in Figure 4.1. The spectrum shows a clear neutron signal on top of a large background contribution. This picture is similar to what has been obtained in Figure 3.11. However, as no cut on an invariant  $\Lambda(1116)$  signal has been applied before, the background is significantly larger. This background can again be attributed to misidentified kaon candidates,

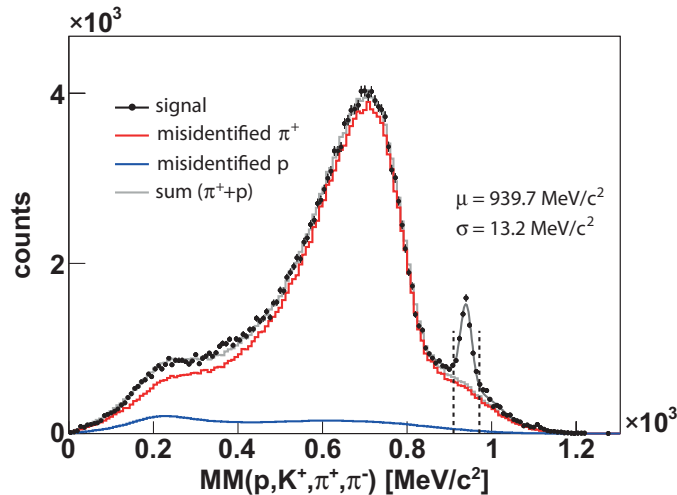


**Figure 4.1:** Missing mass to proton,  $K^+$ ,  $\pi^+$  and  $\pi^-$ . The neutron signal is fitted with a Gaussian function (gray line). Vertical dashed lines indicate the cut region for the neutron signal extraction ( $910 \text{ MeV}/c^2$ - $971 \text{ MeV}/c^2$ ). The contribution by misidentified pions and protons is shown as well (see text for details).





### 4.1.2 Extraction of the $\Sigma$ hyperons

In order to extract  $\Lambda(1405)$  events, it was necessary to identify the intermediate  $\Sigma$  hyperons before. A good signal to background ratio was hereby obtained after the particle tracks have been kinematically refitted (see [Sie10a]). Furthermore, cuts on the event topology and on the quality of the refit were applied. The  $\Sigma^\pm$  hyperons were then reconstructed via the missing mass to proton,  $K^+$  and  $\pi^\mp$ . The two obtained spectra are presented in Figure 4.2 a) and b), respectively. In both cases clear peak structures emerge from a broad background. The peaks can be unambiguously identified with the corresponding  $\Sigma^+$  and  $\Sigma^-$  hyperons, as they are located at the nominal masses of  $1189 \text{ MeV}/c^2$  and  $1197 \text{ MeV}/c^2$ , respectively. The widths of the signals were determined with a Gaussian fit to  $\sigma_{\Sigma^+} = 5.1 \text{ MeV}/c^2$  and  $\sigma_{\Sigma^-} = 6.2 \text{ MeV}/c^2$ . The background in both figures is mainly attributed to misidentified pions and protons. With help of the sideband method, used to describe the neutron spectrum in Figure 4.1, the misidentification background could be fixed in yield and shape, shown in the blue histograms. The other colored histograms are full scale simulations of the reactions (4.15)-(4.22). While the shape of these spectra is given by the simulations themselves, the relative contribution of the different reactions was obtained by a fitting procedure, which will be described later on. At this point only the obtained shapes shall be discussed:

- The **black** histograms represent the summed contribution of the  $\Lambda(1405)$  and  $\Sigma(1385)^0$  simulations. The  $\Sigma^+$  peak in a) results from the decay of  $\Lambda(1405)$  and  $\Sigma(1385)^0$  into the  $\Sigma^+\pi^-$  state. Left to the  $\Sigma^+$  peak a broad structure is visible, which is a consequence of the decay into  $\Sigma^-\pi^+$  pairs. Exactly this second decay channel is responsible for the  $\Sigma^-$  peak in panel b), whereas now the  $\Sigma^+\pi^-$  decay channel creates the broad distribution left to the  $\Sigma^-$  signal.
- The **green** histograms are the results of the simulated reaction (4.17). As  $\Lambda(1520)$  decays into both,  $\Sigma^+\pi^-$  and  $\Sigma^-\pi^+$ , the obtained spectra show a similar behavior as the ones of  $\Lambda(1405)$  and  $\Sigma(1385)^0$  production. The contribution of this signal is rather small.

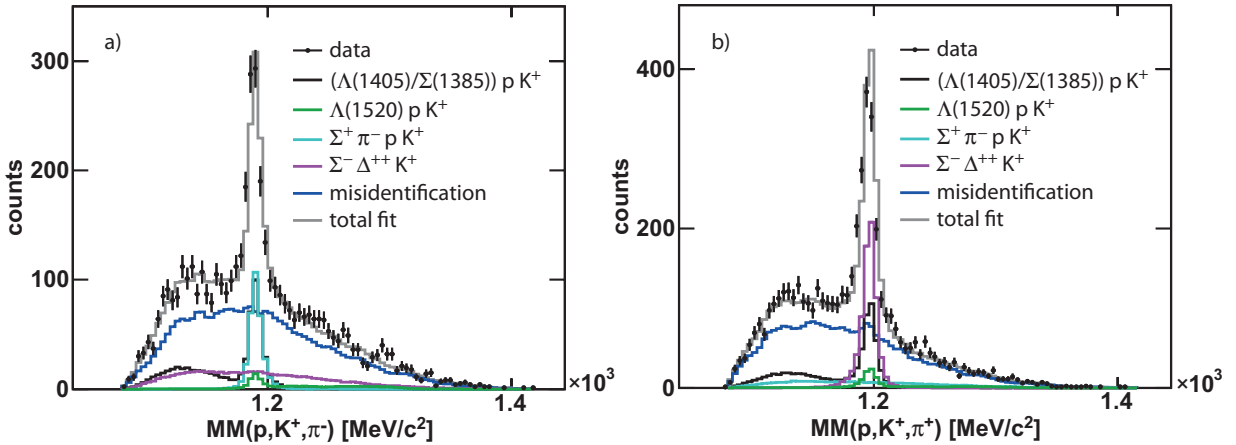


**Figure 4.2:** Missing mass to proton,  $K^+$  and  $\pi^-$  (a) and missing mass to proton,  $K^+$  and  $\pi^+$  (b). The spectra show a  $\Sigma^+$  and a  $\Sigma^-$  signal, respectively. Colored histograms represent simulations of the different reactions (4.15)-(4.22), fitted to the experimental data via a simultaneous fit. See text for details.

- The **light blue** histograms are simulations of the reaction (4.18). Here the  $\Sigma^+\pi^-$  pair is not produced from the decay of a resonance, but the two particles are produced directly. This reaction gives a  $\Sigma^+$  signal in a) and a phase space like distribution in b), contributing to the background below the  $\Sigma^-$  peak.
- The **pink** histograms represent simulations of reaction (4.22). This reaction gives a flat, phase space like distribution in a) and a pure  $\Sigma^-$  signal in b).

The reason why only the reaction (4.18) and (4.22) have been used for the simulations of non-resonant  $\Sigma\pi$  production will be discussed in section 4.2. Important at this point is that the sums of all the simulated contributions (gray histograms) perfectly agree with the experimental data.

### 4.1.3 $\Lambda(1405)$ spectra

In order to analyze the  $\Lambda(1405)$  separately for its two decay channels, the experimental data were divided into two samples, one containing an intermediate  $\Sigma^+$  hyperon and one containing an intermediate  $\Sigma^-$  hyperon. For this purpose,  $3\sigma$  mass cuts around the corresponding  $\Sigma$  signals were applied to the spectra in Figure 4.2. Furthermore, each event was kinematically refitted with the event hypothesis of having either an intermediate  $\Sigma^+$  or  $\Sigma^-$  in the reaction (for details see [Sie10a]). The two kinematic refits delivered  $\chi^2$  values ( $\chi_{\Sigma^+}^2$  and  $\chi_{\Sigma^-}^2$ ) for each event, which quantifies how well the event fits into the corresponding  $\Sigma^+$  or  $\Sigma^-$  hypothesis. An event was then attributed to the  $\Sigma^+\pi^-$  decay channel if it was selected by the mass cut around the  $\Sigma^+$  signal, and if, at the same time, the  $\chi^2$  value for the  $\Sigma^+$  hypothesis was smaller than the one for the  $\Sigma^-$  hypothesis ( $\chi_{\Sigma^+}^2 < \chi_{\Sigma^-}^2$ ). The selection of events belonging to the  $\Sigma^-\pi^+$  decay channel was done accordingly. In this way it was possible to classify each event to one of the two decay channels with either an intermediate  $\Sigma^+$  hyperon or an intermediate  $\Sigma^-$  hyperon.

In order to reconstruct the  $\Lambda(1405)$  spectral shape, the missing mass to the proton and the  $K^+$  was calculated and plotted in Figure 4.3 for both decay channels. Here the refitted particle tracks of the proton and the kaon were used. With this the missing mass distribution is equivalent to the invariant mass distribution of  $\Sigma^+\pi^-$  or  $\Sigma^-\pi^+$ , respectively. In both panels of Figure 4.3

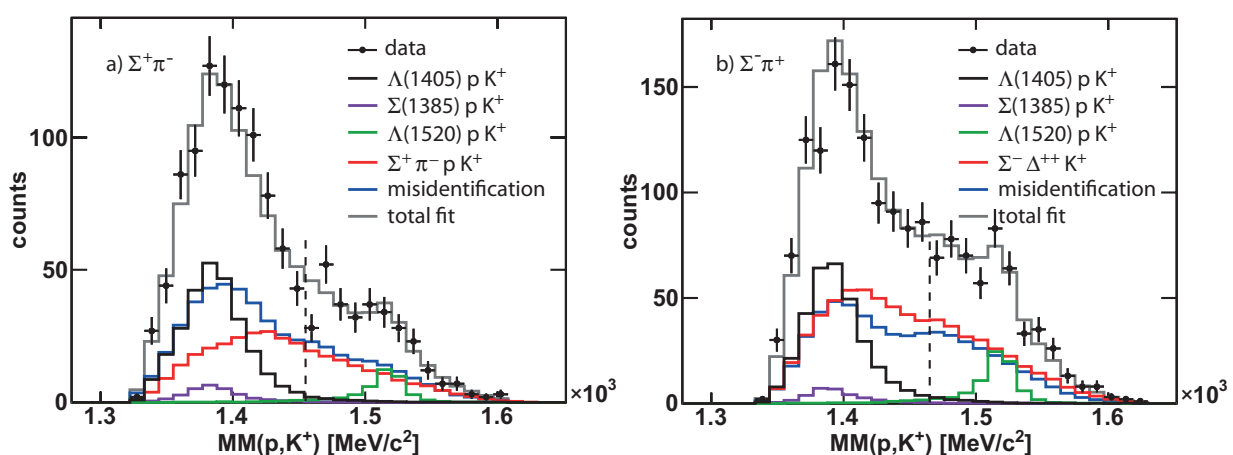


**Figure 4.3:** Missing mass to proton and  $K^+$  for the subsample with an intermediate  $\Sigma^+\pi^-$  state (a) and an intermediate  $\Sigma^-\pi^+$  state (b). Colored histograms show simulations of the different reactions contributing also to the spectra in Figure 4.2. Vertical dashed lines indicate the limit of the fit region (see text for details).

the experimental data show clear peak structures around  $1400 \text{ MeV}/c^2$ , which are located on top of broad distributions. Additionally included in the pictures are the simulations of the different reactions, which were discussed for Figure 4.2.

- The **blue** histograms show again the misidentification background, which has been estimated with the sideband method.
- The **black** histograms are the results of the  $\Lambda(1405)$  simulations, where the shape of the  $\Lambda(1405)$  was assumed to be Breit-Wigner like. However, in order to get a satisfactory agreement with the experimental data, the Breit-Wigner mass had to be set to  $1385 \text{ MeV}/c^2$  instead of  $1405 \text{ MeV}/c^2$ . The Breit-Wigner width was set to its PDG value of  $\Gamma = 50 \text{ MeV}/c^2$  [B<sup>+</sup>12].
- The **violet** histograms are the simulated  $\Sigma(1385)^0$  contributions. As the total cross section for the reaction  $p + p \rightarrow \Sigma(1385)^0 + p + K^+$  was determined to  $\sigma \approx 6 \mu\text{b}$  [A<sup>+</sup>12b, Epp12b], the yield of this resonance in the two spectra of Figure 4.3 is known. The small branching ratio into the charged channels guarantees that this contribution is rather low.
- The **green** histograms represent the simulated  $\Lambda(1520)$  signal. In fact, also the experimental data show an indication of a signal around  $1520 \text{ MeV}/c^2$ .
- The **red** histograms show the simulations of reaction (4.18) in panel a) and of reaction (4.22) in panel b). As the  $\Sigma\pi$  pairs do not stem from one common resonance in these two cases, the obtained distributions are broad and phase space like.

The sums of the five different contributions are illustrated in the gray histograms, which again perfectly describe the experimental distributions.

The overall good agreement in Figure 4.2 and Figure 4.3 was obtained after fitting the experimental data. Indeed, the only contributions which were fixed in yield from the very beginning are the misidentification background and the  $\Sigma(1385)^0$  contribution. The yields of all the other channels were determined by a simultaneous fit of the simulated distributions to the experimental data in the four pictures of Figure 4.2 and Figure 4.3. Four constraints were included in this fit:

1. The branching ratios of the resonances  $\Lambda(1405)$ ,  $\Sigma(1385)^0$  and  $\Lambda(1520)$  into the  $\Sigma^+\pi^-$  or  $\Sigma^-\pi^+$  states were fixed in the simulations to the values listed in the reactions (4.15)-(4.17). Thus, the simulations for each of those reactions were scaled by only one fit parameter.
2. The contributions of the misidentification background and of the simulated  $\Sigma(1385)^0$  were fixed in the four considered pictures.
3. The resolution of the  $\Sigma$  hyperon signals in Figure 4.2 is slightly different in the simulations and the experimental data. Therefore, the spectra in the region around the  $\Sigma$  peaks were not fitted bin-wise, but the integral below the signals was forced to be equal in the simulations and in the experimental data.
4. The experimental data in Figure 4.3 were only fitted in the mass range on the right side of the vertical dashed lines. This choice is important to not bias the extracted  $\Lambda(1405)$  signal. In fact, the  $\Lambda(1405)$  is not expected to be Breit-Wigner like, as it is assumed in the simulations. By excluding the  $\Lambda(1405)$  mass range from the fit, the result is independent from the assumptions made in the simulations. In this way the total  $\Lambda(1405)$  yield was only fixed by the spectra in Figure 4.2.

On the other hand, the contributions of the reactions (4.18) and (4.22), both scaled by one fit parameter, and the contribution of  $\Lambda(1520)$  are especially sensitive to the mass range

above  $\approx 1450 \text{ MeV}/c^2$ . Their yields were therefore mainly fixed by the fit to the spectra in Figure 4.3.

Altogether five fit parameters were used to describe four experimental spectra. The obvious good agreement of the fit result (gray histograms) with the experimental data translates into a normalized  $\chi^2$  value of  $\chi^2/ndf = 1.3$ .

The most prominent effect in the data of Figure 4.3 are the  $\Lambda(1405)$  mass peaks, which are clearly located below  $1400 \text{ MeV}/c^2$ . As will be shown later on, this observation stays true even after applying acceptance and efficiency corrections. The origin of this low mass  $\Lambda(1405)$  signal will be discussed in section 4.3. At this point it shall be demonstrated that these peaks are not created artificially by the applied event selection. Indeed, in order to separate the two decay channels of  $\Lambda(1405)$ , different cuts were used. Primarily,  $3\sigma$  mass cuts around the  $\Sigma$  signals in Figure 4.2 were applied. Secondly, cuts on the quality of the kinematic refits were used to classify each event to one of the two decay channels (see discussion above). Exactly this second cut can be problematic, as it excludes certain phase space regions of the data. This, in turn, could lead to artificial structures in Figure 4.3. In order to make sure that such structures are not the real origin of the low mass “ $\Lambda(1405)$ ” signals, the following consistency check was performed:

The data were not divided into two different subsamples. Instead, each event either fitting into the  $3\sigma$  mass window around the  $\Sigma^+$  or around the  $\Sigma^-$  window was selected. The cuts on the quality of the two kinematic refits ( $\chi^2$  values) were not used. In this way a data sample was obtained which contains both  $\Lambda(1405)$  decay channels ( $\Sigma^+\pi^-$  and  $\Sigma^-\pi^+$ ) and which cannot be biased by any phase space excluding cuts. For this sample the missing mass to proton and  $K^+$  was calculated and the result is plotted in Figure 4.4. Using the scaling factors from the simultaneous fit to the panels of Figure 4.2 and 4.3, the simulations could again be compared to the experimental results. They are presented in the colored histograms. A perfect description of the data is achieved. This indicates that the  $\chi^2$  cuts, applied to separate the decay channels for Figure 4.3, act in the same way on the experimental data and on the simulations. Furthermore, as the  $\Lambda(1405)$  peak is still located below  $1400 \text{ MeV}/c^2$ , it can be excluded that these  $\chi^2$  cuts artificially create the peak structures in Figure 4.3. Therefore, the observed low mass signal must indeed correspond to  $\Lambda(1405)$ .

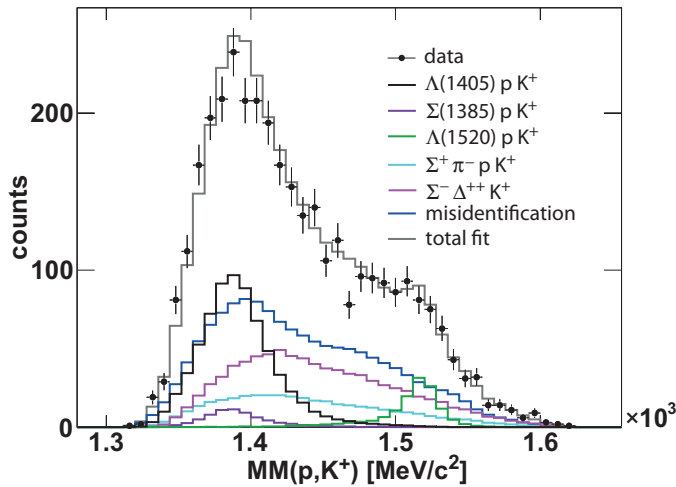


**Figure 4.4:** Missing mass to proton and  $K^+$  without the separation into the two  $\Sigma^\pm\pi^\mp$  decay channels. See text for details.

## 4.2 Evaluation of the simulation model

The contribution of  $\Lambda(1405)$ ,  $\Sigma(1385)^0$  and  $\Lambda(1520)$  could be easily fixed by fitting the spectra in Figure 4.2 and Figure 4.3. For the non-resonant channels, on the other hand, it is at this point not clear which of the reactions (4.18)-(4.22) contribute to the experimental data.

Furthermore, the whole simulation model, used so far, assumes isotropic particle production for all reactions. However, as it was shown in the analysis of  $\Sigma(1385)^+$ , angular distributions might be present. The inclusion of such distributions in the simulations is important in order to correctly reproduce the kinematics of the experimental data. This is also a necessary precondition in order to use the simulations for acceptance and efficiency corrections of the data.

Therefore, several invariant mass distributions and angular distributions are investigated and discussed in the following section. On the basis of these observables, the simulation model is further improved until a satisfactory agreement with the experimental data is achieved.

### 4.2.1 The contribution of $\Delta(1232)$ and $K^{*0}(892)$

First, the data subsample with an intermediate  $\Sigma^+\pi^-$  state is considered. For the non-resonant production of  $\Sigma^+\pi^-$  pairs it is a priori not clear if the four particles  $\Sigma^+$ ,  $\pi^-$ ,  $p$  and  $K^+$  are produced directly via reaction (4.18), or if intermediate resonances like  $K^{*0}(892)$  or  $\Delta^0(1232)$  contribute via reaction (4.20) or (4.19), respectively. The missing mass distribution, investigated in Figure 4.3 a), is not sensitive to this question as all three reactions would result in a phase space like distribution (see red histogram in Figure 4.3 a)).

Therefore, other observables for the same data sample have to be investigated. Figure 4.5 a) displays the invariant mass of  $p$  and  $\pi^-$ , where a possible contribution of  $\Delta^0(1232)$  might show up as a peak structure. In panel b) the invariant mass of  $K^+$  and  $\pi^-$  is shown, which should be sensitive to  $K^{*0}(892)$  production. The data sets in both pictures are the same as illustrated in Figure 4.3 a), only the observable has been changed.

Compared to the experimental data are again the simulations with all the contributions mentioned so far. The scaling factors for the different channels were known from the fitting procedure,

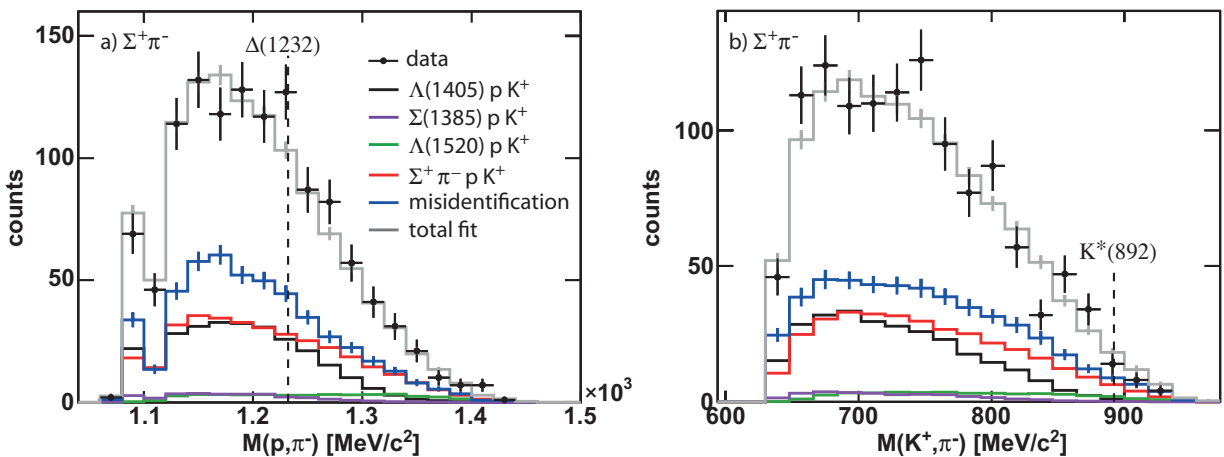


**Figure 4.5:** Invariant mass of proton and  $\pi^-$  (a) and invariant mass of  $K^+$  and  $\pi^-$  (b) for the subsample with an intermediate  $\Sigma^+\pi^-$  state. Vertical dashed lines indicate the nominal masses of  $\Delta^0(1232)$  and  $K^{*0}(892)$ .

discussed above. For the simulations of the non-resonant  $\Sigma^+\pi^-$  production (red histogram) only reaction (4.18) was used. This assumption gives already a rather good description of the experimental data (see gray histograms). The agreement between experimental data and simulations is quantified in a normalized  $\chi^2$  values of  $\chi^2/ndf = 0.8$  in panel a) and  $\chi^2/ndf = 1.9$  in panel b). It is important to notice that no peak like structures appear at the nominal masses of  $\Delta^0(1232)$  and  $K^{*0}(892)$ , indicated by the dashed lines.

In fact,  $\Delta^0(1232)$  is a broad resonance with a width of  $\Gamma \approx 120$  MeV/ $c^2$ , and its spectral shape may therefore overlap with the low mass tail of higher nucleon resonances like  $N^*(1440)$ . This might explain why the spectrum in panel a) is well described by just phase space like simulations. The appearance of a dip at  $M(p,\pi^-) \approx 1100$  MeV/ $c^2$  in the experimental data and in the simulations can be explained by the anti- $\Lambda$  cut, which has been applied to suppress the contribution of the reactions (4.23) and (4.24) in the data analysis.

On the other hand, the missing  $K^{*0}(892)$  signal in panel b) may be attributed to the limited available phase space in  $p + p$  reactions at 3.5 GeV. Indeed, the distribution in  $M(K^+, \pi^-)$  decreases rapidly to a maximum mass of around 930 MeV/ $c^2$ . The production cross section of reaction (4.20) is thus expected to be rather low, so that no clear signal can be observed.

In summary, the obtained results do not allow to completely exclude possible contributions of  $\Delta^0(1232)$  and  $K^{*0}(892)$  production. However, the spectra in Figure 4.5 agree sufficiently well with the assumption that non-resonant  $\Sigma^+\pi^-$  production proceeds only via reaction (4.18), so that this assumption was used to describe the experimental data.

Turning now to the non-resonant  $\Sigma^-\pi^+$  channel, only two reactions are considered at this point. These are the direct production of the four particles  $\Sigma^-$ ,  $\pi^+$ ,  $p$  and  $K^+$  via reaction (4.21), or the production of the proton and the  $\pi^+$  via an intermediate  $\Delta^{++}(1232)$  resonance (see reaction (4.22)). In order to test how much these two reactions contribute, the invariant mass of proton and  $\pi^+$  is investigated in Figure 4.6. The shown spectra represent the same data sample as presented in Figure 4.3 b). In panel a) the experimental data are compared to the sum of simulations where for the non-resonant  $\Sigma^-\pi^+$  production only reaction (4.21) was used. The scaling factors were again taken from the fitting procedure. It is obvious that the gray histogram cannot describe the data. In fact, the experimental distribution shows a kind of a peak structure close to the nominal  $\Delta^{++}(1232)$  mass, which is not reproduced by the broad, phase space like

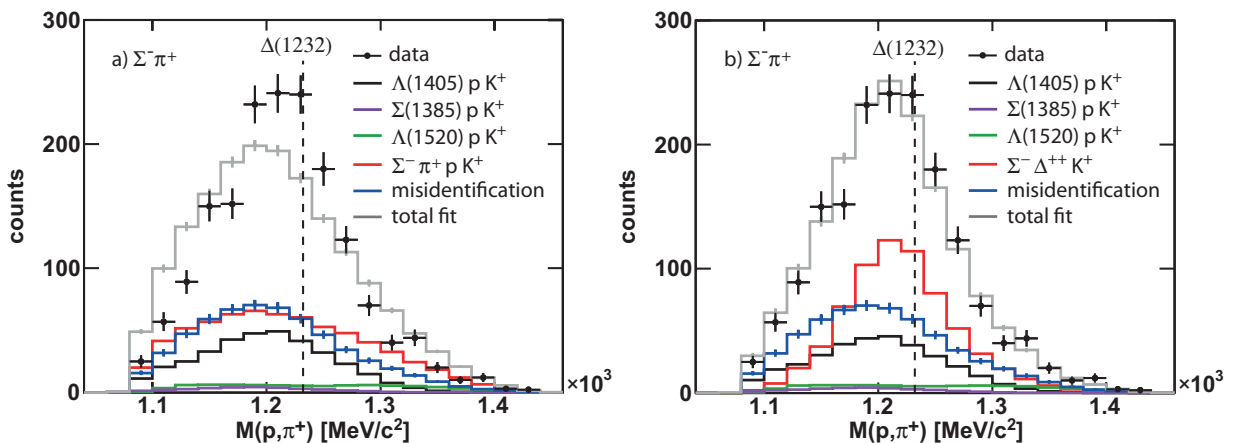


**Figure 4.6:** Invariant mass of proton and  $\pi^+$  for the subsample with an intermediate  $\Sigma^-\pi^+$  state. In a) the experimental data are compared to the simulations where only reaction (4.21) is considered for non-resonant  $\Sigma^-\pi^+$  production. In b) only reaction (4.22) is used instead.

simulation model.

In panel b) the same experimental spectrum as in panel a) is shown. This time, however, both reactions (4.21) and (4.22) were considered in the simulations. The relative contribution of these two channels was a free fit parameter, which was determined via a  $\chi^2$  fit to the experimental data points. The best fit ( $\chi^2/ndf = 1.5$ ) was obtained when only  $\Delta^{++}(1232)$  production is present (see gray histogram in panel b)). From this result it is concluded that indeed all non-resonant  $\Sigma^-\pi^+$  production proceeds via reaction (4.22), and this assumption was used in the analysis.

It is worth to notice that the reactions, considered so far, are indeed the most reasonable ones, but they are actually not the only possible contributions to the spectra in Figure 4.3. In appendix B.2 further observables are studied, where it is, for example, tested if the  $\Sigma$  and the  $K^+$  or the  $\Lambda(1405)$  and the  $K^+$  stem from a common resonance. As no clear indications for those scenarios have been found, it was concluded that the developed model already accounts correctly for the different contributing reactions.

### 4.2.2 Angular distributions in the CMS

The analysis of the  $\Sigma(1385)^+$  hyperon (see chapter 3) has shown that the study of angular distributions plays an essential role. Only if the simulations are able to describe the experimental data in these observables, the simulation model can be assumed to reproduce the kinematics in the data correctly and this finally allows to use the model for acceptance and efficiency corrections. In order to find an appropriate simulation model for the  $\Lambda(1405)$  analysis, the production angle  $\cos(\theta_{CMS}^{\Lambda^*})$  of the  $\Lambda(1405)$  candidate is investigated in Figure 4.7, where panel a) and b) display the results for the  $\Sigma^+\pi^-$  and  $\Sigma^-\pi^+$  data samples, respectively. To calculate this angle, the missing 4-vector to the proton and the  $K^+$  was taken as the 4-vector of the potential  $\Lambda(1405)$  track. Compared to the experimental data is the simulation model, which has been developed in the last sections. In this model the  $\Sigma(1385)^0$  production was simulated following the same angular distribution as extracted for  $\Sigma(1385)^+$  production (see chapter 3). This choice is natural but has indeed only minor influence on the results, as the  $\Sigma(1385)^0$  contributes only very little to the total yield. For all the other reactions no information on angular distributions are available,

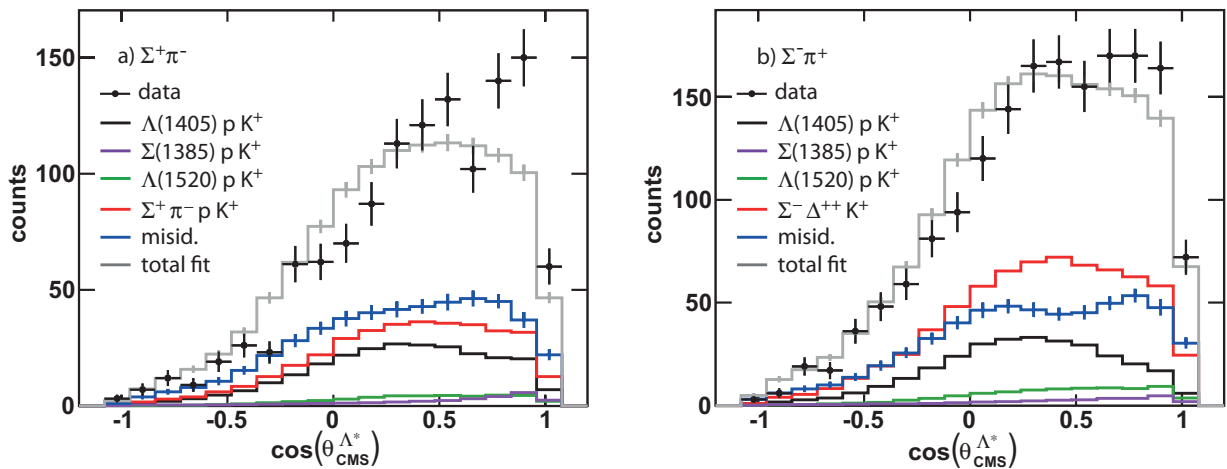


**Figure 4.7:** Angular distribution of the  $\Lambda(1405)$  candidate in the CMS for the  $\Sigma^+\pi^-$  sample (a) and the  $\Sigma^-\pi^+$  sample (b).

and, in a first approach, they were therefore simulated with isotropic production of all particle in the CMS. This most simple assumption does, however, not reproduce the data. In fact, the experimental distributions in both panels show an increased production rate of the  $\Lambda(1405)$  candidate in the forward direction ( $\cos(\theta_{CMS}^{\Lambda^*}) > 0$ ).

To find out which of the contributing reactions is responsible for this behavior, differential cross sections must be determined for all channels. For that purpose, the experimental data were subdivided into three different regions of  $\cos(\theta_{CMS}^{\Lambda^*})$ . In each of these regions the same analysis as for the integrated data sample was applied. This includes the identification of the neutron signal and the fitting of the misidentification background. Afterwards the  $\Sigma^+$  and  $\Sigma^-$  signals were reconstructed, and on the basis of these signals the data were again separated into a  $\Sigma^+\pi^-$  and a  $\Sigma^-\pi^+$  sample. From these samples the two missing mass distributions to proton and  $K^+$  were obtained and were used, together with the  $\Sigma$  spectra, to determine the different yields of all the reactions via the fitting procedure. After subtracting the misidentification background from the  $MM(p, K^+)$  distributions, the experimental data as well as the simulations were corrected for acceptance and efficiency and for the branching ratio of the  $\Sigma^+$  decay into neutron and  $\pi^+$  (BR=48.31%). The corrections were done with the developed simulation model. Cross sections were then obtained by integrating the simulated distributions, which reproduce the experimental data, and normalizing the obtained yields to  $p + p$  elastic data. A detailed explanation on the extraction of the differential cross sections is given in appendix B.1. The whole procedure is conceptually the same as what has been presented for the  $\Sigma(1385)^+$  analysis (see e.g. appendix A.4). Finally, differential cross sections were obtained, which are illustrated in Figure 4.8 a) and b). The pictures show the differential cross sections for  $\Lambda(1405)$  (black data points), for  $\Lambda(1520)$  (green data points) and for the non-resonant  $\Sigma\pi$  channels (4.18) and (4.22) (red data points), respectively. The obtained results need some explanation and interpretation:

- The  $\Lambda(1405)$  and  $\Lambda(1520)$  production cross section appear to be rather isotropic within the errors. This is especially true for  $\Lambda(1405)$ , which indicates that the exchange of a heavy meson (e.g.  $\rho$ ) plays a role in the production process. A more detailed discussion

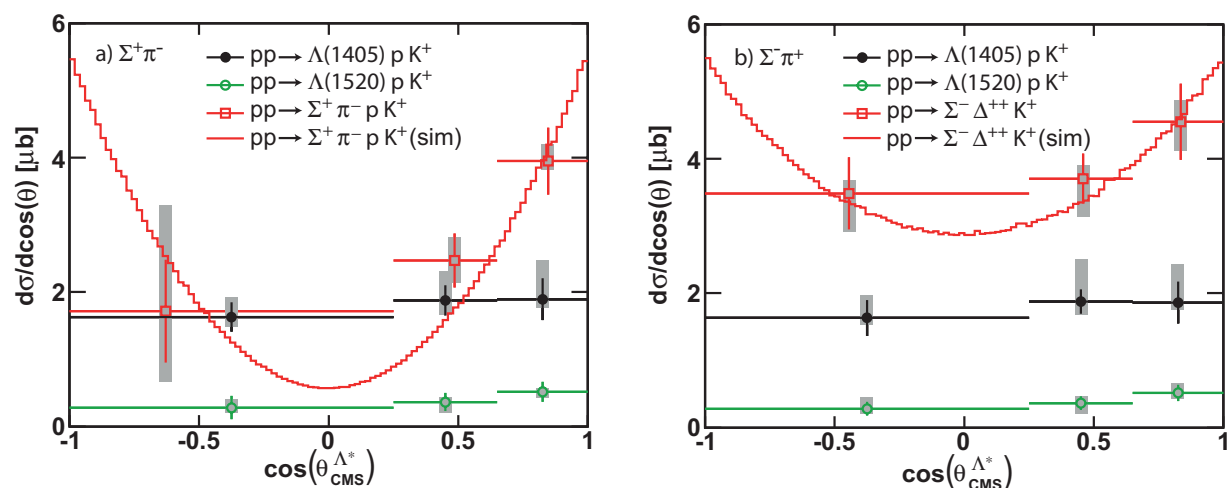


**Figure 4.8:** Differential cross section of  $\Lambda(1405)$ ,  $\Lambda(1520)$  and the non-resonant channels, separated for the two different  $\Sigma\pi$  data samples. Red histograms show the angular distributions in the simulation models of reaction (4.18) and (4.22), respectively. This model was also used for the corrections (see text for details).

about this subject can be found in section 4.3.3. Here, it is only important to notice that the isotropic simulations for  $\Lambda(1405)$  and  $\Lambda(1520)$  production are in agreement with the data, which justifies to use these simulations for the corrections. Furthermore, it has to be mentioned that the cross section points for  $\Lambda(1405)$  and  $\Lambda(1520)$  have the same values in panel a) and b). This has the following reason: In order to extract cross sections, the corrected simulations were integrated instead of the experimental data. This was necessary because of the low statistic in the data. As the branching ratios into  $\Sigma^+\pi^-$  and  $\Sigma^-\pi^+$  were simulated to be the same, also the extracted cross sections must be the same.

- The non-resonant channels show a clear anisotropy, which is the expected behavior if kaon or pion exchange dominates the production. In order to account for this in the simulations, the experimental distributions (red data points) were fitted with even Legendre polynomials of second order. The obtained functions were then used to fold the simulations of reactions (4.18) and (4.22), and these new simulations were again used for the acceptance and efficiency corrections. This procedure was repeated several times until satisfactory agreement between the experimental data and the simulation model was obtained. The red histograms in panel a) and b) show the finally obtained distributions in the simulations. This simulation model was actually already used to obtain the differential cross section points shown in Figure 4.8. The fact that the measured angular distributions are symmetric within the error bars indicates that the used model is appropriate for the corrections. It is interesting to note that the non-resonant  $\Sigma^+\pi^-$  production via reaction  $p + p \rightarrow \Sigma^+ + \pi^- + p + K^+$  in panel a) shows a significantly steeper anisotropy than the non-resonant  $\Sigma^-\pi^+$  production via reaction  $p + p \rightarrow \Sigma^- + \Delta^{++} + K^+$  in panel b). This is in agreement with the trends visible in Figure 4.7, where in panel a) the disagreement with the data is much more prominent than in panel b).
- Both pictures of Figure 4.8 show besides statistical errors also the systematic error bars, indicated by the gray shaded boxes. These errors were determined by changing the cuts of the data analysis simultaneously for experiment and simulations. In fact, the cuts on the  $K^+$  mass, on the neutron peak and on the  $\Sigma^+$  and  $\Sigma^-$  signals were varied by  $\pm 20\%$ . Then the differential cross sections were again determined and the maximum deviation to the values, measured with the original cuts, was taken as one systematic error. Additionally, the anisotropies of the angular distributions, used in the simulation model (red histograms in Figure 4.8), were varied by  $\pm 30\%$ . Also this variation had an influence on the extracted cross section values and therefore gave a second systematic error, which was added linearly to the first one.

In summary, the simulation model could be further tuned by investigating the differential cross sections in Figure 4.8. The new model includes anisotropic production of the non-resonant  $\Sigma\pi$  production channels and isotropic production of  $\Lambda(1405)$  and  $\Lambda(1520)$ . With this model in hand, further angular distributions can be investigated.

### 4.2.3 CMS angles, G-J angles and helicity angles

In order to test if the obtained simulation model describes the kinematics in the experimental data correctly, further angular distributions were investigated. For that purpose, the reaction  $p + p \rightarrow \Lambda(1405) + p + K^+$  with three particles in the final state ( $\Lambda(1405)$ ,  $p$  and  $K^+$ ) was taken as

a working hypothesis. The 4-momentum of the potential  $\Lambda(1405)$  candidate was then again calculated from the missing 4-vector to the proton and the  $K^+$ . As it was pointed out in chapter 3, a three particle production process is normally studied in the CMS, G-J and helicity angular distributions. Following this strategy, the nine angular distributions in the three reference frames were determined separately for the  $\Sigma^+\pi^-$  and the  $\Sigma^-\pi^+$  data samples. The results are presented in the Figures 4.9 and 4.10, respectively. The nomenclature for the sub- and superscripts in the labels is the same as what was used for the  $\Sigma(1385)^+$  analysis. The experimental data are shown inside the HADES acceptance and are compared to the developed simulation model, where the angular distributions for the non-resonant  $\Sigma\pi$  channels are included.

The first row displays the angles of the three particles in the CMS. The angular distributions of the  $\Lambda(1405)$  candidates (panels a)) are now described much better by the simulations, which indicates that the extracted folding functions are appropriate. But also the distributions for the protons (panels b)) and for the kaons (panels c)) are reproduced convincingly.

The G-J angles are shown in the second row of Figure 4.9 and 4.10. Here, only the first two pictures (panels d) and e)) are sensitive to the included anisotropies in the non-resonant simulations. For all three G-J angles an almost perfect agreement is obtained, which indicates that the assumed model works correctly.

Finally, the helicity angles are investigated in the third row of both pictures. These observables are completely independent from the measured angular distributions in the CMS (see discussion in chapter 3). For the  $\Sigma^+\pi^-$  sample the simulation model gives nevertheless a very good description of the data. In the  $\Sigma^-\pi^+$  sample one can see some deviations in panel h). The reason for that is not clear, but interference effects between the different simulated channels might, for example, cause such effects. Despite this difference, the agreement with the data is still satisfactory.

At this point, it has to be mentioned that the developed simulation model is certainly a rather simple approach. Compared to the model, developed for the  $\Sigma(1385)^+$  analysis, here only one observable has been studied to extract angular distributions for the simulations. The reason for that is obviously the limited statistic. By dividing the data into only three samples, as it was done in order to obtain the differential cross sections in Figure 4.8, the statistic in each of the angular bins is already very low (see also appendix B.1). It is therefore not possible to get more than these three data points, which, however, would be necessary in order to develop a more precise model. A consequence of this is that also the folding functions for the simulations are rough estimations, and they do certainly not describe the angular distributions in the data precisely. On the other hand, the goal here was not to deliver precise angular distributions, as it was done in the analysis of the  $\Sigma(1385)^+$ . The statistic in this analysis was just sufficient to find out that the  $\Lambda(1405)$  and the  $\Lambda(1520)$  are produced rather isotropically, whereas the non-resonant channels are not. By taking into account the folding functions for these non-resonant channels, it is then possible to describe all the studied angular distributions in Figure 4.9 and 4.10 in a satisfactory way. Furthermore, even more distributions have been investigated in appendix B.3, and also there the agreement with the data is very good. With this result one can therefore argue that the model seems to reproduce correctly the experimental kinematics, and is hence usable for the correction procedure. This is an important point, as the properties of the  $\Lambda(1405)$  can only be investigated if its spectral shape is acceptance and efficiency corrected. The finally obtained results on this topic are discussed in the next section.

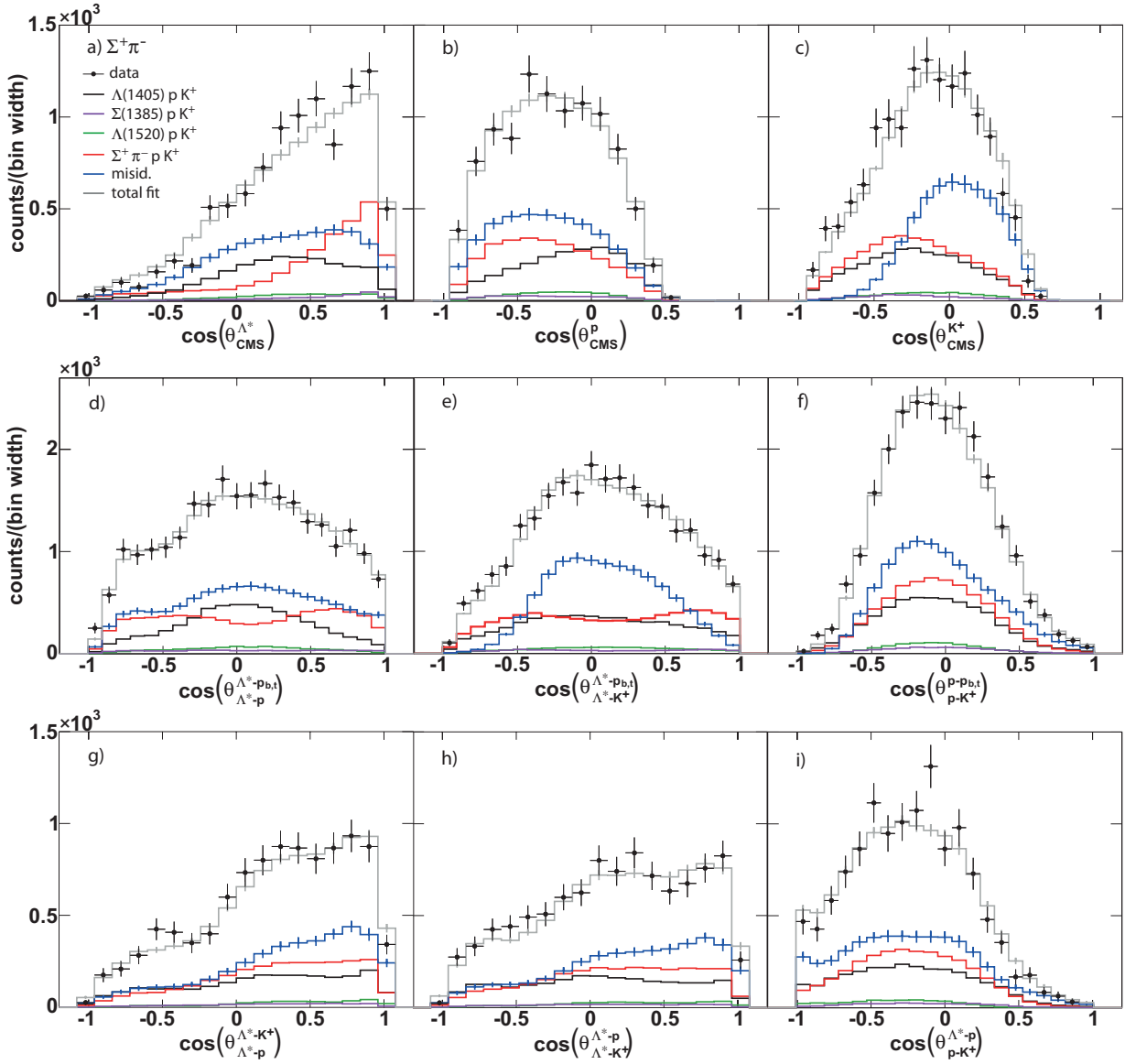


**Figure 4.9:** Angular distributions for the  $\Sigma^+\pi^-$  data sample within the HADES acceptance. The first row shows the production angles of the  $\Lambda(1405)$  candidate, the proton and the  $K^+$  in the CMS. The second row displays the three possible G-J angles. In the third row the three helicity angles are plotted.

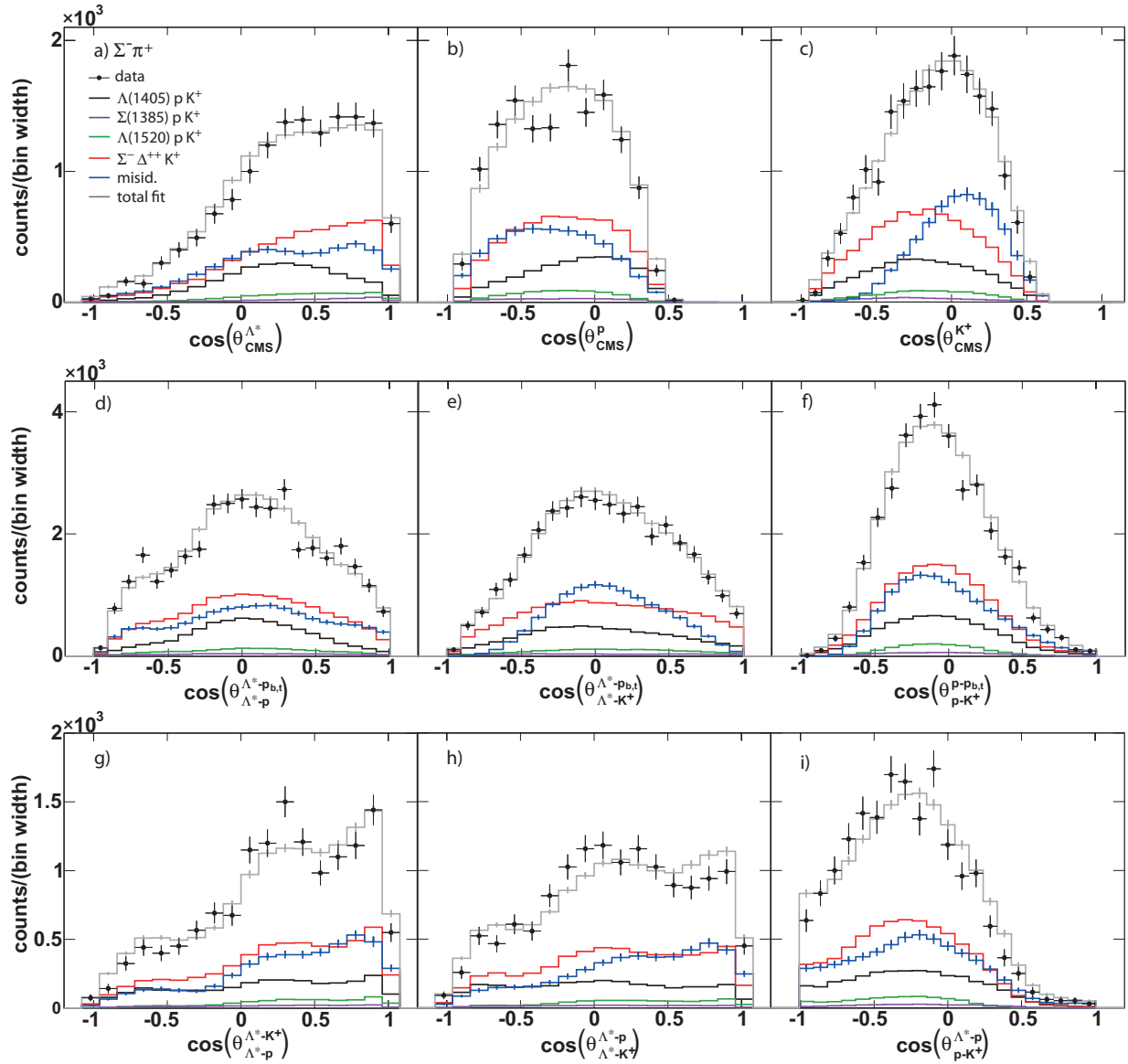


**Figure 4.10:** Angular distributions for the  $\Sigma^- \pi^+$  data sample within the HADES acceptance. The first row shows the production angles of the  $\Lambda(1405)$  candidate, the proton and the  $K^+$  in the CMS. The second row displays the three possible G-J angles. In the third row the three helicity angles are plotted.

## 4.3 Results and discussion

### 4.3.1 Corrected mass spectra

With the developed simulation model, which reproduces the data in all considered observables, the missing mass spectra of Figure 4.3, showing the  $\Lambda(1405)$  signal, could be corrected for acceptance and efficiency. For that purpose, the misidentification background (blue histograms in Figure 4.3) was first subtracted from the data in both pictures so that only the physical contributions remained. For the corrections of the remaining data, the sum of all the simulated reactions was used, and the relative contribution of each reaction was taken from the fit to the data (see section 4.1.1). The corrections were then applied to the experimental data as well as to the simulations. In this step, the spectra for the  $\Sigma^+\pi^-$  data sample were also corrected for the branching ratio of the  $\Sigma^+$  decay ( $\Sigma^+ \rightarrow n + \pi^+$ ,  $BR = 48.31\%$ ). Furthermore, in order to extract cross sections, the data were normalized to  $p + p$  elastic data. The procedure of the corrections was in general the same as what is presented in appendix B.1.

The finally obtained missing mass distributions are displayed in Figure 4.11. Panel a) represents the  $\Sigma^+\pi^-$  sample and panel b) the  $\Sigma^-\pi^+$  sample. As the data have been kinematically refitted, the missing mass distributions to proton and  $K^+$  correspond exactly to the invariant mass distributions of  $\Sigma^+\pi^-$  pairs and  $\Sigma^-\pi^+$  pairs, respectively. Compared to the data are again the different simulated reactions with their sum in the gray histograms, giving an excellent description of the data.

Additionally included in the pictures are the systematic uncertainties. They were extracted in the same way as it was done for Figure 4.8. This means that the data selection cuts were varied by  $\pm 20\%$ , and the anisotropies of the angular distributions in the non-resonant simulations were additionally varied by  $\pm 30\%$ . In this way the gray shaded boxes were obtained, representing the systematic errors on the experimental data. As the applied variations do also influence the extracted relative yields of the different simulated reactions, also the simulations have a certain systematic error, indicated in the shaded colored bands.

The  $\Sigma(1385)^0$ , whose absolute cross section of  $\approx 6 \mu b$  was an external constraint in the analysis, plays a special role. Accounting for the branching ratio of  $BR = 5.85\%$  for the decay  $\Sigma(1385)^0 \rightarrow \Sigma^\pm \pi^\mp$ , the violet histograms contribute to the shown spectra in a) and b) only with  $0.0585 \cdot 6 \mu b = 0.35 \mu b$ . The violet error bands indicate the error on the  $\Sigma(1385)^0$  cross section. In Figure 4.11 c) the sum of the  $\Sigma^+\pi^-$  and  $\Sigma^-\pi^+$  distributions of panel a) and b) is shown. This observable is especially interesting as possible interference terms between isospin 0 and isospin 1 amplitudes should cancel out here (see equations (1.7)-(1.9)) so that only the absolute contributions of the isospin 0 and isospin 1 reactions are visible. However, as the two distributions of the  $\Sigma^+\pi^-$  and the  $\Sigma^-\pi^+$  decay channels (panel a) and b)) are well described by the same  $\Lambda(1405)$  spectral shape, it can anyway be concluded that no large interference effects between  $I = 0$  and  $I = 1$  amplitudes are present in the data. This is completely different in  $\gamma$ -induced reactions measured by the CLAS collaboration (see Figure 1.10).

The spectrum in c) is further characterized by a larger statistic, which allows to unambiguously identify the different structures in the distribution. Indeed, it is interesting to see that a clear  $\Lambda(1520)$  signal is obtained, which is less evident in the single decay spectra of a) and b).

Indicated in the vertical dashed line is the nominal mass of  $\Lambda(1405)$ . It becomes clear that the observed peak in the experimental data is located significantly below this value, and it is therefore well described by the simulated  $\Lambda(1405)$  with a Breit-Wigner mass of  $1385 \text{ MeV}/c^2$  (see black histogram). In fact, the analysis was also performed assuming a Breit-Wigner mass of

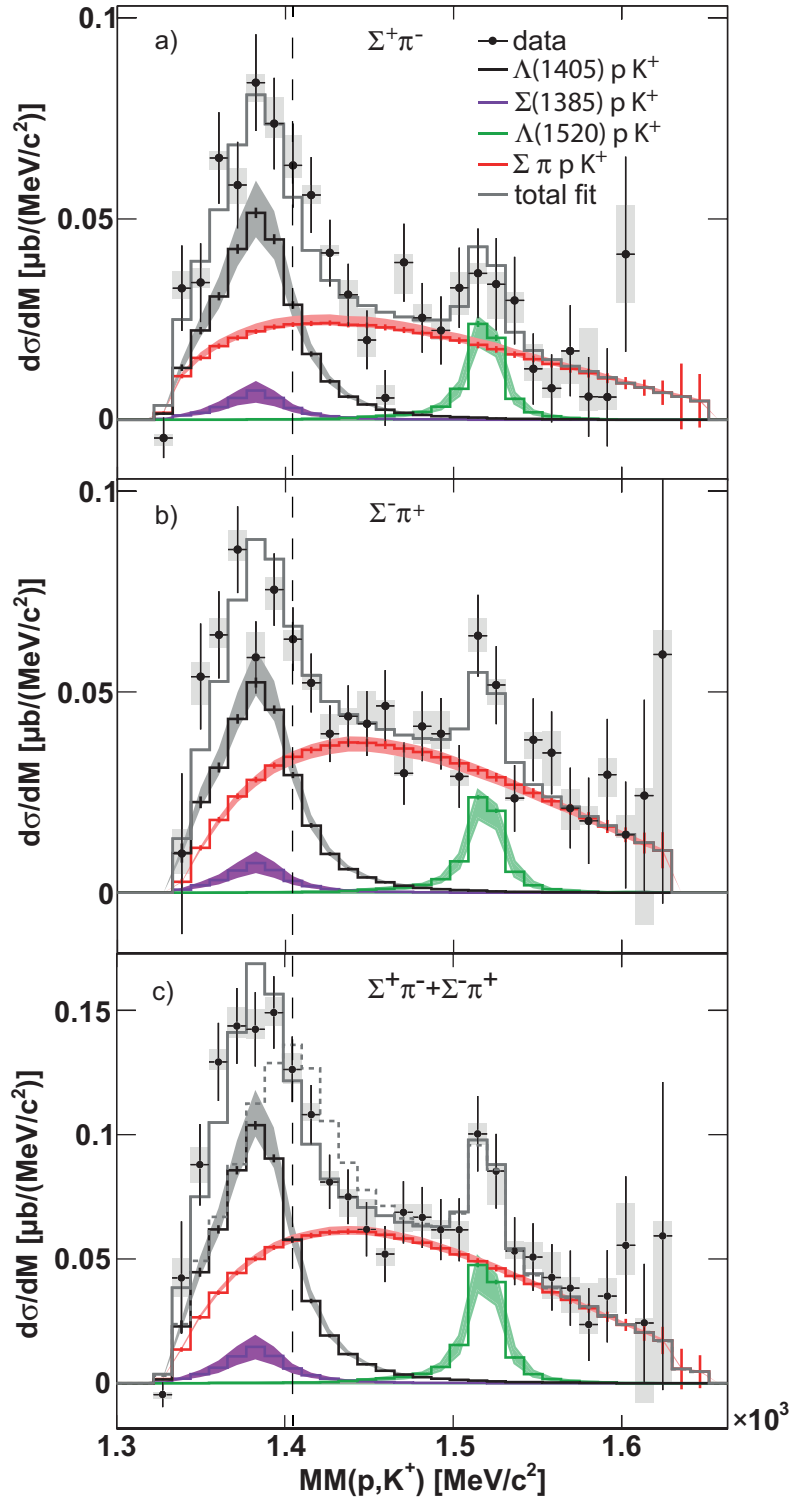


**Figure 4.11:** Missing mass distributions to proton and  $K^+$  for events attributed to the  $\Sigma^+\pi^-$  data sample (a) and the  $\Sigma^-\pi^+$  data sample (b). c): Sum of both spectra from panels a) and b). The gray dashed histogram shows the sum of all simulated channels if  $\Lambda(1405)$  is simulated with its nominal mass of  $1405 \text{ MeV}/c^2$ . Colored histograms in the three panels indicate the contributions of the reactions (4.15)-(4.17) and (4.18) or (4.22), obtained from simulations. Data and simulations are acceptance and efficiency corrected. The gray boxes indicate systematic errors. The vertical dashed line shows the nominal  $\Lambda(1405)$  mass of  $1405 \text{ MeV}/c^2$ .

1405 MeV/c<sup>2</sup> in the  $\Lambda(1405)$  simulations. The obtained distribution is shown in the gray dashed histogram in panel c). It fails to describe the experimental data. This is expressed quantitatively in a normalized  $\chi^2$  value of  $\chi^2/ndf = 2.1$  compared to  $\chi^2/ndf = 0.6$  for the solid gray histogram. From these results it is finally concluded that the reconstructed  $\Lambda(1405)$  indeed shows its mass peak clearly below 1405 MeV/c<sup>2</sup>. Different possible interpretations of this observation are discussed in section 4.3.3.

### 4.3.2 Cross sections

As the data have been acceptance and efficiency corrected and normalized to  $p + p$  elastic data, total production cross sections can be obtained for all the reactions, contributing to Figure 4.11. Therefore, the simulated distributions in panel a) and b) were integrated and eventually corrected for the branching ratio of the decay into  $\Sigma\pi$  states. The results are given in Table 4.1. The first error indicates the statistical error of the experimental data, the second one is the systematic error induced by the normalization to  $p + p$  elastic cross sections, and the third error is obtained from the systematic variation of the cuts and of the angular distributions. Another possibility to extract the cross sections would be to integrate the differential cross sections of Figure 4.8. The obtained values are, however, very close to the values in Table 4.1. The small deviations were included in the systematic errors.

<i>Reaction:</i>	<i>Cross section</i>
$p + p \rightarrow \Lambda(1405) + p + K^+$	$9.2 \pm 0.9 \pm 0.7^{+3.3}_{-1.0} \mu b$
$p + p \rightarrow \Sigma(1385)^0 + p + K^+$	$5.56 \pm 0.48^{+1.94}_{-1.06} \mu b$ (obtained from [Epp12b])
$p + p \rightarrow \Lambda(1520) + p + K^+$	$5.6 \pm 1.1 \pm 0.4^{+1.1}_{-1.6} \mu b$
$p + p \rightarrow \Sigma^+ + \pi^- + p + K^+$	$5.4 \pm 0.5 \pm 0.4^{+1.0}_{-2.1} \mu b$
$p + p \rightarrow \Sigma^- + \Delta^{++}(1232) + K^+$	$7.7 \pm 0.9 \pm 0.5^{+0.3}_{-0.9} \mu b$

**Table 4.1:** Extracted cross sections for the different reactions contributing to the final data sets.

It is instructive to compare the obtained values to measurements of other experiments. In Figure 4.12 the  $\Lambda(1405)$  cross section extracted in this work (red star) and extracted by the ANKE experiment (open black star) is plotted as a function of the excess energy  $\varepsilon$ . The ANKE collaboration also measured  $\Lambda(1405)$  production in  $p + p$  collisions, but they analyzed the neutral decay into  $\Sigma^0\pi^0$  [Z<sup>+</sup>08]. Included in the picture is a compilation of cross sections for the production of the ground state  $\Lambda(1116)$  hyperon ( $p + p \rightarrow \Lambda + p + K^+$ ), taken from [AB<sup>+</sup>10]. These  $\Lambda(1116)$  data points are fitted with a phase space function (black solid line), giving an excellent description of the results [FW97]:

$$\sigma(\varepsilon) = C \cdot \frac{\varepsilon^2}{\left(1 + \sqrt{1 + \frac{\varepsilon}{\alpha}}\right)^2} \quad (4.26)$$

In this parameterization  $\alpha$  accounts for the  $\Lambda - p$  final state interaction. The same function, scaled by a factor  $\frac{1}{3}$ , is shown in the black dashed line. It fits very well through the two available  $\Lambda(1405)$  data points. This is an interesting result as it suggests that  $\Lambda(1116)$  and  $\Lambda(1405)$  production seems to follow the same phase space trend. However, this cannot be seen as an indication for similar

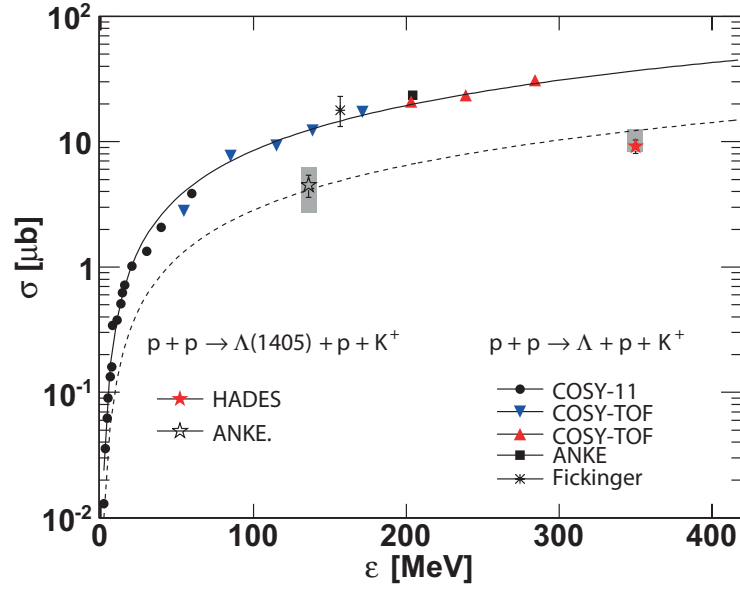


**Figure 4.12:** Cross section of  $p + p \rightarrow \Lambda + p + K^+$  and of  $p + p \rightarrow \Lambda(1405) + p + K^+$  as a function of the excess energy  $\varepsilon$ . The data points are extracted from [AB<sup>+</sup>10] and [Z<sup>+</sup>08]. The solid and dashed lines are fits with a phase space parameterizations (equation (4.26)).

production mechanisms of those two particles. In fact, the  $\Lambda(1405)$  is interpreted as an exotic, molecular like state, whereas  $\Lambda(1116)$  is a usual 3-quark baryon. Their production mechanisms might therefore be completely different.

Turning now to the case of the reaction  $p + p \rightarrow \Sigma(1385)^0 + p + K^+$ , its cross section is displayed as a function of the excess energy in Figure 4.13. Measurements are available from the ANKE collaboration [Z<sup>+</sup>08] (open black star) and at higher energies from Klein et al. [K<sup>+</sup>70] (open blue star). The result of this work is located at intermediate energies of  $\varepsilon \approx 360$  MeV (red star). For the production of the ground state  $\Sigma^0$  a compilation of different experiments is presented as well [AB<sup>+</sup>10, B<sup>+</sup>10, BFM<sup>+</sup>88]. The  $\Sigma^0$  data points are fitted with a phase space function without final state interaction [SC98]:

$$\sigma(\varepsilon) = a \cdot \left(1 - \frac{s_0}{s}\right)^b \cdot \left(\frac{s_0}{s}\right)^c \quad (4.27)$$

where  $a$ ,  $b$  and  $c$  are the free fit parameters. The parameters  $s_0$  and  $s$  are the squared values of the threshold energy of the reaction and the total available energy in the center-of-mass system, respectively ( $\sqrt{s} = \sqrt{s_0} + \varepsilon$ ). The result of the fit is shown in the solid black line.

The cross sections for both,  $\Sigma(1385)^0$  and  $\Sigma^0$  production, seem to saturate for higher energies. This is very similar to the observations made for the  $\Sigma^+$  and  $\Sigma(1385)^+$  cross sections in Figure 3.29. In fact, it is interesting to compare the characteristics of neutral and charged  $\Sigma$  hyperon production. It seems to be surprising that the measured cross section for  $\Sigma(1385)^0$  at  $\varepsilon \approx 360$  MeV is only about  $6 \mu b$ , while at the same excess energy the cross section of  $\Sigma(1385)^+$  production is more than 3.5 times higher ( $\sigma_{\Sigma(1385)^+} \approx 22 \mu b$ ). However, comparing the two Figures 4.13 and 3.29, one can find that the same is true for the ground state  $\Sigma$  hyperons. The  $\Sigma^+$  cross section at  $\varepsilon \approx 360$  MeV is  $\sigma_{\Sigma^+} \approx 50 \mu b$ . In order to get the  $\Sigma^0$  cross section, the phase space fit function in Figure 4.13 is evaluated at this excess energy and delivers  $\sigma_{\Sigma^0} \approx 12 \mu b$ . The

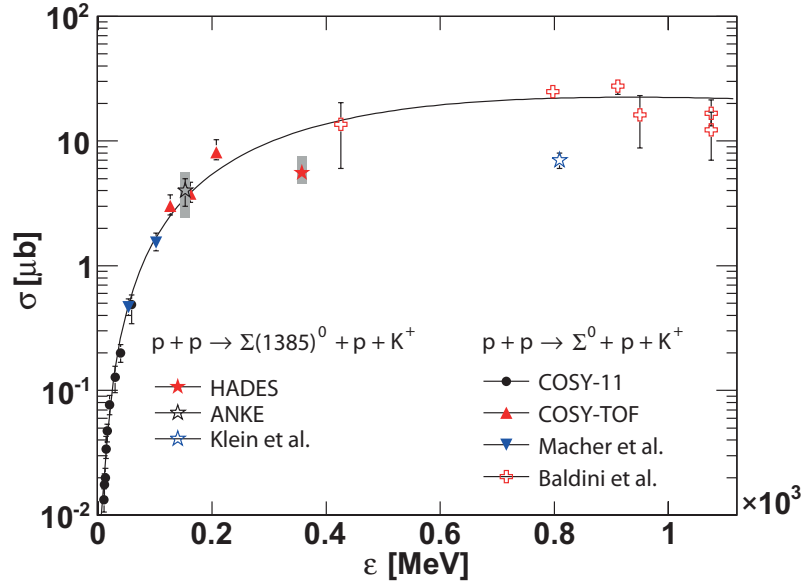


**Figure 4.13:** Cross section of  $p + p \rightarrow \Sigma^0 + p + K^+$  and of  $p + p \rightarrow \Sigma(1385)^0 + p + K^+$  as a function of the excess energy  $\varepsilon$ . The data points are a compilation from different experiments (see text for details). The solid line is a phase space fit (equation (4.27)) to the cross section points for the production of the ground state  $\Sigma^0$  hyperon.

difference between the two values is again a factor of about 3.5.

At higher energies ( $\varepsilon \approx 800$  MeV), the measurements of Klein et al. show a similar hierarchy with  $\sigma_{\Sigma(1385)^+} = 15 \mu b$  and  $\sigma_{\Sigma(1385)^0} = 7 \mu b$ .

The obtained result on the  $\Sigma(1385)^+$  cross section, being significantly larger than the  $\Sigma(1385)^0$  cross section, is thus not surprising and fits well into the general trend observed for ground state and excited  $\Sigma$  hyperon production.

In Figure 4.14 a) and b) the cross section trend of non-resonant  $\Sigma^+\pi^-$  and  $\Sigma^-\pi^+$  production is investigated. Here, only very few data points are available in the literature [BFM<sup>+</sup>88]. The values quoted there refer either to the reaction  $p+p \rightarrow \Sigma^+\pi^-+p+K^+$  or  $p+p \rightarrow \Sigma^-\pi^++p+K^+$ , and no more specification is given. It was shown, however, that the second reaction mainly proceeds via the production of an intermediate  $\Delta^{++}(1232)$ . Furthermore, it is not clear if the quoted values only stand for the pure non-resonant  $\Sigma\pi$  reaction cross sections, or if they include also the contributions from resonance decay like  $\Lambda(1405)/\Sigma(1385)^0/\Lambda(1520) \rightarrow \Sigma^\pm\pi^\mp$ . Therefore, the Figures 4.14 a) and b) show always two points for the measured HADES cross sections. The solid red star stands for the pure non-resonant cross sections of reaction (4.18) and (4.22), respectively. The open red stars correspond to the case where the 33% from the  $\Lambda(1405)$  cross section, the 5.85% from the  $\Sigma(1385)^0$  cross section and the 14% from the  $\Lambda(1520)$  cross section are additionally added. The propagation of the statistical and systematic errors has been done appropriately.

In both pictures of Figure 4.14, fits with the phase space function (4.27) are included (see solid lines). In this case only the black data points were fitted, so that the prediction of the fit function can be compared with this measurement. Indeed, the upper HADES points lie perfectly on those predictions. From these observations it is concluded that the results of this work are consistent with the ones of the other experiments, which makes one confident that the correction procedure and the interpretation of the spectra in Figure 4.11 is reasonable.

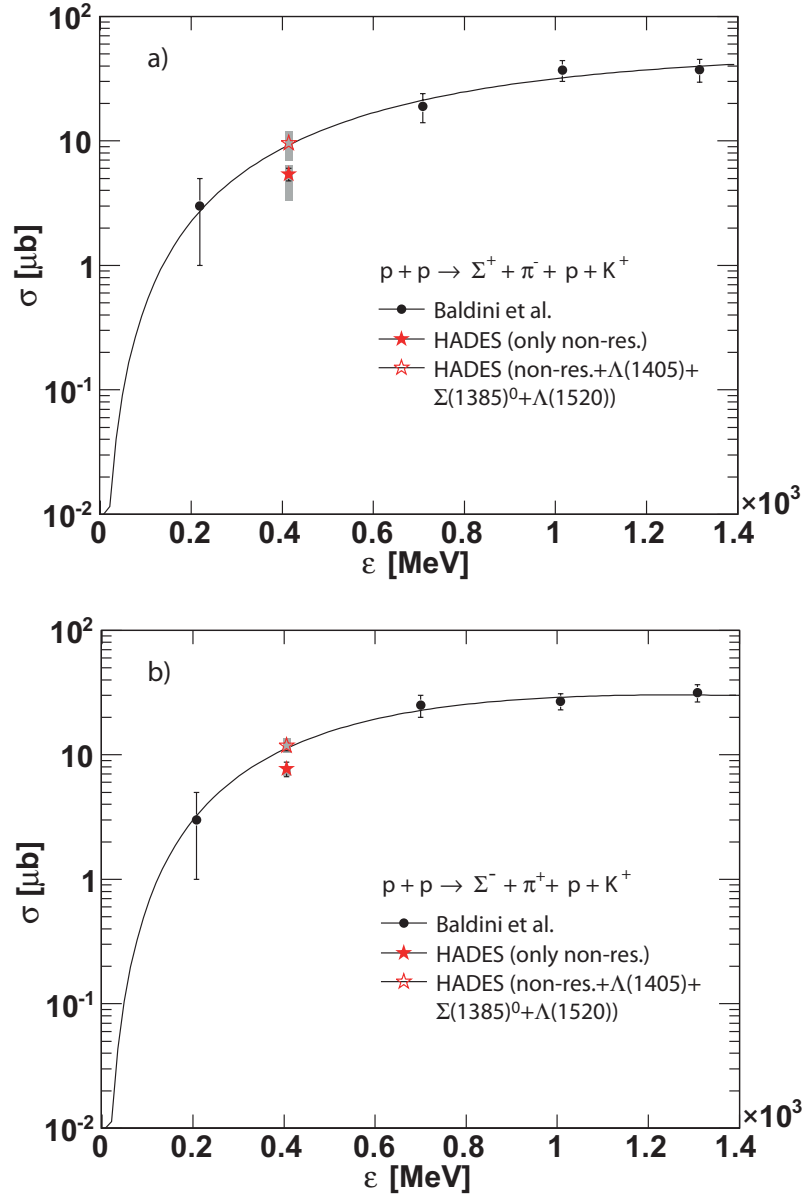


**Figure 4.14:** Cross section of the reaction  $p + p \rightarrow \Sigma^+ + \pi^- + p + K^+$  (a) and  $p + p \rightarrow \Sigma^- + \pi^+ + p + K^+$  (b) as a function of the excess energy  $\varepsilon$ . Data points are taken from [BFM<sup>+</sup>88]. The two HADES data points in each panel show the pure non-resonant cross sections and the case where the contribution from resonance decay is included (see text for details). The solid lines are phase space fits (equation (4.27)) to the black data points only.

Coming finally to the extracted cross section of  $\Lambda(1520)$  production. At the moment this work provides the first measurement of the reaction  $p + p \rightarrow \Lambda(1520) + p + K^+$  so that a comparison to other experiments is not possible. The extracted value of  $\sigma \approx 5.6 \mu b$  is, however, a reasonable result as it is only slightly below the  $\Lambda(1405)$  cross section. This is what one would expect from the lower available phase space for  $\Lambda(1520)$  production.

Summarizing the results of the extracted cross sections, it can be concluded that a very consistent picture is obtained, where all the measured values fit well into the general trend of other experiments. The new HADES measurements probe here an energy range that is rather unexplored so far. Especially the data base on the production of hyperon resonances like  $\Lambda(1405)$ ,  $\Sigma(1385)^0$  and  $\Lambda(1520)$  is really scarce for  $p + p$  reactions. Furthermore, the present work reports for the first time on the observation that  $\Delta^{++}(1232)$  is produced together with  $\Sigma^-$  and  $K^+$ .

These results may have an important impact on transport models. Indeed, the parameterization of particle production in those models relies very much on experimentally determined cross sections [TST99]. The values extracted in this work can therefore be used to improve transport codes for the energy range of SIS18.

### 4.3.3 Interpretation

The most striking result of the presented analysis is certainly the extracted  $\Lambda(1405)$  line shape of Figure 4.11. Particularly the observation that the mass peak appears below  $1400 \text{ MeV}/c^2$  is interesting and not easy to interpret. In the following different possible explanations of this result are addressed, and each of them is discussed critically.

#### 4.3.3.1 $\Lambda(1405)$ or $\Sigma(1385)^0$ ?

In order to achieve a good description of the missing mass spectra in Figure 4.11, the  $\Lambda(1405)$  was simulated as a usual Breit-Wigner with a mass of  $1385 \text{ MeV}/c^2$  and a width of  $50 \text{ MeV}/c^2$  [B<sup>+</sup>12]. Now the question could arise if the observed mass peak really corresponds to  $\Lambda(1405)$  or if everything, which is observed, is just the  $\Sigma(1385)^0$  signal. Indeed, one can give up the constraint of the neutral channel analysis, where the  $\Sigma(1385)^0$  cross section has been determined to  $\approx 6 \mu b$ . The experimental data could then again be fitted in the way it was described in section 4.1.1. But this time the relative  $\Sigma(1385)^0$  contribution was an additional free fit parameter and the  $\Lambda(1405)$  was generated with its PDG values for the mass and the width. The fit result is illustrated in Figure 4.15. The picture shows the corrected mass distribution for the sum of both  $\Sigma\pi$  channels and corresponds therefore to what has been obtained in Figure 4.11 c). Only the systematic errors have not been included this time. One can see that also the new fit (gray histogram) gives a very good description of the experimental data, expressed by a normalized  $\chi^2$  value of  $\approx 1.0$ . The  $\Sigma(1385)^0$  contribution is now dominant, and the  $\Lambda(1405)$  signal, peaking at  $1405 \text{ MeV}/c^2$ , is suppressed. However, the  $\Sigma(1385)^0$  has a width of  $\approx 35 \text{ MeV}/c^2$  so that the relatively broad experimental peak distribution is not matched as well as in Figure 4.11 c). As a consequence, the simulation slightly overshoot the experimental data in the peak region.

One can now extract new cross sections for  $\Lambda(1405)$  and  $\Sigma(1385)^0$  by integrating the simulated distributions. In this way a  $\Lambda(1405)$  cross section of  $\sigma_{\Lambda(1405)} \approx 3 \mu b$  is obtained, which is a factor three smaller than the previous result. This is not problematic as it is anyway not clear which cross section one would expect.

On the other hand, the total  $\Sigma(1385)^0$  cross section is now determined to  $\sigma_{\Sigma(1385)^0} \approx 50 \mu b$ . This

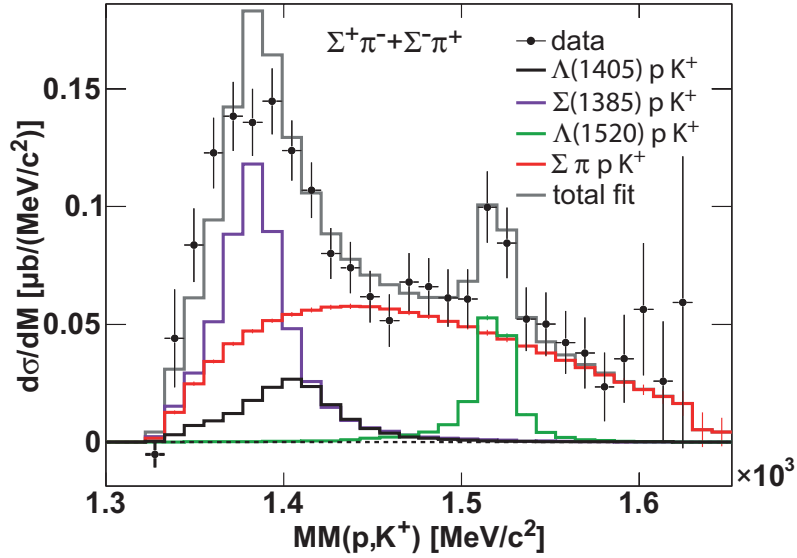


**Figure 4.15:** Corrected missing mass distribution to proton and  $K^+$  for the sum of both  $\Sigma\pi$  channels. The  $\Sigma(1385)^0$  contribution was not constrained in the fitting procedure and the  $\Lambda(1405)$  was generated with its nominal PDG values. See text for details.

value is almost a factor 10 larger than what has been extracted in the neutral channel analysis. Furthermore, this cross section would exceed the  $\Sigma(1385)^+$  cross section by a factor of two. This is in clear disagreement with the observed general trend of  $\Sigma^0 + p + K^+$  production being less probable than the production of  $\Sigma^+ + n + K^+$  (see discussion in section 4.3.2). The result would finally also disagree with the observations made at higher energies ( $\sqrt{s} \approx 3.63$  GeV), where the  $\Sigma(1385)^0 + p + K^+$  cross section was found to be only half of the  $\Sigma(1385)^+ + n + K^+$  cross section [K<sup>+</sup>70].

Following this line of reasoning, it is concluded that the observed mass peak indeed corresponds to the  $\Lambda(1405)$  signal. A scenario, where the signal is attributed to  $\Sigma(1385)^0$ , turns out to be very unlikely.

#### 4.3.3.2 Comparison to other experiments

Before possible interpretations of the observed low mass  $\Lambda(1405)$  signal are discussed, it is instructive to get an overview of the presently available  $\Lambda(1405)$  measurements and to compare them to the results of this work. Such a study is interesting in terms of the two pole structure of  $\Lambda(1405)$ . As pointed out in the introduction, the  $\Lambda(1405)$  is usually assumed to be a coherent sum of two amplitudes, a  $\bar{K}N$  quasi-bound state and a  $\Sigma\pi$  resonance state. The contributions of these two states depends on the initial reaction so that different experiments might see different masses and spectral shapes of  $\Lambda(1405)$ . Figure 4.16 shows a compilation of results from different experiments. As a reference, the vertical red lines are included, which indicate the nominal  $\Lambda(1405)$  mass position.

- In panel a) the summed spectrum of the  $\Sigma^+\pi^-$  and  $\Sigma^-\pi^+$  decay channels, obtained in this work, is again presented. As already mentioned, the observed mass peak is clearly located below 1405 MeV/ $c^2$ .

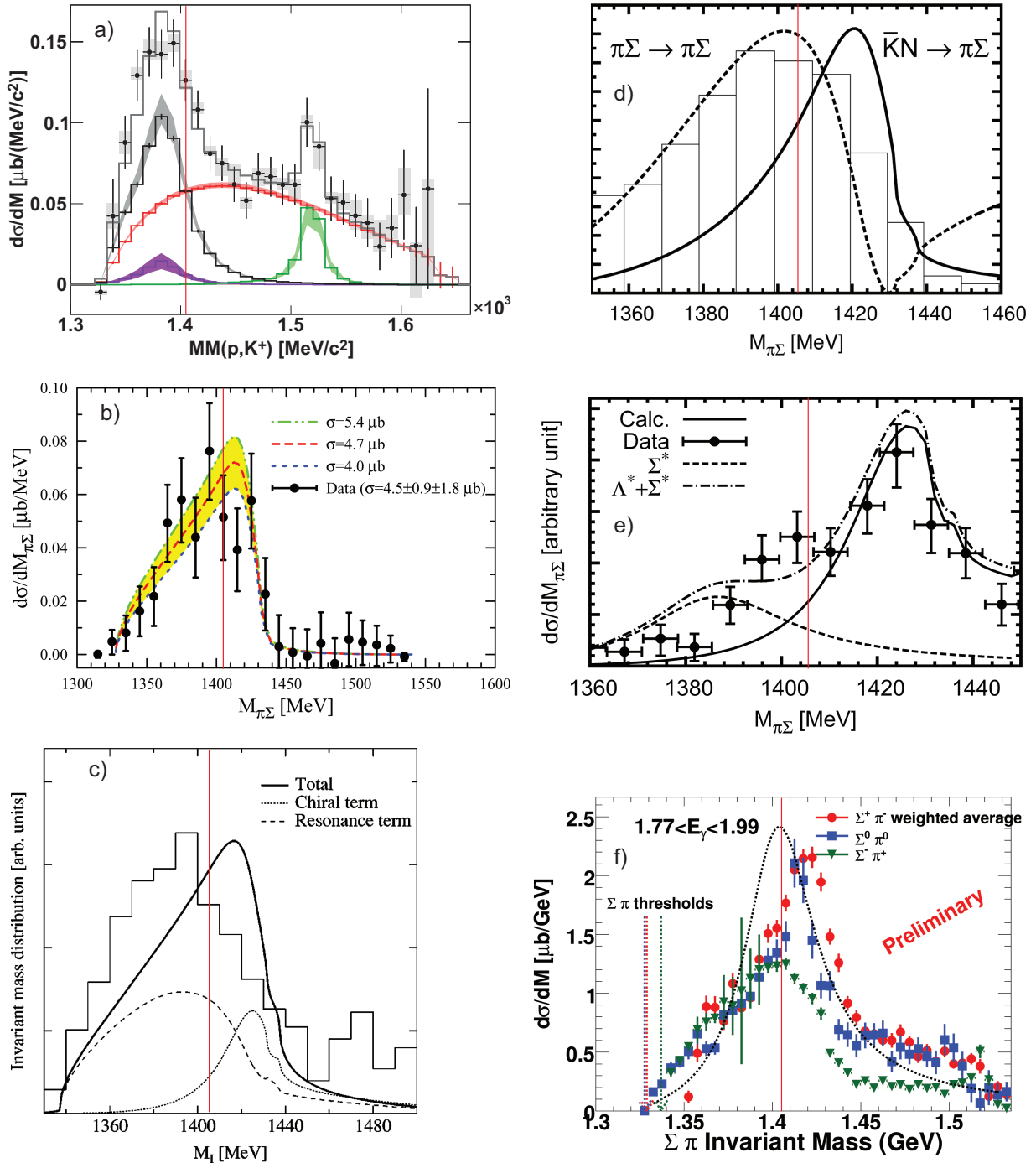


**Figure 4.16:**  $\Lambda(1405)$  spectra measured in different experiments. As a reference, the vertical red lines indicate a mass value of  $1405 \text{ MeV}/c^2$ .

- Panel b) shows the  $\Lambda(1405)$  line shape extracted by the ANKE collaboration [Z<sup>+</sup>08]. In this work  $p + p$  reactions at a beam momentum of 3.65 GeV/c were investigated and the  $\Lambda(1405)$  was reconstructed from its decay into  $\Sigma^0\pi^0$ . Since the statistic is rather low, the position of the mass peak is not very clear in this picture. Nevertheless, the spectrum seems to be not much shifted to low mass values so that this result indeed differs from the HADES measurement in panel a). On the other hand, one has to stress out that the ANKE data are not corrected for any effects of efficiency and acceptance, and it is not clear how much this could influence the observed distribution. The yellow band in panel b) is the result of a recently performed calculation on  $\Lambda(1405)$  production in  $p + p$  reactions [GO07]. The authors of this work used the unitarized coupled channel ansatz, based on the chiral Lagrangian. They considered kaon, pion and rho meson exchange mechanisms in their approach. The resulting spectral shape of the  $\Lambda(1405)$  has contributions from all three mechanisms, whereby each of the exchange processes leads to a different coupling to the two  $\Lambda(1405)$  poles. The obtained agreement between this calculation and the experimental data is rather good. It is, however, obvious that the developed model would not be sufficient to describe the  $\Lambda(1405)$  signal of HADES, as the determined mass peak is located above 1400 MeV/c<sup>2</sup>.
- Turning now to the case of pion-induced reactions. Figure 4.16 c) displays the measured  $\Lambda(1405)$  distributions, reported in [TEFK73]. In this experiment a  $\pi^-$  beam with a momentum of 1.69 GeV/c was impinging on a liquid hydrogen target and the  $\Lambda(1405)$  was reconstructed in the  $\Sigma^+\pi^-$  and  $\Sigma^-\pi^+$  final state. The shown spectrum represents the sum of the two decay channels. It is interesting to see that the  $\Lambda(1405)$  appears clearly below 1405 MeV/c<sup>2</sup> also in this measurement. An interpretation of this result, based again on the unitarized coupled channel approach, is given in [HHO<sup>+</sup>03]. It is concluded there that the observed  $\Lambda(1405)$  peak is partially generated through an intermediate  $N^*$  resonance with a dominant coupling to the second  $\Lambda(1405)$  pole, located at around 1390 MeV/c<sup>2</sup> (see section 1.4). This contribution leads to a broad and low mass  $\Lambda(1405)$  signal, indicated in the dashed line. The theoretical prediction further includes a considerable fraction of a “chiral” term (dotted line), which stems from the  $T_{\bar{K}N-\Sigma\pi}$  scattering amplitude with dominant coupling to the high energy  $\Lambda(1405)$  pole. This contribution results in a narrow signal, which interferes with the first term and generates the solid black  $\Lambda(1405)$  signal. The obtained theoretical model cannot describe the experimental data convincingly, and it is questionable if the spectrum in panel c) is really understood from the theoretical side. Moreover, it seems that a pure contribution of the resonance term (dashed line) would give the best description of the data, but this is not favored by theory.
- The  $\Lambda(1405)$  signal was also extracted in  $K^-$ -induced reactions. In panel d) the  $\Sigma^+\pi^-$  invariant mass distribution, measured in  $K^- + p$  reactions at  $p_{K^-} = 4.2$  GeV/c [Hem85], is presented. This spectrum peaks at around 1400 MeV/c<sup>2</sup> and can be well described by the scattering amplitude  $T_{\Sigma\pi\rightarrow\Sigma\pi}$  (dashed line) [J<sup>+</sup>10]. As the  $\Sigma\pi \rightarrow \Sigma\pi$  amplitude couples to both poles of the  $\Lambda(1405)$  (with dominant weight to the low energy pole), the resulting mass spectrum is the coherent sum of the amplitudes from the low energy pole at  $\approx 1390$  MeV and from the high energy pole at  $\approx 1420$  MeV, resulting in the observed maximum at around 1405 MeV/c<sup>2</sup>.
- Exchanging the proton target by a deuteron target, the observed  $\Lambda(1405)$  properties change significantly. In panel e) the measured  $\Sigma^-\pi^+$  mass distribution for the reaction  $K^- + d \rightarrow \Sigma^- + \pi^+ + n$  at a kaon incident momentum of  $p_{K^-} = 0.8$  GeV/c [B<sup>+</sup>77] is displayed. The

$\Lambda(1405)$  mass peak appears around  $1420 \text{ MeV}/c^2$  in this case. Overlaid to the data is an incoherent sum of a  $\Sigma(1385)^0$  signal and a  $\Lambda(1405)$  signal [JOS09]. The  $\Lambda(1405)$  spectral shape was calculated in the chiral unitary approach. The difference to the  $K^- + p$  reaction (see panel d)) is the spectator neutron, bound in the deuteron system. The binding energy between the proton and the neutron allows here to produce  $\Lambda(1405)$  from the  $K^-p$  initial state via the scattering matrix element  $T_{K^-p \rightarrow \Sigma\pi}$  (see section 1.4). This matrix element mainly couples to the first  $\Lambda(1405)$  pole, and the observed mass spectrum thus appears around  $1420 \text{ MeV}/c^2$ . The theoretical prediction agrees very well with the experimental results.

- The CLAS results for  $\gamma$ -induced reactions are shown in panel f) [MS10]. The same picture was already presented in the introduction. Also here the  $\Lambda(1405)$  is mainly produced via the  $K^-p$  entrance channel [NOTR99] and consequently the observed spectra peak at values clearly above  $1405 \text{ MeV}/c^2$ . It is interesting to see that the distributions of the three  $\Sigma\pi$  decay channels differ significantly from each other. Such an effect is expected if interferences with isospin 1 amplitudes are present. The theoretical prediction in [NOTR99] suggests, however, that the shift of the  $\Sigma^+\pi^-$  and the  $\Sigma^-\pi^+$  distributions with respect to the  $\Sigma^0\pi^0$  distribution should be exactly vice versa. A possible interpretation of these data takes into account two different isospin 1 resonances, located at around  $1410 \text{ MeV}/c^2$  and  $1390 \text{ MeV}/c^2$ . The interference of these amplitudes with the  $\Lambda(1405)$  amplitude allows finally to understand the observed experimental distribution, but the origin of those two  $I = 1$  states is not clear at the moment [Sch12, M<sup>+</sup>13].

In fact, the shown results do not represent the entire data set of  $\Lambda(1405)$ , but even more measurements on its production in  $\gamma$ -, pion- and kaon-induced reactions are currently available. For  $p + p$  reactions, on the other hand, only the ANKE spectrum and the results of this work exist so far. Even though not all data can be shown here, the selected results in Figure 4.16 are representative for all available measurements. In general, it can be concluded that the extracted properties of  $\Lambda(1405)$  differ significantly in the different production mechanisms. As already explained, this is just a consequence of the different couplings to the two  $\Lambda(1405)$  poles.

Another interesting result of Figure 4.16 is that the mass shift to  $\approx 1385 \text{ MeV}/c^2$  is not only present in the HADES data, but that a very similar effect was observed in pion-induced reactions (see panel c)). To strengthen this statement, the two invariant mass spectra of Figure 4.16 a) and c) are directly compared in Figure 4.17. Additionally the result from Engler et al. [EFK<sup>+</sup>65] (open black dots), where the  $\Lambda(1405)$  was also reconstructed in  $\pi^- + p$  reactions, is included in the picture. In both spectra of pion-induced reactions the non-resonant background and the  $\Sigma(1385)^0$  contribution have not been subtracted. The authors of [TEFK73] and [EFK<sup>+</sup>65] claim, however, that the expected  $\Sigma(1385)^0$  contamination is very low. To estimate this contribution, they analyzed the neutral decay of  $\Sigma(1385)^0 \rightarrow \Lambda\pi^0$  and then followed the same line of argumentation, which was used in this work. In this sense all three measurements in Figure 4.17 show the same physical observable, which allows a direct comparison.

It is notable that the three spectra agree very well with each other, all indicating that the  $\Lambda(1405)$  mass peak is shifted to values below  $1405 \text{ MeV}/c^2$ . This might point to an interpretation where the produced  $\Lambda(1405)$  mainly couples to the low energy  $\Sigma\pi$  pole.

Nevertheless, from the theoretical point of view this observation is difficult to understand. In fact, the chiral unitary approach of [GO07] and [HHO<sup>+</sup>03] predicts a  $\Lambda(1405)$  signal clearly above  $1400 \text{ MeV}/c^2$  for  $p + p$  as well as for  $\pi^- + p$  reactions (see Figure 4.16 b) and c)). The understanding of the low mass signals requires additional theoretical effort.

In fact, new calculations have recently been carried out, which aim to explain the HADES data

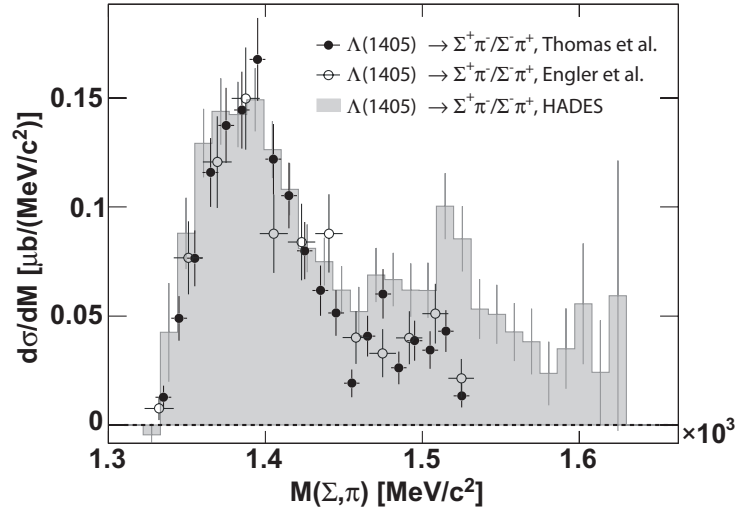


**Figure 4.17:** Comparison of the  $\Sigma\pi$  invariant mass spectrum, obtained in this work and by experiments employing a  $\pi^-$  beam [TEFK73, EFK<sup>+</sup>65]. The spectra with the full and open data points are normalized to the gray shaded HADES spectrum so that a good overlap in the  $\Lambda(1405)$  peak region is obtained.

with help of a phenomenological approach. The results of this work will be discussed in the next part.

#### 4.3.3.3 Interpretation in the phenomenological approach

In the introduction it was already mentioned that there are two different models commonly used to describe the  $\Lambda(1405)$  hyperon. The “chiral” model is based on a coupled channel approach, constrained by chiral dynamics. In this model the  $\Lambda(1405)$  is generated dynamically as an interference of two poles. The first pole is located at higher energies of around 1420 MeV and couples almost completely to the  $\bar{K}N$  channel, while the second pole is located at lower energies of around 1390 MeV and couples strongly to the  $\Sigma\pi$  channel. This chiral model was, for example, used to describe the ANKE results in Figure 4.16 b).

The second model is the so-called “AY” model, where the properties of the  $\Lambda(1405)$  are approached from a phenomenological coupled channel ansatz, *not* constrained by chiral dynamics. The assumption is that the  $\Lambda(1405)$  mainly consists of a single pole, namely the  $\bar{K}N$  quasi-bound state [HW08]. In contrast to the chiral model, this pole is, however, not located at 1420 MeV, but is assumed to be at the nominal  $\Lambda(1405)$  mass of around 1405 MeV. The associated  $\bar{K} - N$  binding energy is thus significantly larger in this approach (see discussion in section 1.5).

The authors of [HKAY12] used this second ansatz for a first theoretical interpretation of the new HADES results. Their procedure shall be briefly discussed in the following.

Starting point is the assumption that the  $\Lambda(1405)$  is mainly produced via the  $T_{\bar{K}N \rightarrow \Sigma\pi}$  scattering matrix element in  $p + p$  reactions. This further implies that the experimentally observed distribution emerges from a dominant coupling to the  $\bar{K}N$  pole. The corresponding t-channel exchange diagram is illustrated in Figure 4.18. The  $\Lambda(1405)$  is generated from the exchange of a non-strange meson, which produces a  $K^-$  and a proton at one vertex, and this meson-baryon pair subsequently couples to the  $\Lambda(1405)$ . It was shown in section 4.2.2 that the  $\Lambda(1405)$  is produced isotropically in the CMS (see Figure 4.8). In [HKAY12] this observation is interpreted as an

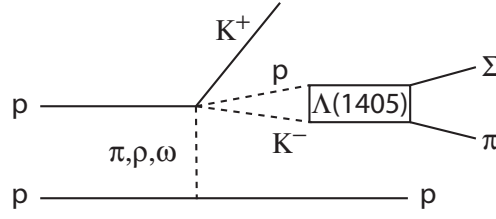


**Figure 4.18:**  $\Lambda(1405)$  production via a t-channel exchange diagram assumed in [HKAY12].

indication that heavy meson exchange ( $m > 2000$  MeV) is present in the  $\Lambda(1405)$  production mechanism. The authors claim that this result is consistent with the observations made by the DISTO experiment [K<sup>+</sup>12b]. The large momentum transfer between the two initial protons is associated with a short collision length. Such a process is one of the key mechanisms to form  $ppK^-$  from the high sticking of the proton and the  $\Lambda(1405)$ . In fact, the HADES data are at the moment systematically analyzed for different reactions, and one aim of these studies is to find some indications for the formation of a  $ppK^-$  bound state [Epp12a].

Coming now to the prediction on the  $\Lambda(1405)$  mass distribution. By implementing the discussed production mechanism, the authors of [HKAY12] developed a model from which they calculated the spectral shape of the  $\Lambda(1405)$ . In order to test their model on the experimental results, they subtracted the non-resonant background, the  $\Sigma(1385)^0$  signal and the  $\Lambda(1520)$  signal from the experimental distribution in Figure 4.11 c). In this way the “pure”  $\Lambda(1405)$  signal was obtained. In fact, this incoherent subtraction of all other contributions implies the assumption that no interference effects are present in the data. It is, however, not clear whether this assumption is justified. A more detailed discussion about this subject will follow in section 4.3.3.4. For now it is just assumed that the pure  $\Lambda(1405)$  spectrum can be accessed in that way. In [HKAY12] this spectrum was then compared to various theoretical predictions. The results are presented in Figure 4.19. The red (a) and magenta (b) curve in the picture correspond to the results of the

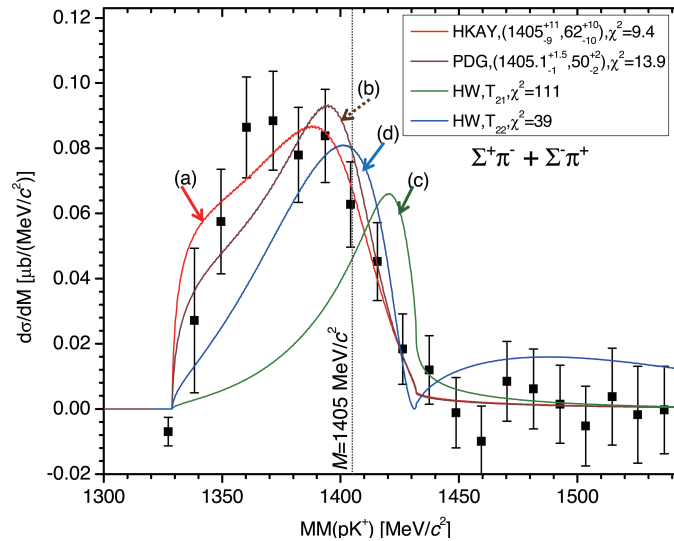


**Figure 4.19:** Missing mass spectrum to proton and  $K^+$  for the sum of the  $\Sigma^+\pi^-$  and  $\Sigma^-\pi^+$  data sample. The contributions of non-resonant background,  $\Sigma(1385)^0$  and  $\Lambda(1520)$  were subtracted from the experimental data in Figure 4.11 c). The data are compared to different theoretical predictions [HKAY12].

AY model. In (a) the mass and the width of  $\Lambda(1405)$  were chosen as free parameters. By fitting the experimental data points, a good description is achieved, whereby the  $\Lambda(1405)$  parameters were determined to:

$$\begin{aligned} m_{\Lambda(1405)} &= 1405_{-9}^{+11} \text{ MeV}/c^2 \\ \Gamma_{\Lambda(1405)} &= 62_{-10}^{+10} \text{ MeV}/c^2 \end{aligned}$$

This result is, within the errors, in perfect agreement with the nominal PDG values for the  $\Lambda(1405)$  [B<sup>+</sup>12]. In fact, by fixing  $m_{\Lambda(1405)}$  and  $\Gamma_{\Lambda(1405)}$  to these nominal values, the AY model (b) can describe the data as well (see magenta line in Figure 4.19). From this point of view the AY model, which assumes that the  $\bar{K}N$  pole is located at  $\approx 1405$  MeV, is in agreement with the experimental results. One should mention that this model reproduces the observed low mass peak of  $\Lambda(1405)$ , even though the  $\Lambda(1405)$  pole mass  $m_{\Lambda(1405)}$  is located above  $1400$  MeV/ $c^2$ . The reason for this is that the AY model accounts for the vicinity of the  $\bar{K}N$  threshold at around  $1430$  MeV/ $c^2$ . This nearby threshold distorts the  $\Lambda(1405)$  line shape so that it is different from a usual Breit-Wigner shape. This effect was not included in the simple simulation model, and, therefore, a Breit-Wigner mass of  $1385$  MeV/ $c^2$  had to be simulated in order to match the data. Turning now to the chiral model predictions. The blue (d) and the green (c) curves correspond to the results, reported in [HW08]. However, the distributions have been modified in order to account for the available phase space volume in the measured  $p + p$  collision system. The blue curve displays the result for  $\Lambda(1405)$  production through the  $T_{\Sigma\pi \rightarrow \Sigma\pi}$  scattering amplitude. As this amplitude mainly couples to the low energy pole, the model gives here an acceptable agreement with the data, but it cannot reach the good fit quality of the AY model. The green curve shows the result if  $\Lambda(1405)$  is produced through the  $T_{\bar{K}p \rightarrow \Sigma\pi}$  amplitude. According to [GO07, HKAY12], this should actually be the dominant production process in  $p + p$  collisions. Here, however, the chiral model completely fails to describe the experimental data because this amplitude has exclusive coupling to the high energy pole at  $\approx 1420$  MeV.

Summarizing the results of Figure 4.19, the AY model gives a significantly better description of the experimentally determined  $\Lambda(1405)$  line shape. The authors of [HKAY12] claim that the new HADES results are valuable for solving the question which of the two presented models is appropriate. Obviously, they conclude that the one pole scenario, with the  $\bar{K}N$  pole at  $1405$  MeV, is clearly preferred compared to the chiral two pole scenario.

One has to stress out at that point that things are probably not such easy. As already mentioned, the model comparison of Figure 4.19 completely neglects possible interference effects with the non-resonant background, which might have a striking influence on the final interpretation. This point will be addressed in the next part.

#### 4.3.3.4 What about interference effects?

So far the experimentally determined missing mass distributions to proton and  $K^+$  of Figure 4.11 have been described by an incoherent sum of the different simulated contributions. In this approach the signal attributed to  $\Lambda(1405)$  appears at around  $1385$  MeV/ $c^2$ . Also the authors of [HKAY12] start from this incoherent approach and describe the low mass  $\Lambda(1405)$  with their AY model. However, it is questionable if the description in such a simple incoherent way is sufficient. Indeed, it is not a priori excluded that interference effects among the different contributing reactions appear. This, on the other hand, might have major impact on the interpretation of the results. One can, for example, imagine that a “standard”  $\Lambda(1405)$ , with its mass peak above

1400 MeV/c<sup>2</sup>, interferes with the non-resonant background, and this leads to an observed mass peak below 1400 MeV/c<sup>2</sup>. The developed simulation model, but also the AY model of [HKAY12], do not take into account this possibility.

The question which is addressed in the following part is therefore:

Is the observed low mass peak a natural property of  $\Lambda(1405)$  in  $p + p$  reactions, or does it (partially) result from interference effects?

To test this interference hypothesis a simple toy model is constructed:

As a starting point, a realistic parameterization of the  $\Lambda(1405)$  line shape is needed. For this purpose, it is assumed that the  $\Lambda(1405)$  produced in the  $p + p$  reactions follows the spectral shape of the chiral model, which has been developed in [GO07] for the description of the ANKE results (see yellow band in Figure 4.16 b)). This assumption is reasonable, as the ANKE collaboration measured  $p + p$  reactions at a center-of-mass energy not far from the HADES energy. Figure 4.20 displays again the predictions from [GO07] (gray shaded band), where one can see that the  $\Lambda(1405)$  peaks at around 1410 MeV/c<sup>2</sup>. In order to parameterize this spectral shape, a similar ansatz as proposed in [JOO<sup>+</sup>03] was used, where the  $\Lambda(1405)$  is generated as an interference of two non-relativistic s-wave Breit-Wigner amplitudes:

$$\frac{d\sigma}{dm} = |T_{\Lambda(1405)}|^2 = C_{p.s.}(m) \left| BW_1(m)e^{i\varphi_1} + BW_2(m) \right|^2 q_{c.m.} \quad (4.28)$$

$$\text{with } BW_i = A_i \frac{1}{m - m_{0,i} + i\Gamma_{0,i}/2}$$

$C_{p.s.}(m)$  accounts for the limited phase space of  $\Lambda(1405)$  production in  $p + p$  reactions at 3.5 GeV kinetic beam energy (see equation (3.16) and appendix B.4);  $q_{c.m.}$  is the decay momentum of  $\Sigma$  and  $\pi$  in the rest frame of the  $\Lambda(1405)$ . For the Breit-Wigner functions a simple s-wave parameterization was chosen with amplitude  $A_i$ , mass  $m_{0,i}$  and width  $\Gamma_{0,i}$ . Since the two Breit-Wigner functions are added coherently, a free phase  $e^{i\varphi_1}$  was introduced as well.

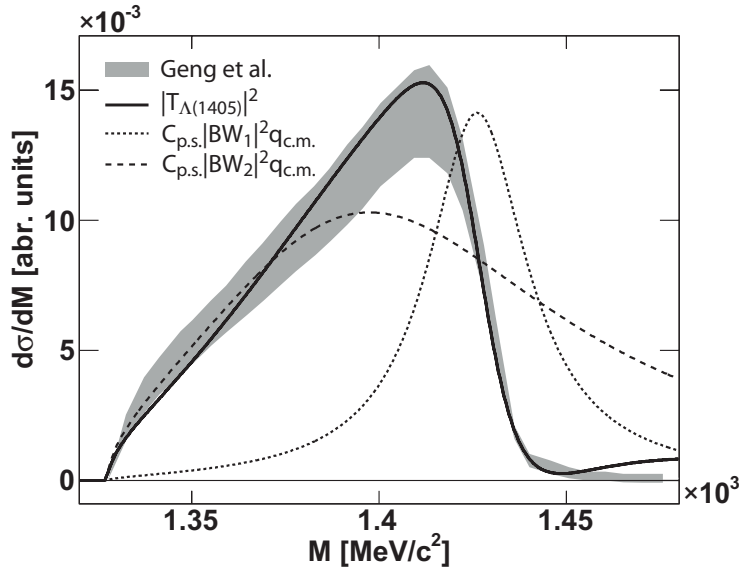


**Figure 4.20:** Coupled channel calculation of the  $\Lambda(1405)$  spectral shape for  $p + p$  reactions from [GO07] (gray band). Solid and dashed lines show  $|T_{\Lambda(1405)}|^2$ ,  $C_{p.s.}(m)|BW_1|^2 q_{c.m.}$  and  $C_{p.s.}(m)|BW_2|^2 q_{c.m.}$  obtained by fitting equation (4.28) to the gray band.

As already discussed in the introduction, the  $\Lambda(1405)$  is commonly assumed to emerge from the interference of two poles in the complex energy plane. A narrow high energy  $\bar{K}N$  quasi-bound state and a broad low energy  $\pi\Sigma$  resonance. Thus, it is reasonable to describe the  $\Lambda(1405)$  as an interference of two Breit-Wigner amplitudes. In [JOO<sup>+</sup>03] a coupled channel chiral unitary approach was used to derive the two pole positions of  $\Lambda(1405)$  at  $z_1 = 1426 + i16$  MeV and at  $z_2 = 1390 + i66$  MeV. These results were used to fix the Breit-Wigner masses and widths in equation (4.28) to  $(m_{0,i}, \Gamma_{0,i}) = (Re(z_i), 2Im(z_i))$ .

The function (4.28) was then fitted to the calculated  $\Lambda(1405)$  spectral shape in Figure 4.20 (gray band), whereby  $A_1$ ,  $A_2$  and  $\varphi_1$  were free fit parameters. The obtained values for the fit parameters are:  $A_1 = 0.19$ ,  $A_2 = 0.68$  and  $\varphi_1 = 157^\circ$ . The result of the fit itself is shown in the solid black line, which describes the predictions from [GO07] fairly well. Particularly the maximum of the distribution at  $\approx 1410$  MeV/ $c^2$  and the steep drop to the  $\bar{K}N$  threshold is reproduced by the simple approach. The dashed lines show the individual contributions of the two Breit-Wigner amplitudes ( $C_{p.s.}(m) |BW_1|^2 q_{c.m.}$  and  $C_{p.s.}(m) |BW_2|^2 q_{c.m.}$ ), where one can see that both, the  $\pi\Sigma$  and the  $\bar{K}N$  pole, contribute to the final spectrum. This picture should be compared to Figure 1.7 b), where the  $\Lambda(1405)$  spectral shape from the  $T_{\pi\Sigma \rightarrow \pi\Sigma}$  scattering element is shown. The model calculations, used there, show similar contributions of the two  $\Lambda(1405)$  poles.

At this point it has to be stressed out that the approach of equation (4.28) is obviously oversimplified and not equivalent to the full-fledged calculation, performed in [GO07]. Nevertheless, it allows to reproduce the predicted  $\Lambda(1405)$  spectral shape in  $p + p$  reactions. Therefore, this approach is further used to test the influence of interference effects.

For this purpose, the experimental spectra of Figure 4.11 a) and b) were fitted simultaneously with the following two functions:

$$\left(\frac{d\sigma}{dm}\right)_{\Sigma^+\pi^-} = \left|A_{\Lambda(1405)}T_{\Lambda(1405)} + e^{i\alpha}A_{\Sigma^+\pi^-}T_{\Sigma^+\pi^-}\right|^2 + \left|BW_{\Sigma(1385)^0}\right|^2 + \left|BW_{\Lambda(1520)}\right|^2 \quad (4.29)$$

$$\left(\frac{d\sigma}{dm}\right)_{\Sigma^-\pi^+} = \left|A_{\Lambda(1405)}T_{\Lambda(1405)} + e^{i\beta}A_{\Sigma^-\pi^+}T_{\Sigma^-\pi^+}\right|^2 + \left|BW_{\Sigma(1385)^0}\right|^2 + \left|BW_{\Lambda(1520)}\right|^2 \quad (4.30)$$

The result of the fit is shown in Figure 4.21 a) and b), where the black points indicate the experimental data (with statistical errors only) and the colored curves correspond to the different contributions in equation (4.29) and (4.30).

In these equations the  $\Sigma(1385)^0$  and the  $\Lambda(1520)$  (violet and green lines) are parameterized as simple Breit-Wigner amplitudes. The parameters of the Breit-Wigner functions were chosen such that  $|BW_{\Sigma(1385)^0}|^2$  and  $|BW_{\Lambda(1520)}|^2$  reproduce the simulated contributions of  $\Sigma(1385)^0$  and  $\Lambda(1520)$  in Figure 4.11 (see violet and green histograms). This implies that the amplitudes  $BW_{\Sigma(1385)^0}$  and  $BW_{\Lambda(1520)}$  were fixed, and they did not contribute with any free fit parameters. Furthermore, it was assumed that the two resonances do not interfere with any other contribution so that only the absolute values  $|BW_{\Sigma(1385)^0}|^2$  and  $|BW_{\Lambda(1520)}|^2$  appear in the two equations.

The black lines in Figure 4.21 a) and b) correspond to the pure  $\Lambda(1405)$  signals ( $|A_{\Lambda(1405)}T_{\Lambda(1405)}|^2$ ). For the parametrization of  $T_{\Lambda(1405)}$ , the function (4.28) was used, for which all parameters have been fixed by the fit in Figure 4.20. Thus, only the amplitude  $A_{\Lambda(1405)}$  remained as a free fit parameter. It determines the absolute contribution of  $\Lambda(1405)$  to the experimental data.

The red lines, given by  $|e^{i\alpha}A_{\Sigma^+\pi^-}T_{\Sigma^+\pi^-}|^2$  and  $|e^{i\beta}A_{\Sigma^-\pi^+}T_{\Sigma^-\pi^+}|^2$ , indicate the pure contributions of the non-resonant  $\Sigma\pi$  reactions. The functions  $T_{\Sigma\pi}$  were parameterized as modified polynomials of fourth order (for details see appendix B.4). The parameters of those polynomials

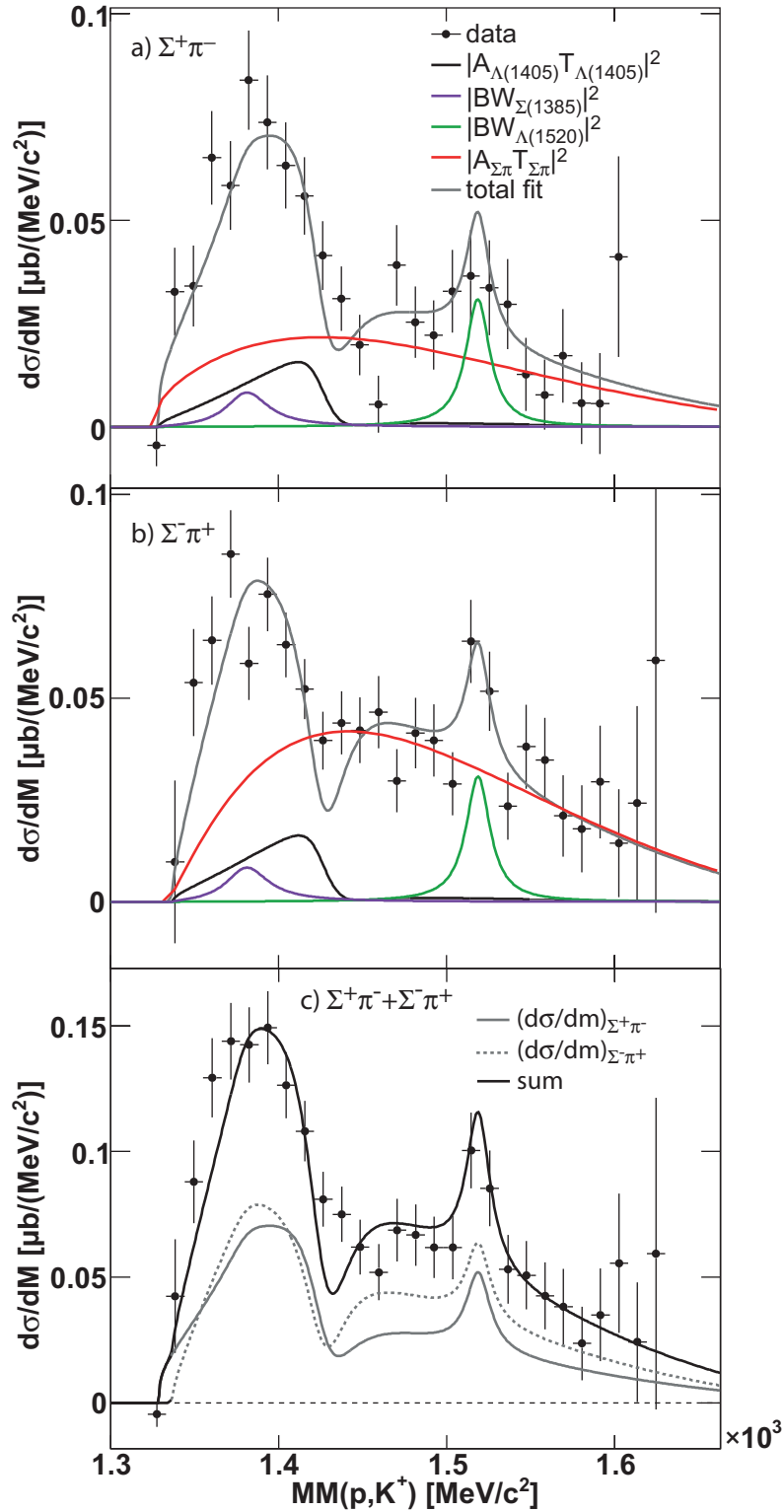


**Figure 4.21:** Missing mass spectrum to proton and  $K^+$  after acceptance and efficiency corrections for the  $\Sigma^+\pi^-$  (a) and  $\Sigma^-\pi^+$  data sample (b) (compare to Figure 4.11). Panel c) shows the sum of panel a) and panel b). The data in a) and b) are simultaneously fitted with the function (4.29) and (4.30), respectively. The colored lines indicate the different contributions which were taken into account in the fit functions (see text for details).

were chosen such that both red lines reproduce the shapes of the simulated distributions in Figure 4.11 (see red histograms).  $A_{\Sigma^+\pi^-}$  and  $A_{\Sigma^-\pi^+}$  were free fit parameters in the equations (4.29) and (4.30). They scale the absolute yields of the non-resonant background. Additionally, two further fit parameters, namely  $e^{i\alpha}$  and  $e^{i\beta}$ , were included. They give a complex phase to the non-resonant background, which determines the interference with the  $\Lambda(1405)$  amplitudes. In fact, the  $\Lambda(1405)$  is parameterized as a sum of two Breit-Wigner functions. A Breit-Wigner function is characterized by a phase jump of  $\pi$  when one passes its pole mass  $m_0$ . Therefore, by varying the phase angles  $\alpha$  and  $\beta$ , one can specify in which mass range constructive and destructive interference between the  $\Lambda(1405)$  and the non-resonant background appears.

In total, the simultaneous fit with the two functions (4.29) and (4.30) contains only five independent, free parameters, namely  $A_{\Sigma^+\pi^-}$ ,  $A_{\Sigma^-\pi^+}$ ,  $\alpha$ ,  $\beta$  and  $A_{\Lambda(1405)}$ . The obtained parameters are listed in Table 4.2.

$A_{\Lambda(1405)}$	$A_{\Sigma^+\pi^-}$	$A_{\Sigma^-\pi^+}$	$\alpha$	$\beta$
1.01	0.89	1.10	$-77^\circ$	$-117^\circ$

**Table 4.2:** Parameter values for  $(\frac{d\sigma}{dm})_{\Sigma^+\pi^-}$  and  $(\frac{d\sigma}{dm})_{\Sigma^-\pi^+}$  obtained by fitting the equations (4.29) and (4.30) to the HADES data points in Figure 4.21 a) and b).

The results of the fit are indicated in the gray lines in Figure 4.21 a) and b).

The included interference terms have a crucial influence on the observed spectra. Even though the assumed  $\Lambda(1405)$  spectral shape peaks around  $1410 \text{ MeV}/c^2$  (black lines), the constructive interference with the non-resonant background at low masses and the destructive interference at higher masses creates peaks clearly below  $1400 \text{ MeV}/c^2$ . With help of this effect it is possible to reproduce the experimental data in a) and b) rather well ( $\chi^2/ndf = 1.25$ ). This is also true for the sum of both  $\Sigma\pi$  data samples in panel c), which is compared to the sum of the functions (4.29) and (4.30). However, the low mass region of all three pictures still seems to be slightly underestimated by the fit functions. Indeed, the agreement between the data and the assumed model is a bit worse than what has been obtained in the incoherent approach of Figure 4.11. Furthermore, the total cross section for the reaction  $p + p \rightarrow \Lambda(1405) + p + K^+$  changes now. By integrating the black lines in panel a) and b), one can deduce  $\sigma_{p+p \rightarrow \Lambda(1405)+p+K^+}$  to  $3.3 \mu\text{b}$ , which is a factor of about three smaller than what has been obtained in Table 4.1. This, however, is not problematic, as it is anyway not known which cross section one would expect.

Summarizing the results of Figure 4.21, one can conclude that interference effects might (partially) explain the observed mass peaks at around  $1385 \text{ MeV}/c^2$  in the experimental data. One has, however, to consider that several simplifications were included in the used toy model. It is, for example, assumed that full interference between the  $\Lambda(1405)$  and the non-resonant background appears. This is justified if those two contributions have the same quantum numbers, but it is not clear if this is really the case. In fact, the  $\Sigma(1385)^+$  resonance, reconstructed in chapter 3, is not shifted in mass, which indicates that no significant interference effects between the signal and the non-resonant background are present in this case. Therefore, the question arises why the  $\Lambda(1405)$  resonance should interfere strongly with the background, while the  $\Sigma(1385)^+$  does not. Probably the degree of interference is indeed overestimated in the developed toy model. Also the assumption about the non-resonant background, being parameterized by a polynomial and having only one complex phase, is already a simplification. Furthermore, the model neglects any interference with the  $\Sigma(1385)^0$  amplitude. In fact,  $\Lambda(1405)$  is a s-wave resonance ( $J = 1/2$ ) while  $\Sigma(1385)^0$  is a p-wave state ( $J = 3/2$ ) so that these two amplitudes should not interfere

in the integrated spectra [JOS09]. However, if the non-resonant background (partially) carries the same quantum numbers as  $\Sigma(1385)^0$ , interference between those two contributions might appear and this can additionally affect the obtained spectra. Also for the  $\Lambda(1520)$  amplitude no interference effects are included, but this should not have any influence on the interpretation of the  $\Lambda(1405)$  signal. Another point concerns the influence of isospin 1 states. The CLAS results indicate that the  $\Lambda(1405)$  spectral shape is rather different for the  $\Sigma^+\pi^-$  and the  $\Sigma^-\pi^+$  decay channels (see Figure 4.16 f)). In [M<sup>+</sup>13] this observation is explained by contributions of  $I = 1$  amplitudes, which, according to the equations introduced in section 1.4, interfere with the  $I = 0$  amplitude of  $\Lambda(1405)$ . With the inclusion of two  $I = 1$  amplitudes, the experimental spectra could be reproduced rather well. Interference with the non-resonant background was, however, not considered in [M<sup>+</sup>13]. In contrast to this, the HADES spectra do not show any obvious difference in the position of the  $\Lambda(1405)$  peaks for the two different decay channels. Therefore, it was assumed that  $I = 1$  amplitudes do not play an essential role in the data, and they were thus not included in the fit.

Despite all the mentioned simplifications, the developed toy model gives still instructive results. It proves that interference effects can influence the observed mass peak of the  $\Lambda(1405)$ , and any more advanced theoretical model should include those effects to really interpret the new data on  $\Lambda(1405)$  production in  $p + p$  reactions.

Besides the discussed interference between  $\Lambda(1405)$  and the other reactions, also another effect could cause the observed mass shift. The presented analysis has shown that a large part of the non-resonant background is attributed to the production of a  $\Delta^{++}(1232)$  resonance together with  $\Sigma^-$  and  $K^+$ . It is possible that the  $\Lambda(1405)$  and the associated proton couple to  $\Delta(1232)$  and  $\Sigma$  via pion exchange [Wei12]. The process is illustrated in Figure 4.22. This kind of final state interaction might influence the observed properties of  $\Lambda(1405)$  and could be (partially) responsible for the low mass peak. Upcoming theory models should also consider those effects for a serious interpretation of the new HADES results.

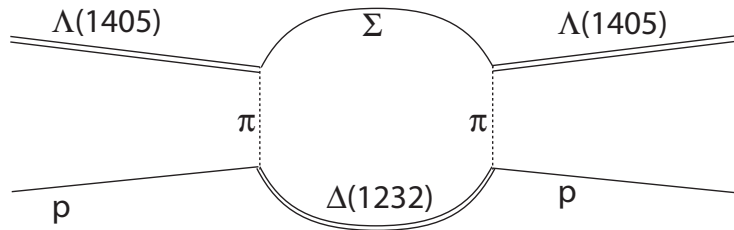


**Figure 4.22:** Final state coupling of the  $\Lambda(1405) - p$  pair to a  $\Delta(1232) - \Sigma$  pair via pion exchange. This coupling could have an influence on the observed  $\Lambda(1405)$  signal [Wei12].

#### 4.3.3.5 Summary

The analysis of  $\Lambda(1405)$  production in  $p + p$  reactions at 3.5 GeV kinetic beam energy has been presented. It was for the first time possible to reconstruct the  $\Lambda(1405)$  spectral shape from the decay into the charged  $\Sigma^\pm\pi^\mp$  states. It was found that several other reactions, like  $\Sigma\pi$  non-resonant production,  $\Sigma(1385)^0$  and  $\Lambda(1520)$  contribute to the final spectra as well. By developing an appropriate simulation model, the experimental data could be corrected for acceptance and efficiency, and for all the mentioned channels cross sections could be extracted. The most striking result of the analysis is the observation that the  $\Lambda(1405)$  mass peak appears around 1385 MeV/ $c^2$ ,

clearly below the nominal mass value. With help of several consistency checks it could be shown that this low mass signal indeed corresponds to  $\Lambda(1405)$ . This new and interesting data stimulated already some new theoretical effort, and first calculations have been performed in order to interpret the results. The authors of [HKAY12] have compared the single pole AY approach to the double pole chiral approach and find that only the first one is able to reproduce the data. The new HADES data could therefore be crucial on answering the long standing question if the  $\Lambda(1405)$  is a pure  $\bar{K}N$  bound state with its pole mass at 1405 MeV (AY model), or if  $\Lambda(1405)$  indeed consist of two poles, with the  $\bar{K}N$  pole at 1420 MeV (chiral model). It was, however, shown that a fair treatment of the new HADES data should take into account that interference effects might shift the mass peak. Furthermore, final state interaction with the associated proton can induce distortions on the observed  $\Lambda(1405)$  spectral shape as well. The HADES data hopefully trigger further theoretical investigations of  $\Lambda(1405)$  production in  $p + p$  collisions. As soon as the different effects of interferences and final state interactions can be controlled, the obtained spectra will help to get deeper insight into the  $\bar{K}N$  interaction below threshold.



## 5 The HADES pion tracker

In the past, HADES has successfully accomplished experiments with proton and heavy ion beams. These measurements are planned to be complemented with pion beam experiments. Since pion beams are secondary beams, special beam pipe systems are used to guide the incoming pions to the experiment. The HADES collaboration is, at the moment, developing a pion tracker system consisting of silicon strip detectors. This system will be placed in the beam pipe and will be used to determine the 3-momenta  $(p_x, p_y, p_z)$  of the beam particles. As these silicon detectors need to identify signals of minimum ionizing pions, their intrinsic noise has to be low. Furthermore, a 2-3 weeks beam time poses considerable requirements on their radiation hardness. To fulfill these demands,  $n^+p$  type silicon detectors are promising and will be used for the HADES tracking system.

This chapter presents some first tests on both, the intrinsic resolution and the radiation hardness of the used silicon detectors. It is subdivided into three parts.

The first section introduces the physics goals behind pion beams. Furthermore, the functional principle of the pion tracker and its setup are discussed.

The resolution and efficiency tests for the silicons are shown in the second part.

In the third section the results of a two days test beam time with protons of 20 MeV is presented. During this beam time, the radiation hardness of the detectors was tested and was found to be in agreement with the results from other experiments. This makes them appropriate for an operation in the planned pion beam experiment.

### 5.1 Pion beam physics and the pion tracker CERBEROS

#### 5.1.1 Physics motivation

The HADES pion beam project foresees to measure elementary reactions  $(\pi^- + p)$  as well as pion-nuclei reactions  $(\pi^- + A)$  at beam momenta of 1-2 GeV/c.

The dynamics in  $\pi^- + p$  reactions differ significantly from the ones in  $p + p$  reactions. In the first case the pion can couple directly to the proton in s-channel, whereas  $p + p$  reactions proceed via the exchange of an additional particle in t- or u-channel. This makes quantitative predictions for proton-induced reactions much more difficult, especially as also final state interactions between two baryons must be considered. The production of hyperons is also very different in the two cases. In pion-induced reactions, the hyperon can be produced with only one further particle (for example  $\pi^- + p \rightarrow \Lambda(1405) + K^0$ ). This is not possible in  $p + p$  reactions, where, due to baryon number conservation, always three particles appear in the final state (for example  $p + p \rightarrow \Lambda(1405) + K^+ + p$ ). The lower number of degrees of freedom in the final state makes the analysis but also the theoretical calculations of pion-induced reactions much easier. The  $\pi^- + p$  experiments are therefore extremely important to further constrain the low energy QCD dynamics.

One focus of the planned beam times is the (re)measurement of hyperon resonances like  $\Lambda(1405)$  and  $\Sigma(1385)$ . The obtained data will be perfectly suited to get additional insight into the  $\bar{K}N$  dynamics below threshold. In fact, measurements on  $\Lambda(1405)$  production in pion-induced reactions exist already, but the obtained statistic is poor. Furthermore, the contamination by the  $\Sigma(1385)^0$  has never been subtracted in these previous experiments (see e.g. [TEFK73]). Therefore, new data, analyzed with similar methods as developed in this work, are highly required. For that purpose, first simulation studies were performed, where it was found that in a 2-3 weeks pion beam time one can exclusively measure the  $\Lambda(1405)$  with considerable statistic. Together with the  $p + p$  results obtained in this work, HADES will be able to provide a substantial contribution to the further understanding of the  $\Lambda(1405)$  resonance. It will also be interesting to see if the observed similarity in the spectral shapes for  $p + p$  and  $\pi^- + p$  reactions (see Figure 4.17) can be confirmed.

But not only strangeness physics is of interest in the planned experiments; also the properties of nucleon resonances will be investigated in detail. Pion-induced reactions allow to produce these resonances in s-channel at a fixed resonance mass  $M_R = \sqrt{s}$ . With the excellent capability of HADES to measure virtual photons decaying into  $e^+ + e^-$ , it becomes possible to measure the Dalitz decay of those resonances (see Figure 5.1). This decay is sensitive to the electromagnetic form factor of the resonance. Since the virtual photon  $\gamma^*$  has a positive  $q^2$  value ( $q^2 = M_{\gamma^*}^2 = M^2(e^+, e^-)$ ), the time like region of the form factor can be scanned by varying the incoming pion momenta. Furthermore, the Vector Dominance Model (VDM) suggest that  $\gamma^*$  production always processes via a vector mesons ( $\rho, \omega, \phi$ ). Thus, the measurement of the form factor will deliver information about the coupling of vector mesons to the resonances, which will help to determine the propagator of the vector mesons in the nuclear medium [KMFF02]. Of particular interest in this context is the coupling of nucleon resonances to the  $\rho$  meson. By varying the  $\pi^-$  beam energy, the resonances can be excited just below or above the  $\omega$  threshold, which allows to disentangle the coupling to the  $\rho$  meson. This information is crucial for the interpretation of the di-lepton spectra, measured by the HADES collaboration.

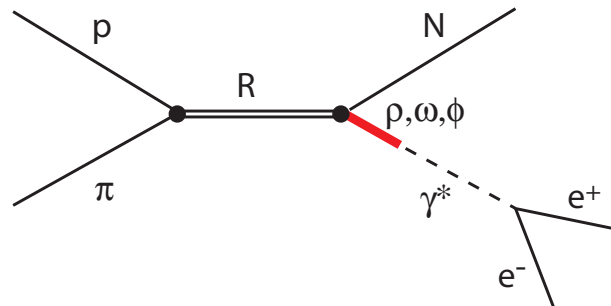


**Figure 5.1:** Nucleon resonance production in pion-induced reaction with subsequent Dalitz decay.

Besides studying elementary  $\pi^- + p$  reactions, it is also planned to impinge pions on nuclei (e.g. C, Cu, Pb, etc.). The particles produced in these reactions are created in a cold nuclear environment at normal nuclear density  $\rho_0$ . As already mentioned, the properties of particles, like their mass and width, are expected to show in-medium modifications. Of special interest is here the possible influences by the partial restoration of chiral symmetry, which is expected to be present already at  $\rho_0$  [Nor98]. Vector mesons are an ideal tool to probe the in-medium modifications because they decay into  $e^+e^-$  pairs. If the decay happens within the medium, the produced leptons can leave the environment almost undistorted, as they only interact via electro-

magnetic interaction. The information of the in-medium vector meson is thus conserved by the leptons (see e.g. [A<sup>+</sup>12c]). By tuning the pion-beam energy, almost recoilless vector mesons can be produced, which increases the probability of an in-medium decay and, thus, makes the in-medium modifications of the particles accessible.

But also for strangeness physics these type of reactions are of great interest. In the introduction it has been shown that the properties of kaons are highly influenced by the surrounding nuclear medium. Pion-induced reactions at HADES open the possibility to measure kaons and anti-kaons at low transverse momentum  $p_t$ . As the low momentum region is especially sensitive to the presence of attractive or repulsive interactions (see e.g [A<sup>+</sup>10]), these measurements will complement ongoing studies of the  $K_S^0$  properties in  $p + p$  and  $p + Nb$  reactions [BC12], and will allow to get a unique insight into the real part of the mean field potentials in the nuclear environment. Furthermore,  $K^-$  are expected to be strongly absorbed in the nuclear medium due to their coupling to resonances like  $\Lambda(1405)$  or  $\Sigma(1385)$ . By studying the production probability of  $K^-$  in different targets, the imaginary part of the potential, which is responsible for the absorption, can be accessed.

Summarizing this introduction, pion beam experiments open a rich field of new and interesting physics. To make such experiments possible, a new detector system, the so-called pion tracker, is currently developed.

### 5.1.2 The pion tracker project

Pion beams are secondary beams. At GSI they are created by shooting high intensity primary particle beams of protons or Nitrogen ions ( $dN/dt \approx 10^{11}$  particles/s) on a Beryllium target. During the collisions, a whole bunch of different particle species is created. The aim is to filter out of this bunch preferably pions with a certain momentum and to guide them to the experiment. For this purpose, a beam line chicane, as indicated in Figure 5.2, is used. The chicane starts at the production target on the left and ends at the HADES target on the right. The beam line is equipped with two dipole magnets, used for bending the particle beam, and several quadrupole

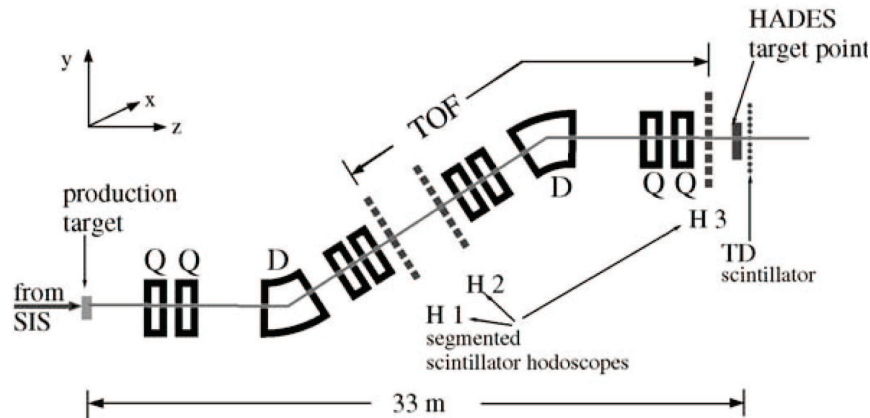


**Figure 5.2:** Beam line chicane at GSI, used to guide a secondary pion beam to the HADES experiment. One of the CERBEROS silicon detectors will be positioned in the dispersive plane at position  $H_2$ ; the second one will be placed in front of the HADES target at the position  $H_3$ .

magnets for focusing.

Depending on the polarization of the dipole magnets, they select either positively or negatively charged particles. Positive pions are contaminated by positrons,  $\mu^+$ ,  $K^+$ , protons and fragments; negative pions are only contaminated by electrons,  $\mu^-$  and  $K^-$ . Considering the corresponding production cross sections, the negative beam is already a rather pure  $\pi^-$  beam, whereas the positive beam contains a large background from protons [D<sup>+</sup>02]. In 2005, the pion beam production has been tested with  $6.5 \cdot 10^{10}$  Nitrogen ions per second impinged on a Be target. A maximum pion intensity of  $1.8 \cdot 10^6$   $\pi^-$  per burst (4s cycle time) at a pion momentum of 1.17 GeV/c has been measured at the HADES target [SKV<sup>+</sup>].

The dipole magnets are not only used to select the particle charge, but also to filter out a certain momentum range. The beam line in Figure 5.2 has a large momentum acceptance of  $\Delta p/p = 10\%$ , which has the advantage that large beam intensities are feasible. However, as HADES wants to analyze exclusive  $\pi^- + p$  reactions, a momentum resolution of around  $\Delta p/p = 0.2\%$  is required. At this point the pion tracker CERBEROS (CEntRal-BEam-tRacker-for-piOnS) comes into the game. It offers an additional possibility to measure the particle momentum without any loss of the beam line acceptance.

CERBEROS consists of two position sensitive silicon detectors, which will be located inside the beam line. In order to avoid too high particle fluxes on the detectors, they must be placed as far as possible from the production target. By performing Monte Carlo simulations, the following setup turned out to be promising [Hie12]: One of the detectors will be placed directly in front of the HADES target, at the position  $H_3$  in Figure 5.2. The second detector will be located in the dispersive plane at the position  $H_2$  between the second and the third quadrupole doublets. In this dispersive plane, the particle beam is defocused over a relatively large area (see Figure 5.3 a)). The defocussing, induced by the dipole magnets, concerns mainly the x- direction and depends on the corresponding momentum of the particles. A measurement of the hit position on the detector thus allows to determine the individual particle momenta with a precision, which is only limited by the position resolution. Figure 5.3 b) shows the momentum-position correlation measured in [D<sup>+</sup>02]. In this work a setup with two scintillators at the positions  $H_1$  and  $H_2$  was used. The calibration was done with a proton beam of 1.6 GeV kinetic energy, for which the expected momentum spread was simulated by varying the magnetic field strengths. The result illustrates that the momentum range of  $\pm 5\%$  around the central momentum is linearly correlated with a position dispersion of about  $\pm 3$  cm.

However, for the reconstruction of the full particle track it will not be sufficient to just measure

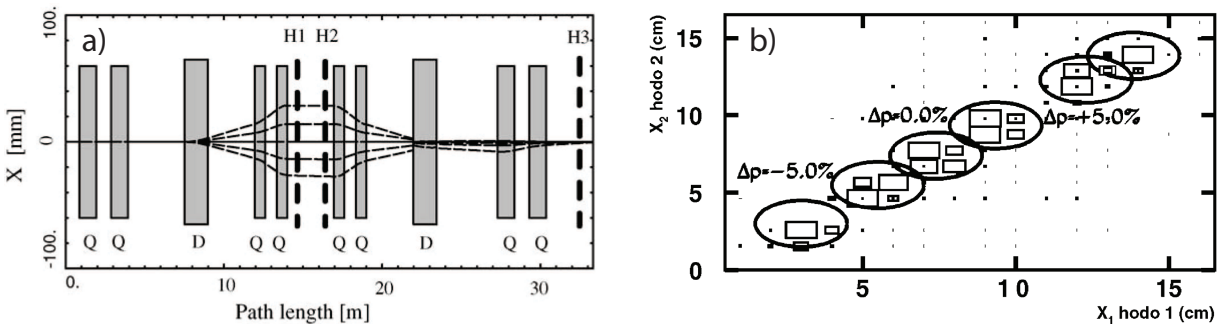


**Figure 5.3:** Panel a): Schematic picture from [D<sup>+</sup>02] illustrating the defocussing of the particle beam between the positions  $H_1$  and  $H_2$  of Figure 5.2. Panel b): Measured and calibrated position-momentum correlation for a proton test run.

one hit position in the dispersive plane. The reason for this is that the secondary particles might enter the beam line under certain angles, which additionally influences the hit position on the detector. In order to disentangle those two effects, a second position measurement is necessary. For that purpose, CERBEROS will be equipped with an additional silicon detector at position  $H_3$ . By combining the hit position in both detectors  $(x_1, y_1, x_2, y_2)$ , the transport equation for the beam optics can be solved, and the 3-momentum  $(p_x, p_y, p_z)$  can be determined for each beam particle individually.

For the upcoming pion beam time at HADES,  $10 \times 10 \text{ cm}^2$   $n^+p$ -type silicon detectors with a width of  $300 \text{ }\mu\text{m}$  will be used for the position measurement. These detectors promise a good signal to background separation and a sufficient radiation hardness. The  $n^+$  and the  $p$  sides are each segmented into 128 individual channels. This guarantees a good position resolution and, at same time, reduces the capacitive noise. As the segmentation is orthogonal on both sides, a combined x-y position information can be obtained from one single detector. Figure 5.4 a) is a front view on the silicon detector, where the silicon material is mounted on a PCB structure (green). The connectors for the readout of the front side and of the back side are shown in black. Each connector combines 32 channels so that four connectors on each side are needed. Panel b) shows a cut through the detector. The terminus  $n^+p$  silicon arises from the  $p$ -type bulk material, into which the highly doped strips are embedded. Three of these silicon detectors are available for the HADES beam time. The measurement of their properties is topic of the next sections.

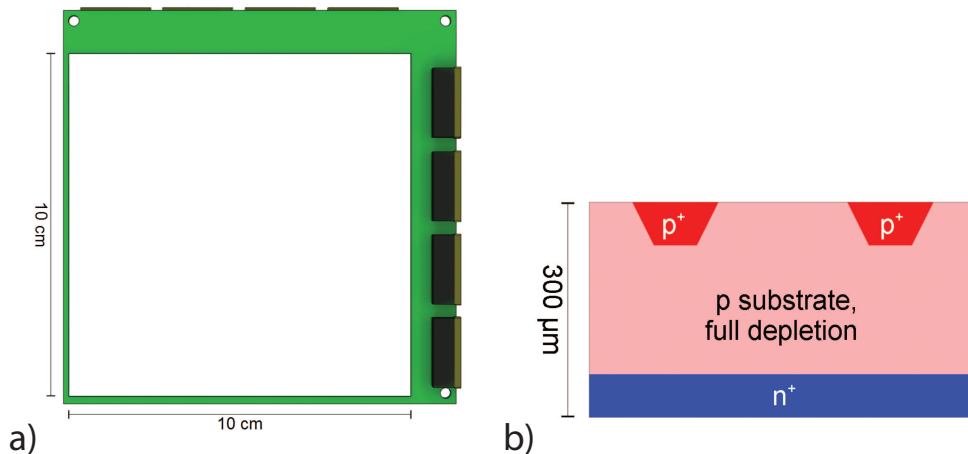


**Figure 5.4:** Figure from [Mac11]. a) shows a model of the silicon detector. b) is a cut through parallel to the  $n$  strips and perpendicular to the  $p$  strips.

## 5.2 Resolution and efficiency of the silicon detectors

In this section the silicon detectors shall be characterized. In the first part the signal to noise separation power for the individual channels is tested. Afterwards, the detector efficiency, which is expected to be above 90%, is measured. For the performed tests special adapter boards have been designed, which allow to put the signal of two neighboring silicon channels together. In this way the 128 channels per side are reduced to 64 channels only. The readout in all experiments was done with Mesytec preamplifiers (MPR64) and shapers (STM16) [Mes12]. Mesytec modules are often employed in nuclear spectroscopy experiments. They are useful because they can measure

adjustable energy ranges and offer the possibility to vary the integration time ( $0.4 \mu\text{s}/1 \mu\text{s}$  or  $2 \mu\text{s}/5 \mu\text{s}$ ) [Mes12]. With such a large integration time, the noise contribution is suppressed from the very beginning.

During the pion beam experiments, the high particle flux requires the use of much faster readout systems. At the moment n-XYTER chips [B<sup>+</sup>06] in combination with a SysCore readout controller are planned to be used. The shorter integration time of  $\approx 100 \text{ ns}$  will, however, increase the noise and reduce the signal to noise ratio. The results presented in this work shall therefore be seen as a detector characterization with idealized conditions, which can later on serve as a reference.

### 5.2.1 Signal to noise ratio

The silicon detectors are supposed to measure the position of traversing pions with momenta of 1-2 GeV. Pions in this energy range are minimum ionizing particles (MIPs); this means that their energy loss in the detector is small. The expected energy loss for a  $300 \mu\text{m}$  thick layer of silicon is around 120 keV. This low energy deposition and the corresponding small electronic signal has to be separated from the noise, caused by the detector system.

To test whether a sufficient signal to noise ratio can be reached, the detector was calibrated with the  $\beta$ -spectrum of a radioactive  $^{207}\text{Bi}$  source. Figure 5.5 a) shows the raw  $^{207}\text{Bi}$   $\beta$ -spectrum of one channel, where the units on the x-axis are ADC channels. At low ADC values a large noise peak is visible. The real signal is separated from the noise and is characterized by a broad exponential distribution, overlaid with four peaks. This structure can be explained as follows:

The electrons emitted from the  $^{207}\text{Bi}$  atom are mainly conversion electrons (CE) [Böt]. They are produced when the Bi core transforms into a  $^{207}\text{Pb}$  core via electron capture, which subsequently deexcites by emission of  $\gamma$ s. These  $\gamma$ s knock out electrons from the inner atomic shells. In this way four dominant electron lines are created with energies of around 482 keV, 554 keV, 976 keV and 1045 keV. Most of the electrons loose only a certain fraction of their energy when passing the

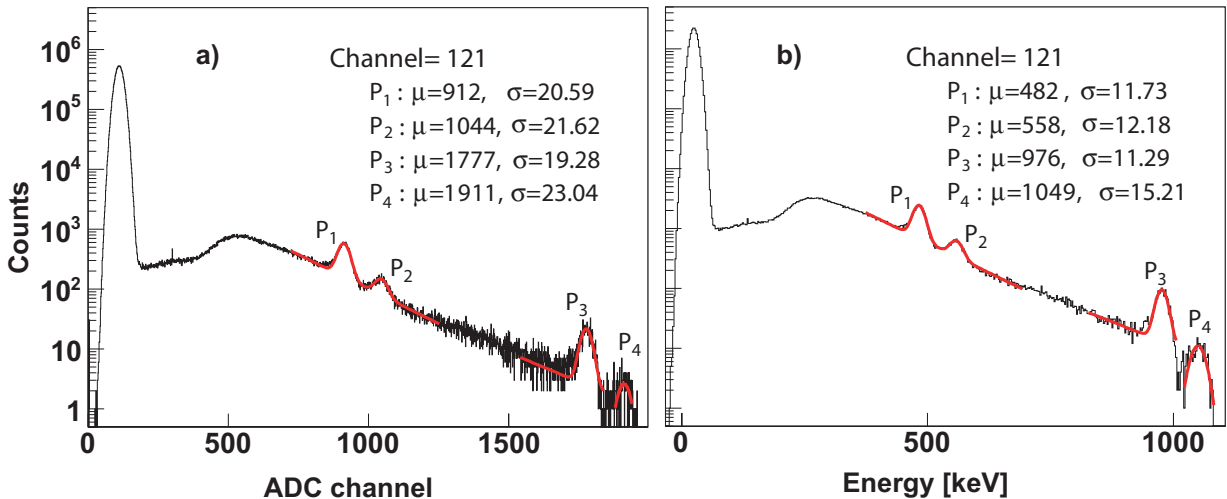


**Figure 5.5:** a): ADC spectrum of channel 121, measured for a  $^{207}\text{Bi}$  source. b): same as a) but after calibrating the x-axis from ADC to energy values. The red lines show fits of exponential plus Gaussian functions. The legends indicate the fit results.

silicon detector and contribute to the broad background spectrum. In some rare cases, however, the electrons are completely absorbed and deposit their whole energy, resulting in mono energetic signal lines. The four peaks in Figure 5.5 a) correspond exactly to the four dominant electron lines of  $^{207}\text{Bi}$ . Since the energy of the peaks is known, they could be used for the detector calibration. The fourth peak, however, has been omitted from the calibration procedure, as its statistic is too low. The calibrated spectrum is shown in panel b). The mean values of Gaussian fits to the four peaks are very close to the nominal values (see legend in b)), indicating that the calibration procedure works correctly.

This procedure was applied to calibrate all of the 128 detector channels. The resulting signal positions, signal widths and noise widths as a function of the channel number are shown in Figure 5.6 for one of the three available detectors. Here the first 64 channels correspond to the

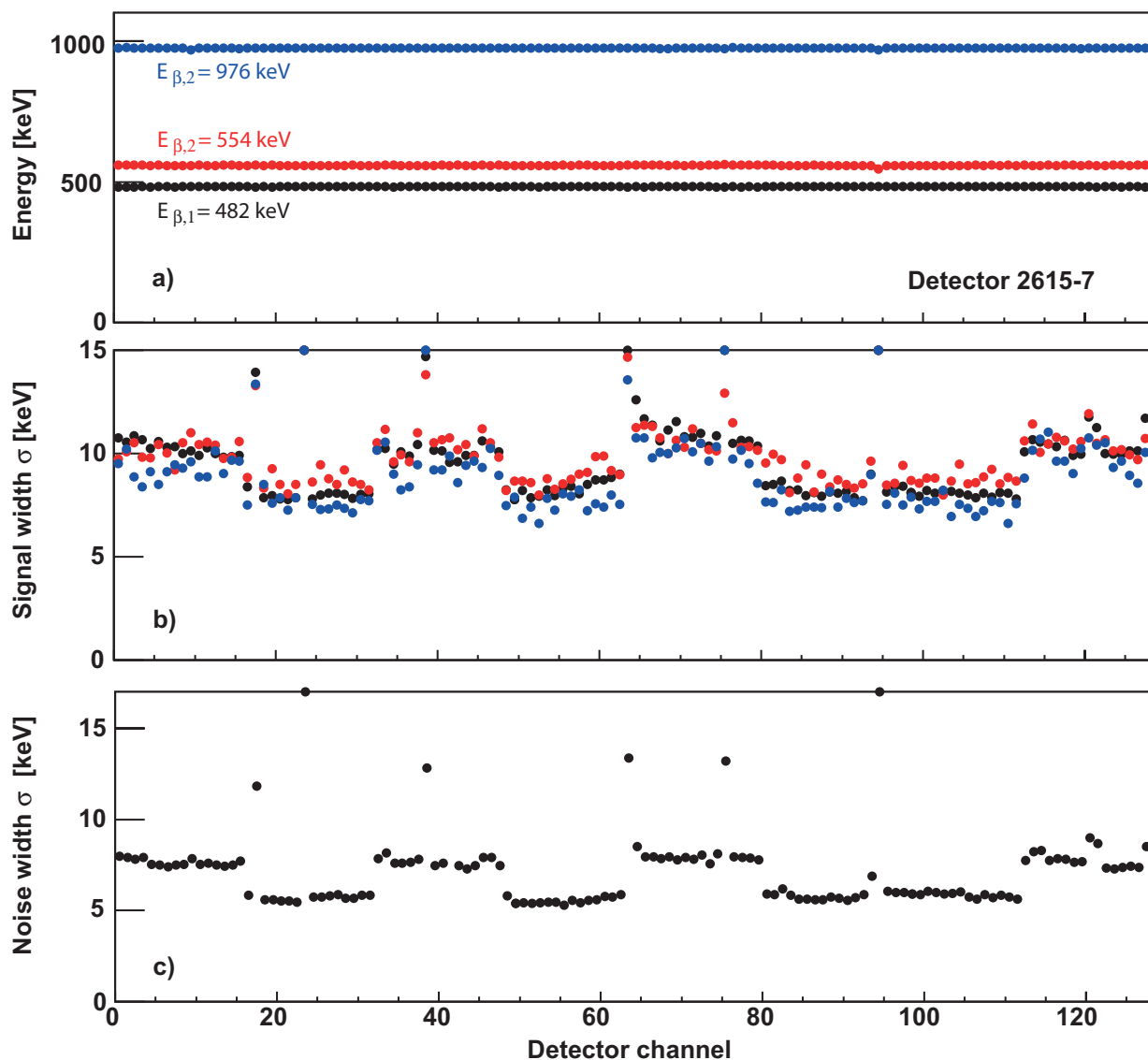


**Figure 5.6:** Detector 2615-7. Channels 0-63 represent the  $p$  side of the detector, channels 64-127 represent the  $n^+$  side. Panel a): Calibrated position of the first three conversion peaks; panel b): calibrated width of the three peaks; panel c): calibrated width of the noise peaks.

signals measured on the  $p$  side of the detector, the remaining channels correspond to the  $n^+$  side. The three signal lines in panel a) are at the correct positions for almost all channels. Only one channel (channel 91) shows shifted signals. Since this channel is very noisy (see panel c)), the calibration procedure did not work properly.

In panel b) the widths of the three signal peaks is shown. Except for the step like structure, which is discussed below, the extracted widths are rather constant, indicating that the different channels behave similar. A few noisy channels can be clearly identified as outliers in the spectrum. They correspond to the outliers in panel c).

The noise width is determined by fitting the calibrated noise peak (see for example Figure 5.5 b)) of each channel with a Gaussian function. The resulting  $\sigma$  values, given in keV, are shown in panel c), where again a step like distribution appears. The reason for these steps is not the detector itself but the readout system. A Mesytec preamplifier can only read 16 channels at once so that eight individual preamplifiers have been used to handle the 128 channels. In fact, two different types of preamplifiers (linear and logarithmic) have been installed, which, according to the setup instructions [Mes12], deliver different noise widths: The intrinsic noise width  $\sigma$  of the linear and logarithmic preamplifiers are  $\left(2.13 + \frac{0.026}{pF}\right)$  keV and  $\left(2.77 + \frac{0.026}{pF}\right)$  keV, respectively. By estimating the capacity of one channel (two strips) to 54 pF, the expected widths are  $\sigma_{lin} = 3.53$  keV and  $\sigma_{log} = 4.17$  keV. This explains the observed steps in the data. It is interesting to notice that also the signal widths (panel b)) are influenced by this effect and therefore follow the step like structure as well.

The measured noise widths of the individual channels were obtained to  $\sigma \approx 5 - 8$  keV ( $1470 - 2350 e^-$ ) (see Figure 5.6 c)). The values are larger than the intrinsic noise of the preamplifiers, which must mainly be attributed to the intrinsic noise of the detector itself. As MIPs are expected to deliver a signal of around 120 keV in 300  $\mu\text{m}$  silicon, the signal to noise ratio is estimated to  $S/N \approx 20$ . Thus, MIPs are completely separated from the noise peaks. With such a good resolution, one could even reconstruct the energy deposition of particles which distribute their signal on several strips.

In appendix C.1 the measurements for the two other detectors can be found. They behave very similar to the detector tested in this section. The presented work proofs that the silicon detectors are in principal well suited for the identification of minimum ionizing pions. Future tests have to check if the n-XYTER readout system also delivers a sufficient signal to noise separation.

### 5.2.2 Detector efficiency

The efficiency of the silicon detectors has been investigated. For this purpose, the detector was placed in between a Strontium  $\beta$ -source and a scintillator. The electrons from the Strontium source passed the silicon, eventually induced a signal, and finally hit the scintillator. In this measurement the scintillator was used as an external trigger for the silicon detector. An efficiency of 100% would mean that every scintillator signal has a corresponding hit in the silicon. A typical hit pattern after noise suppression is shown in Figure 5.7 for  $1.5 \cdot 10^6$  triggered events. Exploiting the orthogonal arrangement of the strips, the channels 0-63 were assigned to the x-position of the hit and the channels 64-127 were assigned to the y-position. In this way the spot of the Strontium source can be clearly identified. The efficiency was determined by extracting the number of hits from the picture and normalizing it to the number of triggered events. The efficiencies for the three different detectors are summarized in Table 5.1. They are all lying above 90%, which is a reasonable value for silicon detectors.

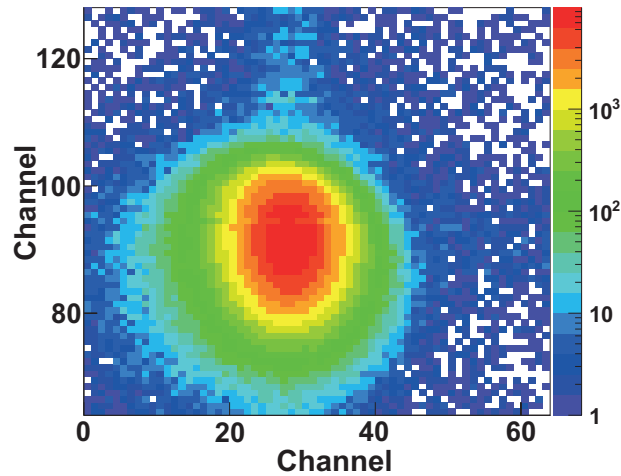


**Figure 5.7:** Hit pattern in one silicon detector. A scintillator served as an external trigger. The signals were induced by the  $\beta$  decay of a Sr source.

<i>Detector</i>	<i>Efficiency</i>
2615-7	97%
2814-24	96%
2814-25	92%

**Table 5.1:** Efficiencies of the three different silicon detectors.

### 5.3 Radiation hardness

During the pion beam experiment, the silicon detectors will be exposed to a high flux of particles. These particles do not only induce a measurable signal by creating electron-hole pairs, but they can also damage the crystal structure of the semiconductor material. Hadrons, for example, can knock out atoms from the lattice site and create vacancies (for details see [Lin03, Wir12]). This so-called non-ionizing radiation influences the performance of the detector and can thus reduce its capabilities. Two prominent effects, caused by this kind of radiation, are listed here:

On the one side, the effective doping is modified by the creation of acceptor like states. At the same time, donor centers can be destroyed by complex defects. These effects reduce the number of electrons as charge carriers and increase the number of holes. This goes hand in hand with a change of the depletion voltage [Mac11]. Furthermore, a  $n$ -doped bulk material will transform, after a certain time of irradiation, into a  $p$ -type bulk. This effect is called type inversion. To avoid this kind of inversion in the HADES beam time,  $n^+p$  detectors are used with  $p$ -type bulk material.

A second undesired effect comes from defects, which are created within the band gap. They can behave like trapping centers, catching up the charge carriers and keeping them for a longer period. This can distort the measurable signal. On the other side, defects which are produced in the middle of the band gap mainly act as additional generation-recombination centers for electron-hole pairs and, hence, increase the leakage current. This, however, increases the noise,

which might make the extraction of MIP signals difficult. The change in the leakage current is thus an appropriate tool to study the radiation damages on the detector.

The following section describes the measurement of the leakage current behavior for detector 2814-25. During a two days beam time at the MLL tandem accelerator in Munich, a high flux of protons with around 20 MeV energy was impinged on the silicon detector. The results of this measurement prove that the used detectors are suited to stand the high particle dose, expected during the pion beam time. Before the setup and the results are presented in the second part of the section, a short introduction into the NIEL hypothesis is given.

### 5.3.1 The NIEL hypothesis

The **Non-Ionizing Energy Loss** hypothesis allows to compare the radiation damage, induced by different particles of different energies. The main assumption is that damages only happen via non-ionizing energy transfer [Lut99], which is proportional to the displacement damage cross section  $D_i(E)$ . This cross section depends itself on the particle species  $i$  and its energy  $E$ . It is quantified for silicon in Figure 5.8. Normally, the  $D_i(E)$  values are normalized to neutrons of 1 MeV energy ( $D_n(1\text{MeV})=95\text{ MeVmb}$ ) by introducing the factor  $\kappa$  [Lin03]:

$$\kappa = \frac{D_i(E)}{D_n(1\text{MeV})} \quad (5.1)$$

The damages, caused by a mono energetic particle flux  $\Phi_i$  (total amount of particles/cm<sup>2</sup> shot on the detector), is then the same as if 1 MeV neutrons with an equivalent flux of  $\Phi_{eq} = \kappa\Phi_i$  would have been used.

These damages increases the leakage current by  $\Delta I$ .  $\Delta I$  depends linearly on  $\Phi$  [RKP96], and, by

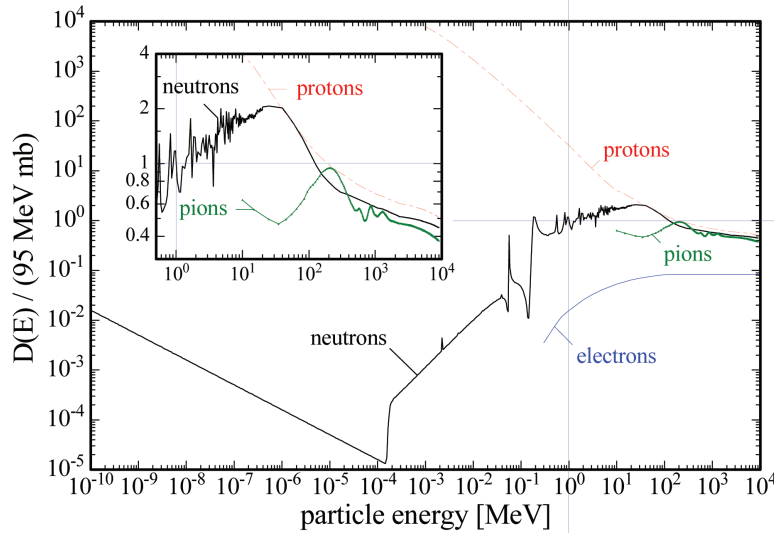


**Figure 5.8:** Picture from [Lin03]: Displacement damage cross section in silicon as a function of energy for different particles species. The blue vertical and horizontal lines indicate the normalization value, given for neutrons at 1 MeV. The inlet shows a zoom in for the energy range of 1 to 10<sup>4</sup> MeV.

using the nomenclature from above, it is given to:

$$\Delta I = V\alpha\Phi_{eq} = d\alpha N_{eq} \quad (5.2)$$

where  $V$  is the irradiated volume and  $\alpha$  is a parameter, which characterizes the sensitivity of the detector to radiation damages. One can cancel out the irradiated area so that the formula is expressed by the detector thickness  $d$  and the number of hitting particles  $N_{eq}$ . For silicons,  $\alpha$  is normally in the order of  $10^{-17} - 10^{-16}$  A/cm. In general,  $\alpha$  depends itself on the temperature  $T$  and the passed time  $t$  since the last irradiation period [RKP96]. The time dependence comes from the fact that the defects in the detector develop as a function of time; they can either disappear, but they can also induce more defects [Wir12]. This so-called annealing is itself strongly temperature dependent.

For the quantification of the radiation hardness, the factor  $\alpha$  is normally used as a reference parameter.

### 5.3.2 Leakage current measurement at MLL

The radiation hardness was measured with a high flux of protons impinged on the silicon detector. During the experiment, the detector was put into a light tight aluminum box with  $2 \mu\text{m}$  thick aluminum entry and exit windows. Behind the aluminum box, a large scintillator was placed, which served as an external trigger. This scintillator measured additionally the total number of particles which passed the detector. The silicon detector was segmented into four different areas (Area 1-Area 4) so that the leakage current could be independently measured in each of these areas. The whole setup (front and side view) is sketched in Figure 5.9. In order to reduce surface cross currents between the areas, the silicon surface was dried by continuously flushing the box with nitrogen. Since the leakage current is not only dependent on the damages in the detector, but also on the temperature, a one wire temperature sensor was mounted on the PCB (green areas in Figure 5.9).

Concerning the readout and data acquisition, an online monitor has been developed. This tool reads the measured current values every second, makes a live current trend plot and saves the

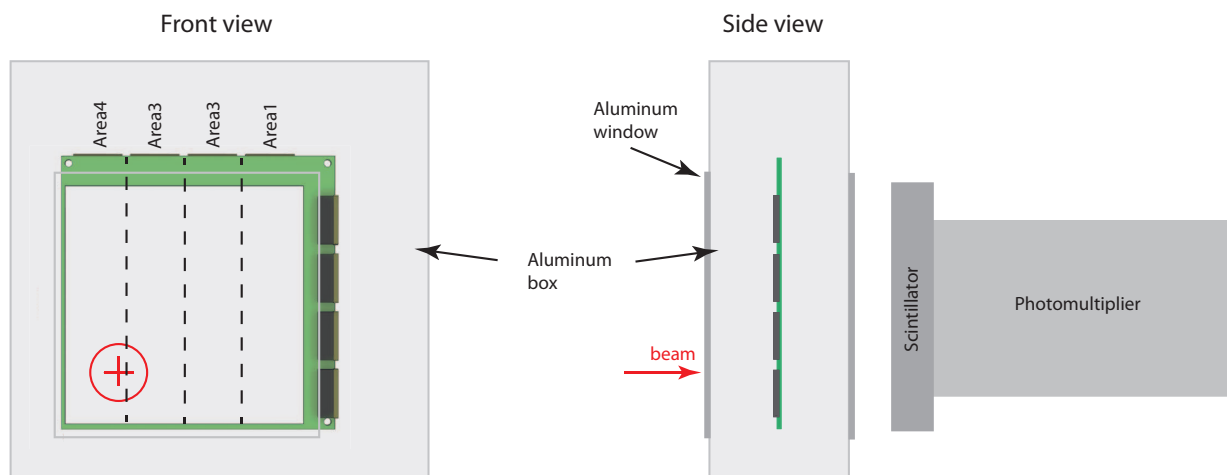


**Figure 5.9:** Sketch of the experimental setup from a front and a side view. The red cross and red arrow indicate the hit position and direction of the beam.

current values in standard root files. With the same time stamp the temperature and the accumulated number of detected protons is read from the temperature device and the scintillator, respectively.

Before the detector was exposed to the proton beam, a 36h test measurement without beam was performed. In Figure 5.10 a) and b) the four measured leakage currents and the temperature are shown as a function of time (in units of minutes). It is obvious that the four currents are quite different in magnitude. This difference was already confirmed by the manufacturer of the silicons and is attributed to single detector strips, which show very high currents. A common feature of the four leakage current curves is that they clearly follow the trend of the temperature curve. This effect is due to the Fermi statistic of the charge carriers. Indeed, for an ideal bulk semiconductor the leakage current is temperature dependent and can be parameterized as follows [LMF99]:

$$I(T) \propto T^2 e^{-\frac{\beta}{T}} \quad (5.3)$$

with  $\beta = \frac{E_g}{2k_b}$

Taking the band gap of silicon ( $E_g = 1.12$  eV) and the Boltzmann constant  $k_b$ ,  $\beta$  is determined to  $\approx 6500$  K. However, this value is idealized and does not have to be valid for realistic detectors.

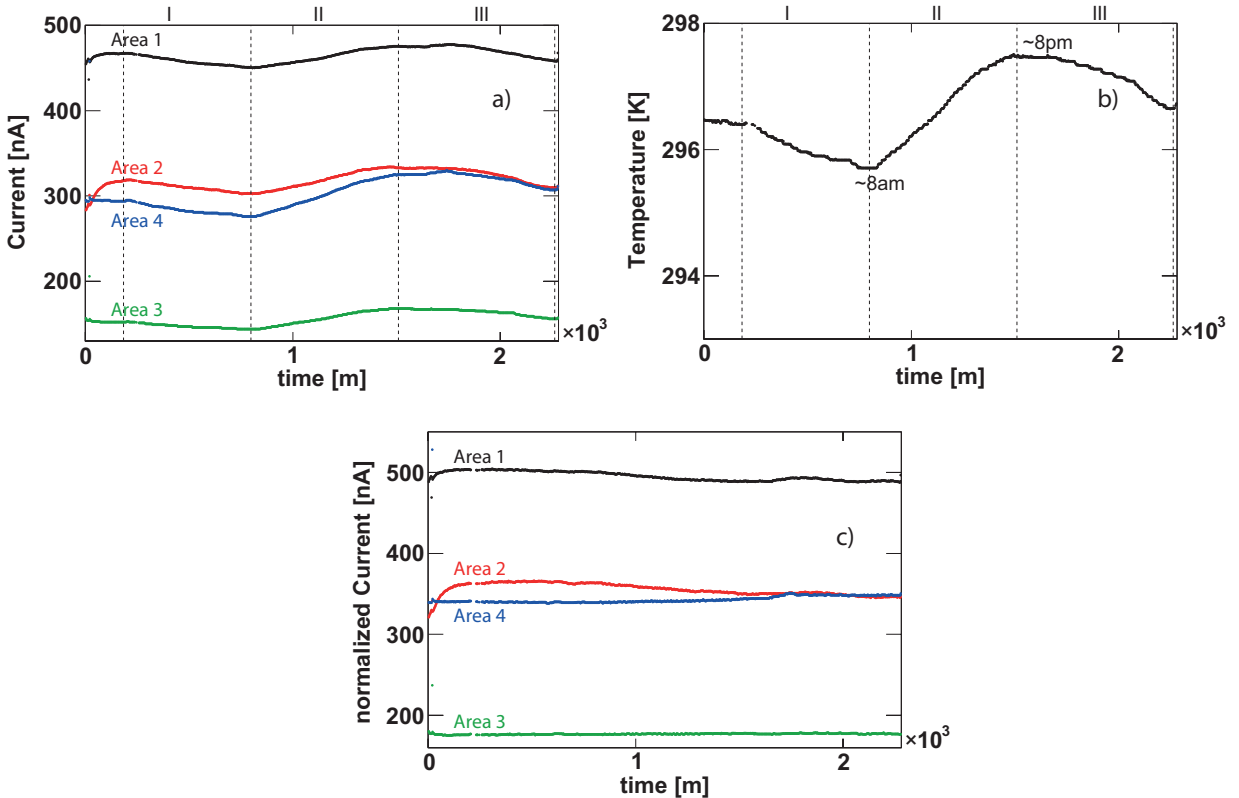


**Figure 5.10:** Currents, temperature and normalized currents as a function of time for 36h of measurement without proton beam. In a) the currents for all channels and in b) the corresponding temperature is plotted. The maximum and minimum in the temperature can be attributed to evening and morning. Panel c): Currents after normalizing to a temperature of 25°C. See text for details.

Hence,  $\beta$  has to be extracted from the data. The way how this was done is exemplified in appendix C.2. By using the experimentally determined values of  $\beta$ , the measured currents could be normalized to a temperature of 25°C (298.15 K). This was done individually for each detector area, and the results are shown in panel c) of Figure 5.10. The normalized currents are rather flat as it should be for a measurement at constant temperature. The remaining small fluctuations in the currents are probably due to surface cross currents, which could not be completely eliminated, even though the detector was flushed with nitrogen.

Important is that the temperature induced current fluctuations are well under control and could be canceled out so that the effect of radiation could finally be tested.

For that purpose, protons from the tandem accelerator at MLL were impinged on the detector. After the 20 MeV protons left the beam pipe, they lost energy in the air and in the aluminum window of the box so that only 15 MeV protons reached the detector. The energy loss estimation was carried out with the program LISE++ [Lab12]. For the measurement of the leakage currents, the beam was not used in continuous mode, but high intensity periods were alternated with periods of no beam. The number of protons passing the silicon and hitting the scintillator is plotted as a function of time in Figure 5.11 a). In total, seven high intensity beam periods, each with  $2.5 \cdot 10^9$  protons, are visible. Hence, a total amount of  $17.5 \cdot 10^9$  protons was passing the detector. Due to a small readout problem, some data points around  $t \approx 2500$  minutes are missing in the picture. In panel b) the currents, normalized to a temperature of 25°C, are plotted. Since the beam was only hitting the lower left part of the detector (see Figure 5.9), the currents in Area 1 and Area 2 are rather flat, whereas step like jumps appear for Area 3 and Area 4. These jumps are time-correlated with the high intensity phases in panel a), and are therefore attributed to increases in the leakage currents due to radiation. Two phases have to be distinguished here:

- **Phase 1:** During the irradiation, the currents were particularly large because the protons ionized the silicon, created electron-hole pairs and, thus, induced a measurable signal.
- **Phase 2:** The beam was turned off and the currents went back to a constant level. However, this level is shifted upwards compared to the one before Phase 1. This shift can be attributed to radiation damages.

By summing up the current jumps in Area 3 and Area 4, the total current increase  $\Delta I$  of

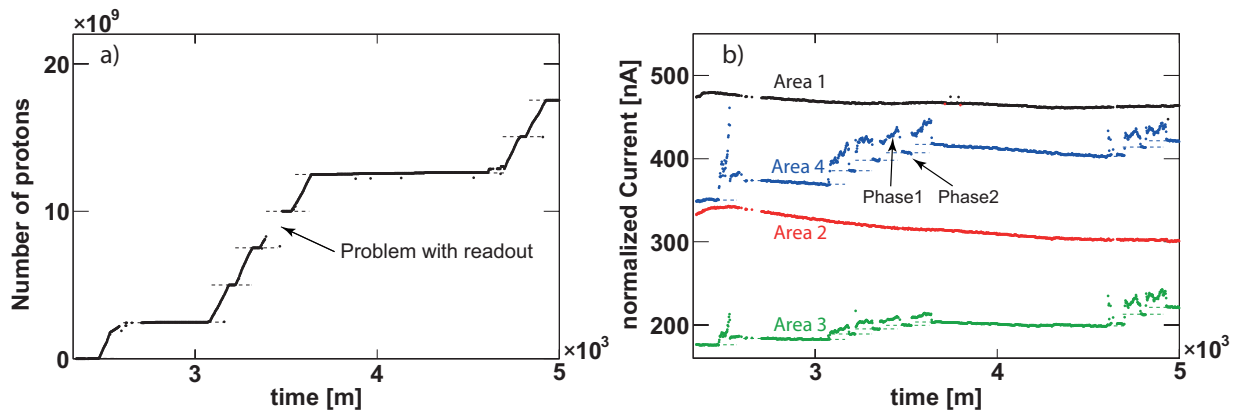


**Figure 5.11:** Panel a): Total number of protons measured in the scintillator. Panel b): Normalized currents during the proton beam. The beam spot was only hitting Area 3 and Area 4 (see Figure 5.9). The meaning of Phase 1 and Phase 2 is explained in the text.

the detector as a function of the equivalent particles dose  $N_{eq}$  can be investigated. In order to determine the equivalent dose, the value  $\kappa \approx 3.0$  for 15 MeV protons was extracted from Figure 5.8. The resulting distribution is shown in Figure 5.12 a). The seven data points were fitted with the function (5.2) (red line), resulting in an  $\alpha$  value of:

$$\alpha_{25^\circ C} = 9.2^{+1.8}_{-1.1} \cdot 10^{-17} \frac{A}{cm}$$

The systematic errors on this quantity was estimated by varying the normalization value  $\beta$  (see equation (5.3)). Instead of the arithmetic mean value  $\bar{\beta}$ , the individual  $\beta$  values from the time ranges I, II and III were used (see appendix C.2). The so obtained difference in the current increase  $\Delta I$  was taken in order to determine the error band in Figure 5.12 a), and the corresponding variation in the extracted  $\alpha$  values was taken as the systematic error on the quoted value.

Panel b) of Figure 5.12 shows  $\alpha$  extracted after normalizing the leakage currents to different temperatures (black dots). This allows to compare the CERBEROS results to the results obtained in other experiments. The authors of [RKP96] measured  $\alpha$  for two different *constant* temperatures (10°C and 25°C). Furthermore, in order to study the time dependence, they extracted two  $\alpha$  values; one directly after the beam period, where  $\alpha$  is rather large, and one after several days of annealing time, where  $\alpha$  is significantly smaller. The result without any annealing (open blue triangle) is quite comparable to the result of this work, where the detector had also almost no time to anneal. In this sense the two measurements are consistent. It has to be mentioned that a normal  $p^+n$ -type silicon detector has been used in [RKP96].

By normalizing the currents to 20°C, the  $\alpha$  value of the CERBEROS detector can be compared to the value quoted in [Lin03]. In this measurement, the used silicon detector had time to anneal at high temperatures of around 60°C. The resulting  $\alpha$  value of  $4.0 \cdot 10^{-17} A/cm$  (open red square in Figure 5.12 b)) is about 50% smaller than the value extracted in this work. This result proofs that annealing indeed helps to reduce the radiation induced damages. On the other hand, the result from Wunstorf et al. (see [Lut99, Wun92]), where  $\alpha$  was measured without annealing, is again close to the CERBEROS result (see open red triangle).

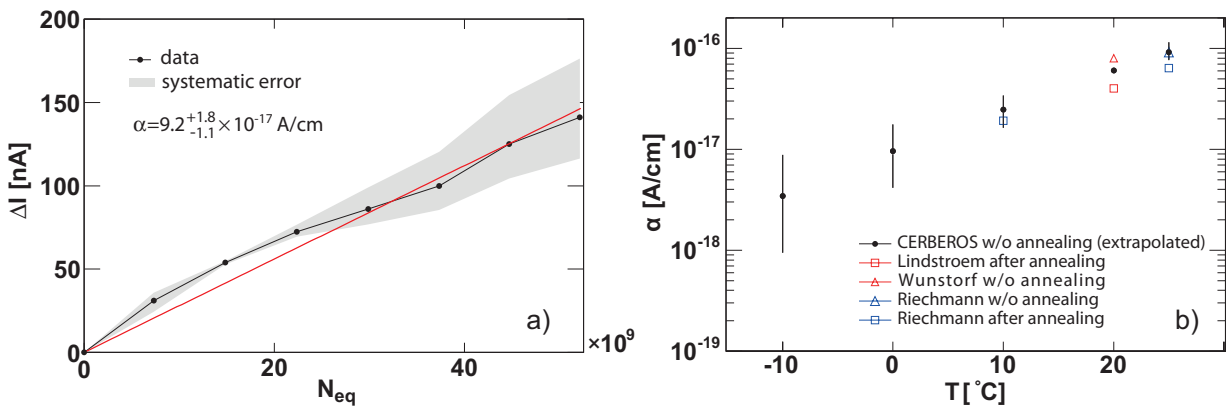


**Figure 5.12:** Panel a): Measured increase in the leakage current as a function of the equivalent particle dose  $N_{eq}$ . Panel b):  $\alpha$  from equation (5.2) for different temperatures and different experiments [RKP96, Lin03, Wun92].

In summary, it can be concluded that the  $n^+p$  detectors unfortunately do not show the expected improved radiation hardness, but they behave similar to normal  $p^+n$  silicon detectors. This information is important in order to estimate if they can survive the expected pion flux.

For that purpose, a beam time of around 25 days is considered. With the expected  $\pi^-$  flux of  $\approx 1 \cdot 10^6 \frac{1}{s}$  at the HADES target (see [SKV<sup>+</sup>]), a total dose of  $2 \cdot 10^{12}$  pions is expected on the detector at position  $H_3$  in Figure 5.2. Taking into account the  $\kappa$  factor for 1 GeV pions ( $\kappa \approx 0.5$ ), this translates into an equivalent dose of  $N_{eq} = 1 \cdot 10^{12}$  and a current increase of  $\Delta I \approx 2.8 \mu A$  at  $T = 25^\circ C$ . Compared to this, the detector at position  $H_2$  in the dispersive plane is expected to see a 10 times larger dose [Fab13] because the beam is still contaminated by other particles than pions in this area of the beam line. Thus, the current increase can be estimated to be about one order of magnitude larger in that case.

It is not clear which influence such a current increase would have for the identification of MIPs, especially if the new readout system is used. To be on the save side, the detector is planned to be cooled down to around  $0^\circ C$  [Wir12]. Compared to  $T = 25^\circ C$ , this reduces the expected leakage current increase and the factor  $\alpha$  by about one order of magnitude (see Figure 5.12) so that the detectors should easily survive the expected particle dose.

The investigation of the leakage current behavior has thus proven that these detectors can indeed be used for the planned pion beam time.



## 6 Summary and Outlook

The thesis has presented the reconstruction of the hyperon resonances  $\Sigma(1385)^+$  and  $\Lambda(1405)$  in  $p + p$  reactions at 3.5 GeV kinetic beam energy. The analyzed data were taken with the HADES experiment at GSI in the year 2007.

First, the reaction  $p + p \rightarrow \Sigma(1385)^+ + n + K^+$  was investigated, where the  $\Sigma(1385)^+$  was reconstructed in the  $\Lambda\pi^+$  decay channel. This reaction has so far never been analyzed in the SIS18 energy range. After selecting the charged particles in the final state with help of  $dE/dx$  and mass cuts, the  $\Lambda$  and the neutron could be identified by using the invariant mass and missing mass methods. Finally, the  $\Sigma(1385)^+$  signal could be accessed in the invariant mass spectrum of  $\Lambda$  and  $\pi^+$ . The different investigated spectra showed a considerable contamination by misidentification background caused by the poor  $K^+$  identification. In order to handle this background, a dedicated sideband method was used, which allowed to determine the relative contributions of misidentified pions and misidentified protons. Physical background, like the non-resonant production of  $\Lambda\pi^+$  pairs, was simulated. In this way all background sources could be evaluated and the pure  $\Sigma(1385)^+$  signal could be extracted. By fitting this signal with a relativistic p-wave Breit-Wigner function, the mass and width of the  $\Sigma(1385)^+$  were determined to  $m_0 = 1383.2 \pm 0.8^{+0.1}_{-1.5}$  MeV/ $c^2$  and  $\Gamma_0 = 40.2 \pm 2.1^{+1.2}_{-2.8}$  MeV/ $c^2$ . These new measurements were included into the particle summary table of the Particle Data Group (PDG) [B<sup>+</sup>12].

Besides extracting the  $\Sigma(1385)^+$  line shape, also the production process of the reaction was investigated. For this purpose, the CMS-, Gottfried-Jackson- and helicity-angle distributions of the three primary particles ( $\Sigma(1385)^+$ ,  $n$  and  $K^+$ ) were studied. In order to understand the observed distributions, a simulation model was developed. This model was used to apply acceptance and efficiency corrections to the experimental data so that differential cross sections could be extracted.

The corrected angular distributions in the different reference frames show strong anisotropies. This indicates that the exchange of (light) strange or non-strange mesons is the main production mechanism in the investigated reaction. One helicity angle distribution further suggests that about 33% of the  $\Sigma(1385)^+$  yield stems from an intermediate heavy  $\Delta^{++}$  resonance, decaying into  $\Sigma(1385)^+$  and  $K^+$ . Also the decay of the  $\Sigma(1385)^+$  in the  $\Lambda\pi^+$  Gottfried-Jackson frame was investigated. The obtained angular distribution shows only a small anisotropy, which might be a hint that also  $K^*$  exchange contributes to the production of the final state particles. Finally, the differential cross section distributions were integrated and a total cross section of  $\sigma = 22.42 \pm 0.99 \pm 1.57^{+3.04}_{-2.23}$   $\mu b$  for the reaction  $p + p \rightarrow \Sigma(1385)^+ + n + K^+$  was extracted. The results of this work were also published in [A<sup>+</sup>12a].

An important success of the presented analysis was the development of a method that allowed to correct the experimental data for the limited HADES acceptance and efficiency. Only in this way differential cross sections could be extracted. On the basis of the presented data, new theory models can be developed and further insight into the production process of the  $\Sigma(1385)^+$  can be gained. Furthermore, the obtained results can help to extend transport models by a more precise treatment of the  $\Sigma(1385)^+$  dynamics. This is important for a reliable interpretation of the  $K^-$  yields measured in heavy ion collisions.

The second part of the thesis was devoted to the analysis of the reaction  $p+p \rightarrow \Lambda(1405)+p+K^+$ , where the  $\Lambda(1405)$  was reconstructed in the charged  $\Sigma^\pm\pi^\mp$  decay channel. The applied analysis methods were similar to those used for the reconstruction of the  $\Sigma(1385)^+$ . The final state particles were also selected via  $dE/dx$  cuts; the intermediate  $\Sigma$  hyperons and the neutron were identified with help of the missing mass method. The remaining data were subdivided into two individual data samples, one containing an intermediate  $\Sigma^+$  hyperon and one containing an intermediate  $\Sigma^-$  hyperon. In this way the two decay channels of the  $\Lambda(1405)$  were separated. The  $\Lambda(1405)$  signal was then reconstructed in the missing mass spectrum to proton and  $K^+$ . This spectrum was again contaminated by misidentification background, which was handled with the same sideband method used for the  $\Sigma(1385)^+$  analysis. Furthermore, also physical background sources turned out to be important. By studying different observables and by comparing the experimental data to simulations, it was found that the reactions  $p+p \rightarrow \Sigma(1385)^0+p+K^+$ ,  $p+p \rightarrow \Lambda(1520)+p+K^+$ ,  $p+p \rightarrow \Sigma^-+\Delta^{++}(1232)+K^+$  and  $p+p \rightarrow \Sigma^++\pi^-+p+K^+$  give considerable contributions to the final data set. The small contribution by  $\Sigma(1385)^0$  could be constrained from the neutral channel analysis [Epp12b], whereas the contributions of all other channels were fixed by a fit to the experimental data.

The obtained simulation model, containing all the mentioned reactions, was further tuned so that it could be used for final acceptance and efficiency corrections. In this way cross sections for the different reactions have been obtained. With help of these corrections also differential cross sections in the CMS were extracted. Here, the  $\Lambda(1405)$  turned out to be produced almost isotropically, which indicates that its production happens in very central  $p+p$  reactions.

The spectral shape of the  $\Lambda(1405)$  was finally investigated in the corrected missing mass distributions to proton and  $K^+$ . Interestingly, the  $\Lambda(1405)$  signal appeared at masses clearly below its nominal mass, namely around 1385 MeV/ $c^2$ . By doing several consistency checks, it could be argued that this signal must indeed correspond to  $\Lambda(1405)$ . Furthermore, the comparison to other measurements of  $\Lambda(1405)$  has shown that a similar mass shift was observed in  $\pi^-+p$  reactions. The origin of this low mass signal was discussed on the basis of different models. A first theoretical approach interprets this signal in the so-called AY-ansatz, where the  $\Lambda(1405)$  is treated as a pure  $\bar{K}N$  quasi-bound state with a binding energy of 27 MeV. This ansatz turned out to describe the observed spectral shape very well. In contrast to this, the chiral ansatz, assuming the  $\Lambda(1405)$  resonance to consist of two poles, gives a less satisfying description of the experimental data. However, it was also pointed out that interference effects might play an important role for the interpretation of the data. With help of a simple approach it was shown that the interference of the  $\Lambda(1405)$  amplitude with the non-resonant background could substantially shift the observed mass signal. This effect could partially explain the observed low mass  $\Lambda(1405)$  signal.

The presented results, which were also published in [A<sup>+</sup>12d, A<sup>+</sup>13], will hopefully trigger new theoretical effort in the sector of  $\Lambda(1405)$  production in proton-proton reactions. The data can then help to answer the long standing question about the single- or double-pole nature of this resonance and will contribute to a better understanding of the low energy  $\bar{K}N$  dynamics. This, on the other hand, is an essential step for any reliable prediction on the in-medium spectral function of anti-kaons.

In the last part of the thesis, first performance tests of multi-strip  $n^+p$ -type silicon detectors were presented. These detectors will be the core of the pion tracker system CERBEROS, which will be used for the measurement of pion-induced reactions at the HADES detector. With help of a  $^{207}\text{Bi}$   $\beta$ -source, the detectors were calibrated and their resolution was investigated. They turned out to show a signal to background ratio of about 20, which is absolutely sufficient for

the identification of minimum-ionizing pion signals. Also their efficiency was determined to be larger than 90%. Additionally, the radiation hardness of these detectors was tested during a two days beam time at the MLL tandem accelerator in Munich. For this purpose, a high intensity proton beam of 20 MeV energy was impinged on the detector. By measuring the increase in the leakage current, the  $\alpha$ -value was determined to  $\alpha_{25^\circ C} = 9.2_{-1.1}^{+1.8} \cdot 10^{-17} \frac{A}{cm}$ . This value is in perfect agreement with the results of other experiments, which indicates that the  $n^+p$ -type silicon detectors show the same radiation hardness as usual  $p^+n$ -type silicons. It was concluded from this result that the detectors should be cooled in order to survive a two weeks pion beam time at GSI.

At the moment, several different HADES projects are investigating the production of strange particles. Besides the presented study of the  $\Lambda(1405)$  and  $\Sigma(1385)^+$  resonance, also the reaction  $p + p \rightarrow \Lambda + p + K^+$  and the associated possible formation of  $ppK^-$  states is analyzed carefully [Epp12a]. The results of this work will help to answer the long-standing question about the existence of deeply bound kaonic clusters. The inclusive production of  $K_S^0$  and  $\Lambda$ s is currently investigated in  $p + p$  and  $p + Nb$  reactions [BC12]. The extracted differential distributions can be compared to the predictions of transport models and can yield information about in-medium scattering cross sections of these particles. Furthermore, these studies will shed new light on the in-medium potentials felt by kaons and  $\Lambda$ s.

Starting from 2014, the experiments of proton-induced reactions will be complemented by a new campaign of pion-induced reactions. Here it is planned to measure elementary as well as pion-nuclei reactions. These experiments are perfectly suited to further investigate the hyperon resonances  $\Lambda(1405)$  and  $\Sigma(1385)$ . Moreover, the production of kaons and anti-kaons in cold nuclear matter can be studied in  $\pi^- + A$  collisions. With all those measurements, HADES will give an important contribution to the interesting topic of strangeness physics and will help to answer the question about the in-medium properties of kaons and anti-kaons.



# A Appendix to the $\Sigma(1385)^+$ analysis

## A.1 Origin of the background

The distribution below and besides the neutron signal in Figure 3.11 is considered.

All channels, which have a proton, a  $K^+$ , a  $\pi^+$  and a  $\pi^-$  in the final state, were simulated with full scale simulations. It turned out that none of these channels can give a contribution to the spectrum left to the neutron peak. This result can be easily understood. Assuming the four final state particles (proton,  $K^+$ ,  $\pi^+$ ,  $\pi^-$ ), baryon number conservation requires another (undetected) baryon in the final state. The cheapest solution for this in terms of energy is a neutron. Instead of a neutron, also a proton could, for example, be created. Charge conservation requires, however, that additionally a negatively charged particle like a  $\pi^-$  has to be produced as well. In this case the missing mass to the four detected particles has to be the invariant mass of the missing proton and  $\pi^-$ , which is at least the sum of the proton and the  $\pi^-$  mass, namely  $938.3 \text{ MeV}/c^2 + 139.6 \text{ MeV}/c^2 = 1077.9 \text{ MeV}/c^2$ . This is more than the neutron mass.

Thus, the only explanation for the structure below and on the left hand side of the neutron signal is misidentification background. It has already been mentioned that none of the final state particles can be identified with 100% purity, for which reason the term *candidates* was introduced. Indeed, it was already shown that especially the kaon candidates suffer from a considerable contamination by misidentified protons and pions (see Figure 3.8 and 3.13). Therefore, the assumption that all the background in Figure 3.11 stems from misidentified kaon candidates is justified, and, as will be shown in appendix A.2, it allows to describe the background perfectly.

One possibility to reduce the misidentification background is to do a new event hypothesis. Instead of tagging the  $K^+$  candidates as kaons, i.e. giving them the nominal  $K^+$  mass, one can also assume them to be pions or protons. Their 4-momentum is thus calculated with the (intentionally wrong) nominal pion or proton mass. With these assumptions the missing mass to proton,  $\pi^+$ ,  $\pi^+$  and  $\pi^-$  ( $\text{MM}(p, \pi^+, \pi^+, \pi^-)$ ) or to proton, proton,  $\pi^+$  and  $\pi^-$  ( $\text{MM}(p, p, \pi^+, \pi^-)$ ) was calculated for all events, contributing to Figure 3.11. The resulting distributions are plotted in Figure A.1, panel a) and b). Both pictures show clear peak structures, indicating missing particles. In panel a) a neutron signal is visible, stemming from the reaction

$$p + p \rightarrow p + \pi^+ + \pi^+ + \pi^- + n \quad (\text{A.1})$$

In panel b) a  $\pi^0$  signal as well as a small  $K^0$  signal are showing up. They dominantly stem from the reactions:

$$p + p \rightarrow p + p + \pi^+ + \pi^- + \pi^0 \quad (\text{A.2})$$

$$p + p \rightarrow p + \Lambda + \pi^+ + K^0 \quad (\text{A.3})$$

For those events, where a neutron, a  $\pi^0$  or a  $K^0$  appears, the former  $K^+$  assumption is obviously wrong and the new event hypothesis is correct. These events contribute to the misidentification

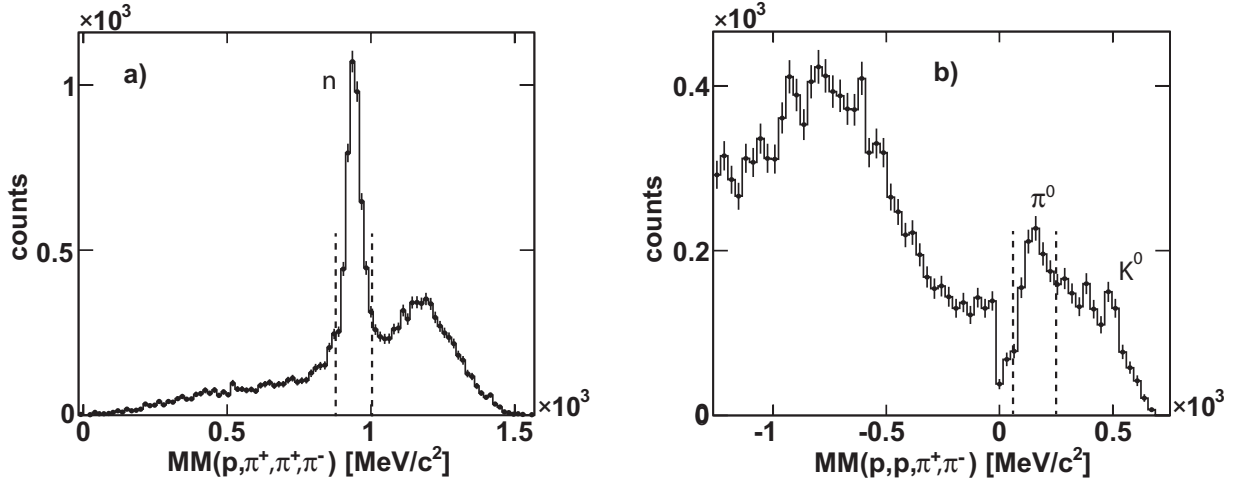


**Figure A.1:** Missing mass to the four detected charged particles with the assumption of the  $K^+$  candidate being either a  $\pi^+$  (a) or a proton (b). Vertical dashed lines indicate anti-cuts applied to the data.

background in Figure 3.11. In order to reject them, anti-cuts on either the neutron or the  $\pi^0$  signal can be applied (see vertical dashed lines in Figure A.1). The  $K^0$  signal was not rejected, as its contribution is very small anyway. With these anti-cuts, the  $MM(p, K^+, \pi^+, \pi^-)$  is again investigated in Figure A.2. Panel a) shows the result before (black data points) and after (red data points) the anti-neutron-cut on  $MM(p, \pi^+, \pi^+, \pi^-)$ . The cut reduces the misidentification background on the left hand side of the neutron peak. Below the neutron peak nothing changes. Panel b) illustrates the case where the anti- $\pi^0$ -cut on  $MM(p, p, \pi^+, \pi^-)$  has been applied (blue data points) and compares it again to the case where no anti-cuts have been used (black data points). Here a weak suppression of the background below the neutron signal is visible. However, it seems that the neutron peak itself is reduced even more by this anti-cut, which is undesirable. Summarizing the results of Figure A.2, none of the anti-cuts helps to reduce the misidentification background in a way that could be helpful for the  $\Sigma(1385)^+$  analysis. For this reason these

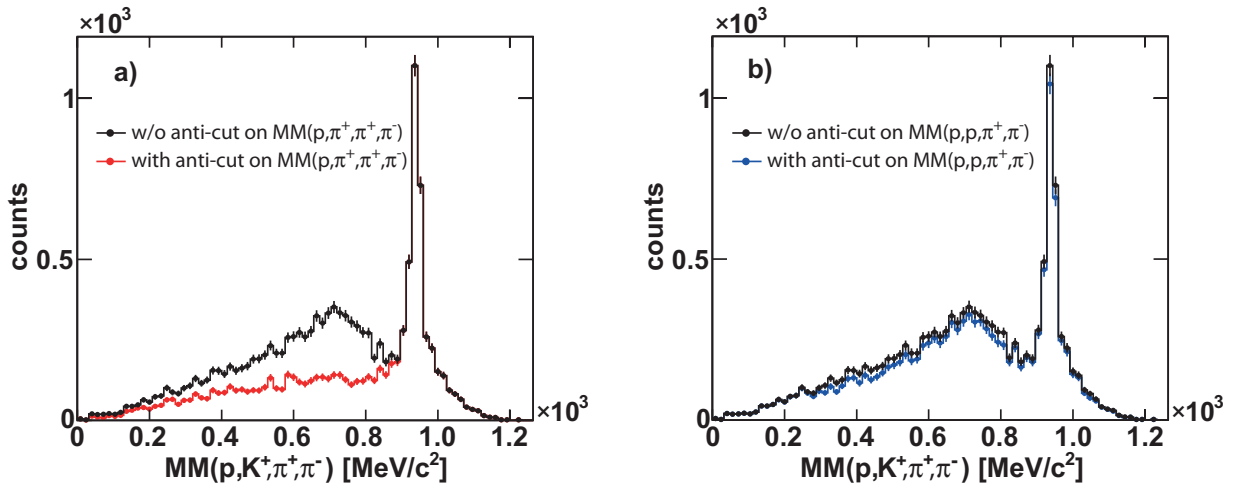


**Figure A.2:** Missing mass to the proton,  $K^+$ ,  $\pi^+$ ,  $\pi^-$  before and after anti-cuts on the neutron signal (a) or the  $\pi^0$  signal (b). See text for details.

cuts were not applied. However, the results from above indicate that the background below the neutron peak in Figure 3.11 does not stem from the reactions (A.1)-(A.3) with only one missing particle in the final state, but from reactions where even more particles are produced.

## A.2 Sideband method

There are two possibilities to handle the misidentification background below and besides the neutron signal in Figure 3.11. One option is to do full scale simulations of all possible contributing reactions; three of them have already been identified (reactions (A.1)-(A.3)). This approach is difficult, as all channels with their corresponding cross sections, which are often not known, have to be included in the simulations. Furthermore, a huge number of events has to be simulated in order to obtain enough statistic. A second option, the one which was used here, is to extract the misidentification background directly from the experimental data. The used method is called sideband analysis. It was initially developed in [Sie10a] and was further improved for this work. The general idea is the following:

The misidentification background is mainly caused by pions and protons, accidentally identified as kaons. If, on purpose, only pions and protons are selected and then tagged as kaons, one obtains a data sample, which contains only wrong kaon candidates. This *fake* data sample can be analyzed in the same way as the *original* data sample of section 3.2 and should thus describe the misidentification background.

In order to find the fake data sample, events with a proton a  $\pi^+$ , a  $\pi^-$  and a  $K^+$  candidate were selected. The identification of protons and pions was done with the same  $dE/dx$  cuts as shown in Figure 3.7. The kaon candidates were not selected by any  $dE/dx$  cut, but every positively charged particle was tagged as a  $K^+$  candidate instead. This guarantees a large contamination by pions and protons. The squared mass distribution of all these kaon candidates is illustrated in Figure A.3. Again signals due to pions and protons are visible, whereas kaons do not show up. Instead of selecting the kaon candidates by cutting around the nominal kaon mass, sideband cuts

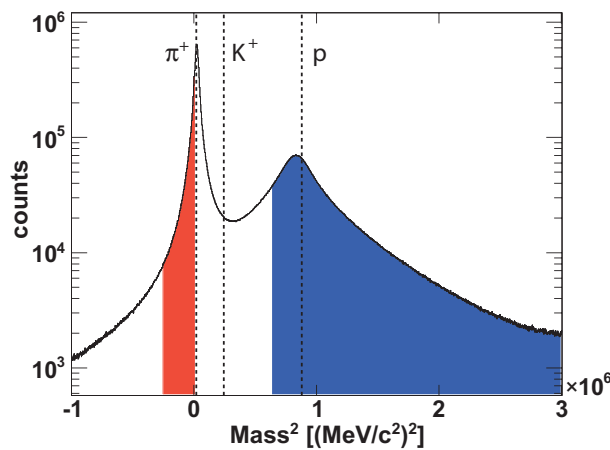


**Figure A.3:** Squared mass of all positively charged particles ( $K^+$  candidates). Vertical dashed lines indicate the nominal squared masses of  $\pi^+$ ,  $K^+$  and protons. The shaded regions indicate the mass areas chosen for the sideband samples.

on the red  $((-500 \text{ MeV}/c^2)^2 - 0 (\text{MeV}/c^2)^2)$  and blue  $((800 \text{ MeV}/c^2)^2 - (2500 \text{ MeV}/c^2)^2)$  shaded areas were applied. In this way two independent data samples were obtained:

1. One sample, containing a proton, a  $\pi^+$ , a  $\pi^-$  and another  $\pi^+$ , on purpose misidentified as a kaon candidate; this sample is from now on tagged as pion sideband sample.
2. One sample, containing a proton, a  $\pi^+$ , a  $\pi^-$  and another proton, on purpose misidentified as a kaon candidate; this sample is from now on tagged as proton sideband sample.

Although the sideband cuts are rather distant from the nominal kaon mass, it turned out that the pion sideband sample still contains real kaons. This is problematic, as a contribution of real kaons will result in a real neutron and a real  $\Sigma(1385)^+$  signal, which is undesired if only the misidentification background shall be modeled. In order to get rid of these true kaons, the kinematics of each pion sideband event were changed in a controlled way so that the real signal due to real kaons is *washed out*. The applied method to do this is schematically illustrated in Figure A.4. The tracks of the  $\pi^-$  and the  $\pi^+$  (not the kaon candidate) were combined to a common, fictive mother track  $X$  (panel a)). Afterwards, the pions were boosted in the rest frame of  $X$  (panel b)), where they are going back to back. Then the pion 3-momenta were rotated randomly within a solid angle of almost  $4\pi$  (panel c)). Their total momenta were unchanged in this way. Finally, the whole system was boosted back in the laboratory system, where the  $\pi^-$  and the  $\pi^+$  have new 3-momenta. On the other hand, the 3-momentum of the mother particle  $X$  stays unchanged (panel d)).

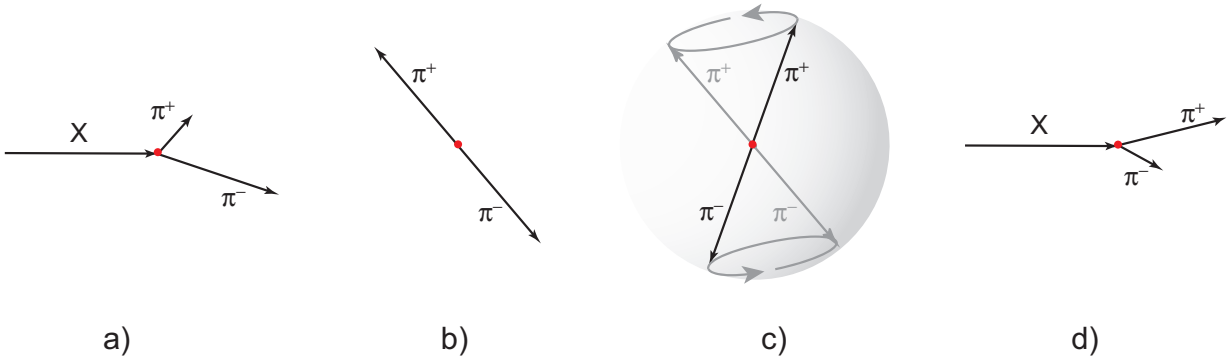


**Figure A.4:** Schematic representation of the pion momentum rotation, explained in the text.

In this way all variables which are calculated with help of the summed vector of the  $\pi^-$  and the  $\pi^+$  are not changed. This is, for example, the case for the variables  $MM(p, K^+, \pi^+, \pi^-)$  and  $M(\Lambda, \pi^+)$ , giving the neutron and the  $\Sigma(1385)^+$  signal in Figure 3.11 and 3.12. A significant change can, however, be observed in the invariant mass spectrum of the proton and the  $\pi^-$  ( $M(p, \pi^-)$ ).

Figure A.5 compares the two cases, before (gray histogram) and after (black histogram) rotating the pion momenta for the pion sideband sample. Before the rotation, a  $\Lambda$  peak is visible, which proves that the sample indeed contains true kaons. After the rotation, this peak is completely gone. Furthermore, it is important to see that, except of the  $\Lambda$  signal, the shape of the distributions are very similar, which indicates that the kinematics are maintained. Thus, a cut around the nominal  $\Lambda$  mass is possible without extracting any  $\Lambda$  signal and, therefore, without extracting a correlated real kaon. For the proton fake sample, the momentum rotation was not necessary as the contamination by real kaons is negligible.

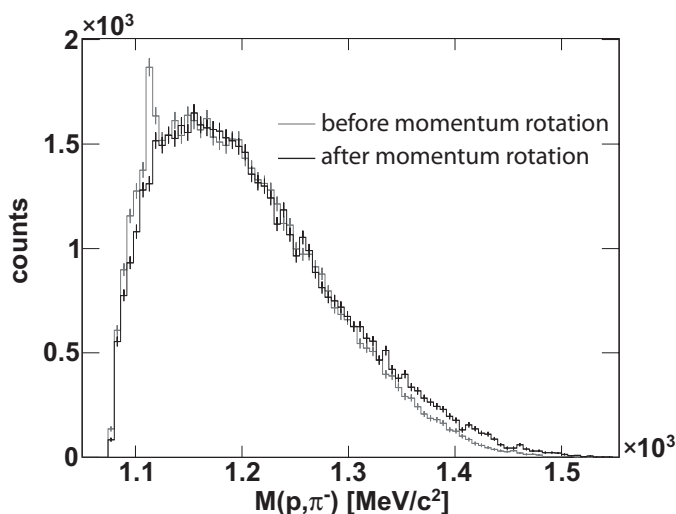


**Figure A.5:** Invariant mass of proton and  $\pi^-$  for the pion sideband sample after cuts on the neutron signal ( $877 \text{ MeV}/c^2 < MM(p, K^+, \pi^+, \pi^-) < 1000 \text{ MeV}/c^2$ ).

In order to describe the misidentification background, the rotated pion sideband sample and the proton sideband sample had to be analyzed in the same way as the original data sample. This includes the same cut on the invariant mass of the proton and the  $\pi^-$ , as it is shown in Figure 3.10. The cut is essential, since it selects a certain phase space region of the data, which has to be modeled correctly by the sideband samples. The vertex cuts, which were mentioned in Table 3.1, were not used, as they do not select a special phase space region, but mainly reduce the statistic of the sideband data.

One could now try to describe the background in Figure 3.11 by plotting the  $MM(p, K^+, \pi^+, \pi^-)$  distributions for the two sideband samples. This, however, does not work in a straight forward way. In general, two problems have to be faced:

1. The kinematics of the kaon candidates in the pion or proton sideband sample are different compared to the kinematics of the original kaon candidates. However, in order to describe the background correctly, also these kinematics have to be modeled correctly.
2. It is not known how much pions and protons contribute to the misidentification background. Thus, a proper scaling factor for each sideband sample has to be found.

The first point becomes clear when one compares the momentum distribution of the original kaon candidates with the one of the sideband samples, as it is done in Figure A.6. The black data points show the distribution of the original kaon candidates ( $f_{K^+}(p)$ ). As only the misidentification background is modeled, an additional cut on  $MM(p, K^+, \pi^+, \pi^-) < 830 \text{ MeV}/c^2$  has been included. In this way the neutron signal in Figure 3.11 was excluded, and consequently only kaon candidates of events which contribute to the spectrum left to the signal were considered.

Compared to the black points are the momentum distributions of the kaon candidates in the pion sideband sample ( $f_{\pi^+}(p)$ ) and in the proton sideband sample ( $f_p(p)$ ), where the same cut on  $MM(p, K^+, \pi^+, \pi^-)$  has been applied before. The candidates of the pion sideband sample peak at low momenta, whereas the candidates of the proton sideband sample have a much broader momentum distribution. It is obvious that the black distribution has the characteristic features of both, the red and the blue distributions.

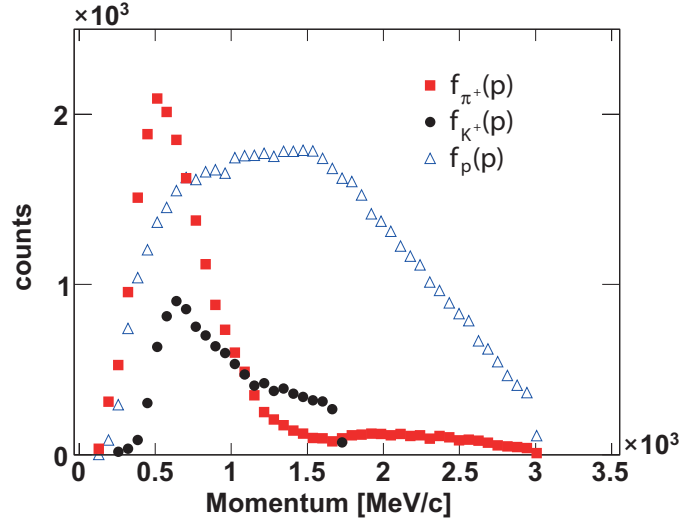


**Figure A.6:** Momentum distribution of kaon candidates of the original data sample ( $f_{K^+}(p)$ ) compared to the distribution of the kaon candidates from the pion sideband sample ( $f_{\pi^+}(p)$ ) and the proton sideband sample ( $f_p(p)$ ).

In order to model the kinematics of the original kaon candidates, the momentum distribution in the sideband samples was adapted to the black data points in Figure A.6. For this purpose, a momentum dependent scaling factor  $\gamma(p)$  was introduced:

$$\gamma(p) = \frac{f_{K^+}(p)}{\alpha f_{\pi^+}(p) + f_p(p)} \quad (\text{A.4})$$

This factor is nothing else but the momentum dependent ratio of the black histogram to the sum of the red and the blue histogram. Additionally, the factor  $\alpha$  was included, which is an unknown scaling factor to  $f_{\pi^+}$ . It accounts for the fact that the relative contribution of misidentified pions and misidentified protons to the original kaon candidates is unknown. By scaling each event of the pion sideband sample by  $\alpha \cdot \gamma(p)$  and each event of the proton sideband sample by  $\gamma(p)$  only, the summed momentum distribution of the two sideband samples would exactly reproduce the momentum distribution of the original kaon candidates. In this way the kinematics are reproduced.

At this point, only the factor  $\alpha$  is still unknown. In order to determine it, the  $\text{MM}(p, K^+, \pi^+, \pi^-)$  distribution is again considered. Each event of the pion and the proton sideband sample was weighted by the corresponding scaling factor ( $\alpha \cdot \gamma(p)$  and  $\gamma(p)$ ), and the summed  $\text{MM}(p, K^+, \pi^+, \pi^-)$  distribution was compared to the original distribution in Figure A.7, which shows the same data as in Figure 3.11. By varying  $\alpha$  in small steps of 0.2 between 0 and 100, the best agreement between the original and the sideband  $\text{MM}(p, K^+, \pi^+, \pi^-)$  distributions could be determined. This agreement was quantified by a  $\chi^2$  value, calculated within a mass range of  $-1000 \text{ MeV}/c^2 < \text{MM}(p, K^+, \pi^+, \pi^-) < 830 \text{ MeV}/c^2$ . The result is plotted in Figure A.7. The red and the blue distributions correspond to the contributions of misidentified pions and misidentified protons, obtained from the sideband samples. Their sum (gray histogram) perfectly describes the data. The best agreement (best  $\chi^2$ ) was obtained for a large contribution of misidentified pions, whereas the contribution of misidentified protons is rather small; thus, the value of  $\alpha$  is large.

With the obtained weighting factors  $\alpha$  and  $\gamma(p)$ , also the background directly below the neutron

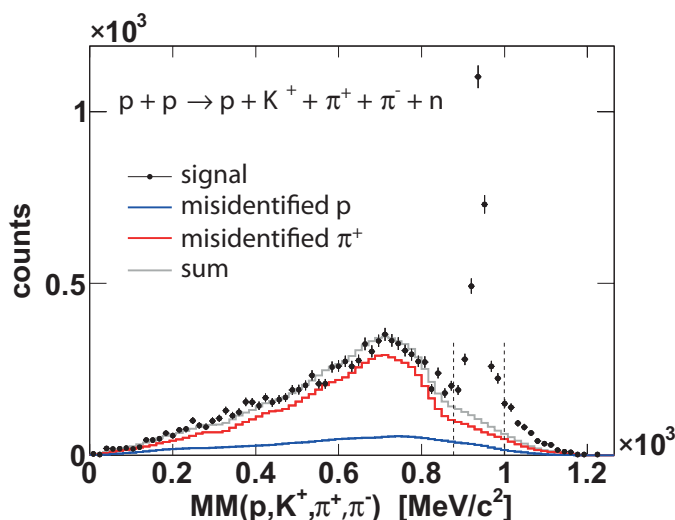


**Figure A.7:** Missing mass distribution to proton,  $K^+$ ,  $\pi^+$  and  $\pi^-$ . Compared are data (black dots) to the sum of misidentification background (gray histogram).

signal is predicted. Furthermore, the misidentification background in other observables, like in the invariant mass spectrum  $M(\Lambda, \pi^-)$  of Figure 3.12, could be modeled.

### A.3 Different Breit-Wigner parameterizations

In the different experiments, performed to measure the  $\Sigma(1385)^+$  resonance, different Breit-Wigner parameterizations were chosen to fit the experimental data. For example, a relativistic s-wave Breit-Wigner with mass dependent width was used in [Bau84], whereas the authors of [ABS81, Bor74] chose a mass independent width. In this part it shall be tested how the choice of the Breit-Wigner parameterization influences the extracted values of  $m_0$  and  $\Gamma_0$ . For that purpose, the same fitting procedure as described in section 3.2.2 was applied to the experimental data in Figure 3.15, and only the Breit-Wigner function (3.16) was exchanged by:

1. A relativistic Jackson p-wave Breit-Wigner without Blatt-Weisskopf correction term.

$$BW = A \cdot C_{Eff}(m) \cdot C_{PS}(m) \cdot \frac{q^2}{q_0^2} \frac{m_0^2 \Gamma_0^2}{(m_0^2 - m^2)^2 + m_0^2 \Gamma^2} \quad (\text{A.5})$$

$$\text{with } \Gamma = \Gamma_0 \frac{m_0 q^3}{m q_0^3}$$

2. A relativistic s-wave Breit-Wigner with mass dependent width, similar to what was used in [Bau84].

$$BW = A \cdot C_{Eff}(m) \cdot C_{PS}(m) \cdot \frac{m_0^2 \Gamma^2}{(m_0^2 - m^2)^2 + m_0^2 \Gamma^2} \quad (\text{A.6})$$

$$\text{with } \Gamma = \Gamma_0 \frac{m_0 q}{m q_0}$$

3. A relativistic s-wave Breit-Wigner with mass independent width, used in [ABS81].

$$BW = A \cdot C_{Eff}(m) \cdot C_{PS}(m) \cdot \frac{m_0^2 \Gamma_0^2}{(m_0^2 - m^2)^2 + m_0^2 \Gamma_0^2} \quad (\text{A.7})$$

4. A non-relativistic p-wave Breit-Wigner with mass dependent width and Blatt-Weisskopf correction term [Fri10].

$$BW = A \cdot C_{Eff}(m) \cdot C_{PS}(m) \frac{1}{q^2} \frac{\Gamma^2/4}{(m_0^2 - m^2) + \Gamma^2/4} \quad (\text{A.8})$$

$$\text{with } \Gamma = \Gamma_0 \frac{m_0 q^3}{m q_0^3} F_1(q)$$

$$\text{and } F_1(q) = \frac{1 + (q_0 R)^2}{1 + (q R)^2}$$

5. A non-relativistic s-wave Breit-Wigner with mass dependent width [Fri10].

$$BW = A \cdot C_{Eff}(m) \cdot C_{PS}(m) \frac{1}{q^2} \frac{\Gamma^2/4}{(m_0^2 - m^2) + \Gamma^2/4} \quad (\text{A.9})$$

$$\text{with } \Gamma = \Gamma_0 \frac{m_0 q}{m q_0}$$

The results of the different fits are summarized in Table A.1.

Breit-Wigner parameterization	$\Sigma(1385)^+$ mass $m_0$ [MeV/c <sup>2</sup> ]	$\Sigma(1385)^+$ width $\Gamma_0$ [MeV/c <sup>2</sup> ]	$\chi^2/ndf$
(3.16)	1383.2±0.8	40.2±2.1	0.92
(A.5)	1385.8±0.9	43.4±2.7	0.89
(A.6)	1382.3±0.8	39.9±2.1	0.84
(A.7)	1384.7±0.9	35.3±1.7	1.95
(A.8)	1383.9±0.9	40.7±2.3	0.92
(A.9)	1386.1±0.9	36.2±1.8	1.77

**Table A.1:** Extracted  $\Sigma(1385)^+$  properties for different Breit-Wigner parameterizations.

The extracted pole mass  $m_0$  is rather stable for all parameterizations. Differences can be seen in the width  $\Gamma_0$  and the fit quality  $\chi^2/ndf$ . Similar values of  $\Gamma_0$  ( $\approx 41$  MeV/c<sup>2</sup>) are obtained for the equations (3.16), (A.5), (A.6) and (A.8), for which also  $\chi^2/ndf$  is stable around 0.9. Only for the parameterizations (A.7) and (A.9), which are both of s-wave type, the fit quality is much lower, correlated with a reduced width of  $\approx 36$  MeV/c<sup>2</sup>. Thus, the extracted properties of the  $\Sigma(1385)^+$  indeed depend on the Breit-Wigner formula, used in the fit. This can partially explain the differences of the presented results to the values quoted in [B<sup>+</sup>12]. However, as the  $\Sigma(1385)^+$  is a  $L = 1$  resonance, it seems to be appropriate to describe it with a p-wave formula, like it was done in this work with formula (3.16).

## A.4 Acceptance and efficiency corrections

The procedure to extract differential cross sections is exemplified with the distribution  $\cos\left(\theta_{CMS}^{\Sigma^*}\right)$  of Figure 3.18. The experimental data were subdivided into seven different regions of  $\cos\left(\theta_{CMS}^{\Sigma^*}\right)$  so that for each region an independent data sample was obtained. Each of those data samples was analyzed in the same way as described in section 3.2:

First, the neutron spectra were investigated in Figure A.8. The results are shown for six out of seven angular bins, where the used area of  $\cos\left(\theta_{CMS}^{\Sigma^*}\right)$  is indicated in the pictures as well. The misidentification background was independently determined for each spectrum. The relative contribution of reaction (3.15) (green histograms) was fixed by the fit to the integral spectrum in Figure 3.14; the contribution of the neutron signal (black histograms) was again determined for each spectrum individually. An excellent agreement between data and simulations is obtained. The background shape, which is different in all six pictures, is reproduced perfectly by the sideband method.

After the extraction of the neutron signals, the invariant mass of  $\Lambda$  and  $\pi^+$  was investigated in Figure A.9. Each spectrum was fitted with the different physical and non-physical background sources and with the Breit-Wigner formula (3.16), as it is described in section 3.2.2. Since the statistic in the individual samples can be rather low, the relative yield of channel (3.14) was estimated from the fit to the integral spectrum in Figure 3.15. To account for possible uncertainties in the yield of the corresponding misidentification background, its contribution was not completely fixed by the fit to the neutron spectrum, but it was allowed to be slightly varied by the fitting procedure. In this way an overall good description of the experimental data was achieved.

Finally, after subtracting all background sources, the pure  $\Sigma(1385)^+$  signals are shown in Figure A.10. These spectra were already corrected for acceptance and efficiency by multiplying the invariant mass distribution ( $Exp(M(\Lambda, \pi^+))$ ) with a one dimensional correction matrix  $M_{eff}^{-1}(M(\Lambda, \pi^+))$  (see also section 2.3.2):

$$Exp_{corr}(M(\Lambda, \pi^+)) = M_{eff}^{-1}(M(\Lambda, \pi^+)) \cdot Exp(M(\Lambda, \pi^+)) \quad (\text{A.10})$$

$$\text{with } M_{eff}(M(\Lambda, \pi^+)) = \frac{Sim_{final}(M(\Lambda, \pi^+))}{Sim_{org}(M(\Lambda, \pi^+))} \quad (\text{A.11})$$

The distributions  $Sim_{final}(M(\Lambda, \pi^+))$  and  $Sim_{org}(M(\Lambda, \pi^+))$  were taken from the simulation model. As explained in section 2.3.2,  $Sim_{org}(M(\Lambda, \pi^+))$  is the original simulated invariant mass distribution of the  $\Sigma(1385)^+$ , whereas  $Sim_{final}(M(\Lambda, \pi^+))$  is the reconstructed invariant mass distribution after processing the simulations through the whole simulation chain and after applying the same cuts as for the experimental data. This simulation chain includes the decay of  $\Sigma(1385)^+ \rightarrow \Lambda + \pi^+ \rightarrow (p + \pi^-) + \pi^+$  with a branching ratio of 56.33% (see channel (3.2)). The LVL1 downscaling factor of three, used during data taking (see chapter 2), was taken into account for the simulations as well. Furthermore, the M3-multiplicity trigger was included into the simulations. In the presented case, isotropic simulations of reaction (3.13) were used.

The  $\Sigma(1385)^+$  yield ( $N_{\Sigma(1385)^+}$ ) could then be extracted from each spectrum of Figure A.10 by integrating the corrected data. The obtained value of  $N_{\Sigma(1385)^+}$  is the total number of  $\Sigma(1385)^+$  hyperons, emitted into the corresponding phase space region and produced during the whole beam time.

This number could be transformed into a cross section by normalizing to the  $p + p$  elastic cross section [HAD11, K<sup>+</sup>71]:

$$\sigma_{\Sigma(1385)^+} = \frac{\sigma_{pp-el}}{N_{pp-el}} \cdot N_{\Sigma(1385)^+} \quad (\text{A.12})$$

$\sigma_{pp-el}$  is the known cross section for elastic scattering of  $p + p$  reactions at 3.5 GeV kinetic beam energy.  $N_{pp-el}$  is the number of reconstructed  $p + p$  elastic events after acceptance and efficiency corrections (see [HAD11]). Finally, the following scaling factor was used:

$$\sigma_{\Sigma(1385)^+} [\mu b] = \frac{1000}{13925 \cdot 1.6 \cdot N_{Files}} \cdot N_{\Sigma(1385)^+} \quad (\text{A.13})$$

with  $N_{Files}$  being the number of analyzed DST files (12271 in the case of this work).

With the knowledge about the individual cross sections in each panel of Figure A.10, the differential cross section as a function of  $\cos(\theta_{CMS}^*)$  can be plotted (see Figure 3.19).

The presented acceptance and efficiency correction procedure is universal and every differential cross section distribution, shown in this work, was extracted in this way. However, as already mentioned, the result of the correction procedure depends on the used simulation model (see e.g. section 2.3.2).

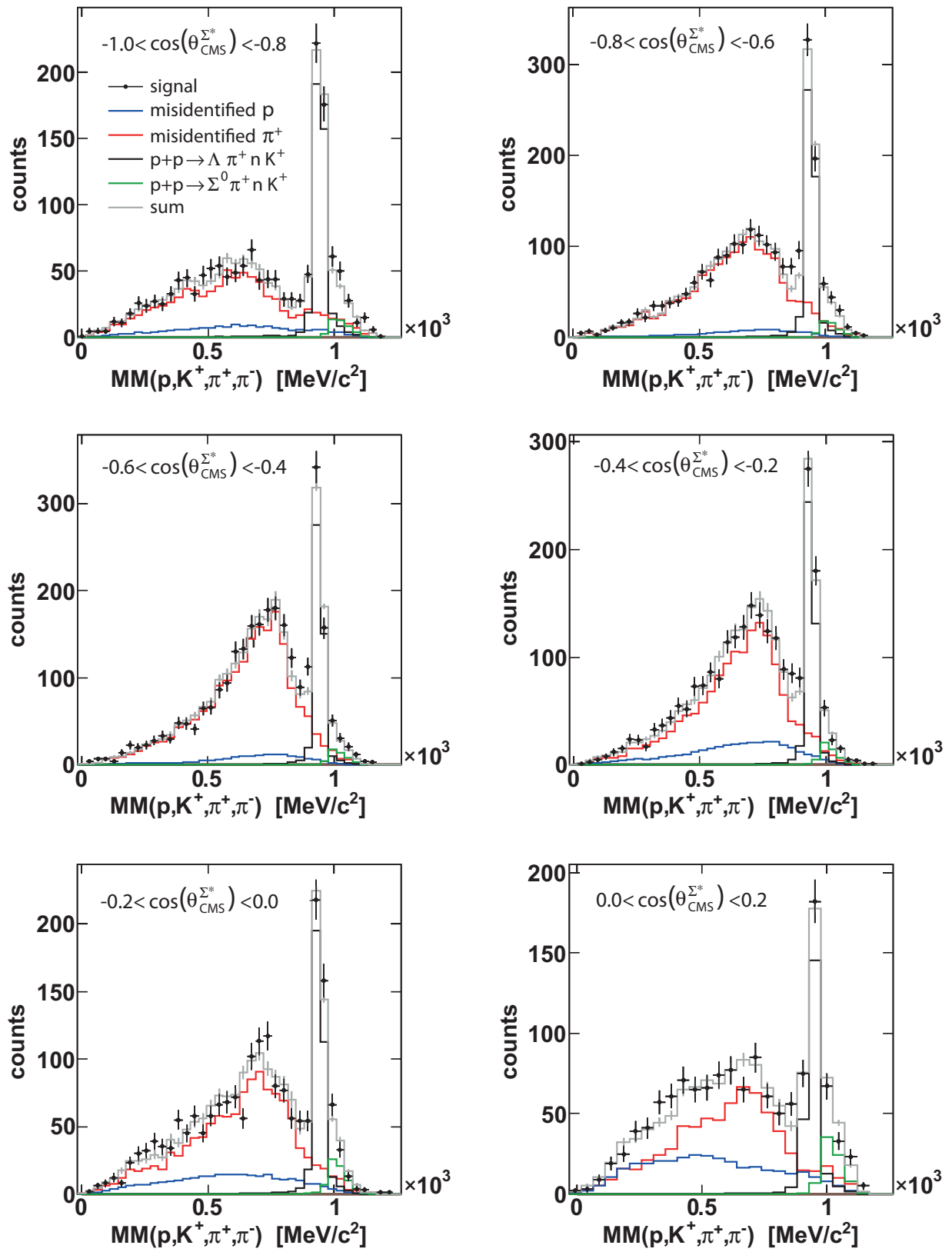


Figure A.8: Missing mass to the proton,  $K^+$ ,  $\pi^+$  and  $\pi^-$  for different regions of  $\cos(\theta_{\text{CMS}}^{\Sigma^*})$ .

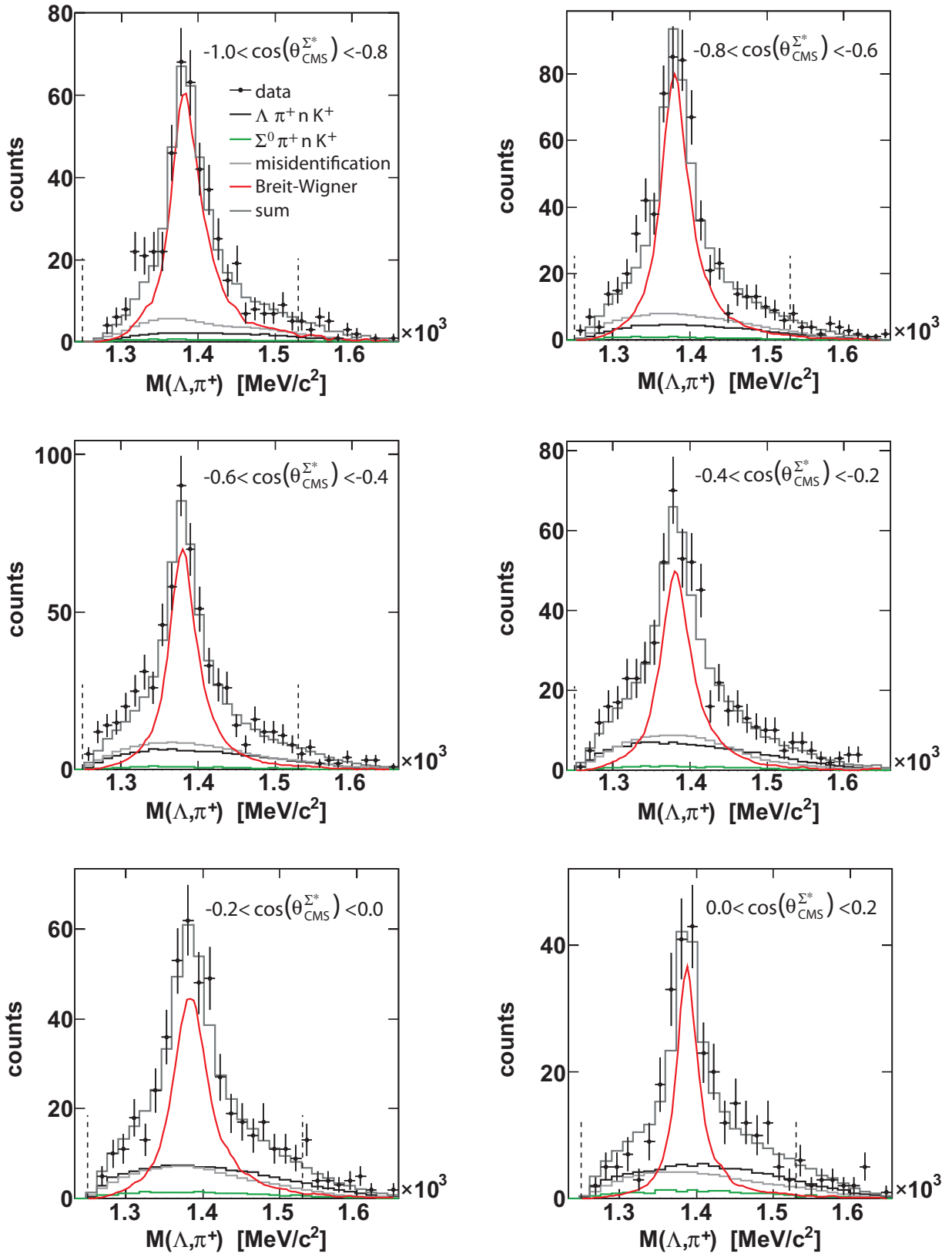
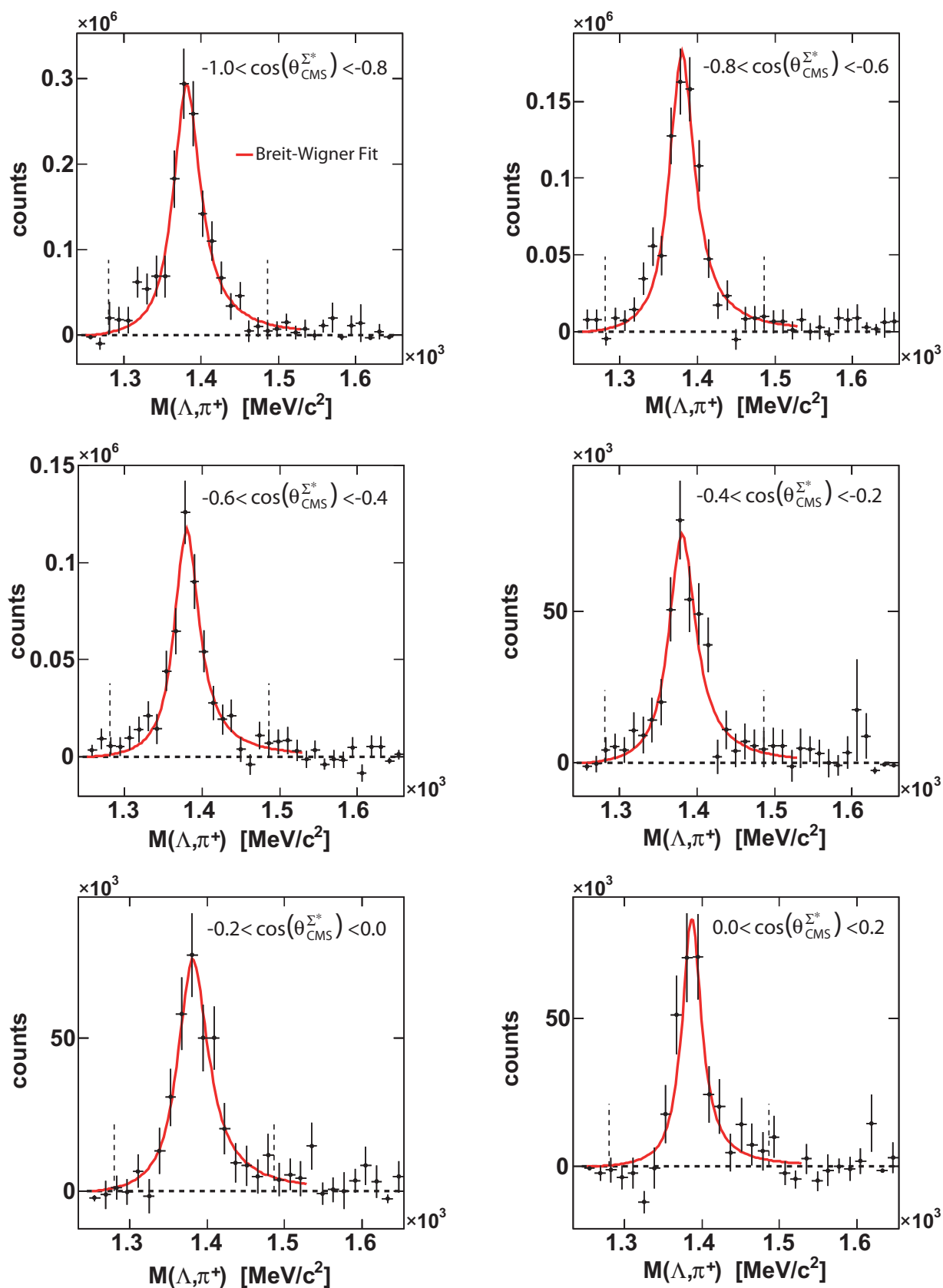


Figure A.9: Invariant mass of  $\Lambda$  and  $\pi^+$  for different regions of  $\cos(\theta_{CMS}^{\Sigma^*})$ .



**Figure A.10:** Invariant mass of  $\Lambda$  and  $\pi^+$  for different regions of  $\cos(\theta_{CMS}^{\Sigma^*})$  after subtracting the background and after correcting the spectra for acceptance and efficiency (see text for details). Breit-Wigner fits are indicated by the solid lines.

## A.5 Test of the simulation model

In the following the simulation model, developed in section 3.3.4, is further tested on several observables.

Besides the already discussed helicity angle distributions, also invariant mass spectra can be used to find evidence for intermediate resonances. Especially the invariant mass of the  $\Sigma(1385)^+$  and the  $K^+$  is interesting in terms of the assumed contribution of a  $\Delta^{++}$ . This observable is studied in Figure A.11, panel a). The good agreement between data and simulations indicates that pure non-resonant  $\Sigma(1385)^+$  simulations (red histogram) would not be sufficient to describe the data. In fact, the inclusion of a certain  $\Delta^{++}$  contribution (blue histogram) helps to account for the enlarged population of low invariant masses. However, the simulation model seems to slightly overshoot the experimental data exactly there, where the  $\Delta^{++}$  simulations are most prominent (see left hand side of the spectrum). This discrepancy can have different reasons. On the one side, the 33% contribution of resonant  $\Sigma(1385)^+$  production is an estimation obtained from Figure 3.24. Using instead a bit lower contribution of  $\Delta^{++}$  formation would already improve the situation. On the other side, the simulated mass and shape of the  $\Delta^{++}$  was obtained from the results in [C<sup>+</sup>68a]. By taking a larger mass of 2050 MeV/c<sup>2</sup>, which is also in perfect agreement with the helicity angle distribution (see Figure 3.24), the invariant mass spectrum might be described better. Furthermore, interference effects between the different  $\Sigma(1385)^+$  production channels can influence the investigated distributions as well. The simple simulation model does not take into account those effects, but assumes that all contributions sum up incoherently.

To find out which of the discussed effects finally causes the small discrepancy is beyond the purpose of this work; it is even not expected that these effects influence the obtained results and their interpretations. Important at this point is only that the spectrum is sufficiently well reproduced by the simulation model.

In panel b) of Figure A.11 the invariant mass of the  $\Sigma(1385)^+$  and the neutron is investigated. This observable could provide information about the possible existence of di-baryon resonances decaying into  $\Sigma(1385)^+$  and neutron. On the other hand, final state interactions between the hyperon and the nucleon would manifest itself in an enlarged population of low invariant masses. The experimental spectrum in panel b) shows neither indications for resonance contributions nor for these final state interactions, but it is perfectly described by the simulation model.

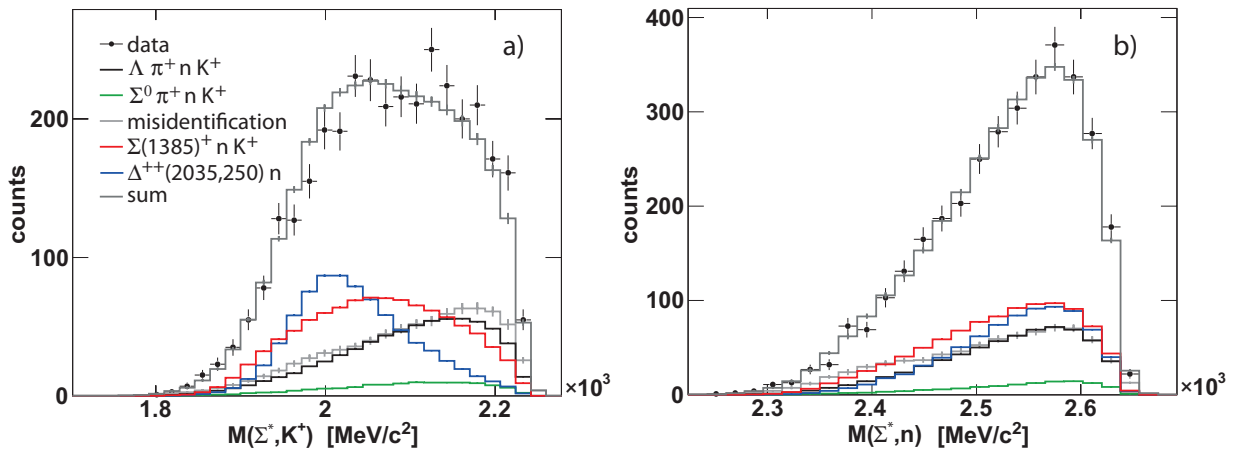


**Figure A.11:** Invariant mass of  $\Sigma(1385)^+$  and  $K^+$  (a) and invariant mass of  $\Sigma(1385)^+$  and neutron (b).

Another observable of interest is the momentum of the produced particles. Indeed, the peripheral character of the reaction and the associated low momentum transfer to the neutron and the  $\Sigma(1385)^+$  influences not only the emission angles of the particles, but also their absolute momenta. Therefore, a full description of the reaction dynamics is only achieved if the simulations reproduce the momentum distributions of the particles as well. To test this, the absolute momentum of the  $\Sigma(1385)^+$  and the neutron in the CMS is investigated in Figure A.12 a) and b), respectively. Also here the predictions of the model are very good. Only the peaking of the neutron momentum at  $p_{CMS}^n \approx 500$  MeV/c (see panel b)) seems to be slightly overestimated. This can again be attributed to the contribution of the  $\Delta^{++}$  simulations, which have a sharp maximum exactly at this position.

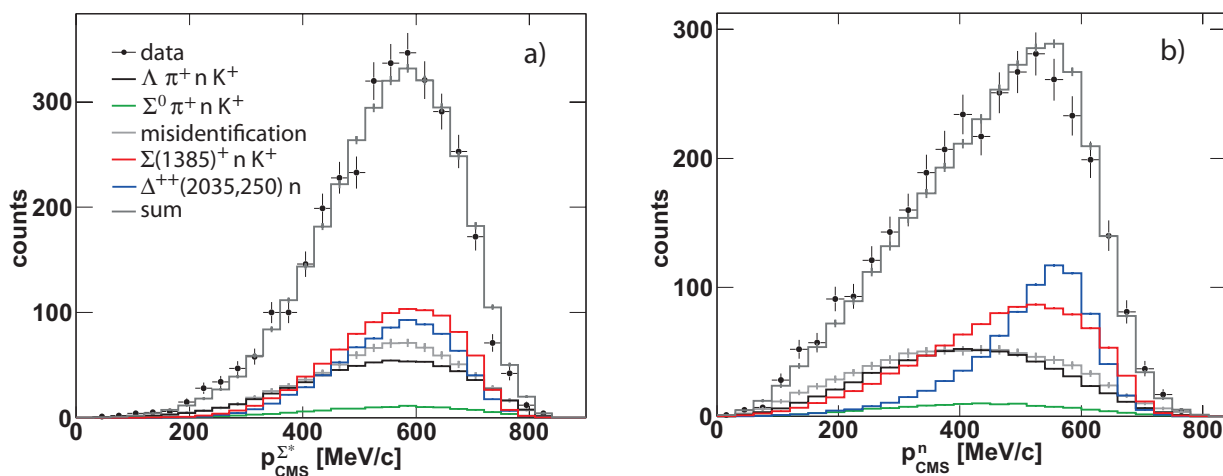


**Figure A.12:** Absolute momentum distribution of the  $\Sigma(1385)^+$  (a) and the neutron (b) in the CMS.

A further test of the simulation model concerns the opening angles between the  $\Sigma(1385)^+$ , the  $K^+$  and the neutron in the CMS, investigated in Figure A.13. The  $\Delta^{++}$  contribution in panel a) (blue histogram) shows smaller opening angles between the  $\Sigma(1385)^+$  and the  $K^+$  compared to the case of non-resonant  $\Sigma(1385)^+$  production (red histogram). This is a pure kinematical effect, attributed to the mass of the  $\Delta^{++}$ . However, the data clearly favor this scenario, which can thus be seen as a further proof that a certain contribution of  $\Delta^{++}$  is necessary in order to describe the data appropriately. The  $\Delta^{++}$  simulations are also needed for the description of the opening angles between the neutron and the  $K^+$  in panel b).

In panel c) the opening angle distribution between the  $\Sigma(1385)^+$  and the neutron is shown, which peaks at opening angles close to  $180^\circ$ . This is simply a consequence of energy and momentum conservation, which forces the  $\Sigma(1385)^+$  and the neutron to be produced almost back to back.

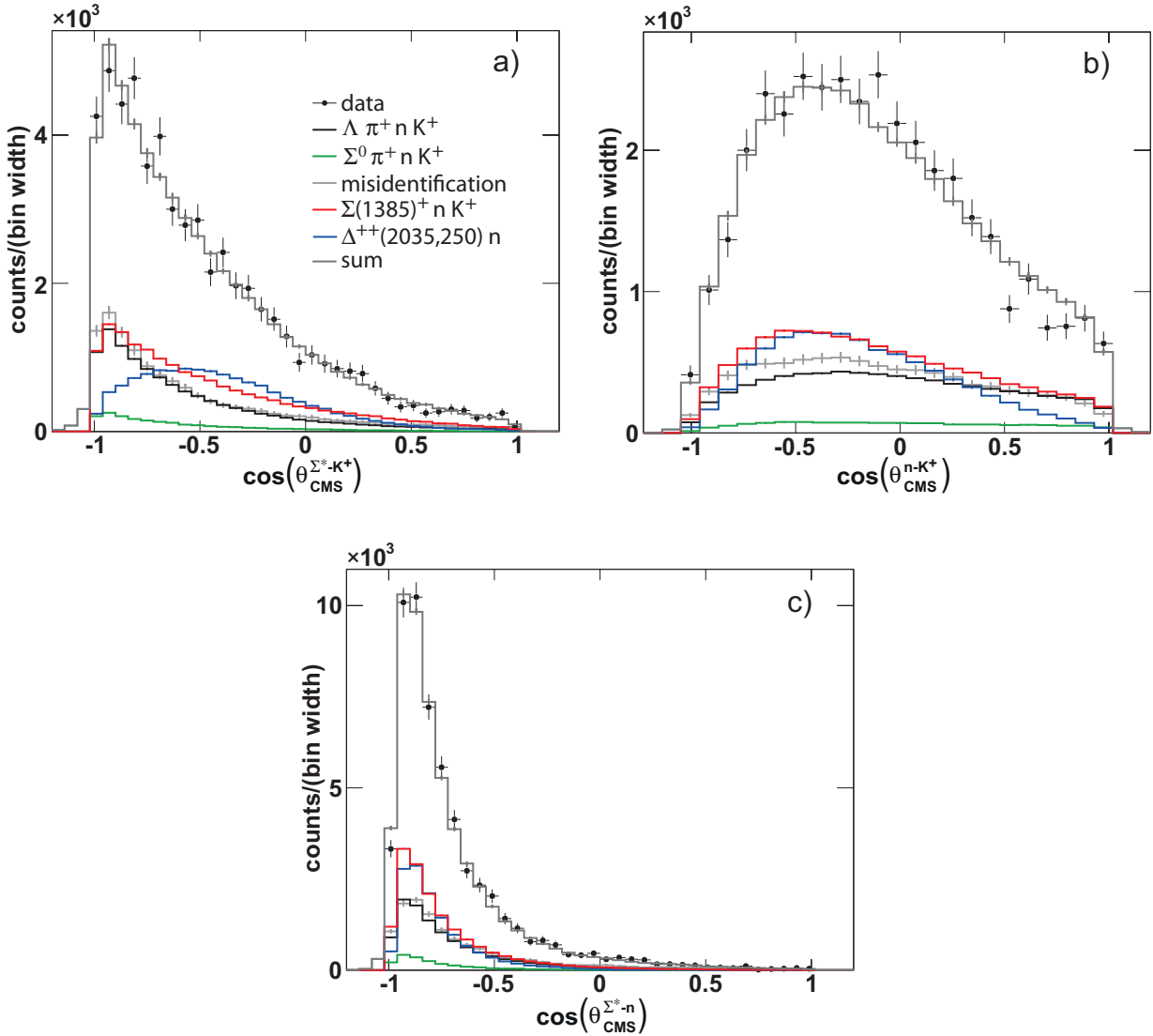


**Figure A.13:** Opening angles between the three primary produced particles ( $\Sigma(1385)^+$ ,  $K^+$  and neutron) in the CMS.

Last but not least, the contribution of the direct  $\Lambda$  and  $\pi^+$  production (reaction (3.14)) is investigated. This channel turned out to be an important background source in the  $\Sigma(1385)^+$  analysis. Till now, it was always assumed that the four particles ( $\Lambda$ ,  $\pi^+$ ,  $n$  and  $K^+$ ) are produced non-resonant in this reaction. On the other hand, it has already been mentioned that the decay of resonances plays a major role for the production of the final state  $\Lambda - K^+$ . The same is true for the production of a neutron and a  $\pi^+$ , which could proceed via an intermediate  $\Delta^+(1232)$  resonance. The possible contribution of these resonances is tested in Figure A.14, where the invariant mass of the neutron and the  $\pi^+$  is investigated in panel a), and the invariant mass of the  $\Lambda$  and the  $K^+$  in panel b). The data show no hints for any resonance structure, but are well reproduced by the non-resonant simulations of channel (3.14) (black histogram). This justifies the assumption that the reaction (3.14) is of non-resonant nature.

In summary, all the investigated observables show an excellent agreement between experiment

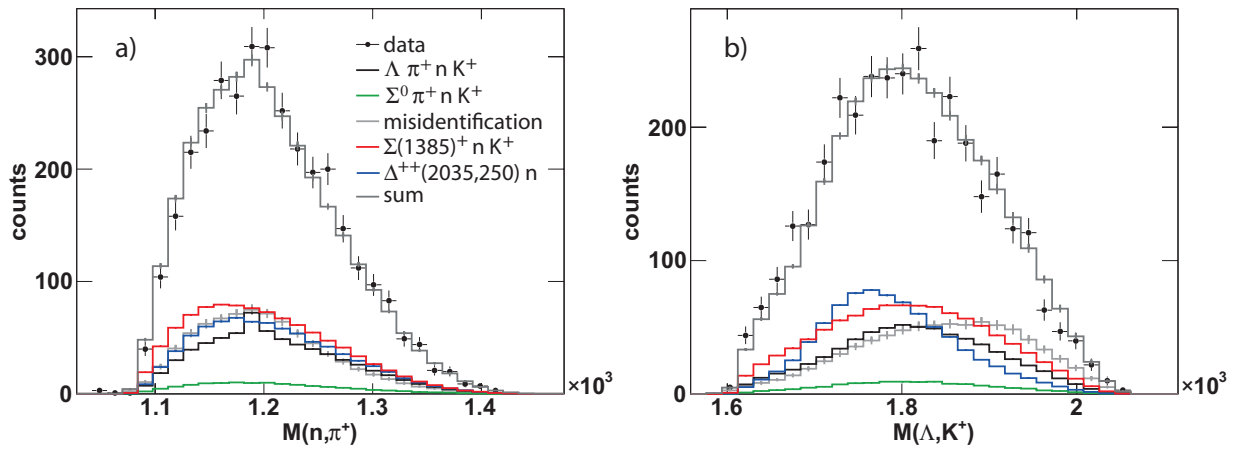


**Figure A.14:** Panel a): Test of possible  $\Delta(1232)$  contribution in the invariant mass of neutron and  $\pi^+$ . Panel b): Search for resonances in the invariant mass distribution of  $\Lambda$  and  $K^+$ .

and simulations. Thus, the obtained model describes the kinematics in the experimental data correctly, and it is therefore suited to be used for the efficiency corrections.



## B Appendix to the $\Lambda(1405)$ analysis

### B.1 Extraction of the differential cross section for $\cos(\theta_{CMS}^{A^*})$

The following part explains how differential cross sections in the observable  $\cos(\theta_{CMS}^{A^*})$  (see Figure 4.7 and 4.8) were obtained. After identifying the four charged particles ( $p, K^+, \pi^+, \pi^-$ ), the data were divided into three different regions of  $\cos(\theta_{CMS}^{A^*})$ . The 4-vector of the potential  $\Lambda(1405)$  candidate was thereby calculated from the missing 4-vector to the proton and the  $K^+$ . Each of the so obtained data samples was analyzed independently, as explained in section 4.1.

First, the neutron was reconstructed and the misidentification background was evaluated in the same way as it was done in Figure 4.1. After selecting the neutron signal, the two  $\Sigma$  hyperons were investigated. The  $\Sigma^+$  signals, obtained by evaluating the missing mass spectra to proton,  $K^+$  and  $\pi^-$ , are shown for the three different angular regions on the left hand side of Figure B.1. The right hand side shows the  $\Sigma^-$  signals in the missing mass distributions to proton,  $K^+$  and  $\pi^+$ . Thus, two neighboring pictures always belong to the same data sample. In all pictures the corresponding angular regions are indicated as well.

By selecting the  $\Sigma$  signals with help of  $3\sigma$  mass cuts and by applying the  $\chi^2$  cuts for the kinematic refits (see section 4.1.3), each sample was further divided into two subsamples, either containing intermediate  $\Sigma^+\pi^-$  pairs or intermediate  $\Sigma^-\pi^+$  pairs. The missing mass to proton and  $K^+$  for these subsamples is presented in Figure B.2 (compare to Figure 4.3). The left hand side shows the results for the  $\Sigma^+\pi^-$  samples, the right hand side for the  $\Sigma^-\pi^+$  samples. Again, two neighboring pictures belong to the same angular region and represent the two different decay channels of  $\Lambda(1405)$ . The different reactions contributing to the data are shown in the colored histograms in Figure B.1 and B.2. The relative yield of each channel was estimated with the same fitting procedure as presented in section 4.1.3. For this purpose, the four pictures in the first row of Figure B.1 and B.2 were fitted simultaneously in order to fix the yield of all contributions in the angular region of  $-1.0 < \cos(\theta_{CMS}^{A^*}) < 0.25$ . For the second row an independent fit was applied, determining the contributions for the second angular region, and so on. The achieved agreement between experimental data and simulations is convincingly good in all 12 pictures.

In a last step, the misidentification background was subtracted from the data so that only the physical sources remained. The experimental as well as the simulated spectra were then corrected for acceptance, efficiency and the branching ratio of the  $\Sigma^+$  decay. For these corrections the simulation model with the corresponding relative contribution of each reaction was used. The results for the two  $\Lambda(1405)$  decay channels in the different angular regions are shown in Figure B.3. Additionally, the spectra have already been normalized with help of  $p + p$  elastic data (see appendix A.4) so that differential cross sections are shown on the y-axis. The experimental data have large statistical fluctuations, especially for the high mass region in the first row. This must be attributed to the very limited statistic in the different data sets. This has as a further consequence that some mass ranges are not even populated by experimental data. Therefore,

in order to extract cross sections, it is not possible to integrate the experimental spectra of Figure B.3. On the other hand, the good agreement between data and simulations (see Figure B.1 and B.2) justifies to integrate the simulated distributions instead. This approach was also chosen in the present analysis. By doing this, a cross section value for each contributing reaction in each of the angular regions could be extracted. The statistical errors on these values were, however, determined from the statistical errors in the experimental data. The differential cross section for all channels as a function of  $\cos(\theta_{CMS}^A)$  is shown in Figure 4.8.

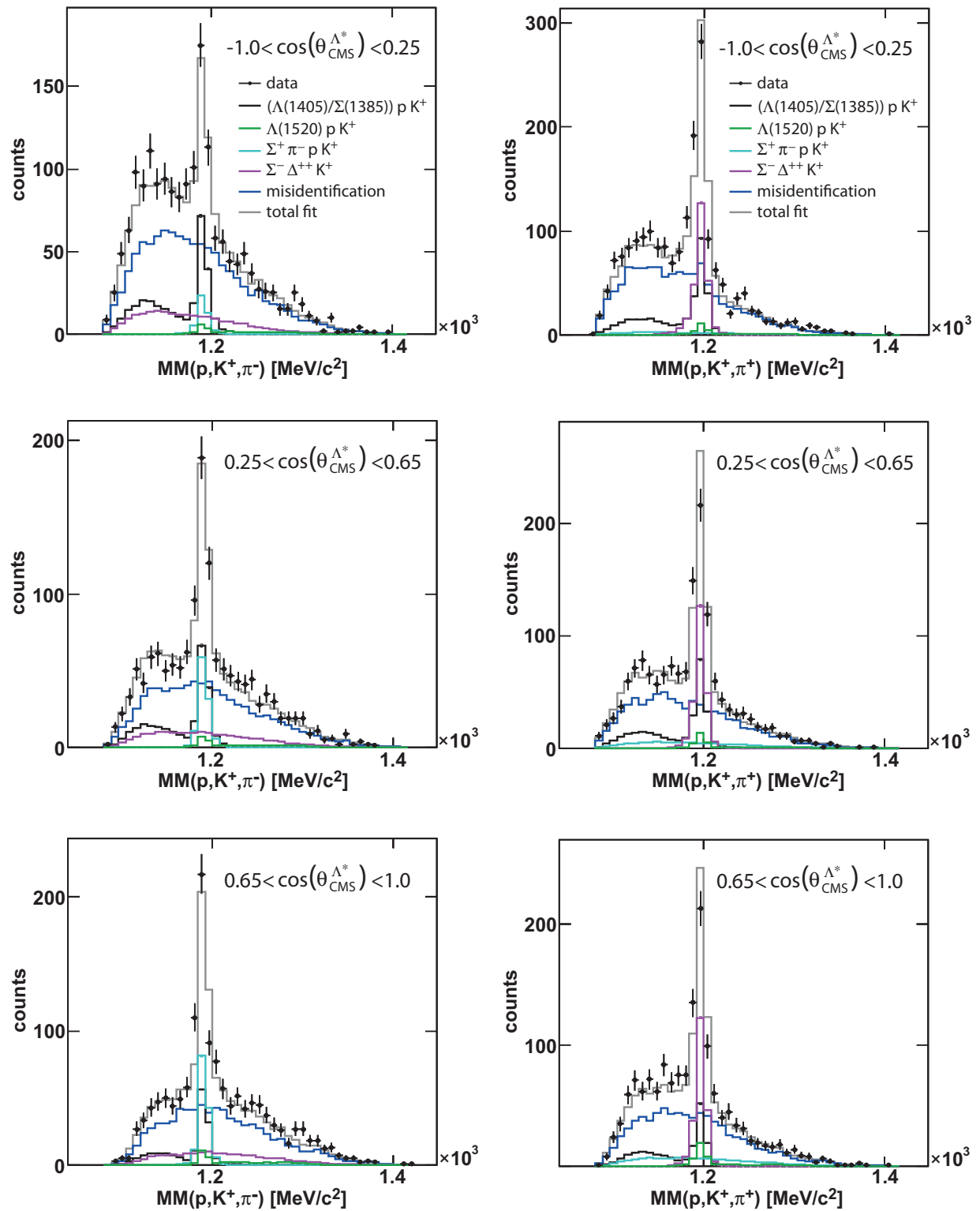


**Figure B.1:** Left hand side: Missing mass to proton,  $K^+$  and  $\pi^-$  showing a  $\Sigma^+$  signal. Right hand side: Missing mass to proton,  $K^+$  and  $\pi^+$  showing a  $\Sigma^-$  signal. The three different rows show the results for the three different angular regions of  $\cos(\theta_{CMS}^{\Lambda^*})$ . Colored histograms indicate the different contributing reactions.

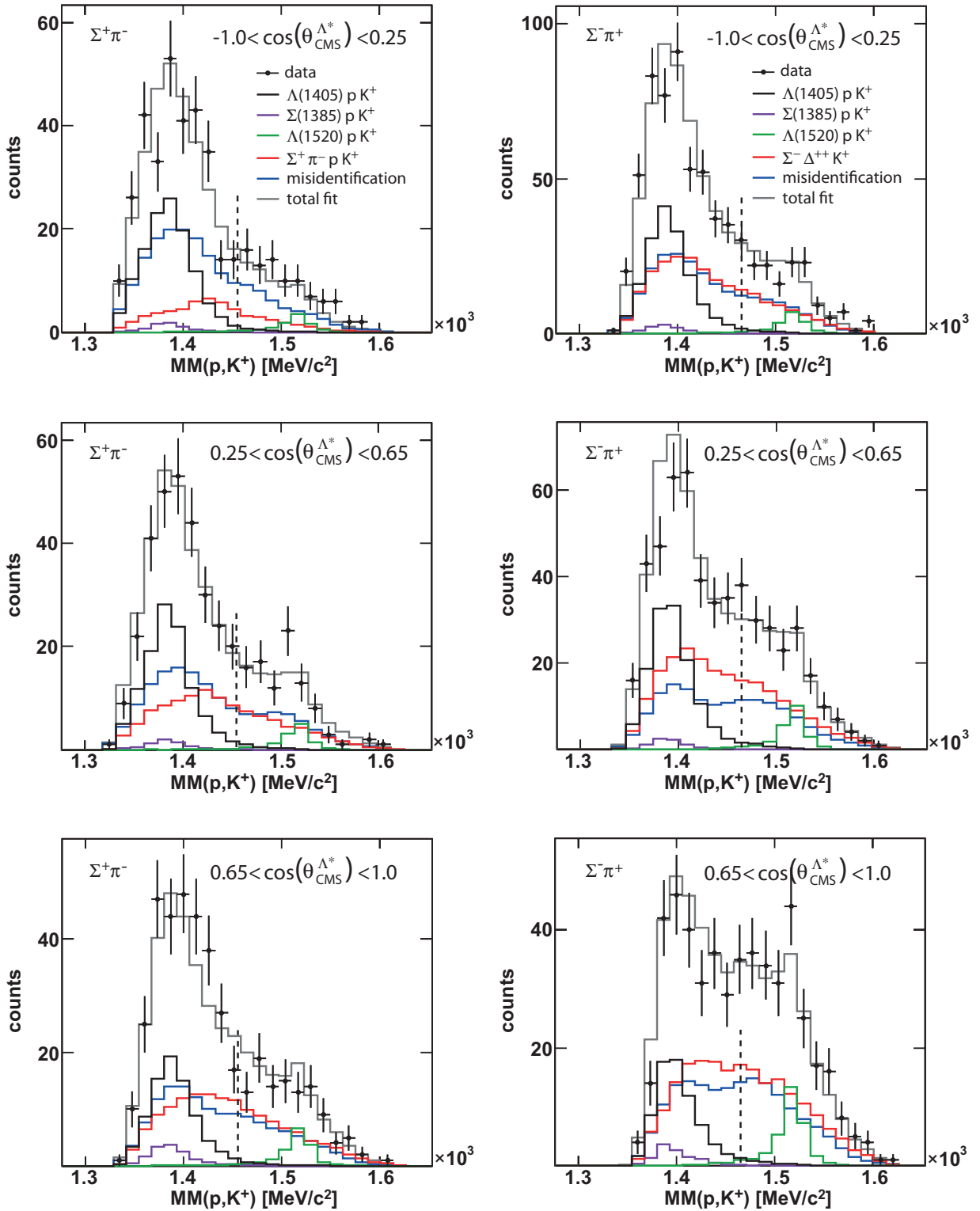


**Figure B.2:** Left hand side: Missing mass to proton and  $K^+$  for the  $\Sigma^+\pi^-$  subsamples. Right hand side: Missing mass to proton and  $K^+$  for the  $\Sigma^-\pi^+$  subsamples. The three different rows show the results for the three different angular regions of  $\cos(\theta_{CMS}^{\Lambda^*})$ . Colored histograms indicate the different contributing reactions.

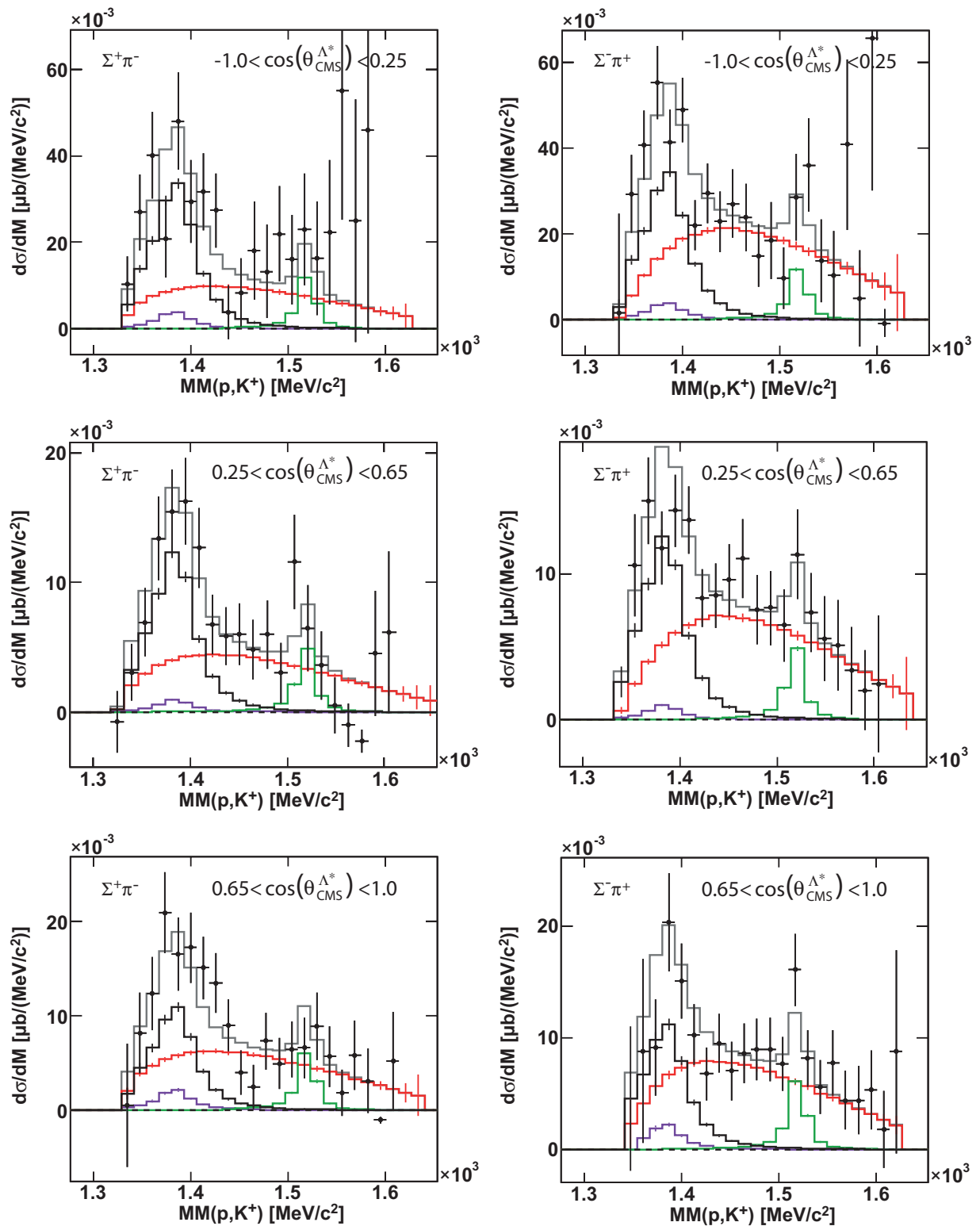


**Figure B.3:** Left hand side: Missing mass to proton and  $K^+$  for the  $\Sigma^+\pi^-$  subsamples. Right hand side: Missing mass to proton and  $K^+$  for the  $\Sigma^-\pi^+$  subsamples. The three different rows show the results for the three different angular regions of  $\cos(\theta_{CMS}^{\Lambda^*})$ . Data and simulations are acceptance and efficiency corrected and normalized with help of the  $p + p$  elastic cross section. The color code is the same as in Figure B.2.

## B.2 Further tests of possible contributing reactions

Besides the already considered reactions (4.15)-(4.22), it might be that even more reactions contribute to the  $\Lambda(1405)$  analysis. Considering for example the non-resonant  $\Sigma\pi$  reactions (4.18) and (4.22), the  $\Sigma$  and the  $K^+$  could be produced via an intermediate  $\Delta$  resonance, as it was the case for the production of  $\Sigma(1385)^+$  and  $K^+$  (see chapter 3). To test this hypothesis, the invariant mass of  $\Sigma$  and  $K^+$  is investigated in Figure B.4. Panel a) displays the result for the  $\Sigma^+\pi^-$  data sample, whereas panel b) illustrates the invariant mass for the  $\Sigma^-\pi^+$  data sample. Overlaid to the experimental data are the different identified contributions. For the non-resonant  $\Sigma\pi$  production channels (red histograms) only the reactions (4.18) and (4.22) have been considered, respectively. The assumed distributions in the simulations give already a very good description of the experimental data, which in turn do not show any significant hint for a resonance contribution. It is therefore concluded that it is sufficient to use the reactions (4.18) and (4.22) for the simulations of the non-resonant  $\Sigma\pi$  production.

Another test concerns the production of  $\Lambda(1405)$ . Till now, it was always assumed that the  $\Lambda(1405)$  and the  $K^+$  do not stem from a resonance, but that they are produced directly via reaction (4.15). To test if this hypothesis is correct, the invariant mass of the  $\Lambda(1405)$  candidate and the  $K^+$  is plotted in Figure B.5 for the  $\Sigma^+\pi^-$  (a) and  $\Sigma^-\pi^+$  (b) data samples, respectively. For that purpose, the 4-vector of the  $\Lambda(1405)$  candidate was calculated from the missing 4-vector to the proton and the  $K^+$  and from that the invariant mass was determined.

Also in these pictures the simulations describe the experimental data rather well and no clear indication of any higher resonances, decaying into  $\Lambda(1405)$  and  $K^+$  can be found. It can therefore be concluded that the developed simulation model is sufficient to describe the experimental data.

Last but not least, the invariant mass of the  $\Lambda(1405)$  candidate and the proton is investigated in Figure B.6. Here it is actually not expected to find any indication of di-baryon resonances. However, the  $\Lambda(1405)$  and the proton might experience final state interactions, which, on the other hand, can distort the measured  $\Lambda(1405)$  line shape. These final state interactions would show up in the investigated distributions. By comparing the simulations to the experimental data in Figure B.6, one does not find an indication for such a process, but again the data are described rather well by the assumed model.

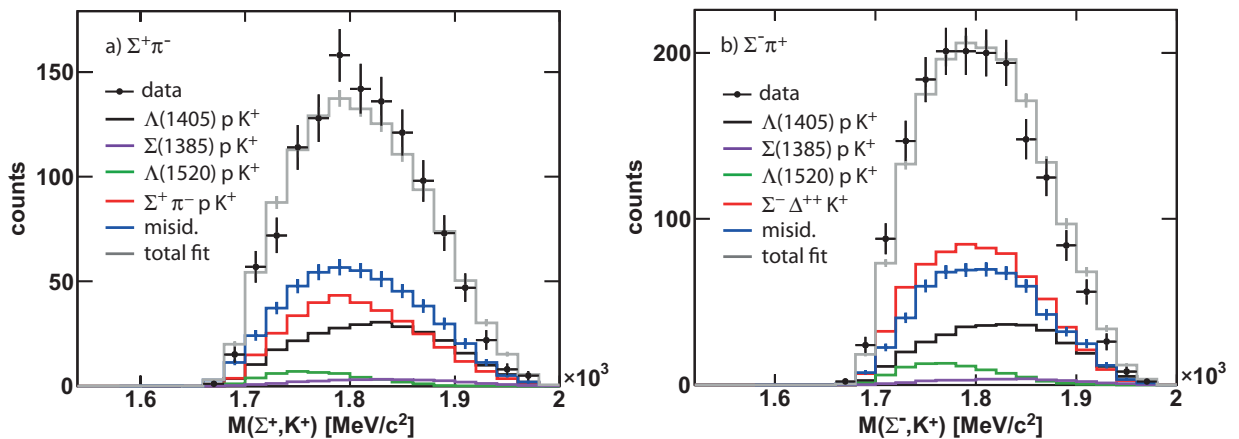


**Figure B.4:** a): Invariant mass of  $\Sigma^+$  and  $K^+$  for the  $\Sigma^+\pi^-$  data sample. b): Invariant mass of  $\Sigma^-$  and  $K^+$  for the  $\Sigma^-\pi^+$  data sample

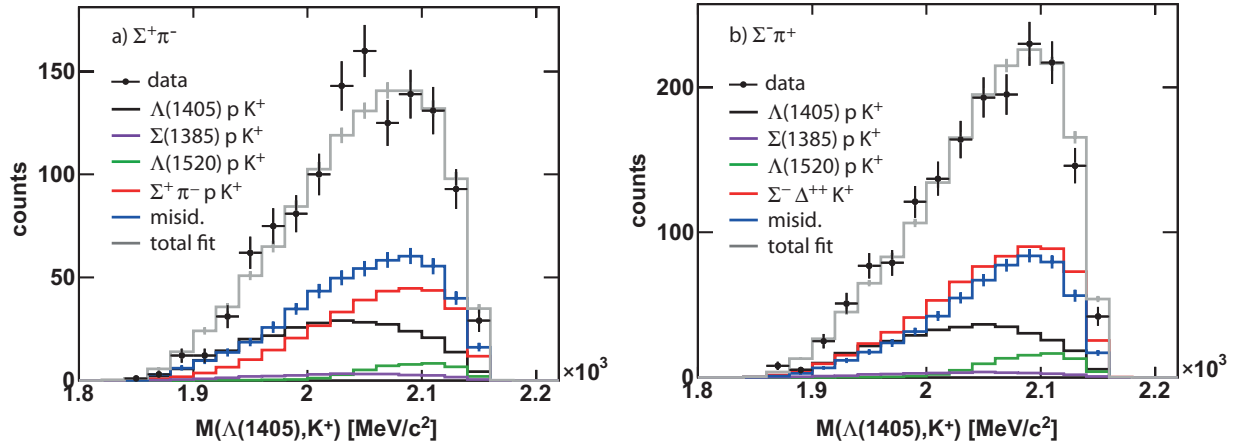


**Figure B.5:** Invariant mass of the  $\Lambda(1405)$  candidate and the  $K^+$  for the  $\Sigma^+\pi^-$  (a) and  $\Sigma^-\pi^+$  (b) data sample.

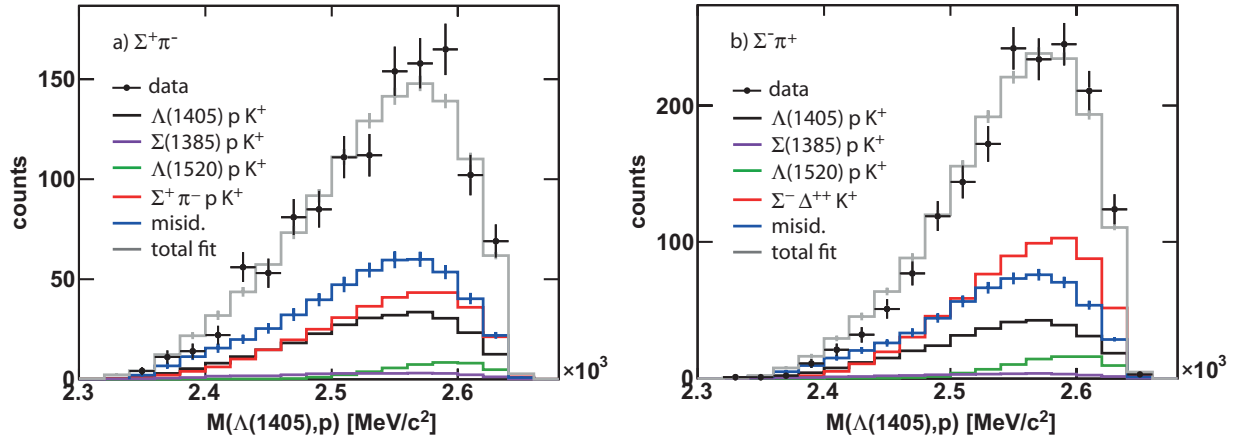


**Figure B.6:** Invariant mass of the  $\Lambda(1405)$  candidate and the proton for the  $\Sigma^+\pi^-$  (a) and  $\Sigma^-\pi^+$  (b) data sample.

It has, however, to be pointed out that the statistic in the data is limited and the different contributions of intermediate resonances or final state interactions, investigated in Figure B.4-B.6, cannot be totally excluded. On the other hand, the simulation model seems to be appropriate for the description of the kinematics in the experimental data, which is a necessary precondition to use this model for the corrections and the interpretation of the data.

### B.3 Additional angular distributions

The investigation of the distributions for the CMS, G-J and helicity angles (see Figure 4.9 and 4.10) has shown that the simulation model reproduces the experimental data satisfactorily in these observables. To make sure that the developed model is suitable for acceptance and efficiency corrections, further angular distribution shall be studied systematically at this point.

First, the opening angles between the  $\Lambda(1405)$  candidate, the proton and the  $K^+$  in the CMS are displayed. The cases of the  $\Sigma^+\pi^-$  sample and of the  $\Sigma^-\pi^+$  sample are presented in Figure B.7 and B.8, respectively. In appendix A.5 it was shown that the opening angle distributions are

sensitive to the underlying production processes of the three particles, and their investigation can therefore be seen as a consistency check of the simulation model. In all of the six pictures the simulations follow the distributions in the experimental data. A small deviation can only be found in Figure B.8, panel b), where the yield on the left hand side of the spectrum is slightly overestimated. This, however, is not significant, and it can still be concluded that the simulation model seems to be appropriate.

A further test concerns the single particle tracks of the final data samples. In fact, only the kaon, the proton and the missing vector to these two particles have been considered so far. The full event consists, however, also of the reconstructed  $\pi^-$  and  $\pi^+$  tracks. Therefore, the track properties of all four particles are investigated in the following. This test is important for the presented analysis. The reason is that the  $\Lambda(1405)$  signal is located at the lower edge of the available phase space (see Figure 4.3 a) and b)). Exactly there the acceptance of HADES shows a steep decrease. Thus, the acceptance corrections are especially sensitive in this region. To be really sure that the simulation model describes the acceptance appropriately and that the corrected  $\Lambda(1405)$  shape is not distorted, it has to be proven that the simulations reproduce the behavior of the single particle tracks correctly and that they cover exactly the same phase space regions as the experimental tracks. For that purpose, the  $\theta$  angles of the proton,  $K^+$ ,  $\pi^-$  and  $\pi^+$  tracks in the laboratory system are studied for the two  $\Sigma\pi$  samples in Figure B.9 and

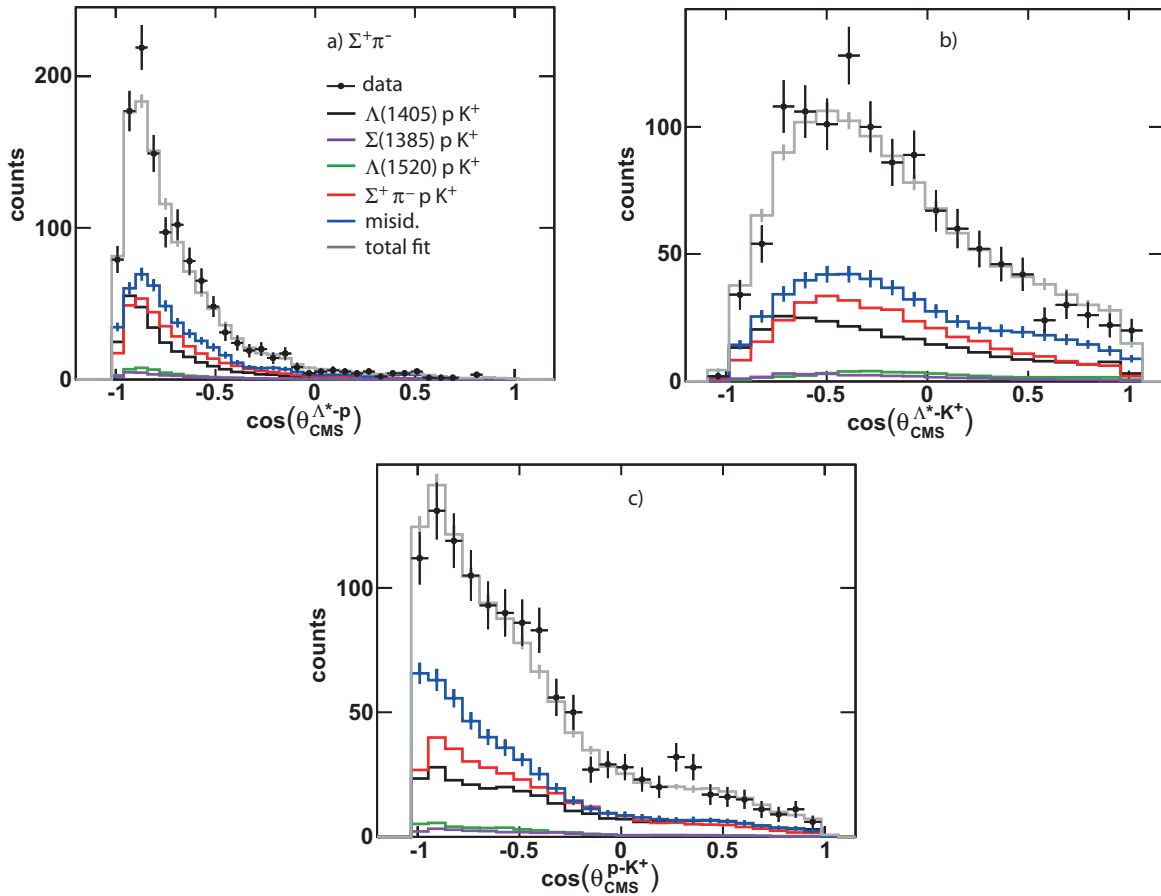


**Figure B.7:** Opening angles between the  $\Lambda(1405)$  candidate, the proton and the  $K^+$  for the  $\Sigma^+\pi^-$  data sample.

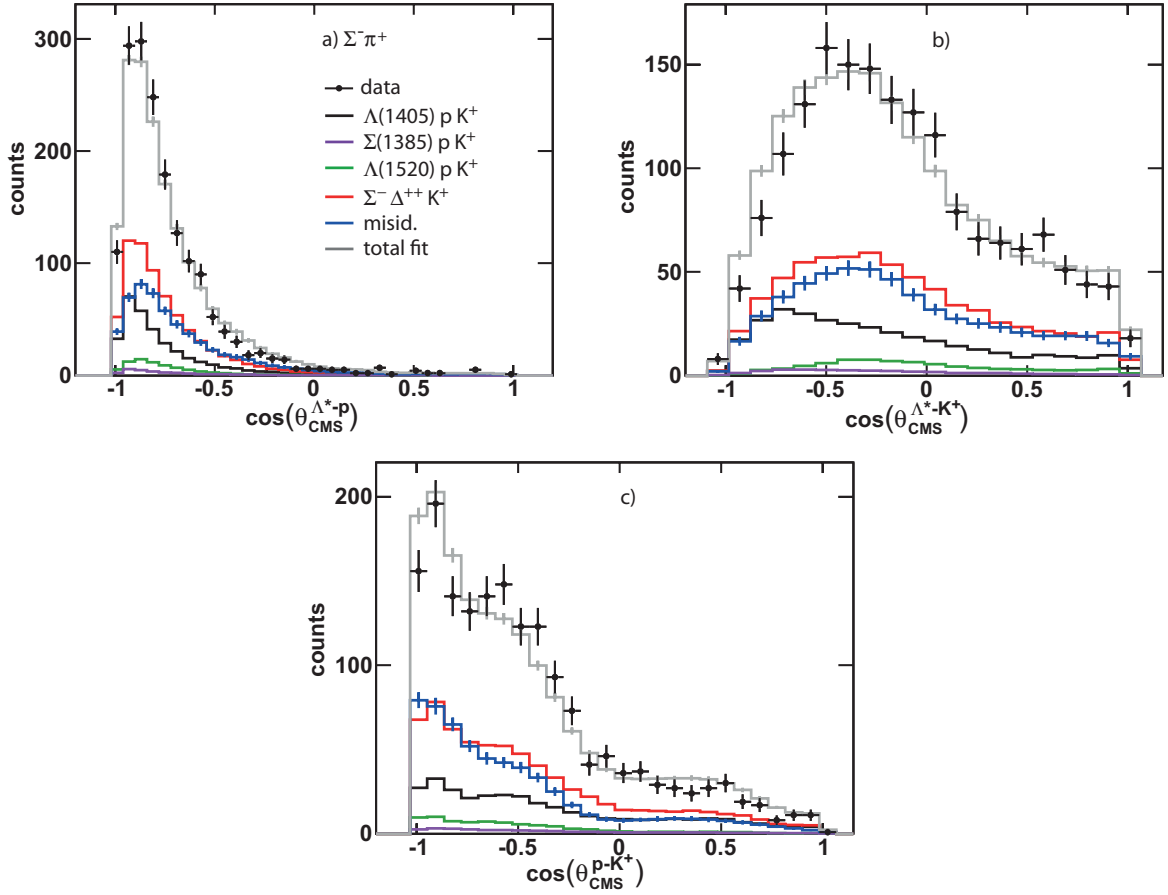


**Figure B.8:** Opening angles between the  $\Lambda(1405)$  candidate, the proton and the  $K^+$  for the  $\Sigma^- \pi^+$  data sample.

B.10. Furthermore, the total momentum of these tracks in the laboratory frame is studied in Figure B.11 and B.12 as well.

It is impressive how well the simulations agree with the data in all pictures. This has certainly to be attributed to the good calibration of the data and the precise incorporation of the detector system into the simulation tools. The fact that the  $\theta$  distributions all start at  $15^\circ$  reproduces the HADES acceptance with its polar coverage from  $15^\circ$ - $85^\circ$ . Especially for the pions, which have rather low momenta and thus experience a strong bending in the magnetic field of HADES, the low theta region is well described. This makes one confident that the simulations in general and the developed simulation model in particular are under control.

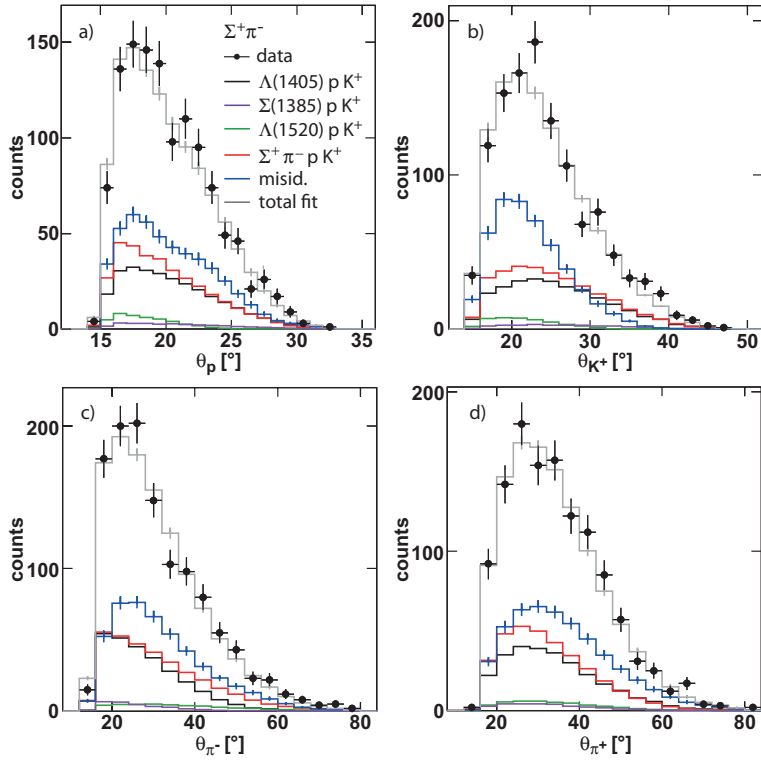


**Figure B.9:**  $\theta$  distribution of proton (a),  $K^+$  (b),  $\pi^-$  (c) and  $\pi^+$  (d) in the laboratory system for events in the  $\Sigma^+\pi^-$  data sample.

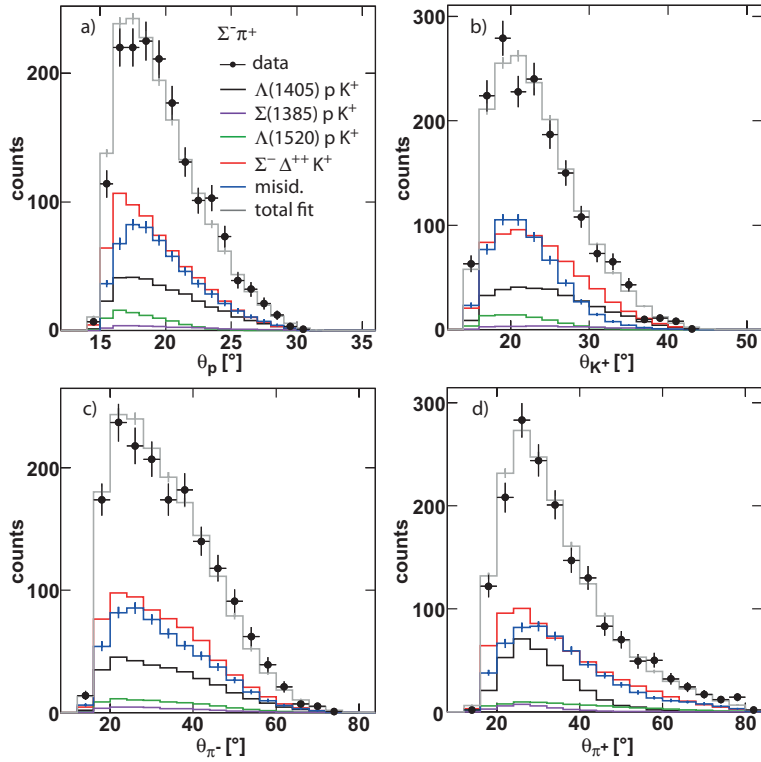


**Figure B.10:**  $\theta$  distribution of proton (a),  $K^+$  (b),  $\pi^-$  (c) and  $\pi^+$  (d) in the laboratory system for events in the  $\Sigma^-\pi^+$  data sample.

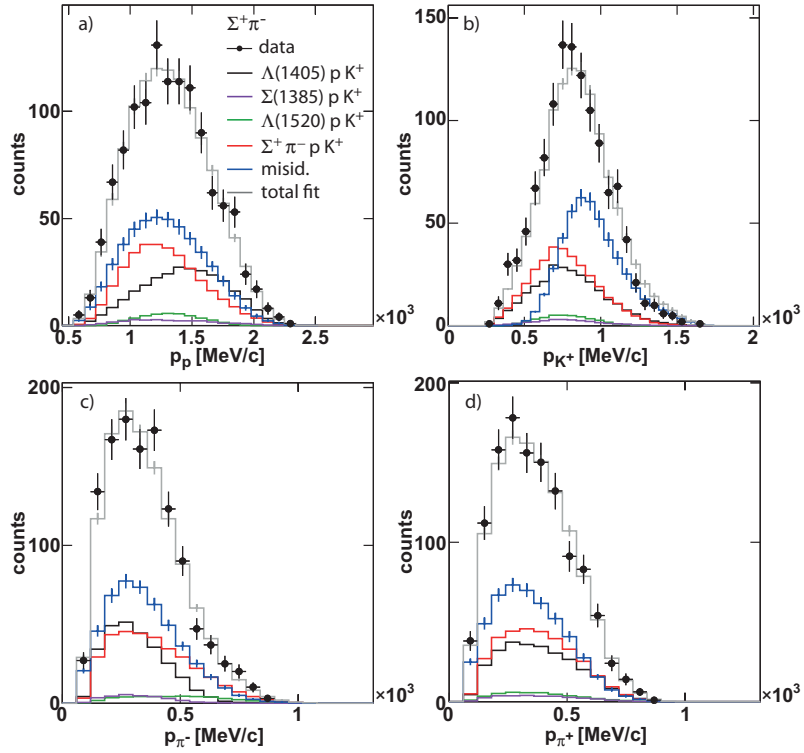


**Figure B.11:** Momentum distribution of proton (a),  $K^+$  (b),  $\pi^-$  (c) and  $\pi^+$  (d) in the laboratory system for events in the  $\Sigma^+\pi^-$  data sample.

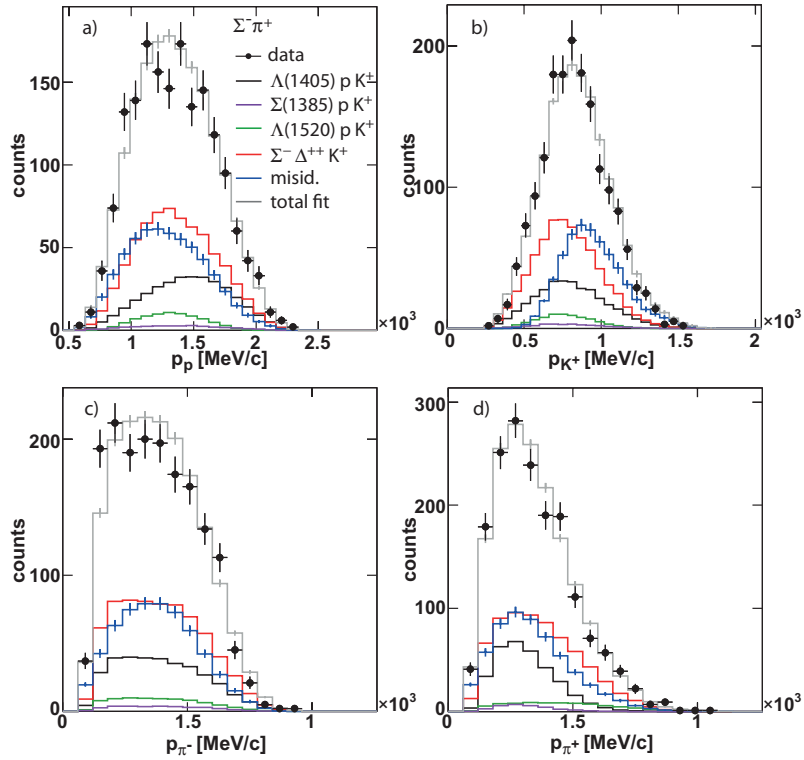


**Figure B.12:** Momentum distribution of proton (a),  $K^+$  (b),  $\pi^-$  (c) and  $\pi^+$  (d) in the laboratory system for events in the  $\Sigma^-\pi^+$  data sample.

## B.4 Parameterization of $C_{eff}(m)$ and $T_{\Sigma\pi}$

The function (4.28), used to parameterize the  $\Lambda(1405)$  line shape, was weighted with a phase space factor  $C_{eff}(m)$ , which accounts for the decreasing available phase space with increasing  $\Lambda(1405)$  mass  $m$ . To determine this factor, simulations were used. The result is shown in black points in Figure B.13 (compare also to Figure 3.16). In order to get an analytical expression for  $C_{eff}(m)$ , the simulated points were fitted with the following function:

$$C_{eff}(m) = A \cdot e^{-km} \quad (\text{B.1})$$

The fit result is shown in the red curve in Figure B.13.

Finally,  $A = 700$  and  $k = 4.947 \cdot 10^{-3} \text{ (MeV/c}^2\text{)}^{-1}$  were used.

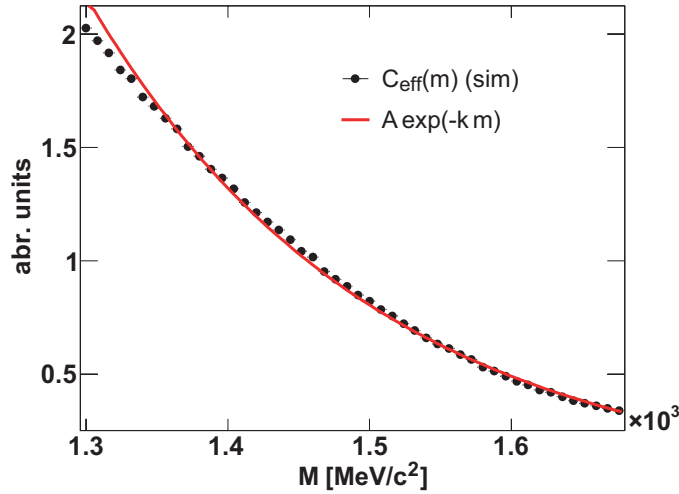


**Figure B.13:** Available phase space in the reaction  $p + p \rightarrow \Lambda(1405) + p + K^+$  as a function of the  $\Lambda(1405)$  mass  $m$ . The black points are results of simulations; the red line is a fit with an exponential function.

The parameterization of  $T_{\Sigma\pi}$  was done with help of simulations as well. The missing mass to proton and  $K^+$  for the reactions (4.18) and (4.22) is shown in Figure B.14 a) and b), respectively. The black points correspond to  $4\pi$  simulations with the event generator PLUTO (see section 2.3). The distributions are the same as what is shown for the non-resonant background in Figure 4.11 a) and b). Analytical expressions were obtained by fitting the two spectra with the functions  $|T_{\Sigma^+\pi^-}|^2$  and  $|T_{\Sigma^-\pi^+}|^2$ . For this purpose, the following parameterization was used:

$$T_{\Sigma\pi}(m) = \left[ \left( q_{c.m.}^{0.3} \right) \left( A_0 + A_1 m + A_2 m^2 + A_3 m^3 + A_4 m^4 \right) \sqrt{500} e^{-0.00897m} \right]^{\frac{1}{2}} \quad (\text{B.2})$$

$q_{c.m.}$  is again the decay momentum of  $\Sigma$  and  $\pi$  for a rest mass of  $m$ . The parameterization of function (B.2) has no physical meaning. It was chosen such to reproduce the simulated distributions in Figure B.14. The fit results with this function is shown in the red lines in panel a) and b). The extracted parameters are summarized in Table B.1.

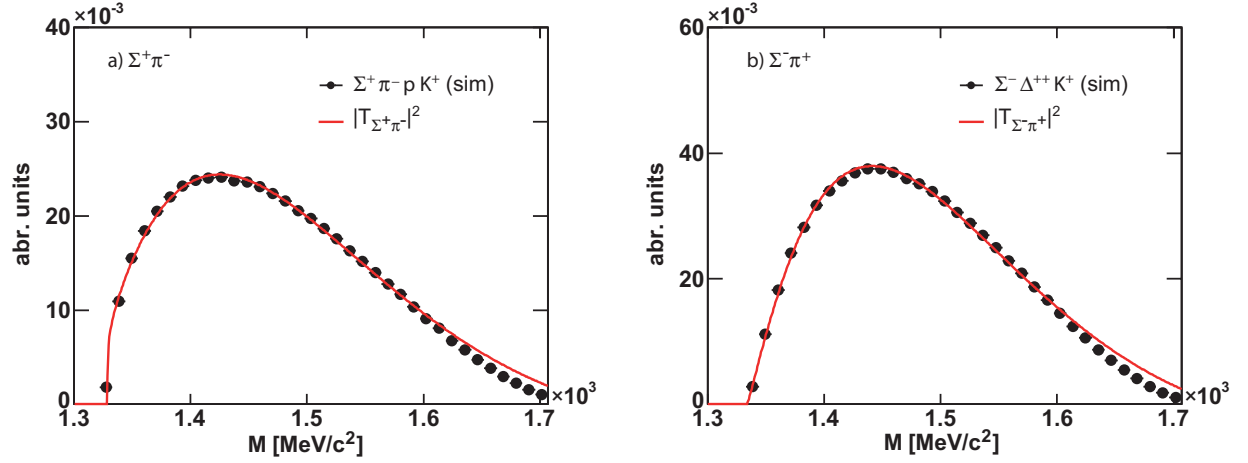


**Figure B.14:** PLUTO simulations of the reaction  $p + p \rightarrow \Sigma^+ + \pi^- + p + K^+$  (a) and  $p + p \rightarrow \Sigma^- + \Delta^{++} + K^+$  (b). The red lines indicate fits with the function (B.2).

$T_{\Sigma\pi}$	$A_0$	$A_1$	$A_2$	$A_3$	$A_4$
$T_{\Sigma^+\pi^-}$	$2.93 \cdot 10^3$	-5.14	$1.05 \cdot 10^{-4}$	$3.22 \cdot 10^{-6}$	$-1.23 \cdot 10^{-9}$
$T_{\Sigma^-\pi^+}$	$1.46 \cdot 10^3$	-4.62	$4.57 \cdot 10^{-4}$	$3.77 \cdot 10^{-6}$	$-1.60 \cdot 10^{-9}$

**Table B.1:** Parameter values for  $T_{\Sigma^+\pi^-}$  and  $T_{\Sigma^-\pi^+}$  according to equation (B.2).



# C Appendix to the pion tracker tests

## C.1 Signal-noise separation of the remaining silicon detectors

In analogy to Figure 5.6, the properties of the detectors 2814-24 and 2815-25 are shown in Figure C.1 and C.2. For the tests of these detectors, the order of the preamplifiers has been changed compared to Figure 5.6 so that the order in the step like structures between channels 16 and 48 is interchanged. In all other sectors the three detectors behave quite similar.

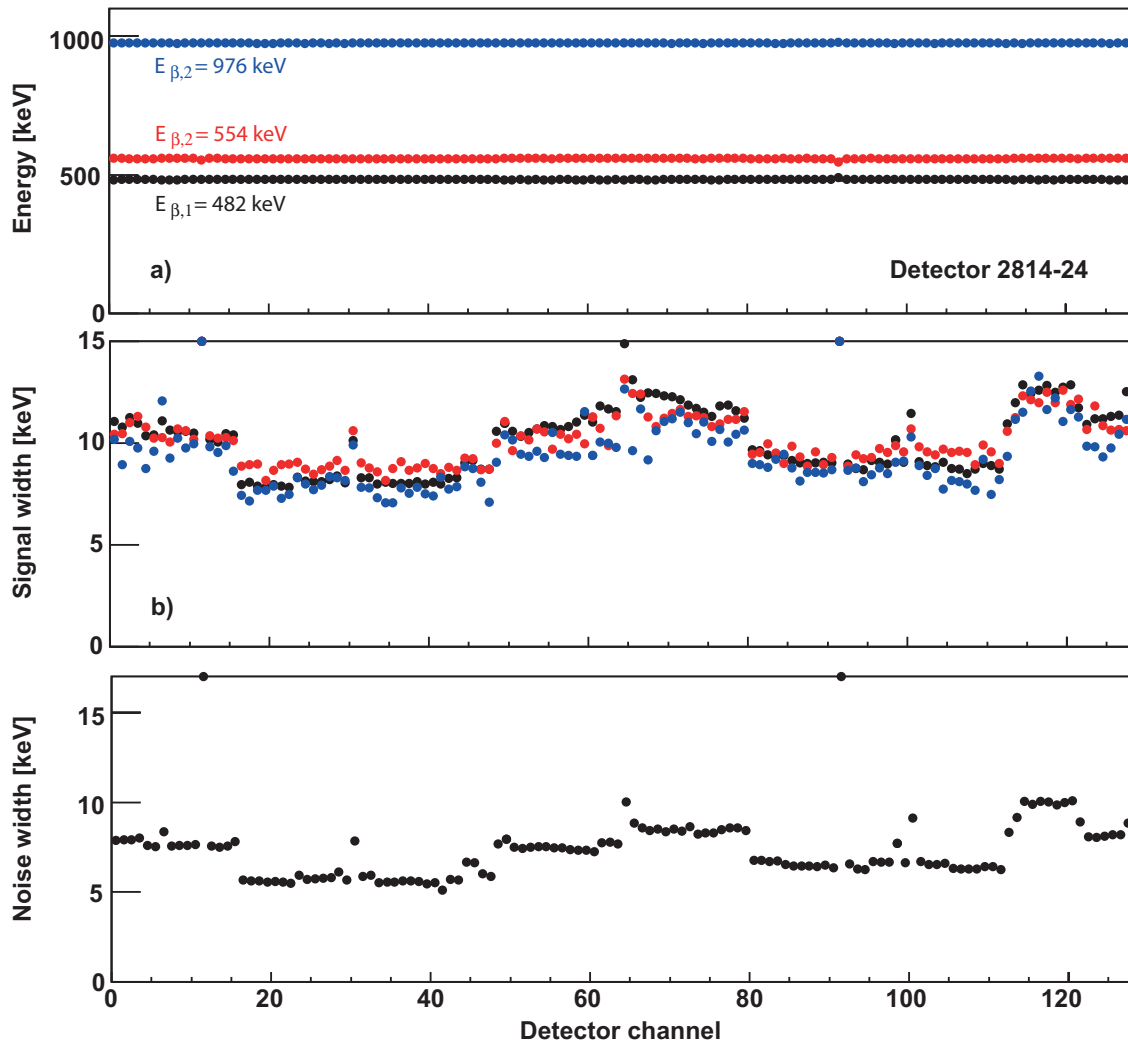


Figure C.1: Detector 2814-24. See description for Figure 5.6.

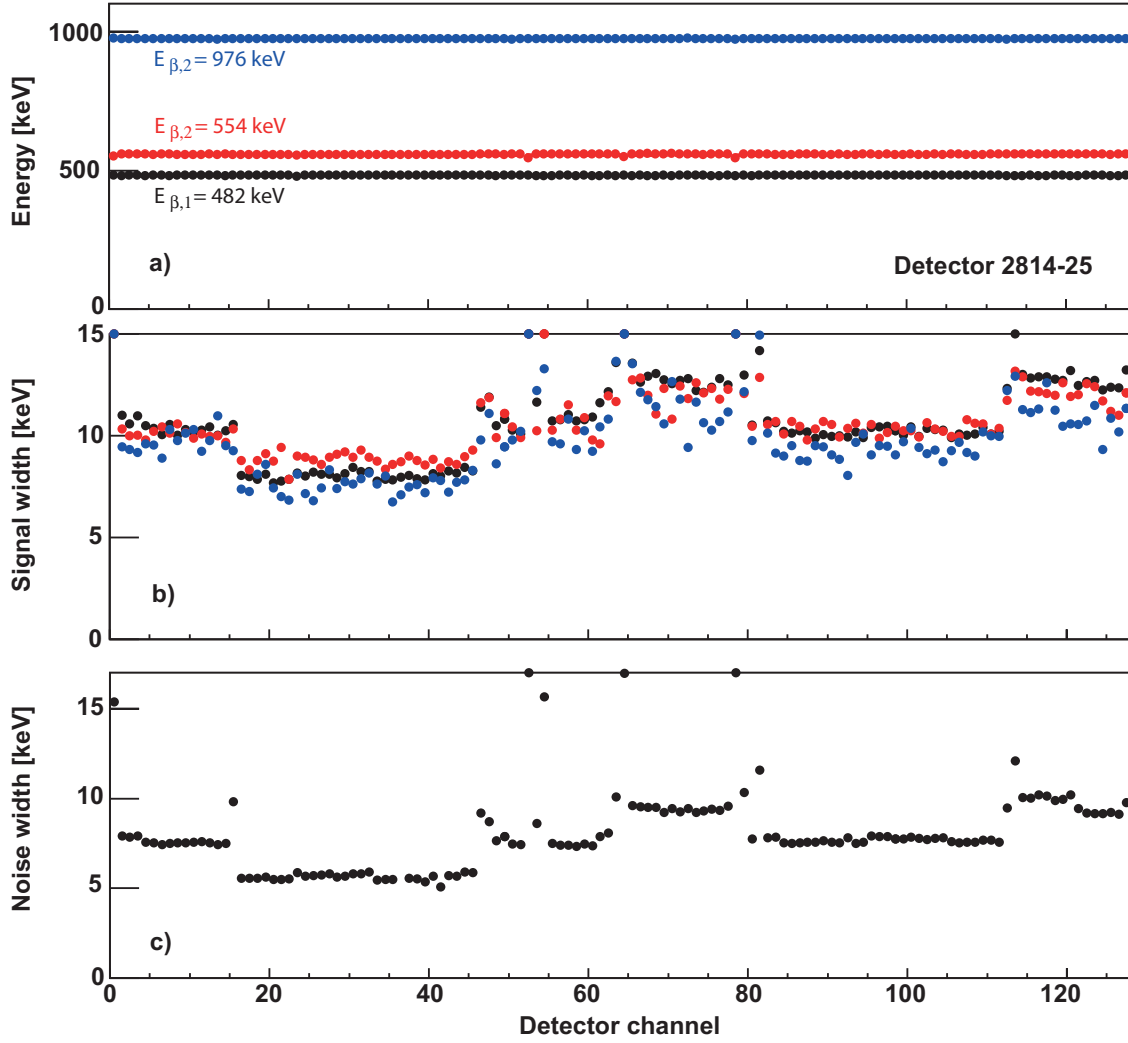


Figure C.2: Detector 2814-25. See description for Figure 5.6.

## C.2 Determination of $\beta$

In order to determine the value  $\beta$ , needed for the temperature normalization of the leakage current in section 5.3, the following procedure was applied:

First, the leakage current curves in Figure 5.10 a) were subdivided into time regions of increasing (day) and decreasing (night) temperatures (time regions I, II and III in Figure 5.10 a)). For each of these regions, the current was plotted as a function of temperature. This was done individually for all detector areas. The results are shown in Figure C.3. The data points in each time region were then fitted with the function:

$$I(T) = AT^2 e^{\left(-\frac{\beta}{T}\right)} \quad (\text{C.1})$$

with the free fit parameters  $A$  and  $\beta$ . The results for  $\beta$  are indicated in the pictures as well. By weighting the  $\beta$  values with the number of data points in the corresponding time region, a mean value  $\bar{\beta}$  was obtained. This mean value was used to normalize the leakage currents so that the current curves in Figure 5.10 c) were obtained. In order to normalize the measured currents

during the beam period (see Figure 5.11 b)), the same method was applied. Instead of using the mean value  $\beta$  for the normalization, also the individual  $\beta$  values from the different time regions can be used. This was done in order to estimate the systematic error on the quantity  $\alpha$  (see Figure 5.12 a)).

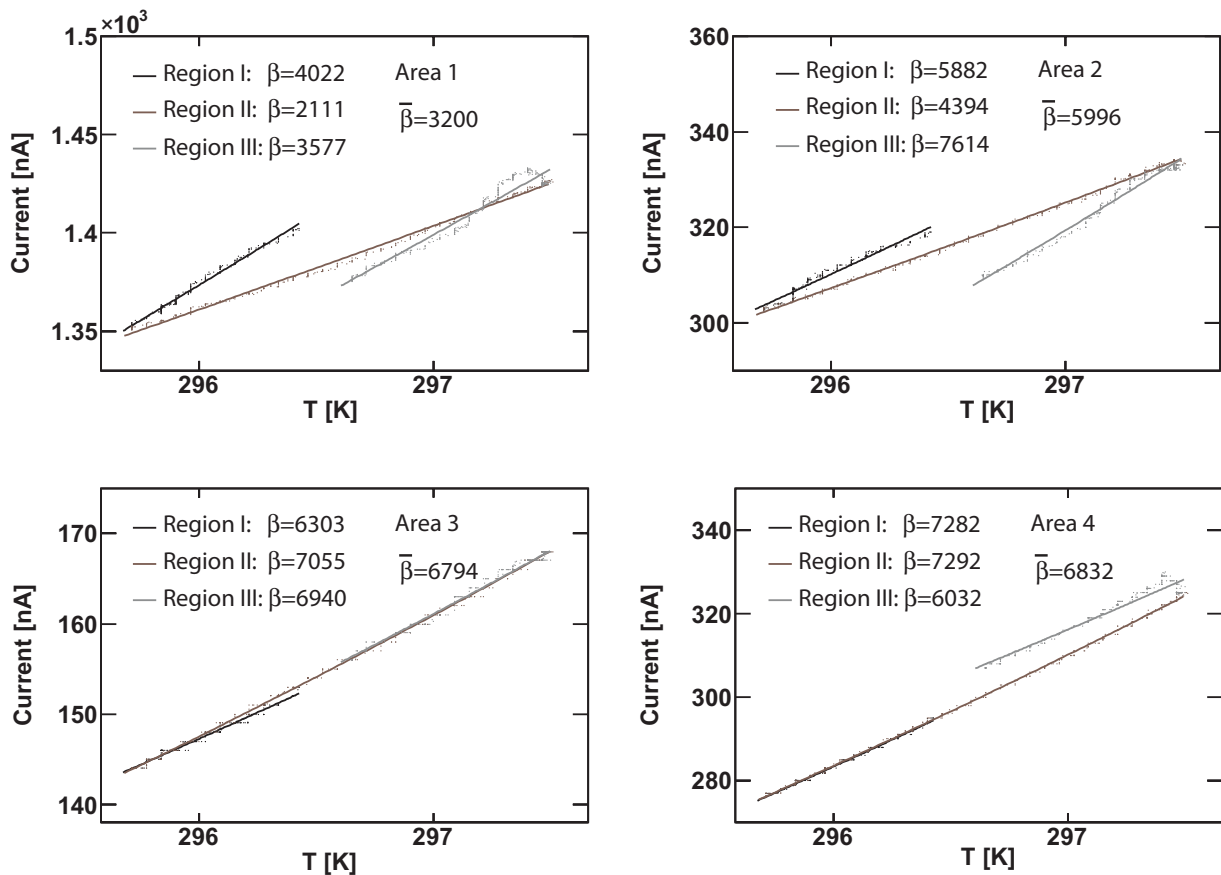


**Figure C.3:** Current vs. temperature for the four different detector areas. The different time regions are shown in the different colors. Fits to the data are indicated as solid lines.



# Bibliography

- [A+61] M. H. Alston et al.  
Study of Resonances of the  $\Sigma - \pi$  System.  
*Phys.Rev.Lett.*, 6:698–702, 1961.
- [A+05a] John Adams et al.  
Experimental and theoretical challenges in the search for the quark gluon plasma: The STAR Collaboration’s critical assessment of the evidence from RHIC collisions.  
*Nucl.Phys.*, A757:102–183, 2005.
- [A+05b] M. Agnello et al.  
Evidence for a kaon-bound state  $K^-pp$  produced in  $K^-$  absorption reactions at rest.  
*Phys.Rev.Lett.*, 94:212303, 2005.
- [A+09a] G. Agakishiev et al.  
Deep sub-threshold  $\Xi^-$  production in Ar+KCl reactions at 1.76 AGeV.  
*Phys.Rev.Lett.*, 103:132301, 2009.
- [A+09b] G. Agakishiev et al.  
 $\phi$  decay: A Relevant source for  $K^-$  production at SIS energies?  
*Phys.Rev.*, C80:025209, 2009.
- [A+09c] G. Agakishiev et al.  
The High-Acceptance Dielectron Spectrometer HADES.  
*Eur.Phys.J.*, A41:243–277, 2009.
- [A+10] G. Agakishiev et al.  
In-Medium Effects on  $K^0$  Mesons in Relativistic Heavy-Ion Collisions.  
*Phys.Rev.*, C82:044907, 2010.
- [A+11] G. Agakishiev et al.  
Dielectron production in Ar+KCl collisions at 1.76 AGeV.  
*Phys.Rev.*, C84:014902, 2011.
- [A+12a] G. Agakishiev et al.  
Baryonic resonances close to the  $\bar{K}N$  threshold: The Case of  $\Sigma(1385)^+$  in pp collisions.  
*Phys.Rev.*, C85:035203, 2012.
- [A+12b] G. Agakishiev et al.  
Determination of the  $\Sigma(1385)^0/\Lambda(1405)$  ratio in p+p collisions at 3.5 GeV.  
*arXiv*, nucl-ex/1202.0232, 2012.
- [A+12c] G. Agakishiev et al.  
First measurement of low momentum dielectrons radiated off cold nuclear matter.  
*Phys.Lett.*, B715:304–309, 2012.
- [A+12d] G. Agakishiev et al.  
Production of  $\Sigma^\pm\pi^\mp pK^+$  in p+p reactions at 3.5 GeV beam energy.  
*Nucl.Phys.*, A881:178–186, 2012.
- [A+13] G. Agakishiev et al.  
Baryonic resonances close to the  $\bar{K}N$  threshold: The case of  $\Lambda(1405)$  in pp collisions.  
*Phys. Rev. C*, 87:025201, 2013.

- [AB<sup>+</sup>10] M. Abdel-Bary et al.  
Production of  $\Lambda$  and  $\Sigma^0$  hyperons in proton-proton collisions.  
*Eur.Phys.J.*, A46:27–44, 2010.
- [ABS81] M. Aguilar-Benitez and J. Salicio.  
A new experimental determination of the resonance parameters of the  $\Sigma^+(1385)$ ,  
 $\Sigma^0(1385)$  and  $\Sigma^-(1385)$  hyperons.  
*Anales de Fisica Serie A*, 77:144–151, 1981.
- [AP<sup>+</sup>04] H. Alvarez-Pol et al.  
A large area timing RPC prototype for ion collisions in the HADES spectrometer.  
*Nucl.Instrum.Meth.*, A535:277–282, 2004.
- [AY02] Yoshinori Akaishi and Toshimitsu Yamazaki.  
Nuclear  $\bar{K}$  bound states in light nuclei.  
*Phys.Rev.*, C65:044005, 2002.
- [AYOW10] Yoshinori Akaishi, Toshimitsu Yamazaki, Mitsuaki Obu, and Masanobu Wada.  
Single-pole nature of  $\Lambda(1405)$  and structure of  $K^-pp$ .  
*Nucl.Phys.*, A835:67–74, 2010.
- [B<sup>+</sup>77] O. Braun et al.  
New Information about the Kaon-Nucleon-Hyperon coupling constants:  
 $g(\bar{K}n\Sigma(1197))$ ,  $g(\bar{K}n\Sigma(1385))$  and  $g(\bar{K}n\Lambda(1405))$ .  
*Nucl.Phys.*, B129:1, 1977.
- [B<sup>+</sup>97] D. Best et al.  
 $K^+$  production in the reaction  $^{58}\text{Ni} + ^{58}\text{Ni}$  at incident energies from 1 AGeV to 2 AGeV.  
*Nucl.Phys.*, A625:307–324, 1997.
- [B<sup>+</sup>06] A. Brogna et al.  
N-XYTER, a CMOS read-out ASIC for high resolution time and amplitude measurements on high rate multi-channel counting mode neutron detectors.  
*Nucl.Instrum.Meth.*, A568:301–308, 2006.
- [B<sup>+</sup>10] A. Budzanowski et al.  
Cross section of the  $pp \rightarrow K^+ \Sigma^+ n$  reaction close to threshold.  
*Phys.Lett.*, B692:10–14, 2010.
- [B<sup>+</sup>11] M. Bazzi et al.  
A New Measurement of Kaonic Hydrogen X rays.  
*Phys.Lett.*, B704:113–117, 2011.
- [B<sup>+</sup>12] J. Beringer et al.  
The Review of Particle Physics.  
*Phys. Rev.*, D86:010001, 2012.
- [Bau84] M. Baubillier et al.  
The reactions  $K^-p \rightarrow \pi^\mp \Sigma(1385)^\pm$  at 8.25 GeV.  
*Z. Phys.*, C23:213, 1984.
- [BC12] Jia-Chii Berger-Chen.  
 $K^0$  production in  $pp$  and  $pNb$  reactions.  
*PoS*, BORMIO2012:013, 2012.
- [BCN66] E. Bierman, A.P. Colleraine, and U. Nauenberg.  
Search for Dibaryon Resonant States.  
*Phys.Rev.*, 147:922–931, 1966.
- [Bet30] H. Bethe.  
Theory of the passage of fast corpuscular rays through matter.  
*Annalen Phys.*, 5:325–400, 1930.

- [Bet07] Siegfried Bethke.  
Experimental tests of asymptotic freedom.  
*Prog.Part.Nucl.Phys.*, 58:351–386, 2007.
- [BFM<sup>+</sup>88] A. Baldini, V. Flaminio, W.G. Moorhead, Douglas R.O. Morrison, and (Ed.) Schopper, H.  
*NUMERICAL DATA AND FUNCTIONAL RELATIONSHIPS IN SCIENCE AND TECHNOLOGY. GRP. 1: NUCLEAR AND PARTICLE PHYSICS. VOL. 12: TOTAL CROSS-SECTIONS FOR REACTIONS OF HIGH-ENERGY PARTICLES (INCLUDING ELASTIC, TOPOLOGICAL, INCLUSIVE AND EXCLUSIVE REACTIONS). SUBVOL.*  
Springer Berlin Heidelberg, 1988.
- [BLR<sup>+</sup>98] G.E. Brown, G.-Q. Li, R. Rapp, M. Rho, and J. Wambach.  
Medium dependence of the vector meson mass: Dynamical and/or Brown-Rho scaling?  
*Acta Phys.Polon.*, B29:2309–2321, 1998.
- [BMN06] B. Borasoy, U.-G. Meissner, and R. Nissler.  
 $K - p$  scattering length from scattering experiments.  
*Phys.Rev.*, C74:055201, 2006.
- [BNW05] B. Borasoy, R. Nissler, and W. Weise.  
Chiral dynamics of kaon-nucleon interactions, revisited.  
*Eur.Phys.J.*, A25:79–96, 2005.
- [Bor74] S. R. Borenstein, G. R. Kalbfleisch, R. C. Strand, V. Vanderburg and J. W. Chapman.  
A determination of the mass, width and the  $(\Sigma\pi/\Lambda\pi)$  branching ratio of the  $\Sigma(1381)$  baryon.  
*Phys. Rev.*, D9:3006, 1974.
- [BR91] G.E. Brown and M. Rho.  
Scaling effective Lagrangians in a dense medium.  
*Phys.Rev.Lett.*, 66:2720–2723, 1991.
- [Böt] S. Böttcher.  
*Analysis of a  $^{207}\text{Bi}$  spectrum measured with a Hamamatsu photo diode, a tsh310 based preamp, and the heti irena.*  
<http://www.icap.uni-kiel.de/et/people/stephan/solo/spectra/irena/2011-06-01-Bi207.pdf>.
- [C<sup>+</sup>68a] W. Chinowsky et al.  
Observation of  $Y^{*+}(1385) K^+$  and  $N^{*++}(1236) \rho^0$  Decays of a Nucleon Resonance.  
*Phys.Rev.*, 171:1421–1428, 1968.
- [C<sup>+</sup>68b] W. Chinowsky et al.  
Production of K mesons in three-body states in proton-proton interactions at 6 BeV/c.  
*Phys.Rev.*, 165:1466–1478, 1968.
- [CER95] CERN.  
*CERN — Geant.*  
[http://www.asdoc.web.cern.ch/wwwasdoc/geant\\_html3/geantall.html](http://www.asdoc.web.cern.ch/wwwasdoc/geant_html3/geantall.html), 1995.
- [D<sup>+</sup>02] J. Diaz et al.  
Design and commissioning of the GSI pion beam.  
*Nucl.Instrum.Meth.*, A478:511–526, 2002.
- [Dan01] Pawel Danielewicz.  
Nuclear equation of state.  
*arXiv*, nucl-th/0112006:24–42, 2001.
- [Daw94] S. Dawson.

- Introduction to the physics of Higgs bosons.  
*arXiv*, hep-ph/9411325, 1994.
- [d'E09] David d'Enterria.  
Jet quenching.  
*arXiv*, nucl-ex/0902.2011, 2009.
- [DGBT54] S. Deser, M.L. Goldberger, K. Baumann, and W. E. Thirring.  
Energy level displacements in pi mesonic atoms.  
*Phys.Rev.*, 96:774–776, 1954.
- [DPR<sup>+</sup>10] Paul Demorest, Tim Pennucci, Scott Ransom, Mallory Roberts, and Jason Hessels.  
Shapiro Delay Measurement of A Two Solar Mass Neutron Star.  
*Nature*, 467:1081–1083, 2010.
- [DT59] R.H. Dalitz and S.F. Tuan.  
A possible resonant state in pion-hyperon scattering.  
*Phys.Rev.Lett.*, 2:425–428, 1959.
- [DT60] R.H. Dalitz and S.F. Tuan.  
The phenomenological description of K -nucleon reaction processes.  
*Annals Phys.*, 10:307–351, 1960.
- [EFK<sup>+</sup>65] A. Engler, H.E. Fisk, R.W. Kraemer, C.M. Meltzer, and J.B. Westgard.  
Spin of the  $Y_0^*(1405)$ .  
*Phys.Rev.Lett.*, 15:224, 1965.
- [Epp12a] E. Epple.  
Exclusive  $pK\Lambda$  production in p + p reactions.  
*PoS*, BORMIO2012:016, 2012.
- [Epp12b] E. Epple.  
Private communication.  
2012.
- [Esk95] K.J. Eskola.  
Formation and evolution of quark - gluon plasma at RHIC and LHC.  
*Nucl.Phys.*, A590:383C–398C, 1995.
- [F<sup>+</sup>07] I. Frohlich et al.  
Pluto: A Monte Carlo Simulation Tool for Hadronic Physics.  
*PoS*, ACAT2007:076, 2007.
- [F<sup>+</sup>10] I. Frohlich et al.  
Design of the Pluto Event Generator.  
*J.Phys.Conf.Ser.*, 219:032039, 2010.
- [Fab13] L. Fabbietti.  
Private communication.  
2013.
- [FGB94] E. Friedman, A. Gal, and C.J. Batty.  
Density dependent K- nuclear optical potentials from kaonic atoms.  
*Nucl.Phys.*, A579:518–538, 1994.
- [FH11] Kenji Fukushima and Tetsuo Hatsuda.  
The phase diagram of dense QCD.  
*Rept.Prog.Phys.*, 74:014001, 2011.
- [Fri10] E. Friedman.  
Private communication.  
2010.
- [FS67] E. Ferrari and S. Serio.

- Three-Body Associated Production in Proton-Proton Collisions and the One-Boson-Exchange Model .  
*Phys.Rev.*, 167:1298–1308, 1967.
- [Fuc06] Christian Fuchs.  
Kaon production in heavy ion reactions at intermediate energies.  
*Prog.Part.Nucl.Phys.*, 56:1–103, 2006.
- [FW97] Goran Faldt and Colin Wilkin.  
Comparison of the near threshold production of eta and K mesons in proton proton collisions.  
*Z.Phys.*, A357:241–243, 1997.
- [G<sup>+</sup>07] A. Gil et al.  
Front-end electronics development for the new resistive plate chamber detector of HADES.  
*JINST*, 2:T11001, 2007.
- [GJ64] K. Gottfried and J. D. Jackson.  
On the Connection between production mechanism and decay of resonances at high-energies.  
*Nuovo Cim.*, 33:309–330, 1964.
- [GO07] L.S. Geng and E. Oset.  
The Role of the  $\Lambda(1405)$  in the  $pp \rightarrow pK^+\Lambda(1405)$  reaction.  
*Eur.Phys.J.*, A34:405–412, 2007.
- [Gup97] Rajan Gupta.  
Introduction to lattice QCD: Course.  
*arXiv*, hep-lat/9807028:83–219, 1997.
- [HAD08] HADES.  
*HADES — HGeant*.  
<http://www-hades.gsi.de/?q=computing>, 2008.
- [HAD09] HADES.  
*HADES Wiki — SimAna, EnergyLossCalibration*.  
<http://hades-wiki.gsi.de/cgi-bin/view/SimAna/EnergyLossCalibration>, 2009.
- [HAD11] HADES.  
*HADES Wiki — SimAna, April07Normalization*.  
<http://hades-wiki.gsi.de/cgi-bin/view/SimAna/Apr07Normalization>, 2011.
- [Hem85] R.J. Hemingway.  
Production of  $\Lambda(1405)$  in  $K^-p$  reactions at 4.2 GeV/c.  
*Nucl.Phys.*, B253:742, 1985.
- [Her96] N. Herrmann.  
Particle production and flow at SIS energies.  
*Nucl.Phys.*, A610:49C–62C, 1996.
- [HHO<sup>+</sup>03] T. Hyodo, A. Hosaka, E. Oset, A. Ramos, and M.J. Vicente Vacas.  
 $\Lambda(1405)$  production in the  $\pi^-p \rightarrow K^0\pi\Sigma$  reaction.  
*Phys.Rev.*, C68:065203, 2003.
- [Hie12] T. Hiennion.  
Private communication.  
2012.
- [HJ12] Tetsuo Hyodo and Daisuke Jido.  
The nature of the  $\Lambda(1405)$  resonance in chiral dynamics.  
*Prog.Part.Nucl.Phys.*, 67:55–98, 2012.

- [HKAY12] M. Hassanvand, S. Z. Kalantari, Y. Akaishi, and T. Yamazaki.  
Theoretical analysis of  $\Lambda(1405) \rightarrow (\Sigma\pi)^0$  mass spectra produced in  $p + p \rightarrow p + \Lambda(1405) + K^+$  reactions.  
*arXiv*, nucl-th/1210.7725, 2012.
- [HNJH03] T. Hyodo, S.I. Nam, D. Jido, and A. Hosaka.  
Flavor SU(3) breaking effects in the chiral unitary model for meson baryon scatterings.  
*Phys.Rev.*, C68:018201, 2003.
- [HOL<sup>+</sup>12] Christoph Hartnack, Helmut Oeschler, Yvonne Leifels, Elena L. Bratkovskaya, and Jörg Aichelin.  
Strangeness Production close to Threshold in Proton-Nucleus and Heavy-Ion Collisions.  
*Phys.Rept.*, 510:119–200, 2012.
- [HW08] Tetsuo Hyodo and Wolfram Weise.  
Effective  $\bar{K}N$  interaction based on chiral SU(3) dynamics.  
*Phys.Rev.*, C77:035204, 2008.
- [IHW11] Y. Ikeda, T. Hyodo, and W. Weise.  
Improved constraints on chiral SU(3) dynamics from kaonic hydrogen.  
*Phys.Lett.*, B706:63–67, 2011.
- [IS07] Y. Ikeda and T. Sato.  
Strange dibaryon resonance in the  $\bar{K}NN - \pi YN$  system.  
*Phys.Rev.*, C76:035203, 2007.
- [J<sup>+</sup>10] D. Jido et al.  
The nature of  $\Lambda(1405)$  hyperon resonance in chiral dynamics.  
*Nucl.Phys.*, A835:59–66, 2010.
- [Jac64] John David Jackson.  
Remarks on the phenomenological analysis of resonances.  
*Nuovo Cim.*, 34:1644–1666, 1964.
- [JM12] Barbara V. Jacak and Berndt Müller.  
The exploration of hot nuclear matter.  
*Science*, 337:310–314, 2012.
- [JOO<sup>+</sup>03] D. Jido, J.A. Oller, E. Oset, A. Ramos, and U.-G. Meissner.  
Chiral dynamics of the two  $\Lambda(1405)$  states.  
*Nucl.Phys.*, A725:181–200, 2003.
- [JOS09] D. Jido, E. Oset, and T. Sekihara.  
Kaonic production of  $\Lambda(1405)$  off deuteron target in chiral dynamics.  
*Eur.Phys.J.*, A42:257–268, 2009.
- [K<sup>+</sup>70] S. Klein et al.  
Four-body strange-particle production in p p collisions at 6 BeV/c.  
*Phys.Rev.*, D1:3019–3030, 1970.
- [K<sup>+</sup>71] R.C. Kammerud et al.  
Large angle proton proton elastic scattering at intermediate momenta.  
*Phys.Rev.*, D4:1309–1324, 1971.
- [K<sup>+</sup>11] D. Keller et al.  
Electromagnetic Decay of the  $\Sigma^0(1385)$  to  $\Lambda\gamma$ .  
*Phys.Rev.*, D83:072004, 2011.
- [K<sup>+</sup>12a] D. Keller et al.  
Branching Ratio of the Electromagnetic Decay of the  $\Sigma^+(1385)$ .  
*Phys.Rev.*, D85:052004, 2012.
- [K<sup>+</sup>12b] P. Kienle et al.

- Formation of the  $S = -1$  resonance  $X(2265)$  in the reaction  $pp \rightarrow X + K^+$  at 2.50 and 2.85 GeV.  
*Eur.Phys.J.*, A48:183, 2012.
- [KMFF02] M.I. Krivoruchenko, B.V. Martemyanov, A. Faessler, and C. Fuchs.  
Electromagnetic transition form-factors and dilepton decay rates of nucleon resonances.  
*Annals Phys.*, 296:299–346, 2002.
- [KN86] D.B. Kaplan and A.E. Nelson.  
Strange Goings on in Dense Nucleonic Matter.  
*Phys.Lett.*, B175:57–63, 1986.
- [Koc95] Volker Koch.  
Introduction to chiral symmetry.  
*arXiv*, nucl-th/9512029, 1995.
- [L<sup>+</sup>99] F. Laue et al.  
Medium effects in kaon and anti-kaon production in nuclear collisions at subthreshold beam energies.  
*Phys.Rev.Lett.*, 82:1640–1643, 1999.
- [L<sup>+</sup>09] K. Lapidus et al.  
Dielectron production in pp and dp collisions at 1.25 GeV/u with HADES.  
*arXiv*, nucl-ex/0904.1128, 2009.
- [Lab12] National Superconducting Cyclotron Laboratory.  
*LISE++*.  
<http://lise.nsl.msu.edu/lise.html>, 2012.
- [Lin03] G. Lindstrom.  
Radiation damage in silicon detectors.  
*Nucl.Instrum.Meth.*, A512:30–43, 2003.
- [LK02] M.F.M. Lutz and C.L. Korpa.  
Selfconsistent propagation of hyperons and anti-kaons in nuclear matter based on relativistic chiral SU(3) dynamics.  
*Nucl.Phys.*, A700:309–329, 2002.
- [LKM08] M.F.M. Lutz, C.L. Korpa, and M. Moller.  
Antikaons and hyperons in nuclear matter with saturation.  
*Nucl.Phys.*, A808:124–159, 2008.
- [LKW92] M.F.M. Lutz, S. Klimt, and W. Weise.  
Meson properties at finite temperature and baryon density.  
*Nucl.Phys.*, A542:521–558, 1992.
- [LMF99] G. Lindstrom, M. Moll, and E. Fretwurst.  
Radiation hardness of silicon detectors: A challenge from high-energy physics.  
*Nucl.Instrum.Meth.*, A426:1–15, 1999.
- [Lor08] M. Lorentz.  
Geladene Kaonen Produktion in Ar + KCl Reaktionen bei 1.756 AGeV.  
Master's thesis, Universität Frankfurt, 2008.
- [LSW94] M.F.M. Lutz, A. Steiner, and W. Weise.  
Kaons in baryonic matter.  
*Nucl.Phys.*, A574:755–787, 1994.
- [Lut99] G. Lutz.  
*Semiconductor Radiation Detectors*.  
Springer, 1999.
- [Lut04] M.F.M. Lutz.

- Chiral symmetry and strangeness at SIS energies.  
*Prog.Part.Nucl.Phys.*, 53:125–136, 2004.
- [M<sup>+</sup>13] K. Moriya et al.  
Measurement of the  $\Sigma\pi$  photoproduction line shapes near the  $\Lambda(1405)$ .  
*arXiv*, nucl-ex/1301.5000, 2013.
- [Mac11] J. Machacek.  
Time Resolution and Radiation Damage Analysis for the HADES Pion Beam Tracker.  
Bachelor Thesis, Technische Universität München, 2011.
- [Mar81] Alan D. Martin.  
Kaon - Nucleon Parameters.  
*Nucl.Phys.*, B179:33, 1981.
- [Mes12] Mesytec.  
*Welcome to mesytec - detector readout systems*.  
<http://www.mesytec.com/silicon.htm>, 2012.
- [Mün10] Robert Münzer.  
Search for  $ppK^-$  state in p+p @ 3.1 GeV.  
*PoS*, BORMIO2010:018, 2010.
- [MOR05] V.K. Magas, E. Oset, and A. Ramos.  
Evidence for the two pole structure of the  $\Lambda(1405)$  resonance.  
*Phys.Rev.Lett.*, 95:052301, 2005.
- [MS10] Kei Moriya and Reinhard Schumacher.  
Properties of the  $\Lambda(1405)$  Measured at CLAS.  
*Nucl.Phys.*, A835:325–328, 2010.
- [NK87] Ann E. Nelson and David B. Kaplan.  
Strange Condensate Realignment in Relativistic Heavy Ion Collisions.  
*Phys.Lett.*, B192:193, 1987.
- [Nor98] W. Norenberg.  
Restoration of chiral symmetry in nucleus-nucleus collisions around 10 GeV/u.  
*Acta Phys.Polon.*, B29:3259–3268, 1998.
- [NOTR99] J.C. Nacher, E. Oset, H. Toki, and A. Ramos.  
Photoproduction of the  $\Lambda(1405)$  on the proton and nuclei.  
*Phys.Lett.*, B455:55–61, 1999.
- [ORB02] E. Oset, A. Ramos, and C. Bennhold.  
Low lying  $S = -1$  excited baryons and chiral symmetry.  
*Phys.Lett.*, B527:99–105, 2002.
- [OT06] E. Oset and H. Toki.  
A Critical analysis on deeply bound kaonic states in nuclei.  
*Phys.Rev.*, C74:015207, 2006.
- [P<sup>+</sup>04] S. Prakhov et al.  
 $K^-p \rightarrow \pi^0\pi^0\Sigma^0$  at  $p_{K^-} = 514\text{MeV}/c - 750\text{MeV}/c$  and comparison with other  $\pi^0\pi^0$  production.  
*Phys.Rev.*, C70:034605, 2004.
- [Ple12] D. Pleiner.  
Hunting the  $ppK^-$ : A kinematic refit for the exclusive analysis of the reaction  $pp \rightarrow pK^+\Lambda$ .  
Master's thesis, Technische Universität München, 2012.
- [PS95] M. E. Peskin and D. V. Schröder.  
*An introduction to quantum field theory*.

- Wetview Press, 1995.
- [RBW05] Th. Roth, M. Buballa, and J. Wambach.  
Medium modifications of antikaons in dense matter.  
*arXiv*, nucl-th/0504056, 2005.
- [RKP96] K. Riechmann, K.T. Knoepfle, and V.M. Pugatch.  
Pion and proton induced radiation damage to silicon detectors.  
*Nucl.Instrum.Meth.*, A377:276–283, 1996.
- [RO00] A. Ramos and E. Oset.  
The Properties of  $\bar{K}$  in the nuclear medium.  
*Nucl.Phys.*, A671:481–502, 2000.
- [RW00] R. Rapp and J. Wambach.  
Chiral symmetry restoration and dileptons in relativistic heavy ion collisions.  
*Adv.Nucl.Phys.*, 25:1, 2000.
- [S<sup>+</sup>05] S. Schael et al.  
Branching ratios and spectral functions of tau decays: Final ALEPH measurements and physics implications.  
*Phys.Rept.*, 421:191–284, 2005.
- [S<sup>+</sup>06] W. Scheinast et al.  
First observation of in-medium effects on phase space distributions of antikaons measured in proton-nucleus collisions.  
*Phys.Rev.Lett.*, 96:072301, 2006.
- [SB08] Jürgen Schaffner-Bielich.  
Hypernuclear Physics for Neutron Stars.  
*Nucl.Phys.*, A804:309–321, 2008.
- [SC98] A. Sibirtsev and W. Cassing.  
Strangeness production in proton proton collisions.  
*arXiv*, nucl-th/9802019, 1998.
- [Sch08] A. Schmah.  
*Produktion von Seltsamkeit in Ar+KCl Reaktionen bei 1.756 AGeV mit HADES*.  
PhD thesis, Technische Universität Darmstadt, 2008.
- [Sch09] A. Schmah.  
Private communication.  
2009.
- [Sch12] R. A. Schumacher.  
Private communication.  
2012.
- [SHHM07] A. Sibirtsev, J. Haidenbauer, H.-W. Hammer, and U.-G. Meissner.  
The  $pp \rightarrow K^+ \Sigma^+ n$  cross section from missing mass spectra.  
*Eur.Phys.J.*, A32:229–241, 2007.
- [Sie10a] J. Siebenson.  
Exclusive analysis of the  $\Lambda(1405)$  resonance in the charged ( $\Sigma\pi$ ) decay channels in proton proton reactions with HADES.  
Master’s thesis, Technische Universität München, 2010.
- [Sie10b] Johannes Siebenson.  
Analysis techniques for the  $\Lambda(1405)$  in p+p reactions.  
*AIP Conf.Proc.*, 1322:389–393, 2010.
- [SKV<sup>+</sup>] B. Spruck, W. König, S. Visotski, R. S. Simon, R. Novotny, and V. Metag.  
*INSTRUMENTS-METHODS-19 Progress on Pion Beam for HADES*.

- <http://citeseerx.ist.psu.edu/viewdoc/summary?doi=10.1.1.161.6489>.
- [SS94] C.M. Shakin and W.-D. Sun.  
Properties of the rho meson in nuclear matter.  
*Phys.Rev.*, C49:1185–1189, 1994.
- [STC<sup>+</sup>12] Irina Sagert, Laura Tolos, Debarati Chatterjee, Jürgen Schaffner-Bielich, and Christian Sturm.  
Soft nuclear equation-of-state from heavy-ion data and implications for compact stars.  
*Phys.Rev.*, C86:045802, 2012.
- [Stu01] C. Sturm.  
*K<sup>+</sup>-Produktion in Schwerionenreaktionen als Sonde für die Inkompressibilität von Kernmaterie*.  
PhD thesis, Technische Universität Darmstadt, 2001.
- [TEFK73] D.W. Thomas, A. Engler, H.E. Fisk, and R.W. Kraemer.  
Strange particle production from  $\pi^-p$  interactions at 1.69 GeV/c.  
*Nucl.Phys.*, B56:15–45, 1973.
- [TST99] Kazuo Tsushima, Alexander Sibirtsev, and Anthony William Thomas.  
Resonance model study of kaon production in baryon baryon reactions for heavy ion collisions.  
*Phys.Rev.*, C59:369–387, 1999.
- [V<sup>+</sup>10] Yu. Valdau et al.  
The energy dependence of the  $pp \rightarrow K^+n\Sigma^+$  reaction close to threshold.  
*Phys.Rev.*, C81:045208, 2010.
- [VHQ72] F. Von Hippel and C. Quigg.  
Centrifugal-barrier effects in resonance partial decay widths, shapes, and production amplitudes.  
*Phys.Rev.*, D5:624–638, 1972.
- [W<sup>+</sup>87] A.B. Wicklund et al.  
Study of the Reaction  $p_{polarized}p \rightarrow p\pi^+n$  with polarized Beam from 1.18 GeV/c to 1.98 GeV/c.  
*Phys.Rev.*, D35:2670, 1987.
- [W<sup>+</sup>11] F.W. Wieland et al.  
Study of the reaction  $\gamma p \rightarrow K^+\Lambda(1520)$  at photon energies up to 2.65 GeV.  
*Eur.Phys.J.*, A47:47, 2011.
- [WCSB12] S. Weissenborn, D. Chatterjee, and J. Schaffner-Bielich.  
Hyperons and massive neutron stars: the role of hyperon potentials.  
*Nucl.Phys.*, A881:62–77, 2012.
- [Web11] M. Weber.  
*Dielektronen Spektroskopie in kalter Kernmaterie*.  
PhD thesis, Technische Universität München, 2011.
- [Wei12] W. Weise.  
Private communication.  
2012.
- [Wir12] J. Wirth.  
Development of a cooling system for a silicon particle detector.  
Bachelor Thesis, Technische Universität München, 2012.
- [Wun92] R. Wunstorf.  
*Systematische Untersuchungen zur Strahlenresistenz von Silizium-Detektoren für die Verwendung in Hochenergiephysik-Experimenten*.

- PhD thesis, Universität Hamburg, 1992.
- [Y<sup>+</sup>10] T. Yamazaki et al.  
Indication of a deeply bound compact  $K^-pp$  state formed in the  $pp \rightarrow p\Lambda K^+$  reaction at 2.85 GeV.  
*Phys.Rev.Lett.*, 104:132502, 2010.
- [Z<sup>+</sup>08] I. Zychor et al.  
Shape of the  $\Lambda(1405)$  hyperon measured through its  $\Sigma^0\pi^0$  Decay.  
*Phys.Lett.*, B660:167–171, 2008.



# Danksagung

Ich bin im Jahre 2008 der Gruppe von Prof. Dr. Laura Fabbietti beigetreten und wurde dort sofort herzlich von dem ganzen Team aufgenommen. Für die freundliche Atmosphäre und die große Hilfsbereitschaft während meiner Werkstudentenzeit, Diplomandenzeit aber speziell der Dissertationszeit, möchte ich mich bei allen Kollegen bedanken.

Ganz besonderer Dank gilt natürlich Prof. Dr. Laura Fabbietti. Wir haben zusammen sehr viel erreicht und ich konnte eine Menge von ihr lernen. Dabei hat sie mich stets gefordert, was zum Teil mit viel Anstrengung und Arbeit verbunden war. Auf der anderen Seite hat sie mich auch während der gesamten Zeit gefördert, mich auf Konferenzen geschickt und mir Verantwortung übertragen. Die Mischung macht's, und so hatte ich doch eine sehr produktive Zeit bei ihr. Dafür möchte ich mich herzlich bedanken und ich wünsche ihr, dass sie weiterhin eine so tolle Gruppe unter sich hat.

Des Weiteren danke ich Dr. Alexander Schmah für die tolle Betreuung während der Diplomarbeit. Von ihm habe ich wirklich eine Menge gelernt, was mir dann in der Dissertation sehr geholfen hat.

Großer Dank geht vor allem an Eliane Epple und Dr. Kirill Lapidus, die mir während der Zeit der Doktorarbeit immer mit gutem Rat zur Seite standen. Unsere Zusammenarbeit und unsere Diskussionen über Physik haben mir immer sehr viel Spass gemacht. Speziell die "secret projects" von Kirill haben stets mein Interesse geweckt, ohne dass ich jemals einen Einblick in diese bekommen hätte.

Großer Dank gilt auch Robert Münzer und Rafal Lalik, mit denen ich eng während der Detektorentests für den Pion Tracker zusammengearbeitet habe. Von beiden konnte ich viel über Elektronik und Hardware lernen. Gerade während der Strahlzeitschichten war ihre Kompetenz besonders hilfreich.

Des Weiteren möchte ich mich bei meinen Kollegen Jia-Chii Berger-Chen und Martin Berger bedanken. Sie waren meine treuen Rauch-Kumpanen für die entspannende Zigarette zwischendurch und wir hatten zusammen sehr viel Spass. Ganz besonders Martins Anti-Welt-Einstellung war immer sehr erfrischend und konnte mich oft aufheitern.

Für eine entspannte Zusammenarbeit während unserer langen GSI Aufenthalte danke ich Dr. Jürgen Friese, der mich in die Geheimnisse des RICH-Detektors eingeweiht hat. Spezieller Dank gilt den HADES Mitgliedern Prof. Dr. Piotr Salabura, Dr. Wolfgang König und Dr. Michael Weber, mit denen ich sehr viel über Physik diskutiert habe, die mir tolle Ratschläge gegeben haben und von denen ich viel lernen konnte. Allgemein möchte ich mich bei der ganzen HADES Kollaboration bedanken, dessen Mitglieder sich wirklich durch wahnsinnig freundschaftlichen Umgang und große Hilfsbereitschaft auszeichnen.

Der größte Dank gilt aber meinen Eltern Christiane und Michael, meiner Schwester Juliane und meiner Freundin Andrea. Sie hatten immer ein offenes Ohr bei allen meinen Problemen und waren mir stets eine große Stütze. Auch wenn ich manchmal genervt war und sie nicht immer fair behandelt habe, haben sie mir das nie übel genommen. Ohne sie hätte ich das alles nicht geschafft.